

**Melting and fragmentation  
of Antarctic tabular icebergs  
tracked with satellite remote sensing  
and artificial intelligence**

**Anne Braakmann-Folgmann**

The University of Leeds

School of Earth and Environment

Submitted in accordance with the requirements for the degree of  
Doctor of Philosophy (PhD)

July, 2023



## Intellectual Property and Publication Statement

The candidate confirms that the work submitted is her own, except where work which has formed part of jointly authored publications has been included. The contribution of the candidate and the other authors to this work has been explicitly indicated below. The candidate confirms that appropriate credit has been given within the thesis where reference has been made to the work of others.

The research described in **chapter 2** has been published as:

Braakmann-Folgmann, A., Shepherd, A., Ridout, A., 2021. Tracking changes in the area, thickness, and volume of the Thwaites tabular iceberg “B30” using satellite altimetry and imagery. *The Cryosphere* 15, 3861–3876. <https://doi.org/10.5194/tc-15-3861-2021>.

Anne Braakmann-Folgmann designed the study together with her supervisor, Andy Shepherd. Andy Ridout provided pre-processed CryoSat elevations. Anne Braakmann-Folgmann then computed iceberg freeboard, area, and volume change, calculated the uncertainties, prepared the figures, wrote the manuscript and revised it according to the reviewers’ comments. Andy Shepherd supervised the work and suggested edits to the manuscript.

The research described in **chapter 3** has been published as:

Braakmann-Folgmann, A., Shepherd, A., Gerrish, L., Izzard, J., Ridout, A., 2022. Observing the disintegration of the A68A iceberg from space. *Remote Sens. Environ.* 270, 112855. <https://doi.org/10.1016/j.rse.2021.112855>.

Anne Braakmann-Folgmann designed the study together with her supervisor, Andy Shepherd. Andy Ridout provided pre-processed CryoSat elevations. Jamie Izzard searched for ICESat-2 tracks sampling the iceberg and pre-processed them during his internship. Anne Braakmann-Folgmann took care of all other processing steps and data acquisition to compute iceberg freeboard. Deriving iceberg outlines and calculating iceberg area were split between Anne Braakmann-Folgmann, Laura Gerrish and Jamie Izzard. Laura Gerrish also produced Figure 1 in the paper. Anne Braakmann-Folgmann calculated iceberg thickness, volume, their changes over time, their corresponding uncertainties and prepared the other figures. Anne Braakmann-Folgmann also wrote the manuscript and adjusted it according to the reviewers’ comments. Andy Shepherd supervised the work and suggested edits to the manuscript.

The research described in **chapter 4** is under review for The Cryosphere and available as pre-print:

Braakmann-Folgmann, A., Shepherd, A., Hogg, D., Redmond, E., 2023. Mapping the extent of giant Antarctic icebergs with Deep Learning. EGU sphere [preprint], <https://doi.org/10.5194/egusphere-2023-858>

Anne Braakmann-Folgmann designed the study together with her supervisors Andy Shepherd and David Hogg. Ella Redmond clicked most of the iceberg outlines, which are used as training data, during her internship, supervised by Anne Braakmann-Folgmann. Anne Braakmann-Folgmann also generated some of the outlines. Anne Braakmann-Folgmann then designed and implemented the U-net architecture, implemented the comparison methods, plotted the figures and wrote the manuscript. Andy Shepherd and David Hogg supervised the work and suggested edits to the manuscript.

This copy has been supplied on the understanding that it is copyright material and that no quotation from the thesis may be published without proper acknowledgement. The right of Anne Braakmann-Folgmann to be identified as author of this work has been asserted by her in accordance with the Copyright, Designs and Patents Act 1988.

© 2023 The University of Leeds and Anne Braakmann-Folgmann

## Acknowledgements

This work was funded by the Barry Slavin Foundation and the UK Natural Environment Research Council (NERC) through National Capability funding, undertaken by a partnership between the Centre for Polar Observation and Modelling and the British Antarctic Survey. I was hosted in the Centre for Polar Observation and Modelling (CPOM) at the University of Leeds.

I would like to express my sincere thanks to my supervisors Prof. Andrew Shepherd and Prof. David Hogg for their guidance, advice and encouragement. I am especially thankful to Andy for creating various opportunities and establishing important contacts, so I could participate in Greenland fieldwork, spend three months at the European Space Agency's  $\phi$ -lab, attend many conferences and publish my findings not only in scientific papers, but also communicate them to a wider public through the media.

Many thanks to my examiners Prof. Anna E. Hogg and Prof. Christian Haas for taking the time to read my thesis and conduct the viva with me. I highly appreciate it! And thank you to Prof. Amanda Maycock for chairing the viva.

I would also like to thank my office mates Amy, Heather, Inès, Isobel, Nitin and Tom as well as Charlie and Lucy for some fun memories including the virtual baking sessions throughout lockdown.

Mama und Papa, vielen herzlichen Dank für eure Unterstützung, Beratung und Aufmunterung! Danke an meine Freunde, die immer an mich geglaubt und diese Arbeit unterstützt haben - vor allem Jule, Moritz, Mareike, Kerstin und Anika.

Thank you also to Daniel, Ronan, Yvan, Vania and Trys for sharing my enthusiasm for ice and helpful conversations!

Finally, thank you to Dr. Veit Helm for inspiring me to pursue a career in polar science during my internship at the Alfred-Wegener-Institute in 2015.



## Abstract

Icebergs release cold, fresh water and terrigenous nutrients as they drift and melt, influencing the local ocean properties and encouraging sea ice formation and biological production. To locate and quantify the freshwater flux from Antarctic icebergs, changes in their area and thickness have to be monitored along their trajectories. In this thesis, I developed novel methodology and datasets from satellite remote sensing observations to quantify the freshwater flux from giant Antarctic icebergs as accurately and efficiently as possible.

First, I investigated and improved the calculation of iceberg thickness from CryoSat-2 satellite altimetry observations. I found that employing consistently processed elevations is essential to detect changes in iceberg freeboard. Moreover, I developed a method to account for the evolution of the snow layer on icebergs during multi-annual drift and assessed its impact on iceberg thickness estimates. Combining these with measurements of iceberg area derived from satellite imagery, I estimate the volume loss ( $378 \pm 57 \text{ km}^3$ ) and freshwater flux ( $106 \pm 35 \text{ Gt}$ ) from the B30 iceberg over 6.5 years.

Next, I built on this methodology and applied it to the A68A iceberg, whose melting affected the ecosystem near South Georgia. I further improved the method by adding ICESat-2 data and automatically collocating altimetry tracks over the floating iceberg with a map of initial iceberg thickness. Overall, A68A released  $802 \pm 34 \text{ Gt}$  of ice along its trajectory and  $152 \pm 61 \text{ Gt}$  through basal melting near South Georgia.

Finally, I developed a deep neural network (based on U-net) to map the extent of giant icebergs in Sentinel-1 imagery. While each manual delineation takes several minutes, U-net reduces the time to 0.01 sec. Evaluating the performance compared to two standard segmentation techniques, I found that U-net achieves a higher  $F_1$  score (0.84 versus 0.62) and is more robust to sea ice, other icebergs and nearby coast.



# Contents

<b>1 INTRODUCTION TO ANTARCTIC TABULAR ICEBERGS</b> .....	1
1.1. Definition and main characteristics of icebergs .....	2
1.2. Importance of icebergs .....	4
1.2.1. Icebergs as a hazard .....	4
1.2.2. Impact on local oceanography and sea ice .....	5
1.2.3. Impact on local biology .....	6
1.2.4. Importance for glaciology .....	8
1.3. Iceberg observations .....	10
1.3.1. Detection of icebergs .....	10
1.3.2. Iceberg abundance and distribution .....	13
1.3.3. Iceberg drift .....	15
1.3.4. Iceberg melting .....	18
1.3.5. Iceberg fragmentation .....	23
1.3.6. Iceberg volume loss and freshwater input .....	25
1.4. Main remaining challenges .....	27
1.5. Thesis aim .....	29
1.6. Thesis objectives .....	29
1.7. Thesis structure .....	30
References .....	31
<b>2 TRACKING CHANGES IN THE AREA, THICKNESS, AND VOLUME OF THE THWAITES TABULAR ICEBERG “B30” USING SATELLITE ALTIMETRY AND IMAGERY</b> .....	43
Abstract .....	44
2.1. Introduction .....	44
2.2. Data and methods .....	47
2.2.1. Iceberg location .....	48
2.2.2. Initial iceberg shape, size and calving position .....	49
2.2.3. Iceberg area .....	49
2.2.4. Iceberg orientation .....	52
2.2.5. Initial iceberg freeboard .....	52
2.2.6. Iceberg freeboard change .....	54
2.2.7. Iceberg thickness .....	56
2.3. Results and discussion .....	58
2.3.1. Iceberg area change .....	58
2.3.2. Iceberg freeboard change .....	60
2.3.3. Iceberg thickness change .....	62
2.3.4. Iceberg volume and mass change .....	64
2.4. Conclusions .....	66
References .....	67
<b>3 OBSERVING THE DISINTEGRATION OF THE A68A ICEBERG FROM SPACE</b> .....	75
Abstract .....	76
3.1. Introduction .....	76

3.2.	Data and methods .....	77
3.3.	Results .....	82
3.4.	Discussion .....	85
3.5.	Conclusions.....	89
	References.....	89
<b>4</b>	<b>MAPPING THE EXTENT OF GIANT ANTARCTIC ICEBERGS WITH DEEP LEARNING.....</b>	<b>97</b>
	Abstract .....	98
4.1.	Introduction.....	98
4.2.	Data and methods .....	100
4.2.1.	Sentinel-1 input imagery .....	101
4.2.2.	Grouping of input images according to environmental conditions.....	103
4.2.3.	Manual delineation of iceberg perimeters.....	104
4.2.4.	Iceberg segmentation with k-means and Otsu.....	105
4.2.5.	Iceberg segmentation with U-net.....	105
4.3.	Results and discussion .....	108
4.3.1.	Performance of the three methods.....	108
4.3.2.	Impact of iceberg size and different environmental conditions .....	109
4.3.3.	Comparison to previous studies .....	115
4.4.	Conclusions.....	116
	References.....	117
<b>5</b>	<b>CONCLUSION, SYNTHESIS AND FUTURE WORK .....</b>	<b>123</b>
5.1.	Summary of main results.....	124
5.1.1.	Tracking changes in the area, thickness, and volume of the Thwaites tabular iceberg “B30” using satellite altimetry and imagery .....	125
5.1.2.	Observing the disintegration of the A68A iceberg from space .....	128
5.1.3.	Mapping the extent of giant Antarctic icebergs with Deep Learning .....	130
5.2.	Synthesis of principal findings .....	133
5.2.1.	New datasets of giant iceberg decay.....	133
5.2.2.	Methodological advances to derive iceberg thickness.....	135
5.2.3.	Methodological advances to derive iceberg area .....	137
5.3.	Recommendations for future work.....	138
5.3.1.	Investigating snow on icebergs and its impact on radar penetration .....	138
5.3.2.	Improving U-net iceberg segmentation with more data.....	141
5.3.3.	Towards tracking freshwater input from giant icebergs operationally.....	143
5.4.	Concluding remarks.....	146
	References.....	147
	<b>APPENDIX A TRACKING CHANGES IN THE AREA, THICKNESS, AND VOLUME OF THE THWAITES TABULAR ICEBERG “B30” USING SATELLITE ALTIMETRY AND IMAGERY .....</b>	<b>155</b>
	<b>APPENDIX B OBSERVING THE DISINTEGRATION OF THE A68A ICEBERG FROM SPACE.....</b>	<b>173</b>
	<b>APPENDIX C MAPPING THE EXTENT OF GIANT ANTARCTIC ICEBERGS WITH DEEP LEARNING .....</b>	<b>179</b>

## List of Figures

Figure 1.1: Cartoon of how a tabular iceberg is formed from a fractured ice shelf. Image credit: Megan Thompson-Munson .....	3
Figure 1.2: Iceberg tracks from all named icebergs between 1978 and 2021 as given by Brigham Young University (Budge and Long, 2018). The naming sectors (A-D) are also shown.	4
Figure 1.3: Anomalies in a) sea surface salinity b) sea surface temperature c) sea ice fraction and d) convective layer depth caused by the inclusion of icebergs in a model. Extracted from Jongma <i>et al.</i> (2009). .....	6
Figure 1.4: Physical, chemical and biological processes induced by icebergs. Extracted from Smith <i>et al.</i> (2013). .....	7
Figure 1.5: Contribution of ice shelf areas to the buttressing of upstream glaciers. Passive shelf areas, which do not lead to a significant speed-up when they are removed, are delineated in red and their percentage is given for each ice shelf. Extracted from Fürst <i>et al.</i> (2016) .....	9
Figure 1.6: Iceberg detection in a SAR image. Extracted from Silva and Bigg (2005) and re-coloured for better differentiation.....	11
Figure 1.7: Backscatter coefficients (range, mean and standard deviation) of different surfaces (marginal ice zone (MIZ), rough first year sea ice (FYR), smooth first year sea ice (FYS), icebergs, multi-year sea ice (MY) and open water (OW) in different wind speeds) in the Weddell Sea. Extracted from Drinkwater (1998) .....	12
Figure 1.8: Mean monthly volume (km <sup>3</sup> per 100x100 km <sup>2</sup> grid cell) of (a) small icebergs in open ocean between 1992-2014 and (b) large icebergs between 2002-2012. The lines in (a) indicate the mean sea ice extent, which impacts where icebergs can be detected. Blue is the mean annual maximum extend, black the mean maximum extend in summer and red the minimum extend in summer. Extracted from Tournadre <i>et al.</i> (2016)..	14
Figure 1.9: Inter-annual variation of total iceberg volume in the open Southern Ocean (All, green) and different sectors (South Atlantic (SA) in black, South Indian (SI) in red and South Pacific (SP) in blue). The seasonal variation is because the detection method only works in open ocean and hence sea ice extent has a large influence on the number of detectable icebergs. It does not reflect actual seasonal changes. Therefore, the yearly maxima are the most representative. Extracted from Tournadre <i>et al.</i> (2016).....	15
Figure 1.10: Main drivers of iceberg drift and resulting iceberg motion. W is wind-related forcing, C is the Coriolis force and O is ocean-current drag. Extracted from Gladstone, Bigg and Nicholls (2001).....	16
Figure 1.11: Exit zones 1-4b, where icebergs leave the Antarctic Coastal Current and turn northwards. These zones are characterised by higher iceberg concentration (colour map). Extracted from Orheim <i>et al.</i> (2022) .....	17
Figure 1.12: Iceberg melt rate (m per day) as a function of ocean temperature above melting. Dots show average side melt rates and triangles represent melting at the base. The relationship derived by Morgan and Budd (1978) is included as a dotted line. Extracted from Russell-Head (1980) .....	19
Figure 1.13: Schematic of processes causing iceberg melting. Extracted from Bigg (2015) and slightly modified .....	20
Figure 1.14: Lab experiment of iceberg melting without (left) and with (right) a background current. From top to bottom, each image is taken 2 minutes apart. The ice block is dyed blue to visualise melting and meltwater distribution. Extracted from Hester <i>et al.</i> (2021).....	21

Figure 1.15: Maps of iceberg freeboard over time together with the location of individual altimetry tracks. Extracted from Jansen, Schodlok and Rack (2007) .....	22
Figure 1.16: Impact of including iceberg fragmentation in a model. The inclusion of a break-up process matches iceberg area observations for the B17a iceberg much better. Extracted from England <i>et al.</i> (2020) .....	24
Figure 1.17: Area change of two giant tabular icebergs. Extracted from Scambos <i>et al.</i> (2008) .....	25
Figure 1.18: Volume loss of two giant tabular icebergs B17A and C19A. Extracted from Bouhier <i>et al.</i> (2018) .....	26
Figure 1.19: Meltwater input from precipitation-evaporation (first panel), icebergs (second panel) and sea ice (third panel) and relative contribution of icebergs compared to precipitation-evaporation and sea ice (lower panels respectively). Extracted from Rackow <i>et al.</i> (2017) .....	27
Figure 2.1: Trajectory of the B30 iceberg as recorded by the Antarctic Iceberg Tracking Database (Budge and Long, 2018): After calving from the Thwaites Ice Shelf in 2012, it followed the coastal current westwards, started drifting north in 2017 and eventually disintegrated in 2019. Black dots mark the positions where CryoSat-2 overflights over the iceberg are available, circles depict the positions of the MODIS and Sentinel-1 images used in this study .....	48
Figure 2.2: Outlines of the B30 iceberg derived from satellite imagery. a) Initial shape (red polygon) of the B30 iceberg determined from MODIS images after calving; the background is a MODIS image on 11 September 2012. b) Polygon outlines derived from further MODIS and Sentinel-1 imagery plotted in polar stereographic projection and used to calculate area change of the B30 iceberg. ....	50
Figure 2.3: Satellite imagery with near-coincident CryoSat-2 tracks of iceberg freeboard and the manually transformed initial polygon shape plotted on top. The initial polygons are used to determine the relative position of each new overpass. ....	52
Figure 2.4: Initial freeboard heights of the B30 iceberg overlain on a MODIS image on 19 March 2012 (before calving). a) Filtered CryoSat-2 measurements of 145 days before calving, b) Gridded CryoSat-2 data, c) Standard deviation of the gridding, d) Number of measurements per grid cell .....	53
Figure 2.5: Example of CryoSat-2 freeboard measurements along one track. The blue line shows which heights were identified as iceberg and the red line shows the remaining heights after filtering out crevasses. ....	54
Figure 2.6: Illustration of how iceberg thickness is calculated at calving (a) and after calving (b) with the different processes affecting iceberg thickness that we account for labelled in red. The ice density profile is calculated using Eq. 3 with ice densities of the Thwaites Ice Shelf by Ligtenberg, Helsen and Van Den Broeke (2011). ....	57
Figure 2.7: Area change of the B30 iceberg from polygons delineated in satellite imagery with their uncertainty (red) and approximations using orthogonal axes provided by the National Ice Center (NIC) assuming an elliptical shape (blue) or using the arc lengths of CryoSat-2 overflights assuming a circular shape (black) over time (a) and as scatter plot (b). To fit the NIC trend line in (a) we only use unique values of orthogonal axes length (thick blue dots). These also define the dates of comparison in (b). ....	59
Figure 2.8: Freeboard change of the B30 iceberg. a-l) Freeboard difference in each grid cell sampled by colocated CryoSat-2 overpasses; the $\Delta t$ values give the time difference between the CryoSat-2 overpass and the corresponding satellite image as an indication of the collocation uncertainty due to iceberg drift; Negative values indicate that the image was taken before the CryoSat overpass. m) mean difference of each new overpass along time. CryoSat-2 tracks that have been colocated are marked with a diamond, but all available CryoSat-2 overpasses have been used to calculate a	

moving mean and fit a polynomial; The shading shows the standard deviations. n) scatter plot of freeboard change from colocated CryoSat-2 tracks versus the same tracks used without collocation .....	61
Figure 2.9: Evolution of the B30 iceberg properties: a) Ice density and snow density, b) Snow water equivalent (SWE) and snow depth accumulation on the B30 iceberg, c) Degree hours that the B30 iceberg experienced, and d) Thickness change of the B30 iceberg with snow accumulation taken into consideration or without. Uncertainties are plotted as shaded areas. ....	63
Figure 2.10: Volume change of the B30 iceberg divided into loss due to basal melting (thickness change, blue) and due to fragmentation (area change, red), as well as total volume loss (black). ....	65
Figure 3.1: Trajectory of A68A (circles colored by date) and historic icebergs (yellow lines, Budge & Long, 2018) overlain on a bathymetric map (GEBCO Compilation Group, 2019; O. Hogg et al., 2016). Selected outlines (date colour coded), altimetry overpasses (grey lines with black marking the parts that sample the iceberg) and key dates are also shown. Panels b and c are zoom regions of interest. ....	77
Figure 3.2: Calculation of initial iceberg freeboard map: (a) CryoSat tracks over the Larsen-C Ice Shelf over 1 year (12 July 2016 - 11 July 2017) before the iceberg calved, cut to the area that later formed the iceberg. (b) The same measurements gridded at 2 km and empty grid cells filled with linear interpolation. (c) Standard deviation within each grid cell. (d) Number of observations averaged per grid cell. The background shows a Sentinel-1 image on 10 July 2017 .....	78
Figure 3.3: Colocation of a sample ICESat-2 track and the corresponding Sentinel-1 image on 18 September 2019: For each altimetry overpass a near-coincident image is used to derive the iceberg's outline at the time of the new overpass (red, panel a). The new outline is transformed to maximize the overlapping area with the previous outline (blue, panel b). This is done iteratively, so we know the transformation of the previous polygon with respect to the initial polygon (black) and can transform the new overpass to the initial situation (panel c). We then grid the new track on the same grid as the initial freeboard measurements and difference it with these initial heights (panel d) .....	79
Figure 3.4: Evolution of iceberg properties based on ERA-5 Reanalysis data (Copernicus Climate Change Service, 2018): (a) Iceberg density and snow density; (b) snow depth and snow water equivalent (SWE) .....	81
Figure 3.5: Maps of the A68A iceberg thickness when it was still part of the Larsen-C Ice Shelf (a) and at later dates as it drifted through the Weddell and Scotia Seas (b-d). The initial thickness is superimposed on a Sentinel-1 image acquired on 10 July 2017, and the region from which A68B was formed is also indicated. On later dates, the iceberg thickness is computed at colocated altimetry overpasses (outlined gridcells, shaded according to date relative to the interval start) and modelled at the mid-point of each interval elsewhere .....	83
Figure 3.6: Time series of changes in the A68A iceberg area (a), freeboard (b), thickness (c) and volume (d). The vertical line marks 21 January 2020, when the iceberg moved from the Weddell to the Scotia Sea (see Figure 3.1). In panel (a) the background shading indicates sea ice concentration around the iceberg (OSI SAF, 2021) and in panel (c) the background shading indicates ocean temperature at the iceberg's base (Boyer et al., 2018).....	84
Figure 3.7: Scatter plots linking the iceberg decay processes to the environmental conditions: Fragmentation rate compared to sea ice concentration (a) and thinning rate compared to ocean temperature (b) in different regions along the trajectory .....	87

Figure 4.1: Spatial and temporal coverage of our dataset: The trajectories (by Budge and Long, 2018) of the seven selected icebergs are colour-coded according to time and black squares indicate the locations of the images used in this study. .... 102

Figure 4.2: Examples of input images (top row) and segmentation maps based on manually derived delineations (bottom row) in different environmental conditions. From left to right these are B31 in open ocean, B41 surrounded by sea ice, B42 with nearby fragments, C34 and another similar sized iceberg, B41 close to the coast and B30 appearing dark. .... 103

Figure 4.3: Modified U-net architecture as used in this paper ..... 107

Figure 4.4: Examples of input images (first column) and segmentation maps generated by U-net (second and third column showing the probability map and final segmentation map respectively), Otsu (fourth column), k-means (fifth column), and from manual delineations (last column). We picked these images for illustration to cover each category of environmental conditions twice and to include all icebergs (labelled on the right). .... 111

Figure 5.1: Evolution of ice and snow density (a), snow water equivalent (SWE) and snow depth (b), and iceberg thickness with and without considering a snow layer (c) over the lifetime of the B30 iceberg..... 126

Figure 5.2: Area estimates for the B30 iceberg over time based on manual delineation (red), compared to arc-lengths of altimetry overflights assuming a circular iceberg shape (black) and semi axes lengths provided by NIC assuming an elliptical iceberg shape (blue). Unique observations of semi axes are marked with thick blue dots and determine the times of correlation in (b). .... 127

Figure 5.3: Automated colocation of altimetry tracks over the floating iceberg with respect to the initial iceberg outline. The new outline (red) is derived from a near-coincident image (a) and the overlapping area to the previous outline (blue) is maximised (b). This iterative procedure yields the translation and rotation with respect to the initial outline (black, b) and allows us to transform the altimetry track accordingly (c). The new track is then gridded on the same grid as the initial freeboard and subtracted from it (d). .... 129

Figure 5.4: Impact of different environmental conditions on the skill of automated methods to segment Sentinel-1 images into the largest iceberg and background. The first column shows Sentinel-1 input images in different conditions (as labelled on the right), and the following columns show the segmentation maps produced by U-net, Otsu, k-means and manual delineation..... 132

Figure 5.5: Trajectories (a) and thickness change of B30 (b) and A68A (c) icebergs on common axes ..... 134

Figure 5.6: Trajectories of further icebergs, where datasets of iceberg imagery and outlines have been generated ..... 135

Figure 5.7: Maps of initial iceberg freeboard from individual tracks (a), gridded (b), and their standard deviation (c) of the B30 iceberg (top row) and the A68A iceberg (bottom row) ..... 137

Figure 5.8: Schematic overview of acquired/future data (black/grey boxes) and useful comparisons to investigate differences in penetration depth (green arrows) and snow depth (blue arrows) over an iceberg. Copyright of satellite and airplane icons: NASA, ESA, Airbus and BAS ..... 140

Figure 5.9: Time series of predicted outlines for the B35 iceberg. Outlines are derived from the binary segmentation maps using OpenCV's findContours function. a-u) shows the outlines of the different methods overlain on the input images and shaded in the respective colour. v) shows the resulting area estimates over time on a log scale . 144

## List of Tables

Table 3.1: Annual change in the A68A iceberg area, thickness and volume in different regions along its trajectory.....	85
Table 4.1: Performance metrics with standard deviations of U-net, Otsu and k-means across all test data sets (191 images). The median absolute area deviation (MAD) is given with 25 % and 75 % quantiles instead of standard deviation. Except the F1 score, all measures are percentages. Arrows indicate whether high (up) or low (down) numbers are desirable. The best score per metric is highlighted in bold. ....	109
Table 4.2: Performance of the three methods for each test data set (iceberg). The number of images per iceberg and their minimum and maximum size is also given. Note that most images of B30 are rescaled, so it appears smaller in the images. Except the F <sub>1</sub> score, all measures are percentages. Arrows indicate whether high (up) or low (down) numbers are desirable. The best score per iceberg and metric are highlighted in bold. ....	110
Table 4.3: Performance of the three methods in different environmental conditions. The first column also indicates how often these conditions occur in our data set. Except the F <sub>1</sub> score, all measures are percentages. Arrows indicate whether high (up) or low (down) numbers are desirable. The best values per category and metric are highlighted in bold.....	114



## Abbreviations

AIT	Antarctic Iceberg Tracking database
ASAR	Advanced Synthetic Aperture Radar
BYU	Brigham Young University
CFAR	Constant False Alarm Rate
CRISTAL	Copernicus polaR Ice and Snow Topography Altimeter
CRYOVEX	CRYOsat Validation EXperiment
CTD	Conductivity, Tempereature and Depth
DEFIANT	Drivers and Effects of Fluctuations in sea Ice in the ANTArctic
ECMWF	European Centre for Medium-Range Weather Forecasts
ENVISAT	ENVIronmental SATellite
ERA5	5 <sup>th</sup> generation of ECMWF Atmospheric Reanalysis
ERS	European Remote Sensing satellite
ESA	European Space Agency
EW	Extra Wide
FN	False Negatives
FP	False Positives
FYR	Rough First Year sea ice
FYS	Smooth First Year sea ice
GETASSE30	Global Earth Topography And Sea Surface Elevation at 30 arc second resolution
GIS	Geographic Information System
GPS	Global Positioning System
GPU	Graphics Processing Unit
GRD	Ground Range Detected
HH	Horizontal transmit and Horizontal receive
HV	Horizontal transmit and Vertical receive
ICESat	Ice, Cloud and land Elevation Satellite

IW	Interferometric Wide
MAD	Median Absolute Deviation
MAE	Mean Absolute Error
MIZ	Marginal Ice Zone
MODIS	MODerate resolution Imaging Spectroradiometer
MY	Multi-Year sea ice
NASA	National Aeronautics and Space Administration
NIC	National Ice Center
OW	Open Water
POCA	Point Of Closest Approach
RAM	Random-Access Memory
RGB	Red, Green, Blue
RMSE	Root Mean Square Error
SAR	Synthetic Aperture Radar
SARIn	Synthetic Aperture Radar INterferometric
SNAP	SeNtinel Application Platform
SWE	Snow Water Equivalent
TN	True Negatives
TP	True Positives

# 1

# INTRODUCTION TO ANTARCTIC TABULAR ICEBERGS

1.1.	Definition and main characteristics of icebergs.....	2
1.2.	Importance of icebergs .....	4
1.2.1.	Icebergs as a hazard .....	4
1.2.2.	Impact on local oceanography and sea ice .....	5
1.2.3.	Impact on local biology .....	6
1.2.4.	Importance for glaciology .....	8
1.3.	Iceberg observations.....	10
1.3.1.	Detection of icebergs .....	10
1.3.2.	Iceberg abundance and distribution .....	13
1.3.3.	Iceberg drift.....	15
1.3.4.	Iceberg melting .....	18
1.3.5.	Iceberg fragmentation .....	23
1.3.6.	Iceberg volume loss and freshwater input .....	25
1.4.	Main remaining challenges .....	27
1.5.	Thesis aim.....	29
1.6.	Thesis objectives .....	29
1.7.	Thesis structure.....	30
	References .....	31

In this chapter, I introduce icebergs as an important part of the polar environment. Starting with a definition of icebergs and their main characteristics, I then explain how they interact with and affect their surrounding while they drift and melt. I also outline what we can learn from them for climate science and glaciology. The next section summarises how icebergs have been monitored and what we have learnt about them so far, focussing on remote sensing observations of icebergs. Finally, I provide a synopsis of remaining challenges and state how my thesis work addresses some of these. Throughout the thesis, I focus on the largest, tabular icebergs around Antarctica.

### 1.1. Definition and main characteristics of icebergs

An iceberg is a large floating piece of ice, which has calved from an ice shelf or a glacier. According to the International Ice Patrol, icebergs have a freeboard (i.e. height above the waterline) of at least 5 m and a minimum length of 15 m. Smaller pieces are called bergy bits or growlers. Marine terminating glaciers are mainly found in the Arctic and around the Antarctic Peninsula and calve rather small icebergs due to their smaller, bedrock-confined calving front (Bigg, 2015; Sulak *et al.*, 2017; Dryak and Enderlin, 2020). Smaller icebergs can have a variety of shapes including sloped, dome-shaped, pinnacles, tabular and weathered (Romanov, Romanova and Romanov, 2012). In contrast, a large part of the Antarctic continent is fringed with ice shelves (Rignot *et al.*, 2013; Shepherd, Fricker and Farrell, 2018), which calve much larger tabular icebergs (Romanov, Romanova and Romanov, 2012; Bigg, 2015). These icebergs are usually several kilometres long and can reach lengths of hundreds of kilometres in exceptional cases (Arrigo and van Dijken, 2003; Bigg, 2015; Budge and Long, 2018). Because the ice shelves are already floating, the resulting icebergs have a relatively flat surface and are called tabular icebergs (Figure 1.1). Depending on the thickness of the mother ice shelf, these bergs have keel depths of 140 – 600 m (Dowdeswell and Bamber, 2007).

The U.S. National Ice Center (NIC) names and tracks icebergs that are at least 18.5 km (10 nautical miles) long or cover an area of at least 68.6 km<sup>2</sup> (20 square nautical miles). These are also called giant icebergs (Bigg, 2015). They are named with a letter indicating from which sector in Antarctica they calved (A = 0-90° W, Weddell Sea and Bellingshausen Sea, B = 90-180° W, Amundsen and Eastern Ross Sea, C=90-180° E, Western Ross and Wilkes Land Sea, D=0-90° E, Amery and Eastern Weddell Sea, see Figure 1.2) and a sequential number. A68, for example, was the 68<sup>th</sup> iceberg from the first quadrant recorded by NIC. When an iceberg breaks into two or more pieces and each of the pieces is large enough to be tracked, they are called A68A and A68B

for example, using ascending letters according to when the pieces have broken off. The larger of the two pieces, also referred to as the mother iceberg, receives the lower letter (e.g. A68A). In this thesis, I focus on such giant tabular Antarctic icebergs that are named and tracked by the NIC.

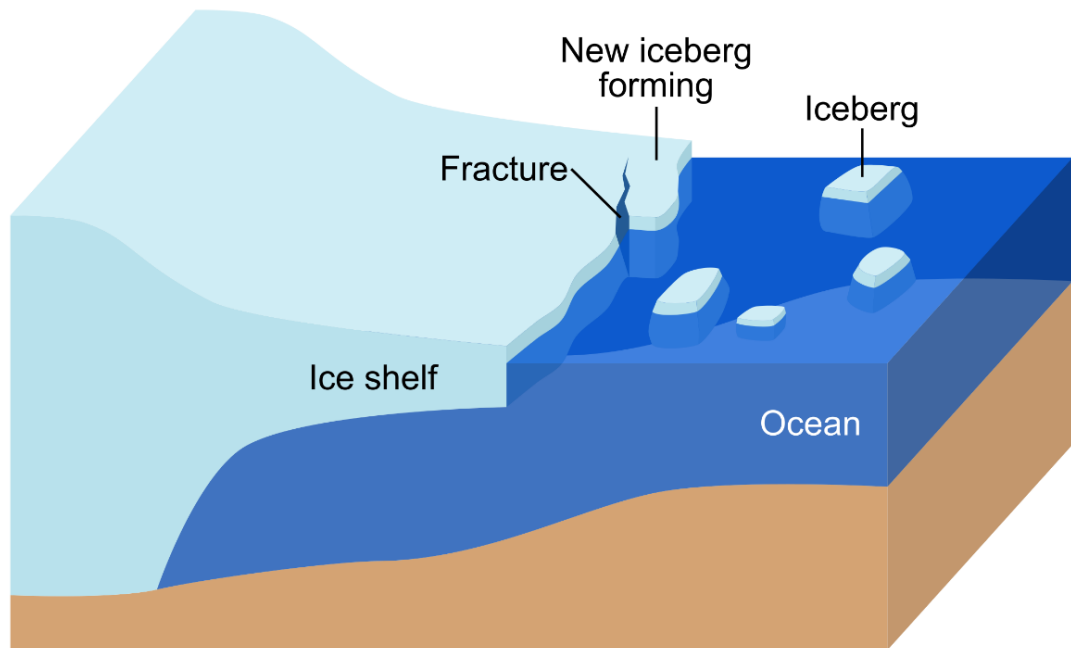


Figure 1.1: Cartoon of how a tabular iceberg is formed from a fractured ice shelf. Image credit: Megan Thompson-Munson

Annual calving flux estimates around Antarctica range from 1089 Gt (Rignot *et al.*, 2013) over 1300 and 1332 Gt (Gladstone, Bigg and Nicholls, 2001; Depoorter *et al.*, 2013) to 2016 Gt (Jacobs *et al.*, 1992). The most recent estimate by Greene *et al.* (2022) is 1411 Gt per year. This is in the same order of magnitude as basal ice shelf melting, meaning that icebergs account for about half of all ice loss from Antarctica (Depoorter *et al.*, 2013; Rignot *et al.*, 2013; Adusumilli *et al.*, 2020). This already makes them a significant component of the polar environments. Giant icebergs contribute about half of all iceberg calving (Duprat, Bigg and Wilton, 2016). At any time, about 50-90 large icebergs are tracked by the NIC, containing 6,000-18,000 km<sup>2</sup> of ice in total (Tournadre *et al.*, 2015). The largest iceberg on the NIC record was B15, which calved in 2000 from the Ross Ice Shelf and was initially 295 km long with an area of 11,000 km<sup>2</sup> (Arrigo and van Dijken, 2003; Budge and Long, 2018). Figure 1.2 shows all recorded positions of giant Antarctic icebergs since 1978.

## 1.2. Importance of icebergs

Icebergs influence and interact with their environment along their drift trajectory in a number of ways. They pose a hazard to shipping and marine infrastructure in case of collision. Scientifically, the release of cold, fresh meltwater is the main interest, as it influences the local ocean circulation, facilitates sea ice formation and fosters biological production. Moreover, icebergs indicate how ice shelves will react to warming ocean and air temperatures, as icebergs experience them already today when reaching lower latitudes.

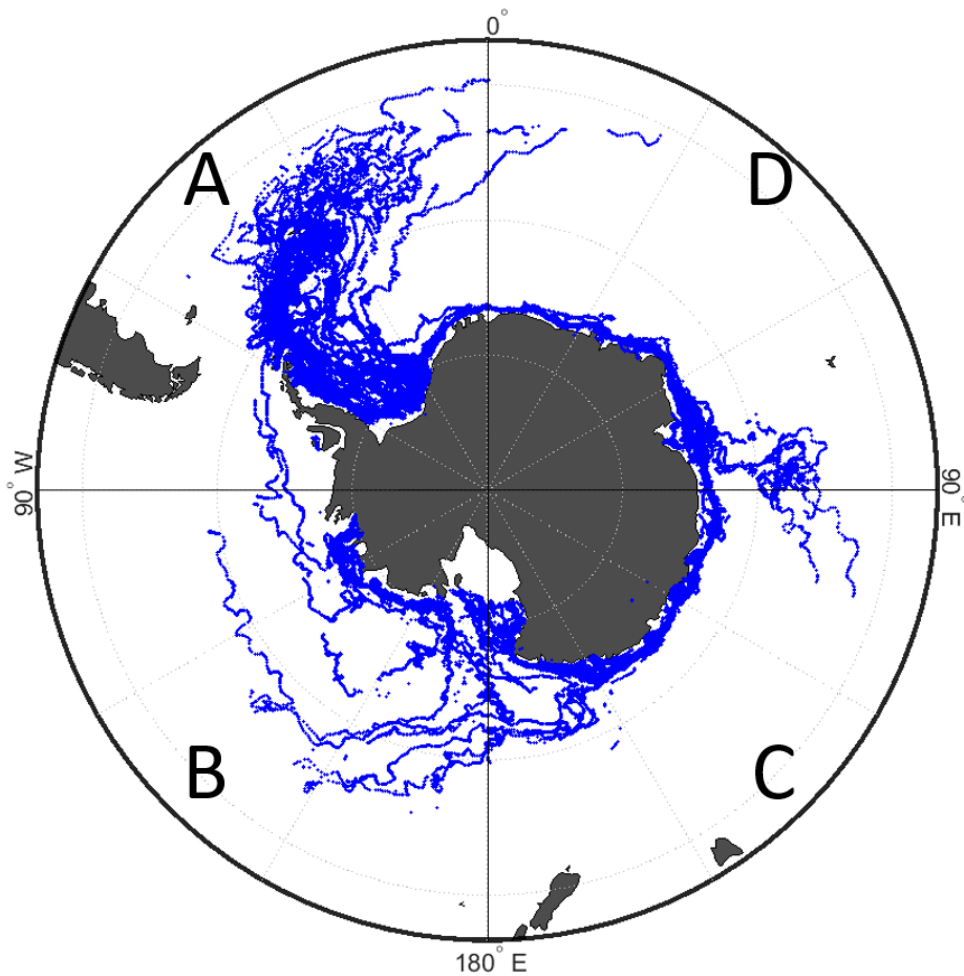


Figure 1.2: Iceberg tracks from all named icebergs between 1978 and 2021 as given by Brigham Young University (Budge and Long, 2018). The naming sectors (A-D) are also shown.

### 1.2.1. Icebergs as a hazard

The most commonly known hazard of icebergs lies in potential collisions with ships (Savage, 2007; Liu, Amdahl and Løset, 2011; Romanov, Romanova and Romanov, 2012; Bigg *et al.*, 2018). The International Ice Patrol was founded after *Titanic* sank due to a collision with an iceberg

(Murphy and Cass, 2012). Today, and especially in the Arctic also offshore structures are endangered by collision with icebergs (Savage, 2007; Eik and Gudmestad, 2010) and cables and pipelines can potentially be damaged by the deep iceberg keels (Savage, 2007; Bigg, 2015). Apart from man-made structures, icebergs also frequently collide with ice shelves or other icebergs, which can induce calving of new icebergs or fragmentation of the existing ones (MacAyeal *et al.*, 2008).

When icebergs ground on the sea bed, they leave plough marks, which are also used to derive iceberg- and hence ice shelf thicknesses of the past (Wise *et al.*, 2017). Vice versa, if iceberg thickness is known, iceberg grounding provide independent estimates of sea floor topography (Liu *et al.*, 2022). The downside is that grounding or scouring icebergs kill or damage the benthos and thereby mobilize carbon (Dunlop, Barnes and Bailey, 2014; Barnes, 2017). In case of occasional iceberg scouring, the regions become recolonised and more diverse in species. However, if scouring happens too frequently, the slow growing benthic fauna cannot recover (Gutt, 2001). The weight of a grounded, capsizing iceberg can also trigger submarine landslides (Normandeau *et al.*, 2021). And finally, depending on the location, the sheer size of a grounded iceberg can block access of penguin colonies to their feeding grounds (Kooyman *et al.*, 2007) or alter the local ocean currents (Robinson and Williams, 2012). It can also prevent sea ice from breaking up (Remy *et al.*, 2008), which in turn reduces phytoplankton growth and primary production (Arrigo *et al.*, 2002; Arrigo and van Dijken, 2003).

### **1.2.2. Impact on local oceanography and sea ice**

Icebergs release cold freshwater along their drift trajectory as they melt. The freshwater input leads to a cooling and freshening of the surrounding sea water (Jenkins, 1999; Helly *et al.*, 2011; Merino *et al.*, 2016 and Figure 1.3). Lower sea surface temperatures in turn also cool the local air temperature, acting as a negative climate feedback (Schloesser *et al.*, 2019). In terms of density change, the freshening effect dominates over the cooling and therefore density is reduced (Stephenson *et al.*, 2011). This means that the meltwater plume rises and as it rises, it causes ocean mixing and upwelling (Huppert and Turner, 1978; Helly *et al.*, 2011; Stephenson *et al.*, 2011 and Figure 1.4). On the other hand, meltwater intrusion causes an intensified stratification of the ocean, where less mixing and convective overturning take place (Merino *et al.*, 2016). This results in sub-surface warming and acts as a positive feedback (Schloesser *et al.*, 2019). While the cooling effect stimulates Antarctic bottom water formation, the stronger stratification rather hinders it (Jongma *et al.*, 2009). Modelling studies, however, found a net increase in production of Antarctic bottom water by 10 % due to dynamic icebergs (Jongma *et al.*, 2009; Martin

and Adcroft, 2010). Helly *et al.* (2011) analysed conductivity, temperature and depth (CTD) measurements around a giant iceberg and found that deep water down to 1500 m depth and 19 km away from were affected. The effects persist for at least 10 days after iceberg transit (Helly *et al.*, 2011).

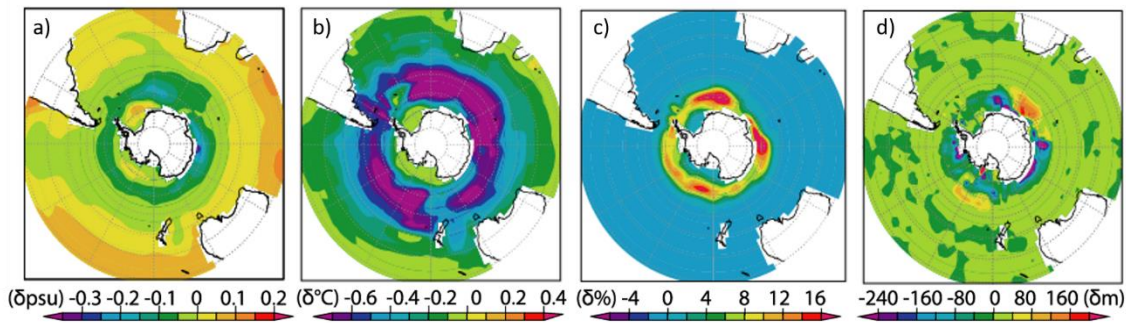


Figure 1.3: Anomalies in a) sea surface salinity b) sea surface temperature c) sea ice fraction and d) convective layer depth caused by the inclusion of icebergs in a model. Extracted from Jongma *et al.* (2009).

Because iceberg melting reduces the temperature and salinity of the surface water, it also facilitates sea ice formation (Jongma *et al.*, 2009; Marsh *et al.*, 2015). Jongma *et al.* (2009) found that sea ice extent grows by 12 % due to the freshening effect and by 6 % due to the cooling effect when icebergs were included in a model (Figure 1.3). Merino *et al.* (2016) found an increase in both sea ice concentration and sea ice thickness across the Southern Ocean except in the Bellingshausen Sea. Overall, annual mean sea ice volume is around 10 % higher and the amplitude of the seasonal cycle rises (Merino *et al.*, 2016). On local scales, icebergs provoke sea ice ridging upstream of their drift trajectory (Hunke and Comeau, 2011; Morison and Goldberg, 2012). Downstream they leave a wake of open water behind, where new ice can form (Hunke and Comeau, 2011; Morison and Goldberg, 2012; Bigg, 2015).

### 1.2.3. Impact on local biology

Apart from delivering cold freshwater during the melt process, icebergs also contain terrigenous nutrients, which are released as they melt, and act as a fertilizer to the surrounding ocean (Smith *et al.*, 2013 and Figure 1.4). In large parts of the Southern Ocean productivity is iron-limited (Raiswell *et al.*, 2008). Icebergs were found to deliver a manifold of bio-available iron to the Southern Ocean compared to atmospheric dust (Raiswell *et al.*, 2016). However, it is not yet well understood, how the iron is distributed within icebergs, i.e. different icebergs – even from the same glacier – exhibit varying concentrations and it is unclear whether e.g. the bottom contains more iron than upper layers (Hopwood *et al.*, 2019). Other research suggests that bergs from

the sectors A and D contain more nutrients due to the geology of this area (Duprat, Bigg and Wilton, 2016).

In addition to the release of micro-nutrients, upwelling further increases the availability of macro-nutrients and both foster biological production (Schwarz and Schodlok, 2009 and Figure 1.4). This mainly holds true for free-drifting icebergs in open water (Smith *et al.*, 2013), as a surrounding sea ice cover would hinder phytoplankton growth. However, even for icebergs surrounded by sea ice, primary production can occur in the wake of icebergs (Jacobs, Gordon and Amos, 1979). The higher availability of nutrients leads to diatom species growth, higher phytoplankton and microbial abundance (Smith *et al.*, 2007; Vernet *et al.*, 2011). In situ measurements underneath and near the C18A iceberg also indicate that the biomass and organic carbon fluxes were twice as high as at the control site (Smith *et al.*, 2011). The authors therefore estimate an overall mass flux of 350 tons per day and an organic carbon flux of 15.8 tons per day caused by the C18A iceberg (Smith *et al.*, 2011). Overall, 10-20% of the Southern Ocean downward carbon flux is due to iceberg fertilisation (Duprat, Bigg and Wilton, 2016), acting as a negative climate feedback (Wu and Hou, 2017). As a consequence of the increased food availability, higher krill concentration and more seals and whales have been observed near icebergs (Vernet *et al.*, 2012). Several studies also document 2-6 times higher abundance of sea birds around icebergs (Smith *et al.*, 2007; Ruhl *et al.*, 2011; Joiris, 2018).

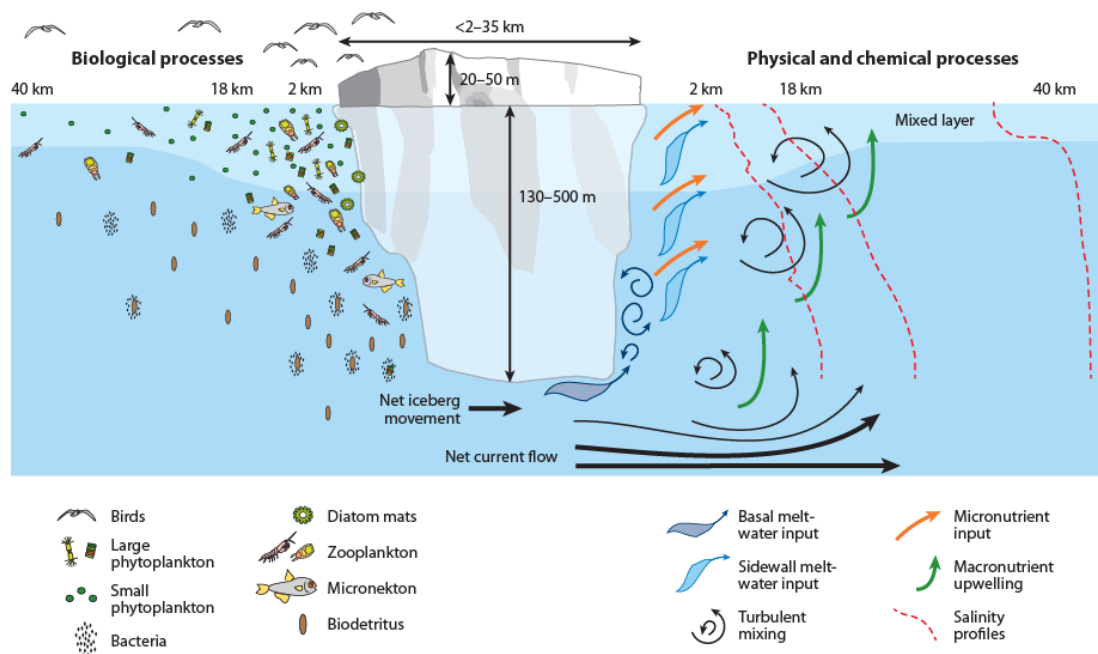


Figure 1.4: Physical, chemical and biological processes induced by icebergs. Extracted from Smith *et al.* (2013).

The area of impact is around 4-10 times the iceberg's length and is observed both upstream and downstream along the drift trajectory. The upstream effect is due to the buoyancy of the melt-water plume, which gets transported there by the ocean currents (Duprat, Bigg and Wilton, 2016). Time-wise, enhanced chlorophyll levels can be observed for more than a month after iceberg passage (Duprat, Bigg and Wilton, 2016).

### 1.2.4. Importance for glaciology

Iceberg calving can have an effect on the stability of the remaining mother ice shelf (Jansen *et al.*, 2015; Borstad, McGrath and Pope, 2017; Hogg and Gudmundsson, 2017) and flow speed of upstream glaciers (De Angelis and Skvarca, 2003; Rignot *et al.*, 2004; De Rydt *et al.*, 2021). Buttressing refers to the stabilizing effect that ice shelves have on the inland ice sheet (Shepherd, Fricker and Farrell, 2018). How much impact a calving event has, depends on how much the lost part contributed to the buttressing effect and the new ice front geometry (Jansen *et al.*, 2015; Fürst *et al.*, 2016). Ice shelf areas that contribute little to the stability of the ice shelf and do not cause a speed-up, if they are removed, are called passive shelf areas. These were mapped and quantified by Fürst *et al.* (2016) and are shown in Figure 1.5.

As giant icebergs calve from the Antarctic ice shelves, they inherit many of their physical characteristics and experience similar stress environments (Gade, 1979; Scambos *et al.*, 2005; Engelhardt and Engelhardt, 2017). A huge difference, however, is that icebergs drift and often turn North at some point (Gladstone, Bigg and Nicholls, 2001; Orheim *et al.*, 2022), which exposes them to warmer water, waves and warmer air temperatures that drive their decay (Scambos *et al.*, 2008; Bigg, 2015). As these conditions might also occur at ice shelf fronts in the future, with air and ocean temperatures increasing and sea ice cover reducing, studying iceberg decay can act as a proxy to predict the response of the Antarctic ice shelves to such conditions (Scambos *et al.*, 2005). Dryak and Enderlin (2020) find high correlation between melt rates of icebergs around the Antarctic Peninsula and ablation rates of nearby glaciers, following that submarine melting is the dominating driver for both. Another already documented similarity is hydro-fracturing: When air temperatures are warm enough to saturate surface melting on an iceberg, this can lead to a rapid disintegration within a short time period (Scambos *et al.*, 2008). The same mechanism caused the collapse of the Wilkins, George VI and Larsen-A and -B ice shelves (Rott, Skvarca and Nagler, 1996; Scambos, Hulbe and Fahnestock, 2003; Rack and Rott, 2004; Scambos *et al.*, 2009) and has been observed on other ice shelves prior to a series of calving events (Liu *et al.*, 2015). Furthermore, the same models are used for basal melting of ice-shelves and icebergs (Hellmer and Olbers, 1989; Holland and Jenkins, 1999; Jansen, Schodlok

and Rack, 2007; Bouhier *et al.*, 2018). Fragmentation processes are still not fully understood and remain hard to model for both ice-shelves and icebergs (Savage, 2007; Bassis, 2011; Bigg, 2015; Huth *et al.*, 2022). Therefore, understanding these processes better would be of mutual interest.

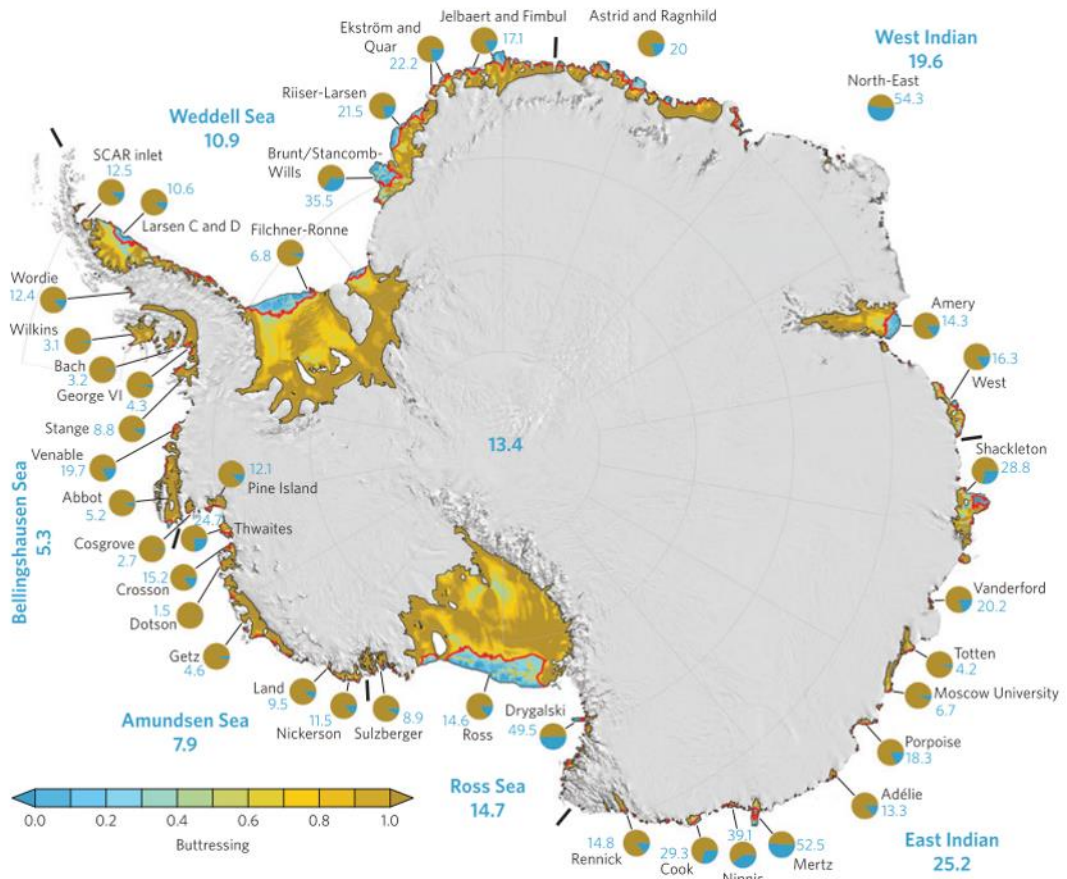


Figure 1.5: Contribution of ice shelf areas to the buttressing of upstream glaciers. Passive shelf areas, which do not lead to a significant speed-up when they are removed, are delineated in red and their percentage is given for each ice shelf. Extracted from Fürst *et al.* (2016)

Another overlap, which has not yet received much attention, is to study the characteristics of snow on icebergs and radar penetration through this snow pack (Scambos *et al.*, 2008; Han *et al.*, 2019). Determining snow depth and the scattering horizon from CryoSat-2 over Antarctic sea ice are subject to ongoing research and currently hinder reliable sea ice thickness products for Antarctica (Giles, Laxon and Worby, 2008; Willatt *et al.*, 2010; Kern and Ozsoy, 2019; Kacimi and Kwok, 2020). Therefore, studying snow on icebergs in more detail and assessing the differences or similarities of snow and scattering horizons on icebergs, (warming) ice sheets and sea ice is also of common interest across the community.

### 1.3. Iceberg observations

In this section, I review previous studies on how icebergs can be observed and what we have already learnt from these observations. I begin with methods to automatically detect icebergs in satellite data, move on to observations of iceberg abundance and distribution, and then summarise drivers and observations of iceberg drift and iceberg decay. The focus lies on satellite remote sensing observations, but I also include some studies using in situ data or modelling.

#### 1.3.1. Detection of icebergs

NIC detects the largest icebergs by manual inspection of optical and SAR imagery every week and provides the central position and semi axes lengths operationally. This database is complemented by manual analysis of lower resolution scatterometry data by the Brigham Young University, who publish daily central positions every few years (Stuart and Long, 2008, 2011; Budge and Long, 2018). While these databases supply operational estimates of the largest icebergs' position from manual analysis, many other studies have proposed automated detection techniques, but are not applied operationally.

Most studies suggest to detect icebergs in synthetic aperture radar (SAR) imagery (Willis *et al.*, 1996; Gill, 2001; Silva and Bigg, 2005; Wesche and Dierking, 2012; Frost, Ressel and Lehner, 2016; Mazur, Wåhlin and Krężel, 2017; Collares *et al.*, 2018; Barbat, Wesche, *et al.*, 2019; Koo *et al.*, 2021 and Figure 1.6). SAR imagery is independent of daylight and clouds (Collares *et al.*, 2018) and offers high spatial resolution. Optical imagery, in contrast, is limited to daylight and cloud free conditions (Sandven, Babiker and Kloster, 2007). Furthermore, icebergs, sea ice, adjacent ice shelves and glaciers as well as clouds all appear white in these images, complicating iceberg detection (Mazur, Wåhlin and Krężel, 2017). Apart from some early work, exploiting the iceberg shadows in Landsat images (Williams and Macdonald, 1995; Sandven, Babiker and Kloster, 2007), synthetic aperture radar (SAR) imagery has been used instead.

In most SAR images, icebergs stand out as bright targets in front of a dark ocean or sea ice background (Young *et al.*, 1998; Wesche and Dierking, 2012; Mazur, Wåhlin and Krężel, 2017). However, this is not always the case: Iceberg backscatter depends on the properties of the snow on top (Ulaby and Long., 2014). When the snow is dry, icebergs appear as bright targets, but when the surface is thawing, they appear as dark objects – revealing a similar backscatter to their background or even darker than that (Young *et al.*, 1998; Wesche and Dierking, 2012). This poses a big challenge for an automated detection. Furthermore, the backscatter varies slightly with incidence angle (Wesche and Dierking, 2012; Mazur, Wåhlin and Krężel, 2017). Also the

backscatter of the background is variable: Ocean backscatter is determined by surface roughness, i.e. wind speed, where rougher sea appears brighter (Drinkwater, 1998; Ulaby and Long., 2014, Figure 1.7). The backscatter of sea ice is complex and depends on the age, roughness, liquid water and salt content of the ice and overlaying snow (Ulaby and Long., 2014). So, wind roughened sea and deformed sea-ice have higher backscatter (Drinkwater, 1998; Figure 1.7), decreasing the contrast to icebergs.

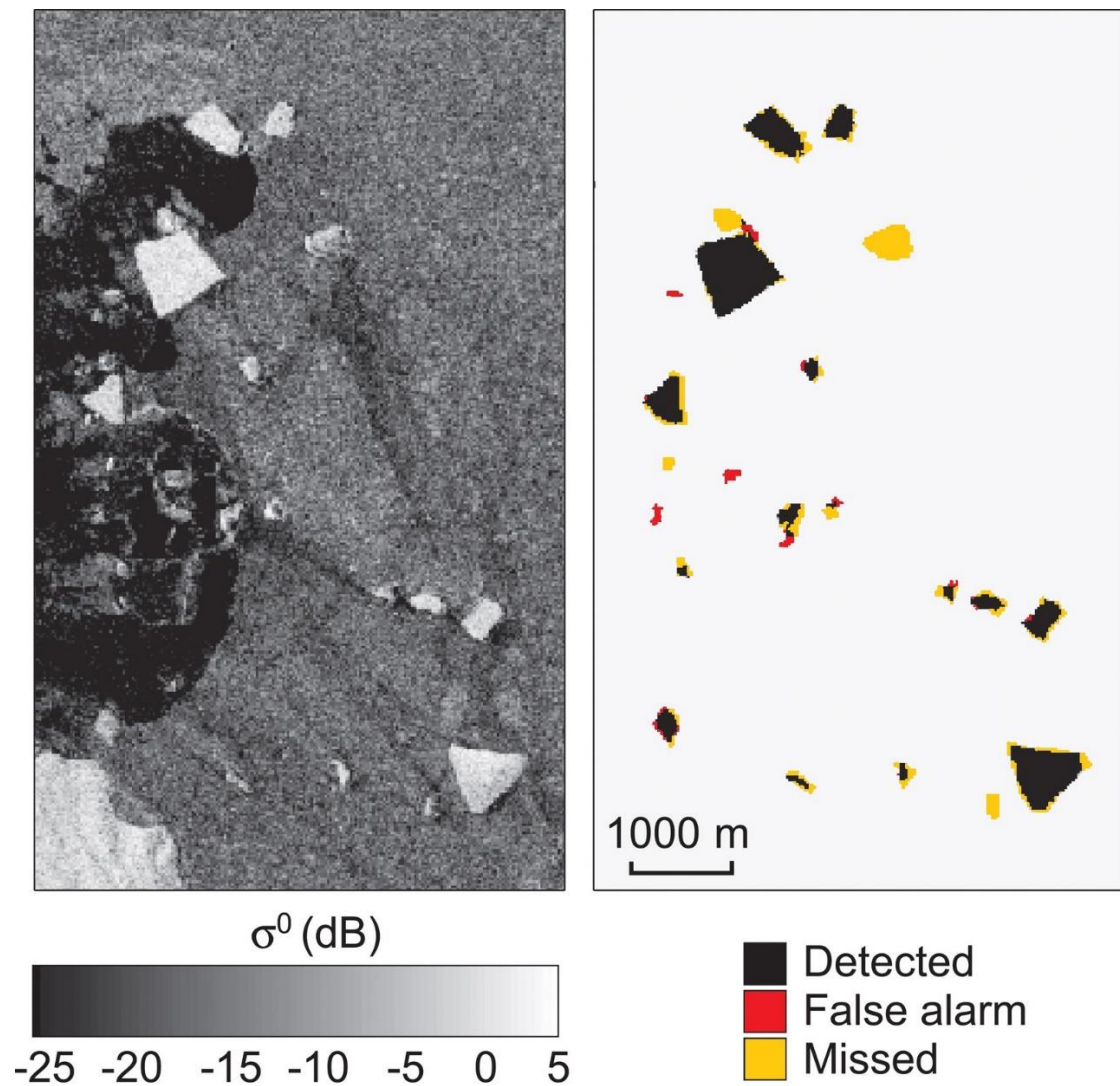


Figure 1.6: Iceberg detection in a SAR image. Extracted from Silva and Bigg (2005) and re-coloured for better differentiation

Most methods employ different forms of thresholding (Willis *et al.*, 1996; Gill, 2001; Wesche and Dierking, 2012; Frost, Ressel and Lehner, 2016; Mazur, Wählín and Krężel, 2017). Alternatively, two studies used the k-means (Macqueen, 1967) segmentation method (Collares *et al.*, 2018) and a variation of this (Koo *et al.*, 2021). Others employ edge detection techniques followed by pixel bonding (Williams, Rees and Young, 1999) or a watershed algorithm (Silva and

Bigg, 2005). The most elaborate approaches involves a graph-based segmentation and Ensemble Forest Committee classification algorithm (Barbat, Wesche, *et al.*, 2019) and fuzzy contrast enhancement followed by a stochastic segmentation approach (Lopez-Lopez *et al.*, 2021). While all of these, still utilize SAR images, Tournadre *et al.* (2008) demonstrated the possibility to detect small icebergs floating in open ocean using satellite altimetry, as their presence alters the received waveforms. This method was later extended to several altimeters and applied over many years (Tournadre, Girard-Ardhuin and Legrésy, 2012; Tournadre *et al.*, 2015, 2016).

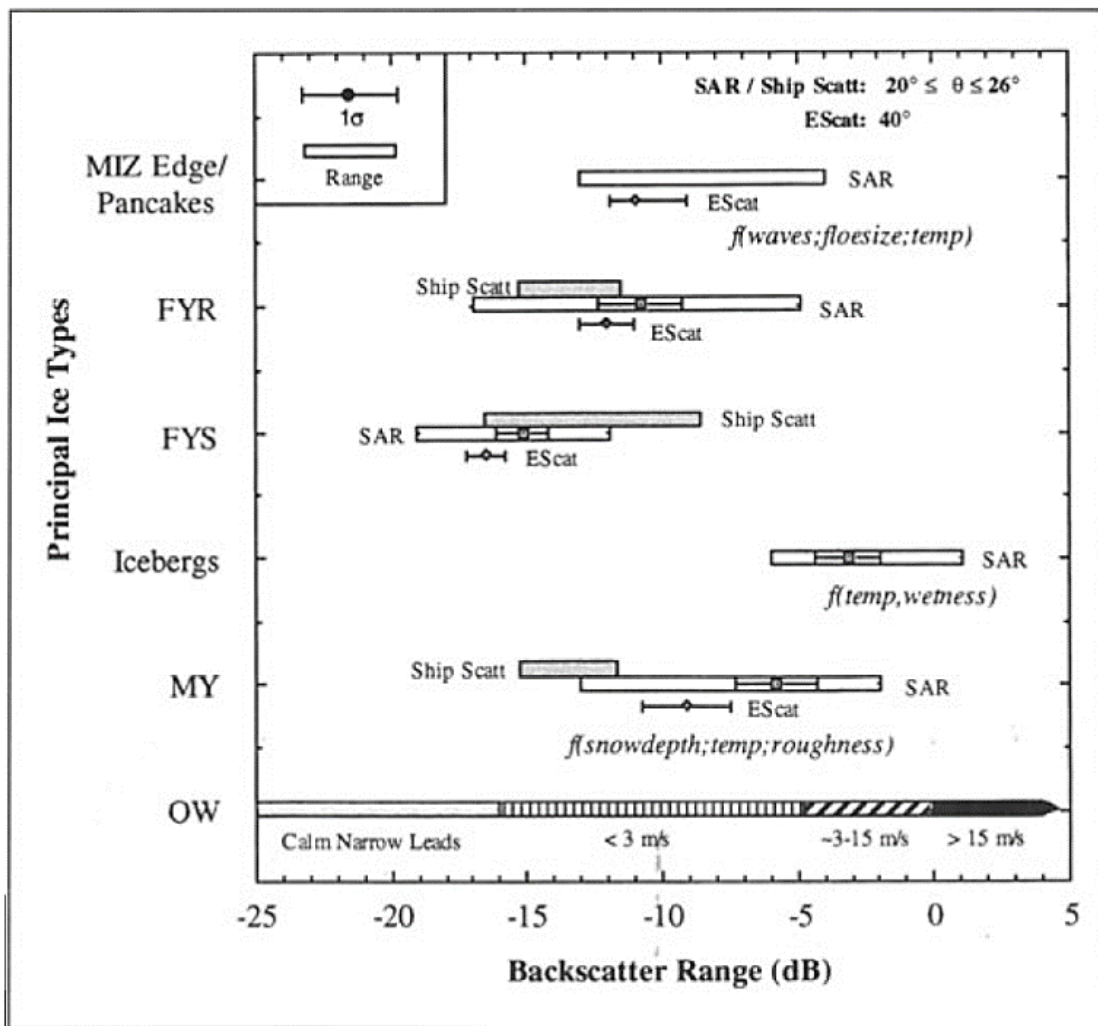


Figure 1.7: Backscatter coefficients (range, mean and standard deviation) of different surfaces (marginal ice zone (MIZ), rough first year sea ice (FYR), smooth first year sea ice (FYS), icebergs, multi-year sea ice (MY) and open water (OW) in different wind speeds) in the Weddell Sea. Extracted from Drinkwater (1998)

The remaining challenges are manifold: Some of these techniques are limited to austral winter images (Young *et al.*, 1998; Williams, Rees and Young, 1999; Silva and Bigg, 2005) or still require manual intervention (Young *et al.*, 1998; Silva and Bigg, 2005; Lopez-Lopez *et al.*, 2021). Dark

icebergs remain a problem for all existing methods using SAR images. Many studies also report degrading accuracies in high wind conditions (Willis *et al.*, 1996; Frost, Ressel and Lehner, 2016; Mazur, Wåhlin and Krężel, 2017). Deformed sea ice or sea ice in general is also mentioned to lead to false detections (Willis *et al.*, 1996; Silva and Bigg, 2005; Tournadre, Whitmer and Girard-Arduin, 2008; Wesche and Dierking, 2012; Mazur, Wåhlin and Krężel, 2017; Koo *et al.*, 2021). And finally, clusters of several bergs and berg fragments too close to each other have been found to pose a problem (Williams and Macdonald, 1995; Williams, Rees and Young, 1999; Frost, Ressel and Lehner, 2016; Barbat, Wesche, *et al.*, 2019; Koo *et al.*, 2021). So far, previous studies have also focused on smaller icebergs and perform worse for larger ones or are not even applicable there (Willis *et al.*, 1996; Tournadre, Whitmer and Girard-Arduin, 2008; Wesche and Dierking, 2012; Mazur, Wåhlin and Krężel, 2017). Where reported, the detection rates range from 60 % (Williams and Macdonald, 1995) to 93.6 % (Barbat, Wesche, *et al.*, 2019).

### 1.3.2. Iceberg abundance and distribution

A few of the detection methods have been implemented on larger scales to derive overall iceberg volume and distributions. Wesche and Dierking (2015) applied their automated threshold-based iceberg detection algorithm (Wesche and Dierking, 2012) and manual corrections to a Radarsat mosaic of Antarctica from austral spring 1997, extending around 200 km into the Southern Ocean. From this snapshot, they find almost 7000 icebergs (0.3 to 4747.7 km<sup>2</sup> in area). They calculate that these icebergs contain 5200-7400 Gt of freshwater, which is a multitude of the annual calving flux, suggesting a life cycle of several years. Similarly, Barbat *et al.* (2019a) applied their detection algorithm (Barbat, Wesche, *et al.*, 2019) to three Radarsat mosaics from 1997, 2000 and 2008. They find total iceberg mass of around 4600, 6900 and 5300 Gt in the respective years and estimate an average residence time of 4-6 years in the coastal zones. Mazur *et al.* (2019) applied their detection algorithm (Mazur, Wåhlin and Krężel, 2017) to SAR images of the Amundsen Sea embayment over 6 years and manually tracked some of the detected icebergs. They found a mean annual surface area of 1537.5 km<sup>2</sup>, which is 2.5 times the annual calving rate and derive a mean iceberg age of 2.5 years in this area. All three studies, however, only cover parts of the Southern Ocean, close to the coast.

In contrast, the ALTIBERG database (Tournadre *et al.*, 2015) allows for statistics on small icebergs (< 8 km<sup>2</sup>) in open ocean over 23 years. Tournadre *et al.* (2016) combined these with the databases of large icebergs (>200 km<sup>2</sup>) by NIC and BYU (Stuart and Long, 2008). They found that the size distribution follows a -3/2 power law, with the smallest icebergs (< 1 km<sup>2</sup>) making up for 77 % of all detections and the largest class of 1000-10,000 km<sup>2</sup> accounting for only 0.4 % of the

total population. This is in good agreement with a study by Wesche and Dierking (2015). On the other hand, the largest icebergs contribute 67.1% of the total iceberg area (Tournadre *et al.*, 2016) and hence an even larger percentage of total iceberg volume - as larger bergs are also thicker (Bigg *et al.*, 1997).

Ship observations complement the satellite data to derive iceberg abundance and distribution over the whole Southern Ocean and several decades. Since 1947 iceberg sightings have been recorded on a number of ships travelling to Antarctica (Romanov, Romanova and Romanov, 2017; Orheim *et al.*, 2022). Romanov *et al.* (2017) evaluate 60,000 observations from these cruises between 1997 and 2014 to map the iceberg concentration and find that on average  $132,269 \pm 7\%$  icebergs are present in the Southern Ocean at any time. They also estimate the instantaneous iceberg area and volume to be  $55,805 \text{ km}^2 \pm 32\%$  and  $16,893 \text{ km}^3 \pm 33\%$  respectively. Their area and volume estimates are based on average observed iceberg length and freeboard for different iceberg shapes (Romanov, Romanova and Romanov, 2012), focussing on small and medium-sized icebergs. Furthermore, they employ a constant freeboard to thickness and length to width ratio, which leads to the high uncertainties and will not represent giant icebergs accurately, but allows for an overall estimate of total iceberg volume. Likewise, Orheim *et al.* (2022) analyse ship observations between 1976 and 2009 and derive a similar concentration map as well as a very similar instantaneous number of icebergs of 130,000 icebergs.

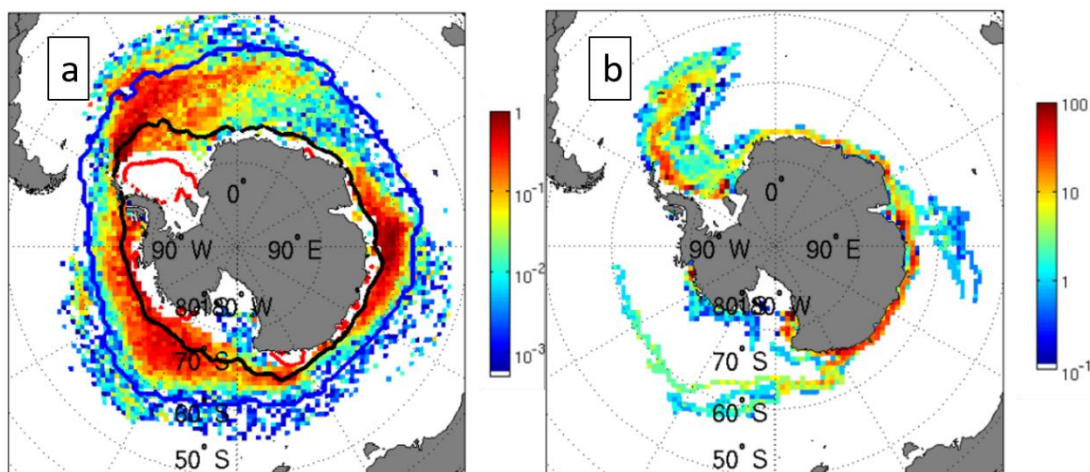


Figure 1.8: Mean monthly volume ( $\text{km}^3$  per  $100 \times 100 \text{ km}^2$  grid cell) of (a) small icebergs in open ocean between 1992-2014 and (b) large icebergs between 2002-2012. The lines in (a) indicate the mean sea ice extent, which impacts where icebergs can be detected. Blue is the mean annual maximum extend, black the mean maximum extend in summer and red the minimum extend in summer. Extracted from Tournadre *et al.* (2016)

Spatially, icebergs are most abundant close to the coast – near their calving position and following the Antarctic coastal current – and along the ‘iceberg alley’, which follows a current along

the eastern side of the Antarctic Peninsula and then turning north east towards and beyond South Georgia (Tournadre *et al.*, 2016, Figure 1.8). The spatial patterns of small and large bergs are similar, as most of the small icebergs calve from large icebergs, but the smaller ones take slightly different routes and spread the freshwater further (Tournadre *et al.*, 2016). These maps are also in good agreement with the ones produced from ship-borne observations (Romanov, Romanova and Romanov, 2017; Orheim *et al.*, 2022).

On inter-annual timescales, it is apparent from several data sets that the calving, abundance and distribution of small to medium sized icebergs is relatively constant (Mazur, Wåhlin and Kalén, 2019; Orheim *et al.*, 2022). In contrast, giant iceberg calving is episodic (MacAyeal *et al.*, 2008; Greene *et al.*, 2022), leading to high inter-annual variability in the distribution of giant icebergs as well as total iceberg area and volume, where they contribute the most (Jacka and Giles, 2007; Tournadre *et al.*, 2016; Mazur, Wåhlin and Kalén, 2019 and Figure 1.9). A seasonal analysis of ship observations is hampered by the fact that they mainly stem from austral summer months and the few winter observations sample other areas of lower sea ice concentration (Orheim *et al.*, 2022). The altimetry data are affected in a similar way, as it has to date only been applicable in open ocean and therefore sea ice extent is negatively correlated with the amount of icebergs detected, meaning that no seasonal differences were derived from this dataset, either (Tournadre *et al.*, 2016, Figure 1.9).

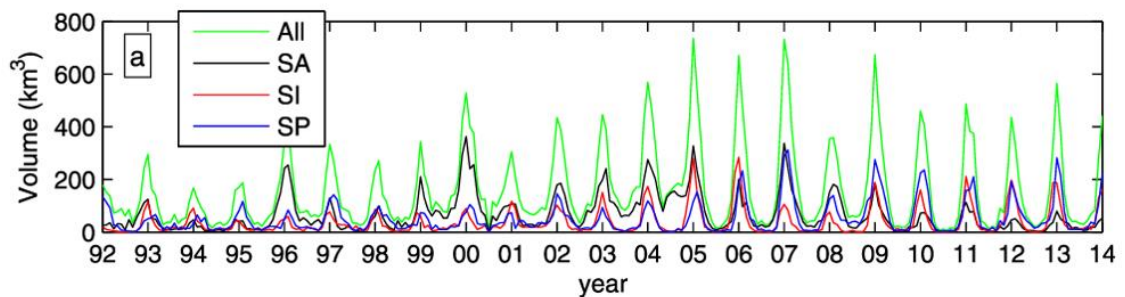


Figure 1.9: Inter-annual variation of total iceberg volume in the open Southern Ocean (All, green) and different sectors (South Atlantic (SA) in black, South Indian (SI) in red and South Pacific (SP) in blue). The seasonal variation is because the detection method only works in open ocean and hence sea ice extent has a large influence on the number of detectable icebergs. It does not reflect actual seasonal changes. Therefore, the yearly maxima are the most representative. Extracted from Tournadre *et al.* (2016).

### 1.3.3. Iceberg drift

Iceberg distributions correlate with the calving rates of the adjacent ice shelves and glaciers only within a narrow band close to the coast (Romanov and Romanova, 2018). Unless they ground on shallower parts of the sea floor, where giant icebergs can even last for decades (Barbat *et al.*,

## 1. Introduction to Antarctic tabular icebergs

2021), they drift and therefore get redistributed (Romanov and Romanova, 2018; Mazur, Wåhlin and Kalén, 2019).

Iceberg drift is caused by a number of forces (Bigg *et al.*, 1997 and Figure 1.10). For large icebergs ocean currents are the main driver of iceberg drift (Crepon, Houssais and Guily, 1988; Wagner, Dell and Eisenman, 2017; Romanov and Romanova, 2018). They can therefore also act as tracers of the ocean currents (Williams, Rees and Young, 1999). With a draft of several hundred meters, their net movement is generally slower and slightly diverted (Ekman spiral) compared to the surface current (Morgan and Budd, 1978). In areas of weaker or absent ocean currents, wind becomes the dominating factor (Romanov and Romanova, 2018). Smaller icebergs with less mass are less affected by ocean currents and three times more by wind (Crepon, Houssais and Guily, 1988; Rackow *et al.*, 2017; Wagner, Dell and Eisenman, 2017). In contrast, the impact of wind decreases to less than 10 % for bergs longer than 12 km (Wagner, Dell and Eisenman, 2017). The magnitude of Coriolis force depends on iceberg mass, and hence larger (heavier) icebergs veer more to the left (Gladstone *et al.*, 2001; Orheim *et al.*, 2022). When icebergs are surrounded by sea ice, sea ice drag becomes a relevant factor (Lichey and Hellmer H., 2001). In case of a nearly closed sea ice cover, icebergs and the surrounding sea ice can form a solid block with coherent drift and the sea ice drift, which is mainly forced by wind, steers the icebergs (Vinje, 1980; Schodlok *et al.*, 2006). Depending on the thickness and age of the sea ice, sea ice concentrations of 86-93 % are needed for the sea ice to control iceberg drift (Lichey and Hellmer H., 2001; Schodlok *et al.*, 2006).

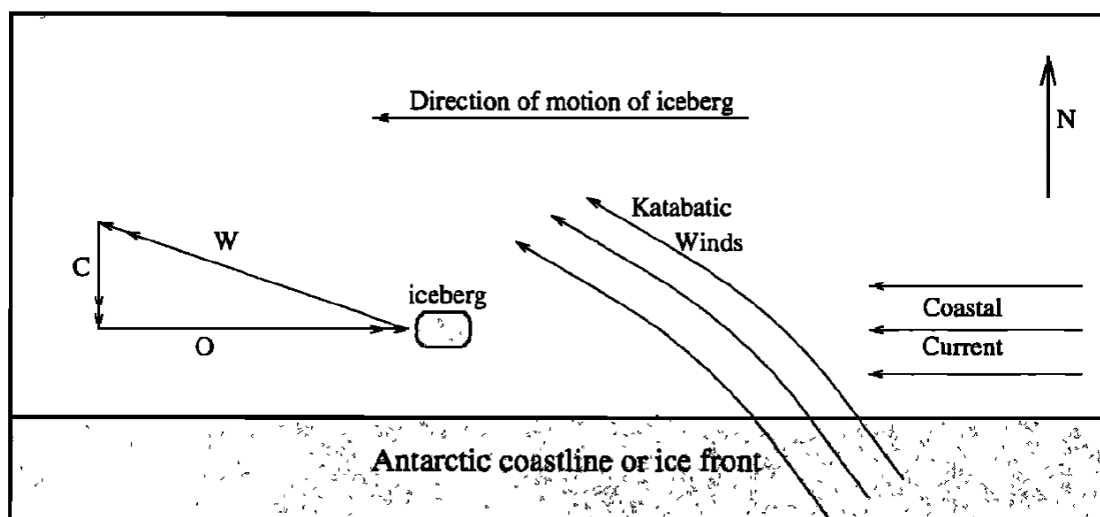


Figure 1.10: Main drivers of iceberg drift and resulting iceberg motion. W is wind-related forcing, C is the Coriolis force and O is ocean-current drag. Extracted from Gladstone, Bigg and Nicholls (2001)

Most icebergs initially follow the Antarctic Coastal Current (Orheim et al., 2022) driving them counter-clockwise along the coast (Tchernia and Jeannin, 1984). Four ‘exit routes’ have been identified, where some of these icebergs turn north (Figure 1.11) until they reach and follow the clock-wise Antarctic Circumpolar Current (Tchernia and Jeannin, 1984; Gladstone, Bigg and Nicholls, 2001; Orheim et al., 2022). The largest exit zone is the ‘iceberg alley’ (Stuart and Long, 2011; zone 3 in Figure 1.11). While icebergs drifting just east of the Antarctic Peninsula tend to move uniformly northwards, icebergs following exit paths 4a and 4b (Figure 1.11) were found to take more meandering paths (Schodlok et al., 2006). Because wind and the Coriolis force act differently on different sized icebergs, bigger bergs tend to stay in the Antarctic Coastal Current longer and tend to take more northerly routes after exiting along the Antarctic Peninsula (Orheim et al., 2022). This also explains the iceberg concentration maps for small and large icebergs (Figure 1.8, Tournadre et al., 2016) and the routes of the largest icebergs recorded by BYU (Figure 1.2, Budge and Long, 2018). It should, however, be noted that the recorded giant iceberg trajectories end when the icebergs fall below the aerial and length thresholds to be tracked, but will survive a bit longer (Rackow et al., 2017).

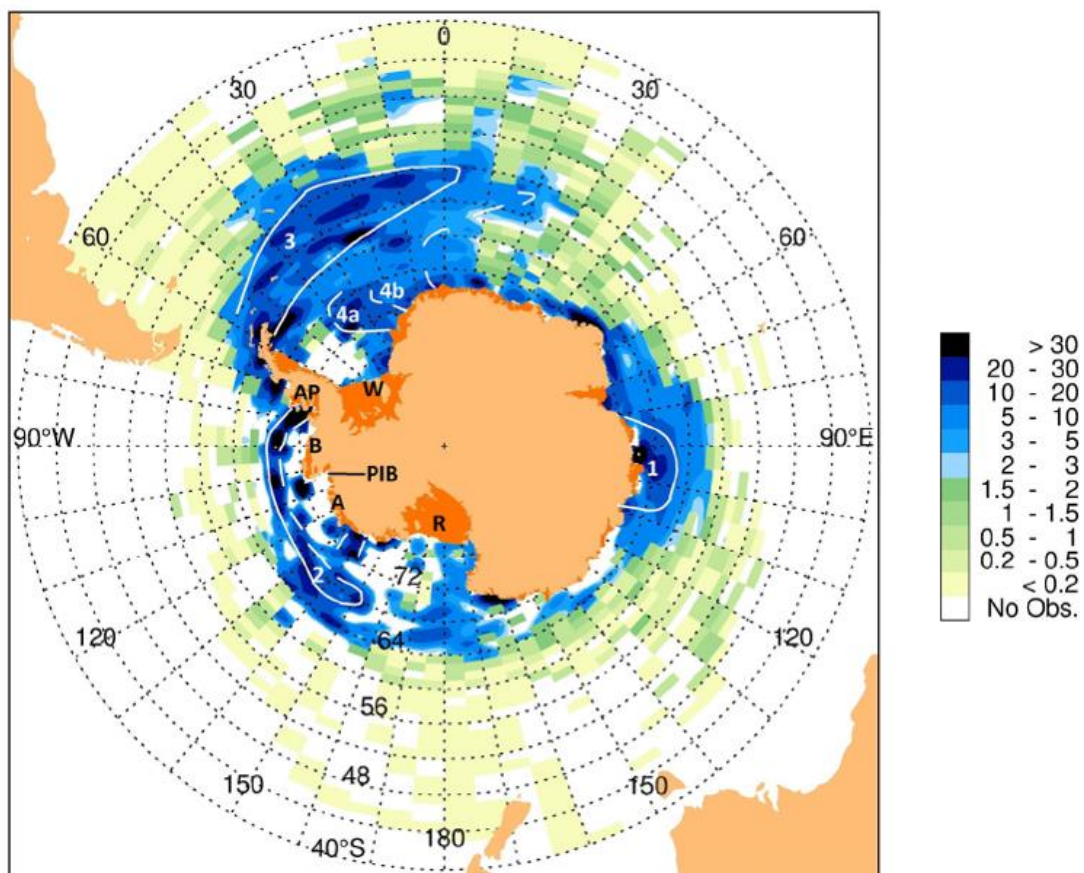


Figure 1.11: Exit zones 1-4b, where icebergs leave the Antarctic Coastal Current and turn northwards. These zones are characterised by higher iceberg concentration (colour map). Extracted from Orheim *et al.* (2022)

Budge and Long (2018) calculated average drift speeds for the giant icebergs in their database (Figure 1.2) and found 1.45 km/day near land, 4.83 km/day in sea ice and 5.02 km/day in open ocean. Koo *et al.* (2021) tracked the giant B43 iceberg and found a maximum drift speed of 20 km/day. Other studies include smaller icebergs, but are limited to specific regions: Mazur *et al.* (2019) find average drift speeds of 4.32 km/day in the Amundsen Sea. In the Weddell Sea similar drift speeds between 3.2 km/day and 7.5 km/day have been reported using satellite observations (Gladstone and Bigg, 2002; Collares *et al.*, 2018; Barbat *et al.*, 2021). However, a mean speed of 13.7 km/day in the coastal current of the Weddell Sea was measured by buoys sending daily GPS positions (Schodlok *et al.*, 2006). Generally, larger icebergs have been found to move more slowly than smaller ones (Rackow *et al.*, 2017). All of these studies find great variation in daily drift speed with minima around zero and maxima around 50 km/day (Tchernia and Jeannin, 1984; Aoki, 2003; Schodlok *et al.*, 2006). Seasonal variations in drift speed are related to variations in ocean current speed (Aoki, 2003) and sea ice cover (Lichey and Hellmer H., 2001).

### 1.3.4. Iceberg melting

Iceberg drift and decay influence each other, since drift depends on the (remaining) iceberg mass and iceberg decay depends on the surrounding environmental conditions, which evolve with the drift. Hence, iceberg models often combine drift and decay (Bigg *et al.*, 1997; Wagner, Dell and Eisenman, 2017). In the following, I will first outline the drivers of iceberg melting and how these are represented in iceberg models. Then I will describe how iceberg melting can be observed using satellite remote sensing techniques and summarise previously observed melt rates.

Initially, iceberg melting was modelled to investigate whether towing icebergs as freshwater supply from polar regions to arid regions like Australia would be possible and profitable (Weeks and Campbell, 1973; Morgan and Budd, 1978; Schwerdtfeger, 1979; Lawson and Russell-Head, 1982). These studies found that melt rates increase from a few meters per year in cold near-coastal waters to about 100 m/year near the convergence using heat transfer theory (Morgan and Budd, 1978 and Figure 1.12). Neshyba and Josberger (1980) summarised the findings from several laboratory, theoretical and in situ studies and conclude that melting is proportional to the temperature above freezing  $T_d^{1.6}$ . Likewise, Russell-Head (1980) derived a simple relationship where the daily melt rate  $R$  [m] is modelled as a function of ocean temperature [ $^{\circ}\text{C}$ ] and  $1.8^{\circ}\text{C}$  are added to yield temperature above freezing:  $R = 0.018 (T + 1.8)^{1.5}$ . Their and Morgan and Budd (1978)'s graph are shown in Figure 1.12.

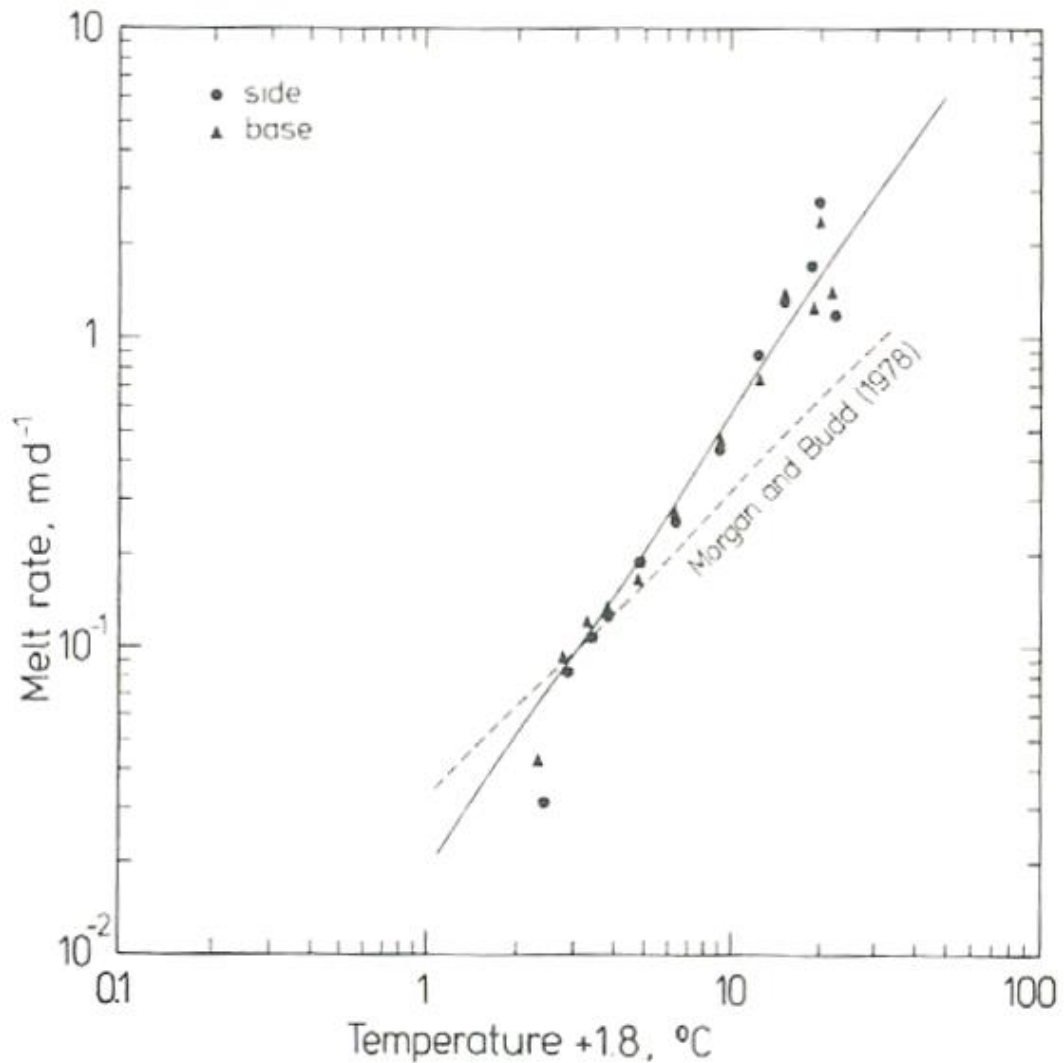


Figure 1.12: Iceberg melt rate (m per day) as a function of ocean temperature above melting. Dots show average side melt rates and triangles represent melting at the base. The relationship derived by Morgan and Budd (1978) is included as a dotted line. Extracted from Russell-Head (1980)

More recent models of iceberg melting consider more complex interaction with the environment based on three main processes: (i) wave erosion at the waterline (ii) sidewall melting through buoyant convection and (iii) melting at the iceberg's base (Bigg *et al.*, 1997; England *et al.*, 2020; Wagner *et al.*, 2017 and Figure 1.13). The first two terms act on the sides of the iceberg, reducing iceberg area. Here, waves are dominating over the melting term (Silva, Bigg and Nicholls, 2006; Kubat *et al.*, 2007). Wave erosion depends on sea state (Bigg *et al.*, 1997), ocean temperature (Rackow *et al.*, 2017) and sea ice concentration, which dampens the waves (Gladstone, Bigg and Nicholls, 2001; England, Wagner and Eisenman, 2020). Sidewall melting through buoyant convection is a function of ocean temperature (England, Wagner and

Eisenman, 2020). The last term refers to melting at the iceberg's base, reducing iceberg thickness. The most common representation is based on forced convection and depends on the temperature difference between the iceberg and the surrounding ocean, their relative velocity and iceberg length (Weeks and Campbell, 1973; Bigg *et al.*, 1997; England, Wagner and Eisenman, 2020). Alternatively, a thermal turbulent exchange model, which was developed for ice shelves (Hellmer and Olbers, 1989; Holland and Jenkins, 1999), is used (Silva, Bigg and Nicholls, 2006; Jansen, Schodlok and Rack, 2007). Bouhier *et al.* (2018) compared both representations to observations of two giant icebergs (B17A and C19A) and found better agreement with the latter model. While wave erosion is the dominating factor in the beginning, (basal) melting becomes the main driver after a few years (Rackow *et al.*, 2017). Finally, surface melt and air forced convection should be mentioned as additional drivers of iceberg decay (Bigg *et al.*, 1997; Savage, 2007). Compared to basal melt, side melt and wave action, they contribute very little to iceberg decay, though (Schwerdtfeger, 1979; Kubat *et al.*, 2007; Savage, 2007). Only towards the end of an iceberg's life cycle, extensive surface melting can cause hydrofracturing and a rapid disintegration of large icebergs (Scambos *et al.*, 2008).

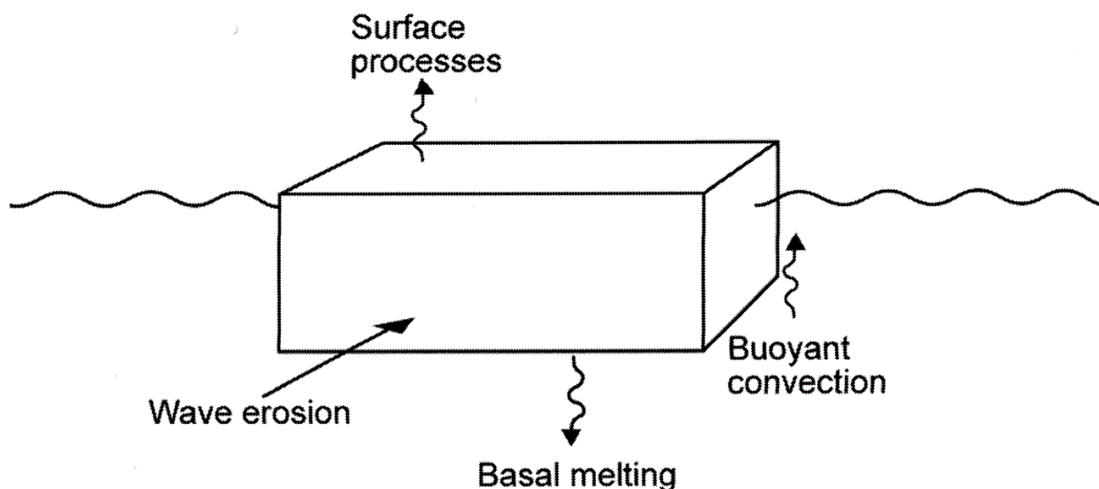


Figure 1.13: Schematic of processes causing iceberg melting. Extracted from Bigg (2015) and slightly modified

Lab experiments have shown that only in a quiescent state icebergs melt equally from all sides. In strong relative current speeds, sidewall melting is more pronounced than basal melting and fastest at the side facing the current (Hester *et al.*, 2021 and Figure 1.14). At the base of the iceberg, a 50% increase in melt rate has been observed at about 2.5 times the iceberg draft away from the front (Hester *et al.*, 2021). For a 400 m draft, this would mean that melting is strongest 1 km away from the side facing the current. These experiments have also shown that the aspect

ratio (length/draft) has a large impact on the overall melt rate. As sidewall melting is quicker than basal melting and smaller icebergs have a lower aspect ratio, their overall melting is an average of side and basal melting. For giant icebergs, in contrast, the surface at the base is significantly larger than the side walls and hence the overall melt rate is approximately equal to the basal melt rate (Hester *et al.*, 2021) and lower than for small bergs (Kubat *et al.*, 2007; Hester *et al.*, 2021). The spreading of the meltwater is determined by the relative velocity between the ocean current and the meltwater plume. Laboratory experiments have shown that in low relative velocities the meltwater spreads at the surface. In contrast, in high relative velocities the plume distributes over the depth of the iceberg draft and is transported away from the iceberg, enhancing further melting (FitzMaurice, Cenedese and Straneo, 2017; Hester *et al.*, 2021).

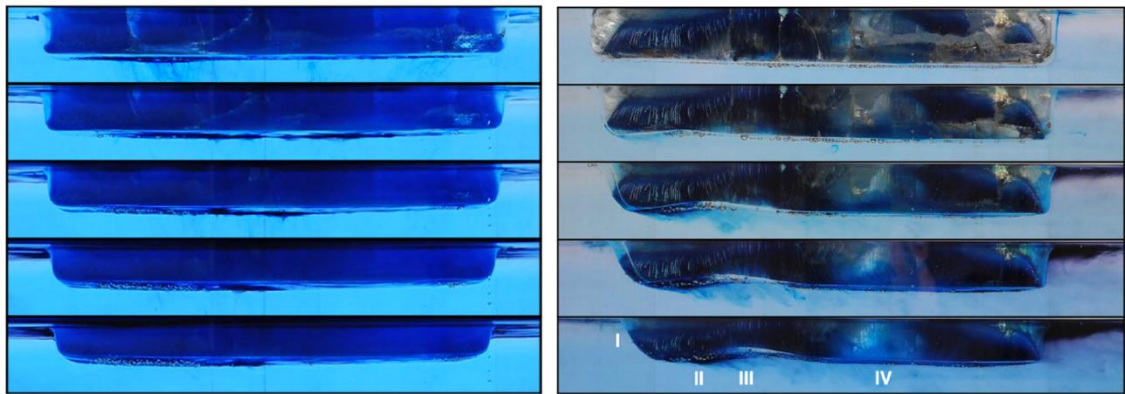


Figure 1.14: Lab experiment of iceberg melting without (left) and with (right) a background current. From top to bottom, each image is taken 2 minutes apart. The ice block is dyed blue to visualise melting and meltwater distribution. Extracted from Hester *et al.* (2021)

Increased and improved satellite remote sensing techniques offer the possibility to observe the decay of giant icebergs from space. Repeat satellite altimetry measurements of iceberg freeboard allow to quantify the thickness change, and hence basal melting of selected tabular icebergs (Scambos *et al.*, 2005, 2008; Jansen, Schodlok and Rack, 2007; Tournadre *et al.*, 2015; Bouhier *et al.*, 2018; Li *et al.*, 2018; Han *et al.*, 2019). Different strategies have been used to compare subsequent altimetry tracks over drifting and rotating icebergs: The easiest approach is to assume even iceberg thickness and to compare different freeboard observations regardless of where they sample the iceberg (Scambos *et al.*, 2008; Bouhier *et al.*, 2018). Others only calculate freeboard change where the satellite tracks intersect, significantly reducing the number of observations (Li *et al.*, 2018; Han *et al.*, 2019). The most elaborate approach is to build a map of initial freeboard pre-calving from several tracks, while the iceberg only moves with the ice shelf and to then collocate subsequent tracks over the floating iceberg with the initial thickness

map (Jansen, Schodlok and Rack, 2007 and Figure 1.15). The latter two methods are more accurate, but require near coincident satellite imagery to know where each track samples the iceberg.

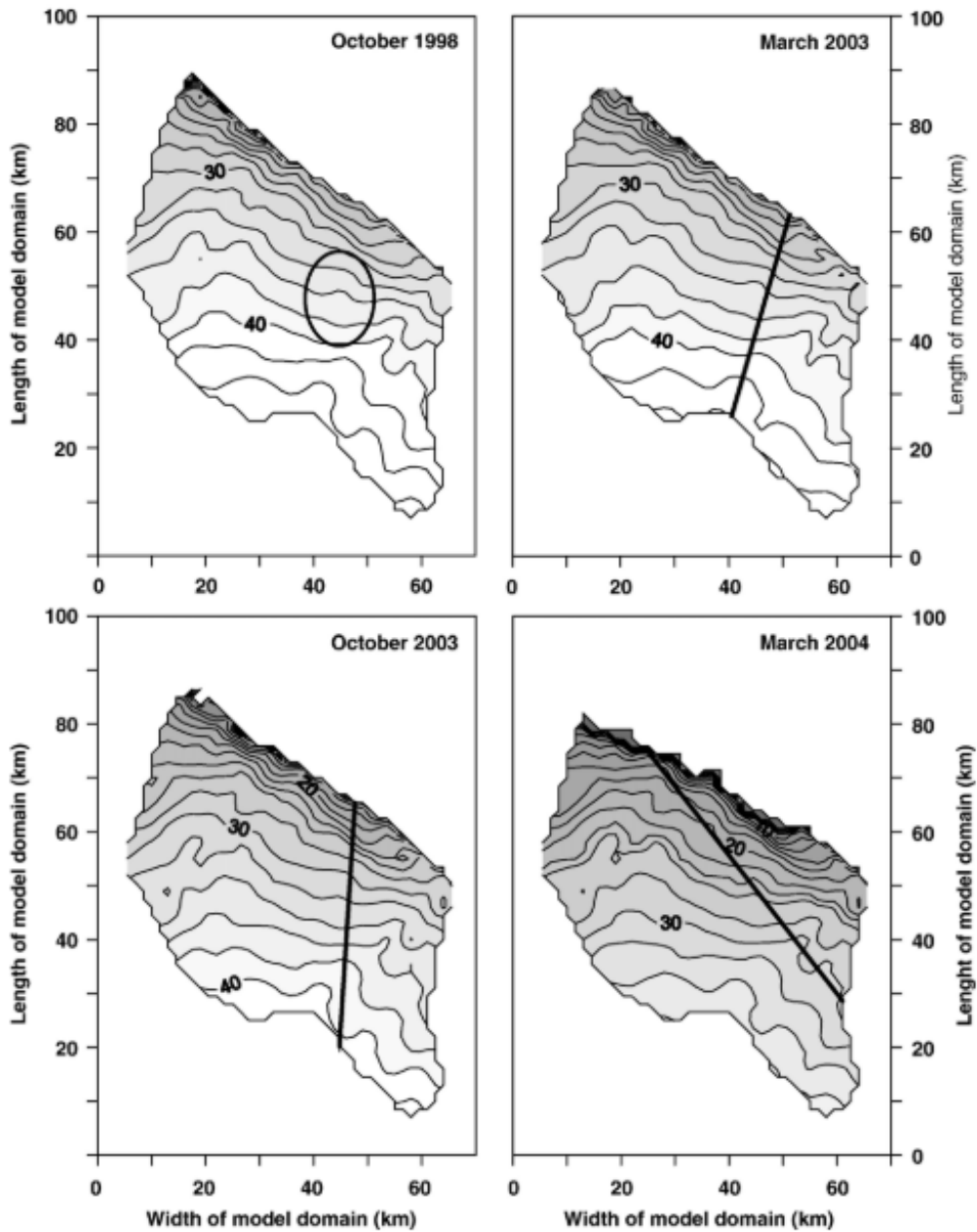


Figure 1.15: Maps of iceberg freeboard over time together with the location of individual altimetry tracks. Extracted from Jansen, Schodlok and Rack (2007)

Another challenge is that estimates of iceberg density, snow depth and snow density are required to convert iceberg freeboard observations to thickness estimates and that they evolve over several years of iceberg drift. Therefore, some studies stick with observations of freeboard change rather than calculating actual thickness change and freshwater inputs (Scambos *et al.*,

2008; Li *et al.*, 2018). Other studies simply use a fixed freeboard to thickness ratio of 1:8 (Tournadre *et al.*, 2015; Bouhier *et al.*, 2018). Jansen, Schodlok and Rack (2007) also employ an empirical relationship of freeboard to thickness, ignoring additional snowfall during the drift, but model the initial iceberg density as an exponential decrease from ice density to snow density. Han *et al.* (2019) account for snowfall during the iceberg drift, but assume bulk densities of 300 and 917 kg/m<sup>3</sup> for snow and iceberg respectively.

The observed rates of freeboard and thickness change are highly dependent on the location of the chosen iceberg, i.e. whether it is surrounded by sea ice, grounded or drifting in open ocean and on the surrounding ocean temperature and currents. Li *et al.* (2018) for example found a freeboard reduction of 0.02 m/month during a 22-month grounding period and 0.76 m/month for the same iceberg (C28B) when it was drifting in open ocean. Scambos *et al.* (2008) observe essentially no freeboard change for the A22A iceberg while it is drifting in the Weddell Sea surrounded by sea ice, but about 1 m/month of freeboard loss in the Scotia Sea. Similarly, Jansen *et al.* (2007) observe an increase in basal melting (thickness change) of 0.2 m/month close to the Ronne Ice Shelf to 13.5 m/month in the Scotia Sea, which they relate to changes in ocean temperature and current speed. Dryak and Enderlin (2020) find melt rates between 0.15 – 3 m/month around the Antarctic Peninsula and a high correlation with ablation rates of nearby glaciers, following that submarine melting is the dominating driver for both. The observation time also affects the results, because icebergs drift through these different environments and tend to decay more slowly in the beginning, i.e. close to their origin. Han *et al.*, (2019) studied the A68A iceberg in the beginning of its life cycle and found a small basal melt rate of 1.07 m/month. In contrast, Tournadre *et al.* (2015) and Bouhier *et al.* (2018) only start their analysis once icebergs reach open ocean and find much higher melt rates of around 3 m/month and 1-20 m/month respectively. Shipborne observations have found dissolution rates of 0.9-1.5 m/month (Jacka and Giles, 2007) to 3.6 m/month (Hamley and Budd, 1986) in water temperatures of 1°C, which is within the satellite derived estimates.

### **1.3.5. Iceberg fragmentation**

Apart from melting, iceberg fragmentation contributes to the decay process and breakage is even the dominant mechanism for larger icebergs (Hamley and Budd, 1986; Tournadre *et al.*, 2015; England, Wagner and Eisenman, 2020). However, fracturing is not very well understood and stochastic in nature (Savage, 2007; Bassis, 2011). This makes it hard to predict iceberg fragmentation and such processes are often missing in iceberg models (Bouhier *et al.*, 2018; England,

Wagner and Eisenman, 2020). The importance of including fragmentation processes to yield realistic iceberg life times and trajectories, which agree with observations, has been demonstrated by England *et al.* (2020) and is visualised in Figure 1.16. The only mechanism included in some models is the ‘footloose mechanism’, which has been described by Wagner *et al.* (2014): Erosion at the waterline forms a subsurface ‘foot’, which induces an upwards buoyancy stress and causes calving once the ‘foot’ has grown to a certain length. For a 300 m thick iceberg, a 72 m foot will lead to a calving event of 780 m length. In situ observations of giant icebergs in the Ross Sea show that also collisions with other giant bergs or nearby ice shelves can trigger break-ups (MacAyeal *et al.*, 2008). Scambos *et al.* (2008) combine in situ observations with satellite measurements and describe three kinds of fragmentation processes for giant icebergs: rift calvings, edge wastings and rapid disintegration. Rift calvings can occur at any time during the iceberg life cycle along pre-existing fractures. Edge wastings occur regularly outside the sea ice edge and rapid disintegration involves a series of calving events at the end of an iceberg’s life (Scambos *et al.*, 2008). Rift calving has also been observed by Goodman *et al.* (1980), who found that small initial cracks propagate in each oscillation of ocean swell until the iceberg fractures. Most recently, another break up mechanism has been observed and modelled for the A68 iceberg: In this case ocean current shear was found to have triggered break up (Huth *et al.*, 2022).

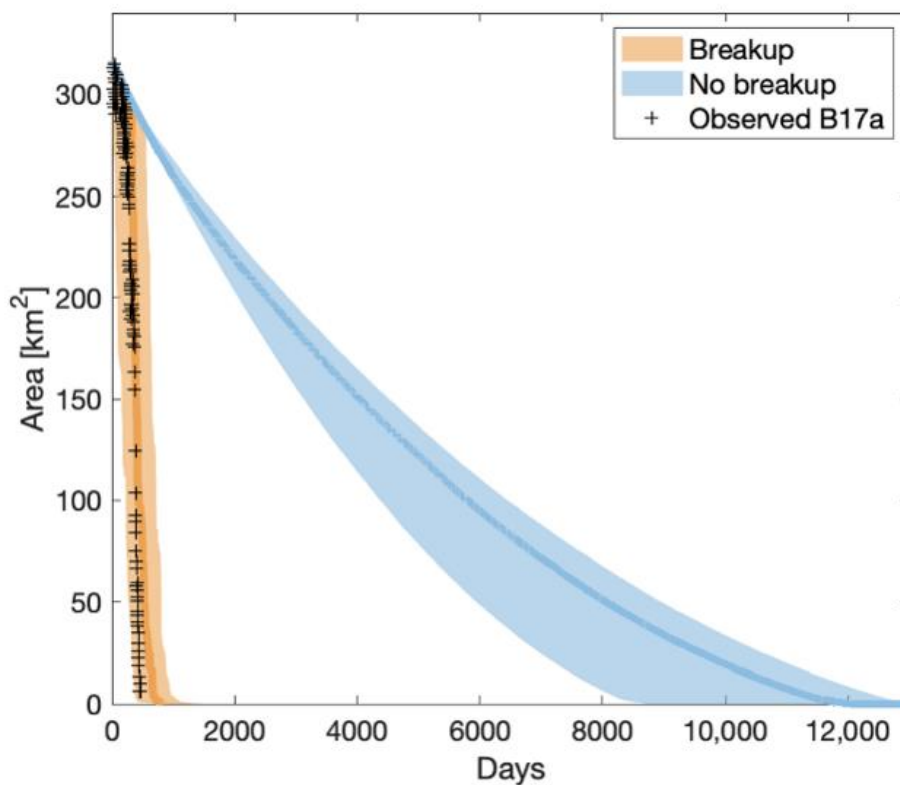


Figure 1.16: Impact of including iceberg fragmentation in a model. The inclusion of a break-up process matches iceberg area observations for the B17a iceberg much better. Extracted from England *et al.* (2020)

Iceberg fragmentation and sidewall melting can be observed in satellite imagery and calculated from a time series of iceberg outlines (Scambos *et al.*, 2008; Bouhier *et al.*, 2018; Li *et al.*, 2018; Han *et al.*, 2019; Lopez-Lopez *et al.*, 2021). Just like the observations of thickness change, also rates of area change are often related to the surrounding conditions. Scambos *et al.* (2008) find that fragmentation accelerates once the iceberg is no longer sheltered by sea ice. Rapid fragmentation is observed when the firm is saturated with surface melt water (Figure 1.17). Han *et al.* (2019) and Lopez-Lopez *et al.* (2021) studied the A68A iceberg during the first 1.5 years after calving, when it was still surrounded by sea ice. They both find a minor decrease in iceberg area of 2 % (Han *et al.*, 2019) and 3.7 % after a further two months (Lopez-Lopez *et al.*, 2021). In contrast, Bouhier *et al.* (2018) only start their study once icebergs have reached open water. For C19A they find that area loss increased from 2.6 km<sup>2</sup>/day in colder waters to 9.5 km<sup>2</sup>/day when ocean temperature was above zero. In the last 10 days, the iceberg then lost two major pieces of 340 and 370 km<sup>2</sup>. Li *et al.* (2018) report that for their two icebergs (C28A and C28B) area decreased steadily throughout austral summer at a rate of 8.1-16.5 km<sup>2</sup>/month. They attribute these changes to edge wastings, sidewall melting and wave erosion. During austral winter they observe a few sudden fragmentation events – interpreted as rift calvings triggered by ocean swell and basal melting, but otherwise iceberg area remains constant.

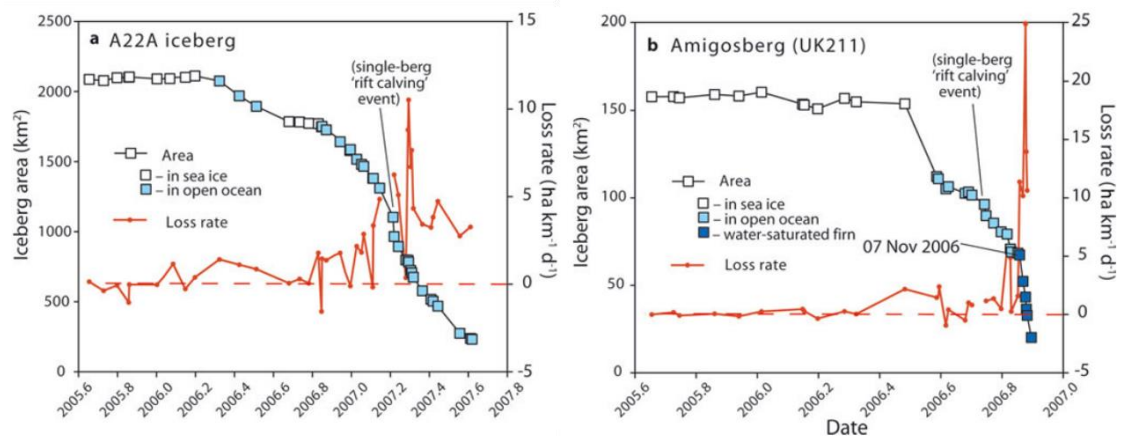


Figure 1.17: Area change of two giant tabular icebergs. Extracted from Scambos *et al.* (2008)

### 1.3.6. Iceberg volume loss and freshwater input

When estimates of iceberg area and iceberg thickness change are combined (Bouhier *et al.*, 2018) or when assumptions are made for iceberg thickness (Silva, Bigg and Nicholls, 2006; Barbat *et al.*, 2021), it is also possible to estimate iceberg volume loss and freshwater inputs. Alternatively, iceberg volume and volume change – especially of smaller icebergs – can be calculated from digital elevation models. The digital elevation models can either be derived from TANDEM-X SAR interferometry (Dammann *et al.*, 2019), WorldView stereo-satellite images (Enderlin and

Hamilton, 2014; Enderlin *et al.*, 2016, 2018; Dryak and Enderlin, 2020) or in some parts of the Arctic by using the ArcticDEM (Shiggins, Lea and Brough, 2022).

Bouhier *et al.* (2018) estimated the volume loss of two giant icebergs in the Southern Ocean and found that melting was the dominant factor for the B17A iceberg, contributing more than 60 % to the total volume loss. However, for the C19A iceberg, fragmentation was the dominant component, contributing 75 % to the overall volume loss (Bouhier *et al.*, 2018 and Figure 1.18). In both cases, fragmentation accelerates towards the end. Barbat *et al.* (2021) estimate the total mass loss of icebergs in the Weddell Sea over 10 years by tracking 414 icebergs with surface areas between 3.4 km<sup>2</sup> and 3612 km<sup>2</sup>. They derive a total volume loss of 683 Gt/year and an average disintegration rate of 37 %/year in this area. The loss rate is generally higher for small icebergs, though (Kubat *et al.*, 2007), meaning that large bergs can survive for many years or even decades (Budge and Long, 2018). Barbat *et al.* (2021) also estimate the decrease in iceberg mass per size class. While icebergs of 1–10 km<sup>2</sup> only contribute 0.2 Gt/year, the largest icebergs > 1000 km<sup>2</sup> contribute 498 Gt/year, which is the majority of the observed overall mass loss.

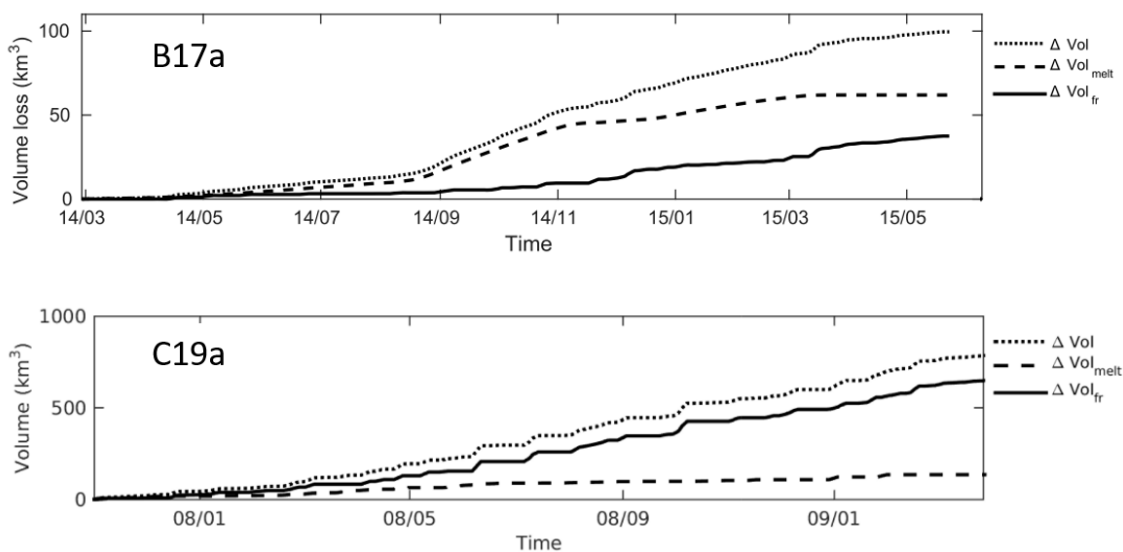


Figure 1.18: Volume loss of two giant tabular icebergs B17A and C19A. Extracted from Bouhier *et al.* (2018)

This makes iceberg melting a significant contribution to the overall freshwater budget of the Southern Ocean. Compared to the excess of precipitation over evaporation (P-E), iceberg melting contributes 5-20 % across the Southern Ocean (Marsh *et al.*, 2015; Rackow *et al.*, 2017). South of 63°S, total iceberg melting even reaches 66 % of P-E (Silva, Bigg and Nicholls, 2006). And in some areas including coastal areas, the Scotia Sea, the western Weddell Sea and Pridz Bay iceberg melting exceeds P-E (Gladstone, Bigg and Nicholls, 2001; Silva, Bigg and Nicholls,

2006; Marsh *et al.*, 2015; Rackow *et al.*, 2017 and Figure 1.19). Compared to the freshwater input from melting sea ice, iceberg meltwater contributes more than 20 % along the sea ice edge (Rackow *et al.*, 2017), but is an order of magnitude smaller across the whole Southern Ocean (Marsh *et al.*, 2015). Outside the sea ice edge, iceberg melting is the sole freshwater contribution from frozen ice (Rackow *et al.*, 2017 and Figure 1.19). Compared to coastal sea ice production rates (opposite sign), iceberg meltwater flux is also 5-20 % according to Rackow *et al.* (2017) and more than 100 % according to Marsh *et al.* (2015) in some places around the coast.

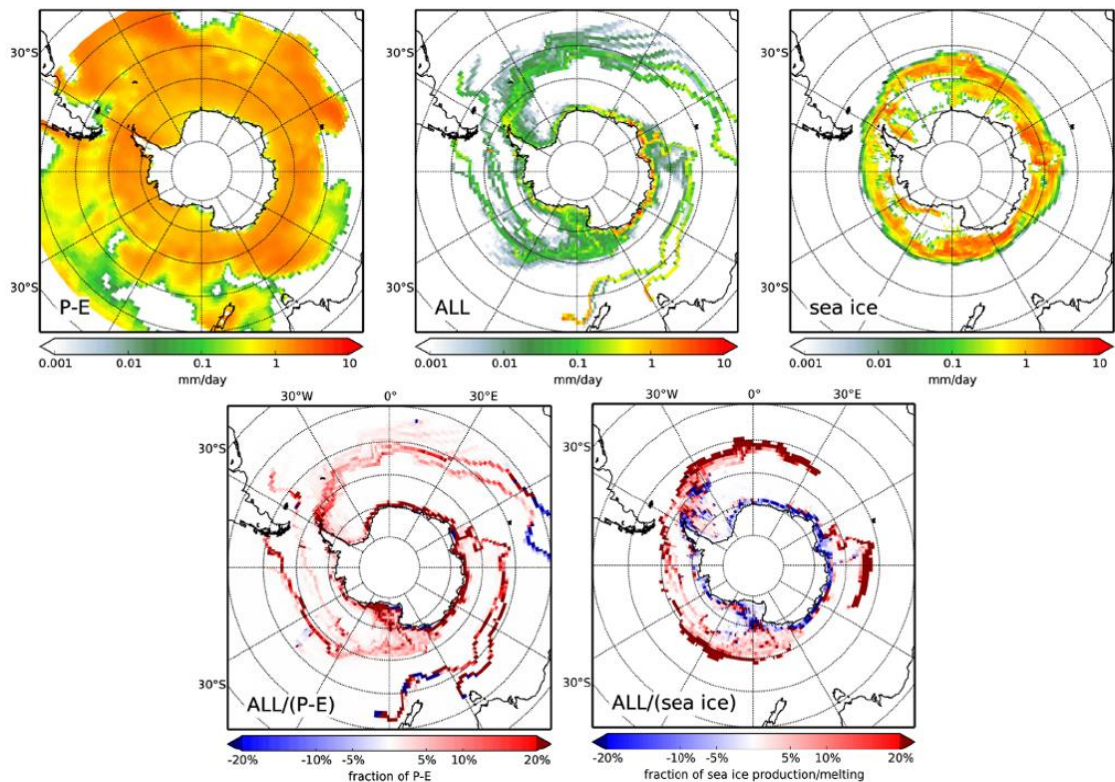


Figure 1.19: Meltwater input from precipitation-evaporation (first panel), icebergs (second panel) and sea ice (third panel) and relative contribution of icebergs compared to precipitation-evaporation and sea ice (lower panels respectively). Extracted from Rackow *et al.* (2017)

## 1.4. Main remaining challenges

After an introduction to the importance of icebergs and a summary of what previous studies have already found out, I now point out some of the remaining challenges.

Many studies stress the need for an improved representation of icebergs as a freshwater source around Antarctica (Merino *et al.*, 2016; Stern, Adcroft and Sergienko, 2016; Schloesser *et al.*, 2019). To date, most global climate models are lacking realistic freshwater fluxes from icebergs (Jongma *et al.*, 2009) and giant icebergs are not included in any of them (Schloesser *et al.*, 2019; Huth *et al.*, 2022).

Iceberg models are usually based on work by Bigg *et al.* (1997), which was developed for icebergs in the Arctic and they all make a number of simplifications: Some models neglect sea ice (Wagner, Dell and Eisenman, 2017), which can have significant impact on the steering and sheltering of icebergs (Schodlok *et al.*, 2006). Also iceberg grounding is sometimes not resolved (Wagner, Dell and Eisenman, 2017), but can significantly increase the iceberg life cycle (Barbat, Rackow, *et al.*, 2019). Furthermore, models treat icebergs as non-interacting passive particles (Rackow *et al.*, 2017; Wagner, Dell and Eisenman, 2017), although melting icebergs have been shown to influence ocean properties (Jenkins, 1999; Helly *et al.*, 2011; Merino *et al.*, 2016). It is also challenging to account for the rotation of icebergs, so most models assume a fixed orientation relative to the currents (Bigg *et al.*, 1997), choose random orientations (Wagner, Dell and Eisenman, 2017) or treat them as points (Rackow *et al.*, 2017). The main problem, however, is that iceberg fragmentation processes are hard to predict or their cause is not understood well enough yet (Rackow *et al.*, 2017; Wagner, Dell and Eisenman, 2017; Huth *et al.*, 2022) and therefore missing in models (Rackow *et al.*, 2017). This is also stressed by the fact that a new break-up mechanism has been found and described only very recently (Huth *et al.*, 2022). A missing representation of fragmentation mechanisms has large implications for iceberg drift, decay and life time (Wagner, Dell and Eisenman, 2017). Observations could help to understand some of these processes better.

Another major problem is that most models only include smaller icebergs (Gladstone, Bigg and Nicholls, 2001; Merino *et al.*, 2016; Schloesser *et al.*, 2019; Huth *et al.*, 2022). This leads to a misrepresentation in several ways: It introduces geographic biases, as small icebergs melt further south than larger ones (Silva, Bigg and Nicholls, 2006; Stern, Adcroft and Sergienko, 2016; Rackow *et al.*, 2017; England, Wagner and Eisenman, 2020; Huth *et al.*, 2022). Moreover, it leads to an artificial seasonality, which is no longer the case when giant icebergs are added (Rackow *et al.*, 2017). In terms of iceberg decay, it biases the decay rates, as small icebergs melt quicker (Kubat *et al.*, 2007; Hester *et al.*, 2021). These shortcomings have implications for the circulation and stratification of the Southern Ocean (England, Wagner and Eisenman, 2020), sea ice formation (Stern, Adcroft and Sergienko, 2016), biochemistry (Rackow *et al.*, 2017) and the Southern Ocean's carbon cycle (Smith *et al.*, 2011). Therefore, "the impact of icebergs on climate cannot be assessed without an accurate representation of their drift trajectories, breakup, and meltwater distribution." (Huth *et al.*, 2022)

Especially for giant icebergs, satellite measurements are a very powerful tool to study icebergs and to quantify their freshwater flux. Here, methods have been developed to study selected icebergs (Jansen, Schodlok and Rack, 2007; Scambos *et al.*, 2008; Bouhier *et al.*, 2018; Li *et al.*,

2018; Han *et al.*, 2019). To date, these methods are quite tedious, though, and cannot be automated. Extending them to all giant icebergs for an operational scenario requires automation of several steps, but the most laborious task is to derive iceberg outlines. Automated detection techniques have so far focussed on detecting smaller icebergs (Willis *et al.*, 1996; Tournadre, Whitmer and Girard-Ardhuin, 2008; Wesche and Dierking, 2012; Mazur, Wåhlin and Krężel, 2017). Applications are limited to a selected region (Mazur, Wåhlin and Kalén, 2019), near-coastal waters (Wesche and Dierking, 2015; Barbat, Rackow, *et al.*, 2019) or open ocean (Tournadre, Whitmer and Girard-Ardhuin, 2008; Tournadre *et al.*, 2015). They also struggle with the varying appearance of icebergs, sea ice, and ocean in SAR imagery in certain conditions (see Section 1.3.1). For operational observations of iceberg thickness, a harmonisation and synthesis of existing methods would be desirable. So far, they take different approaches to handle altimetry tracks over a floating iceberg and to convert freeboard to thickness. A better representation of the snow layer on top of icebergs and the evolution of snow and ice density over several years, when the iceberg is experiencing a variety of environmental conditions, would improve the accuracy of thickness estimates and hence melt rates. Similarly, an investigating of the scattering horizon of altimeters in such a thick and old snowpack is yet missing.

## 1.5. Thesis aim

The aim of this thesis is to develop novel methodology and datasets from satellite remote sensing observations to quantify the freshwater flux from giant Antarctic icebergs as accurately and efficiently as possible.

## 1.6. Thesis objectives

To address the thesis aim, the following research objectives have been defined:

1. Develop methodology to derive estimates of iceberg thickness change with improved accuracy. This will be achieved through (i) the use of consistently processed elevation data, (ii) an automatic collocation of altimetry tracks over the floating iceberg with heights pre-calving and (iii) considering the evolution of snow and ice density during a multi-annual drift
2. Create new datasets of changes in area, freeboard, thickness, volume and mass of two giant icebergs along their trajectories. This will be achieved by applying the improved methodology to the B30 and A68A icebergs

3. Develop a novel algorithm for automatic iceberg segmentation in SAR imagery to improve efficiency. This will be achieved by training a deep neural network
4. Evaluate the accuracy of different methods to automatically derive iceberg area. This will be achieved by first comparing estimates from (i) orthogonal axes lengths and (ii) arc-lengths of altimetry overpasses to manually derived outlines and later by applying (iii) a k-means segmentation approach, (iv) an Otsu thresholding technique and (v) my neural network approach to SAR imagery and again assessing them compared to manually derived outlines

## 1.7. Thesis structure

In Chapter 2, I investigate area, thickness and volume changes of the B30 iceberg from a synergy of satellite imagery and altimetry observations. Here, I investigate the methodology in detail, quantify the impact of certain processing steps and develop most of the methodological advances. I also compare manual delineations of iceberg area to two simple approximations of iceberg area in this chapter. Chapter 3 builds on Chapter 2 and applies a similar method to the famous A68A iceberg. Here, I extend the use of satellite altimetry to include measurements from ICESat-2 and improve the method by automating the collocation step for altimetry observations. In both chapters, mass loss and freshwater flux of these icebergs are derived along their trajectory and in Chapter 3 the impact on the local ecosystem is discussed. Chapter 4 then addresses the remaining bottleneck that iceberg outlines require manual delineation. In this chapter, I suggest a neural network approach to automatically segment giant icebergs in SAR imagery and compare the results to two standard-segmentation methods. Chapter 5 finally sums up the main findings, provides a synthesis of the three results chapters and proposes directions of future research. Chapters 2, 3 and 4 have been written as independent journal articles to convey the results to the research community. Author contribution statements are provided at the beginning of this thesis and each chapter. The work from Chapter 2 has been published in *The Cryosphere* and the work from Chapter 3 has been published in *Remote Sensing of Environment*. The work from Chapter 4 is currently under review in *The Cryosphere*. Small additions have been made to the chapters after the viva. The published/submitted papers are appended (Appendices A, B and C).

## References

- Adusumilli, S. *et al.* (2020) 'Interannual variations in meltwater input to the Southern Ocean from Antarctic ice shelves', *Nature Geoscience*, 13(9), pp. 616–620. doi: 10.1038/s41561-020-0616-z.
- De Angelis, H. and Skvarca, P. (2003) 'Glacier surge after ice shelf collapse', *Science*, 299(5612), pp. 1560–1562. doi: 10.1126/science.1077987.
- Aoki, S. (2003) 'Seasonal and spatial variations of iceberg drift off Dronning Maud Land, Antarctica, detected by satellite scatterometers', *Journal of Oceanography*, 59(5), pp. 629–635. doi: 10.1023/B:JOCE.0000009592.45617.dd.
- Arrigo, K. R. *et al.* (2002) 'Ecological impact of a large Antarctic iceberg', *Geophysical Research Letters*, 29(7), pp. 8-1-8–4. doi: 10.1029/2001GL014160.
- Arrigo, K. R. and van Dijken, G. L. (2003) 'Impact of iceberg C-19 on ross sea primary production', *Geophysical Research Letters*, 30(16), pp. 1–4. doi: 10.1029/2003GL017721.
- Barbat, M. M., Wesche, C., *et al.* (2019) 'An adaptive machine learning approach to improve automatic iceberg detection from SAR images', *ISPRS Journal of Photogrammetry and Remote Sensing*. Elsevier, 156(August), pp. 247–259. doi: 10.1016/j.isprsjprs.2019.08.015.
- Barbat, M. M., Rackow, T., *et al.* (2019) 'Three Years of Near-Coastal Antarctic Iceberg Distribution From a Machine Learning Approach Applied to SAR Imagery', *Journal of Geophysical Research: Oceans*, 124(9), pp. 6658–6672. doi: 10.1029/2019JC015205.
- Barbat, M. M. *et al.* (2021) 'Automated iceberg tracking with a machine learning approach applied to SAR imagery : A Weddell sea case study', *ISPRS Journal of Photogrammetry and Remote Sensing*. Elsevier B.V., 172(December 2020), pp. 189–206. doi: 10.1016/j.isprsjprs.2020.12.006.
- Barnes, D. K. A. (2017) 'Iceberg killing fields limit huge potential for benthic blue carbon in Antarctic shallows', *Global Change Biology*, 23(7), pp. 2649–2659. doi: 10.1111/gcb.13523.
- Bassis, J. N. (2011) 'The statistical physics of iceberg calving and the emergence of universal calving laws', *Journal of Glaciology*, 57(201), pp. 3–16. doi: 10.3189/002214311795306745.
- Bigg, G. (2015) *Icebergs: Their Science and Links to Global Change*. Cambridge University Press. doi: doi:10.1017/CBO9781107589278.
- Bigg, G. R. *et al.* (1997) 'Modelling the dynamics and thermodynamics of icebergs', *cold regions science and technology*, 26(2), pp. 113–135. doi: 10.1016/S0165-232X(97)00012-8.

- Bigg, G. R. *et al.* (2018) 'A model for assessing iceberg hazard', *Natural Hazards*. Springer Netherlands, 92(2), pp. 1113–1136. doi: 10.1007/s11069-018-3243-x.
- Borstad, C., McGrath, D. and Pope, A. (2017) 'Fracture propagation and stability of ice shelves governed by ice shelf heterogeneity', *Geophysical Research Letters*, 44(9), pp. 4186–4194. doi: 10.1002/2017GL072648.
- Bouhier, N. *et al.* (2018) 'Melting and fragmentation laws from the evolution of two large Southern Ocean icebergs estimated from satellite data', *Cryosphere*, 12(7), pp. 2267–2285. doi: 10.5194/tc-12-2267-2018.
- Budge, J. S. and Long, D. G. (2018) 'A Comprehensive Database for Antarctic Iceberg Tracking Using Scatterometer Data', *IEEE Journal of Selected Topics in Applied Earth Observations and Remote Sensing*, 11(2), pp. 434–442. doi: 10.1109/JSTARS.2017.2784186.
- Collares, L. L. *et al.* (2018) 'Iceberg drift and ocean circulation in the northwestern Weddell Sea, Antarctica', *Deep-Sea Research Part II: Topical Studies in Oceanography*. Elsevier Ltd, 149(March), pp. 10–24. doi: 10.1016/j.dsr2.2018.02.014.
- Crepon, M., Houssais, M. N. and Guily, B. Saint (1988) 'The drift of icebergs under wind action', *Journal of Geophysical Research*, 93.
- Dammann, D. O. *et al.* (2019) 'Iceberg topography and volume classification using TanDEM-X interferometry', *Cryosphere*, 13(7), pp. 1861–1875. doi: 10.5194/tc-13-1861-2019.
- Depoorter, M. A. *et al.* (2013) 'Calving fluxes and basal melt rates of Antarctic ice shelves', *Nature*. Nature Publishing Group, 502(7469), pp. 89–92. doi: 10.1038/nature12567.
- Dowdeswell, J. A. and Bamber, J. L. (2007) 'Keel depths of modern Antarctic icebergs and implications for sea-floor scouring in the geological record', *Marine Geology*, 243(1–4), pp. 120–131. doi: 10.1016/j.margeo.2007.04.008.
- Drinkwater, M. R. (1998) 'Satellite Microwave Radar Observations of Antarctic Sea Ice', *Analysis of SAR Data of the Polar Oceans*, pp. 145–187. doi: 10.1007/978-3-642-60282-5\_8.
- Dryak, M. C. and Enderlin, E. M. (2020) 'Analysis of Antarctic Peninsula glacier frontal ablation rates with respect to iceberg melt-inferred variability in ocean conditions', *Journal of Glaciology*, 66(257), pp. 457–470. doi: 10.1017/jog.2020.21.
- Dunlop, K. M., Barnes, D. K. A. and Bailey, D. M. (2014) 'Variation of scavenger richness and abundance between sites of high and low iceberg scour frequency in Ryder Bay, west Antarctic Peninsula', *Polar Biology*, 37(12), pp. 1741–1754. doi: 10.1007/s00300-014-1558-y.

- Duprat, L. P. A. M., Bigg, G. R. and Wilton, D. J. (2016) 'Enhanced Southern Ocean marine productivity due to fertilization by giant icebergs', *Nature Geoscience*, 9(3), pp. 219–221. doi: 10.1038/ngeo2633.
- Eik, K. and Gudmestad, O. T. (2010) 'Iceberg management and impact on design of offshore structures', *Cold Regions Science and Technology*. Elsevier B.V., 63(1–2), pp. 15–28. doi: 10.1016/j.coldregions.2010.04.008.
- Enderlin, E. M. *et al.* (2016) 'Iceberg meltwater fluxes dominate the freshwater budget in Greenland's iceberg-congested glacial fjords', *Geophysical Research Letters*, 43(21), pp. 11,287–11,294. doi: 10.1002/2016GL070718.
- Enderlin, E. M. *et al.* (2018) 'Greenland iceberg melt variability from high-resolution satellite observations', *Cryosphere*, 12(2), pp. 565–575. doi: 10.5194/tc-12-565-2018.
- Enderlin, E. M. and Hamilton, G. S. (2014) 'Estimates of iceberg submarine melting from high-resolution digital elevation models: Application to Sermilik Fjord, East Greenland', *Journal of Glaciology*, 60(224), pp. 1111–1116. doi: 10.3189/2014JoG14J085.
- Engelhardt, H. and Engelhardt, M. (2017) 'An equatorward force acting on large floating ice masses: Polfluchtkraft', *Annals of Glaciology*, 58(74), pp. 144–151. doi: 10.1017/aog.2017.17.
- England, M. R., Wagner, T. J. W. and Eisenman, I. (2020) 'Modeling the breakup of tabular icebergs', *Science Advances*, 6(51), pp. 1–9. doi: 10.1126/sciadv.abd1273.
- FitzMaurice, A., Cenedese, C. and Straneo, F. (2017) 'Nonlinear response of iceberg side melting to ocean currents', *Geophysical Research Letters*, 44(11), pp. 5637–5644. doi: 10.1002/2017GL073585.
- Frost, A., Ressel, R. and Lehner, S. (2016) 'Automated iceberg detection using high resolution X - band SAR images', *Canadian Journal of Remote Sensing*, 42(4). doi: <https://doi.org/10.1080/07038992.2016.1177451>.
- Fürst, J. J. *et al.* (2016) 'The safety band of Antarctic ice shelves', *Nature Climate Change*, 6(5), pp. 479–482. doi: 10.1038/nclimate2912.
- Gade, H. G. (1979) 'Melting of Ice in Sea Water: A Primitive Model with Application to the Antarctic Ice Shelf and Icebergs', *Journal of Physical Oceanography*, pp. 189–198. doi: 10.1175/1520-0485(1979)009<0189:moiiisw>2.0.co;2.
- Giles, K. A., Laxon, S. W. and Worby, A. P. (2008) 'Antarctic sea ice elevation from satellite radar altimetry', *Geophysical Research Letters*, 35(3), pp. 1–5. doi: 10.1029/2007GL031572.
- Gill, R. S. (2001) 'Operational detection of sea ice edges and icebergs using SAR', *Canadian Journal of Remote Sensing*, 27(5), pp. 411–432. doi: 10.1080/07038992.2001.10854884.

- Gladstone, R. and Bigg, G. R. (2002) 'Satellite tracking of icebergs in the Weddell Sea', *Antarctic Science*, 14(3), pp. 278–287. doi: 10.1017/S0954102002000032.
- Gladstone, R. M., Bigg, G. R. and Nicholls, K. W. (2001) 'Iceberg trajectory modeling and meltwater injection in the Southern Ocean', *Journal of Geophysical Research: Oceans*, 106(C9), pp. 19903–19915. doi: 10.1029/2000jc000347.
- Goodman, D. J., Wadhams, P. and Squire, V. A. (1980) 'The Flexural Response of a Tabular Ice Island to Ocean Swell', *Annals of Glaciology*, 1, pp. 23–27. doi: 10.3189/s0260305500016906.
- Greene, C. A. *et al.* (2022) 'Antarctic calving loss rivals ice-shelf thinning', *Nature*. Springer US, 609(7929), pp. 948–953. doi: 10.1038/s41586-022-05037-w.
- Gutt, J. (2001) 'On the direct impact of ice on marine benthic communities, a review', *Polar Biology*, 24(8), pp. 553–564. doi: 10.1007/s003000100262.
- Hamley, T. C. and Budd, W. F. (1986) 'Antarctic Iceberg Distribution and Dissolution', *Journal of Glaciology*, 32(111), pp. 242–251. doi: 10.1017/s0022143000015574.
- Han, H. *et al.* (2019) 'Changes in a giant iceberg created from the collapse of the Larsen C Ice Shelf, Antarctic Peninsula, derived from Sentinel-1 and CryoSat-2 data', *Remote Sensing*, 11(4), pp. 1–14. doi: 10.3390/rs11040404.
- Hellmer, H. H. and Olbers, D. J. (1989) 'A two-dimensional model for the thermohaline circulation under an ice shelf', *Antarctic Science*, 1(4), pp. 325–336. doi: 10.1017/S0954102089000490.
- Helly, J. J. *et al.* (2011) 'Cooling, dilution and mixing of ocean water by free-drifting icebergs in the Weddell Sea', *Deep-Sea Research Part II: Topical Studies in Oceanography*. Elsevier, 58(11–12), pp. 1346–1363. doi: 10.1016/j.dsr2.2010.11.010.
- Hester, E. W. *et al.* (2021) 'Aspect ratio affects iceberg melting', *Physical Review Fluids*. American Physical Society, 6(2), p. 23802. doi: 10.1103/PhysRevFluids.6.023802.
- Hogg, A. E. and Gudmundsson, G. H. (2017) 'Commentary: Impacts of the Larsen-C Ice Shelf calving event', *Nature Climate Change*. Nature Publishing Group, 7(8), pp. 540–542. doi: 10.1038/nclimate3359.
- Holland, D. M. and Jenkins, A. (1999) 'Modeling thermodynamic ice-ocean interactions at the base of an ice shelf', *Journal of Physical Oceanography*, 29(8 PART 1), pp. 1787–1800. doi: 10.1175/1520-0485(1999)029<1787:mtioia>2.0.co;2.
- Hopwood, M. J. *et al.* (2019) 'Highly variable iron content modulates iceberg-ocean fertilisation and potential carbon export', *Nature Communications*. Springer US, 10(1). doi: 10.1038/s41467-019-13231-0.

- Hunke, E. C. and Comeau, D. (2011) 'Sea ice and iceberg dynamic interaction', *Journal of Geophysical Research: Oceans*, 116(5), pp. 1–9. doi: 10.1029/2010JC006588.
- Huppert, H. E. and Turner, J. S. (1978) 'On melting icebergs', *Nature*, 271, pp. 46–48.
- Huth, A. *et al.* (2022) 'Ocean currents break up a tabular iceberg', *Science advances*, 8(42), p. eabq6974. doi: 10.1126/sciadv.abq6974.
- Jacka, T. H. and Giles, A. B. (2007) 'Antarctic iceberg distribution and dissolution from ship-based observations', *Journal of Glaciology*, 53(182), pp. 341–356. doi: 10.3189/002214307783258521.
- Jacobs, S. S. *et al.* (1992) 'Melting of ice shelves and the mass balance of Antarctica', *Journal of Glaciology*, 38(130), pp. 375–387. doi: 10.1017/S0022143000002252.
- Jacobs, S. S., Gordon, A. L. and Amos, A. F. (1979) 'Effect of glacial ice melting on the Antarctic Surface Water', *Nature*, 277(February), pp. 469–471.
- Jansen, D. *et al.* (2015) 'Brief Communication: Newly developing rift in Larsen C Ice Shelf presents significant risk to stability', *Cryosphere*, 9(3), pp. 1223–1227. doi: 10.5194/tc-9-1223-2015.
- Jansen, D., Schodlok, M. and Rack, W. (2007) 'Basal melting of A-38B: A physical model constrained by satellite observations', *Remote Sensing of Environment*, 111(2), pp. 195–203. doi: 10.1016/j.rse.2007.03.022.
- Jenkins, A. (1999) 'The impact of melting ice on ocean waters', *Journal of Physical Oceanography*, 29(9), pp. 2370–2381. doi: 10.1175/1520-0485(1999)029<2370:TIOmio>2.0.CO;2.
- Joiris, C. R. (2018) 'Seabird hotspots on icebergs in the Amundsen Sea, Antarctica', *Polar Biology*. Springer Berlin Heidelberg, 41(1), pp. 111–114. doi: 10.1007/s00300-017-2174-4.
- Jongma, J. I. *et al.* (2009) 'The effect of dynamic-thermodynamic icebergs on the Southern Ocean climate in a three-dimensional model', *Ocean Modelling*. Elsevier Ltd, 26(1–2), pp. 104–113. doi: 10.1016/j.ocemod.2008.09.007.
- Kacimi, S. and Kwok, R. (2020) 'The Antarctic sea ice cover from ICESat-2 and CryoSat-2: freeboard, snow depth and ice thickness', *The Cryosphere Discussions*, pp. 1–33. doi: 10.5194/tc-2020-145.
- Kern, S. and Ozsoy, B. (2019) 'An attempt to improve snow depth retrieval using satellite microwave radiometry for rough antarctic sea ice', *Remote Sensing*, 11(19). doi: 10.3390/rs11192323.
- Koo, Y. *et al.* (2021) 'Semi-automated tracking of iceberg B43 using Sentinel-1 SAR images via Google Earth Engine', *The Cryosphere*, 15(May), pp. 4727–4744. doi: <https://doi.org/10.5194/tc-15-4727-2021>.

- Kooyman, G. L. *et al.* (2007) 'Effects of giant icebergs on two emperor penguin colonies in the Ross Sea, Antarctica', *Antarctic Science*. University of Leeds, 19(1), pp. 31–38. doi: 10.1017/S0954102007000065.
- Kubat, I. *et al.* (2007) 'An Operational Iceberg Deterioration Model', in *Proceedings of the Seventeenth International Offshore Polar Engineering Conference*.
- Lawson, J. D. and Russell-Head, D. S. (1982) 'AUGMENTATION OF URBAN WATER BY ANTARCTIC ICEBERGS', *Coastal Engineering Proceedings*. doi: <https://doi.org/10.1061/9780872623736.159>.
- Li, Tian *et al.* (2018) 'Monitoring the tabular icebergs C28A and C28B calved from the Mertz Ice Tongue using radar remote sensing data', *Remote Sensing of Environment*. Elsevier, 216(July 2017), pp. 615–625. doi: 10.1016/j.rse.2018.07.028.
- Lichey, C. and Hellmer H., H. H. (2001) 'Modeling giant-iceberg drift under the influence of sea ice in the Weddell Sea, Antarctica', *Journal of Glaciology*, 47(158), pp. 452–460. doi: 10.3189/172756501781832133.
- Liu, X. *et al.* (2022) 'Grounding event of iceberg d28 and its interactions with seabed topography', *Remote Sensing*, 14(1). doi: 10.3390/rs14010154.
- Liu, Y. *et al.* (2015) 'Ocean-driven thinning enhances iceberg calving and retreat of Antarctic ice shelves', *Proceedings of the National Academy of Sciences of the United States of America*, 112(11), pp. 3263–3268. doi: 10.1073/pnas.1415137112.
- Liu, Z., Amdahl, J. and Løset, S. (2011) 'Integrated numerical analysis of an iceberg collision with a foreship structure', *Marine Structures*. Elsevier Ltd, 24(4), pp. 377–395. doi: 10.1016/j.marstruc.2011.05.004.
- Lopez-Lopez, L. *et al.* (2021) 'On the detection and long-term path visualisation of a-68 iceberg', *Remote Sensing*, 13(3), pp. 1–13. doi: 10.3390/rs13030460.
- MacAyeal, D. R. *et al.* (2008) 'Tabular iceberg collisions within the coastal regime', *Journal of Glaciology*, 54(185), pp. 371–386. doi: 10.3189/002214308784886180.
- Macqueen, J. (1967) 'SOME METHODS FOR CLASSIFICATION AND ANALYSIS OF MULTIVARIATE OBSERVATIONS', in *Proceedings of the fifth Berkeley symposium on mathematical statistics and probability*. California: University of California Press., pp. 281–297.
- Marsh, R. *et al.* (2015) 'NEMO-ICB (v1.0): Interactive icebergs in the NEMO ocean model globally configured at eddy-permitting resolution', *Geoscientific Model Development*, 8(5), pp. 1547–1562. doi: 10.5194/gmd-8-1547-2015.

- Martin, T. and Adcroft, A. (2010) 'Parameterizing the fresh-water flux from land ice to ocean with interactive icebergs in a coupled climate model', *Ocean Modelling*. Elsevier Ltd, 34(3–4), pp. 111–124. doi: 10.1016/j.ocemod.2010.05.001.
- Mazur, A. K., Wåhlin, A. K. and Kalén, O. (2019) 'The life cycle of small-to medium-sized icebergs in the Amundsen sea embayment', *Polar Research*, 38, pp. 1–17. doi: 10.33265/polar.v38.3313.
- Mazur, A. K., Wåhlin, A. K. and Krężel, A. (2017) 'An object-based SAR image iceberg detection algorithm applied to the Amundsen Sea', *Remote Sensing of Environment*, 189, pp. 67–83. doi: 10.1016/j.rse.2016.11.013.
- Merino, N. *et al.* (2016) 'Antarctic icebergs melt over the Southern Ocean : Climatology and impact on sea ice', *Ocean Modelling*. Elsevier Ltd, 104, pp. 99–110. doi: 10.1016/j.ocemod.2016.05.001.
- Morgan, V. I. and Budd, W. F. (1978) 'the Distribution, Movement and Melt Rates of Antarctic Icebergs', in *Iceberg Utilization*. Iowa State University Research Foundation, pp. 220–228. doi: 10.1016/b978-0-08-022916-4.50025-x.
- Morison, J. and Goldberg, D. (2012) 'A brief study of the force balance between a small iceberg, the ocean, sea ice, and atmosphere in the Weddell Sea', *Cold Regions Science and Technology*. Elsevier B.V., 76–77, pp. 69–76. doi: 10.1016/j.coldregions.2011.10.014.
- Murphy, D. L. and Cass, J. (2012) 'The International Ice Patrol: Safeguarding Life and Property at Sea', in *Coast Guard Journal of Safety & Security at Sea, Proceedings of the Marine Safety & Security Council*.
- Neshyba, S. and Josberger, E. G. (1980) 'On the estimation of Antarctic iceberg melt rate', *Journal of Physical Oceanography*, 10(10), pp. 1681–1685. doi: [https://doi.org/10.1175/1520-0485\(1980\)010<1681:OTEOAI>2.0.CO;2](https://doi.org/10.1175/1520-0485(1980)010<1681:OTEOAI>2.0.CO;2).
- Normandeau, A. *et al.* (2021) 'Submarine landslides triggered by iceberg collision with the seafloor', *Nature Geoscience*. Springer US, 14(8), pp. 599–605. doi: 10.1038/s41561-021-00767-4.
- Orheim, O. *et al.* (2022) 'Antarctic iceberg distribution revealed through three decades of systematic ship-based observations in the SCAR International Iceberg Database', *Journal of Glaciology*, pp. 1–15. doi: 10.1017/jog.2022.84.
- Rack, W. and Rott, H. (2004) 'Pattern of retreat and disintegration of the Larsen B ice shelf, Antarctic Peninsula', *Annals of Glaciology*, 39, pp. 505–510. doi: 10.3189/172756404781814005.

- Rackow, T. *et al.* (2017) 'A simulation of small to giant Antarctic iceberg evolution: Differential impact on climatology estimates', *Journal of Geophysical Research : Oceans*, pp. 3170–3190. doi: 10.1002/2016JC012513
- Raiswell, R. *et al.* (2008) 'Bioavailable iron in the Southern Ocean: The significance of the iceberg conveyor belt', *Geochemical Transactions*, 9, pp. 1–9. doi: 10.1186/1467-4866-9-7.
- Raiswell, R. *et al.* (2016) 'Potentially bioavailable iron delivery by iceberg-hosted sediments and atmospheric dust to the polar oceans', *Biogeosciences*, 13(13), pp. 3887–3900. doi: 10.5194/bg-13-3887-2016.
- Remy, J. P. *et al.* (2008) 'Impact of the B-15 iceberg "stranding event" on the physical and biological properties of sea ice in McMurdo Sound, Ross Sea, Antarctica', *Antarctic Science*, 20(6), pp. 593–604. doi: 10.1017/S0954102008001284.
- Rignot, E. *et al.* (2004) 'Accelerated ice discharge from the Antarctic Peninsula following the collapse of Larsen B ice shelf', *Geophysical Research Letters*, 31(18), pp. 2–5. doi: 10.1029/2004GL020697.
- Rignot, E. *et al.* (2013) 'Ice-shelf melting around Antarctica', *Science*, 341(6143), pp. 266–270. doi: 10.1126/science.1235798.
- Robinson, N. J. and Williams, M. J. M. (2012) 'Iceberg-induced changes to polynya operation and regional oceanography in the southern Ross Sea, Antarctica, from in situ observations', *Antarctic Science*, 24(5), pp. 514–526. doi: 10.1017/S0954102012000296.
- Romanov, Y. A. and Romanova, N. A. (2018) 'Icebergs in the Southern Ocean and Factors Defining Their Distribution', *Russian Meteorology and Hydrology*, 43(3), pp. 178–187. doi: 10.3103/S1068373918030068.
- Romanov, Y. A., Romanova, N. A. and Romanov, P. (2012) 'Shape and size of Antarctic icebergs derived from ship observation data', *Antarctic Science*, 24(1), pp. 77–87. doi: 10.1017/S0954102011000538.
- Romanov, Y. A., Romanova, N. A. and Romanov, P. (2017) 'Geographical distribution and volume of Antarctic icebergs derived from ship observation data', *Annals of Glaciology*, 58(74), pp. 28–40. doi: 10.1017/aog.2017.2.
- Rott, H., Skvarca, P. and Nagler, T. (1996) 'Rapid collapse of northern Larsen Ice Shelf, Antarctica', *Science*, 271(5250), pp. 788–792. doi: 10.1126/science.271.5250.788.
- Ruhl, H. A. *et al.* (2011) 'Seabird aggregation around free-drifting icebergs in the northwest Weddell and Scotia Seas', *Deep-Sea Research Part II: Topical Studies in Oceanography*. Elsevier, 58(11–12), pp. 1497–1504. doi: 10.1016/j.dsr2.2010.11.028.

- Russell-Head, D. S. (1980) 'The Melting of Free-Drifting Icebergs', *Annals of Glaciology*, 1, pp. 119–122. doi: 10.3189/s0260305500017092.
- De Rydt, J. *et al.* (2021) 'Drivers of Pine Island Glacier speed-up between 1996 and 2016', *Cryosphere*, 15(1), pp. 113–132. doi: 10.5194/tc-15-113-2021.
- Sandven, S., Babiker, M. and Kloster, K. (2007) 'Iceberg observations in the barents sea by radar and optical satellite images', in *Proceedings of the Envisat Symposium*.
- Savage, S. B. (2007) 'Aspects of Iceberg Deterioration and Drift', *Geomorphological Fluid Mechanics*, pp. 279–318. doi: 10.1007/3-540-45670-8\_12.
- Scambos, T. *et al.* (2005) 'ICESat profiles of tabular iceberg margins and iceberg breakup at low latitudes', *Geophysical Research Letters*, 32(23), pp. 1–4. doi: 10.1029/2005GL023802.
- Scambos, T. *et al.* (2008) 'Calving and ice-shelf break-up processes investigated by proxy: Antarctic tabular iceberg evolution during northward drift', *Journal of Glaciology*, 54(187), pp. 579–591. doi: 10.3189/002214308786570836.
- Scambos, T. *et al.* (2009) 'Ice shelf disintegration by plate bending and hydro-fracture: Satellite observations and model results of the 2008 Wilkins ice shelf break-ups', *Earth and Planetary Science Letters*, 280(1–4), pp. 51–60. doi: 10.1016/j.epsl.2008.12.027.
- Scambos, T. A., Hulbe, C. and Fahnestock, M. (2003) 'Climate Induced Ice Shelf Disintegration in the Antarctic Peninsula', *Antarctic Research Series*, 79(Antarctic Peninsula Climate Variability: Historical and Paleoenvironmental Perspectives), pp. 79–92. Available at: <https://doi.org/10.1029/AR079p0079>.
- Schloesser, F. *et al.* (2019) 'Antarctic iceberg impacts on future Southern Hemisphere climate', *Nature Climate Change*. Springer US, 9(9), pp. 672–677. doi: 10.1038/s41558-019-0546-1.
- Schodlok, M. P. *et al.* (2006) 'Weddell Sea iceberg drift: Five years of observations', *Journal of Geophysical Research: Oceans*, 111(6), pp. 1–14. doi: 10.1029/2004JC002661.
- Schwarz, J. N. and Schodlok, M. P. (2009) 'Impact of drifting icebergs on surface phytoplankton biomass in the Southern Ocean: Ocean colour remote sensing and in situ iceberg tracking', *Deep-Sea Research Part I: Oceanographic Research Papers*, 56(10), pp. 1727–1741. doi: 10.1016/j.dsr.2009.05.003.
- Schwerdtfeger, P. (1979) 'Review: On icebergs and their uses. A report to the Australian Academy of Science', *Cold Regions Science and Technology*, 1(1), pp. 59–79. doi: 10.1016/0165-232x(79)90020-x.
- Shepherd, A., Fricker, H. A. and Farrell, S. L. (2018) 'Trends and connections across the Antarctic cryosphere', *Nature*, 558(7709), pp. 223–232. doi: 10.1038/s41586-018-0171-6.

- Shiggins, C. J., Lea, J. M. and Brough, S. (2022) 'Automated ArcticDEM iceberg detection tool : insights into area and volume distributions , and their potential application to satellite imagery and modelling of glacier-iceberg-ocean systems', *The Cryosphere Discussions*, di(August), pp. 1–24.
- Silva, T. A. M. and Bigg, G. R. (2005) 'Computer-based identification and tracking of Antarctic icebergs in SAR Computer-based identification and tracking of Antarctic icebergs in SAR images', (May 2018). doi: 10.1016/j.rse.2004.10.002.
- Silva, T. A. M., Bigg, G. R. and Nicholls, K. W. (2006) 'Contribution of giant icebergs to the Southern Ocean freshwater flux', *Journal of Geophysical Research*, 111(July 2005), pp. 1–8. doi: 10.1029/2004JC002843.
- Smith, K. L. *et al.* (2007) 'Free-drifting icebergs: Hot spots of chemical and biological enrichment in the Weddell Sea', *Science*, 317(5837), pp. 478–482. doi: 10.1126/science.1142834.
- Smith, K. L. *et al.* (2011) 'Carbon export associated with free-drifting icebergs in the Southern Ocean', *Deep-Sea Research Part II: Topical Studies in Oceanography*. Elsevier, 58(11–12), pp. 1485–1496. doi: 10.1016/j.dsr2.2010.11.027.
- Smith, K. L. *et al.* (2013) 'Icebergs as unique lagrangian ecosystems in polar seas', *Annual Review of Marine Science*, 5(August 2012), pp. 269–287. doi: 10.1146/annurev-marine-121211-172317.
- Stephenson, G. R. *et al.* (2011) 'Subsurface melting of a free-floating Antarctic iceberg', *Deep-Sea Research Part II: Topical Studies in Oceanography*. Elsevier, 58(11–12), pp. 1336–1345. doi: 10.1016/j.dsr2.2010.11.009.
- Stern, A. A., Adcroft, A. and Sergienko, O. (2016) 'The effects of Antarctic iceberg calving-size distribution in a gloabl climate model', *Journal of Geophysical Research: Oceans*, pp. 1–14. doi: 10.1002/2016JC011835
- Stuart, K. M. and Long, D. G. (2008) 'Analysis of antarctic iceberg and sea ice melting patterns using quikscat', *International Geoscience and Remote Sensing Symposium (IGARSS)*. IEEE, 5(1), pp. 192–195. doi: 10.1109/IGARSS.2008.4780060.
- Stuart, K. M. and Long, D. G. (2011) 'Tracking large tabular icebergs using the SeaWinds Ku-band microwave scatterometer', *Deep-Sea Research Part II: Topical Studies in Oceanography*. Elsevier, 58(11–12), pp. 1285–1300. doi: 10.1016/j.dsr2.2010.11.004.
- Sulak, D. J. *et al.* (2017) 'Iceberg properties and distributions in three Greenlandic fjords using satellite imagery', *Annals of Glaciology*, 58(74), pp. 92–106. doi: 10.1017/aog.2017.5.
- Tchernia, P. and Jeannin, P. F. (1984) 'Circulation in antarctic waters as revealed by iceberg tracks 1972–1983', *Polar Record*, 22(138), pp. 263–269. doi: 10.1017/S0032247400005386.

- Tournadre, J. *et al.* (2015) 'Large icebergs characteristics from altimeter waveforms analysis', *Journal of Geophysical Research: Oceans*, 120(3), pp. 2121–2128. doi: <https://doi.org/10.1002/2014JC010502>.
- Tournadre, J. *et al.* (2016) 'Antarctic icebergs distributions 1992–2014', *Journal of Geophysical Research: Oceans*. John Wiley & Sons, Ltd, 121(1), pp. 327–349. doi: 10.1002/2015JC011178.
- Tournadre, J., Girard-Ardhuin, F. and Legrésy, B. (2012) 'Antarctic icebergs distributions, 2002–2010', *Journal of Geophysical Research: Oceans*, 117(5), pp. 2002–2010. doi: 10.1029/2011JC007441.
- Tournadre, J., Whitmer, K. and Girard-Ardhuin, F. (2008) 'Iceberg detection in open water by altimeter waveform analysis', *Journal of Geophysical Research: Oceans*, 113(8), pp. 2–9. doi: 10.1029/2007JC004587.
- Ulaby, F. T. and Long, D. G. (2014) *Microwave radar and radiometric remote sensing*. The University of Michigan Press.
- Vernet, M. *et al.* (2011) 'Impacts on phytoplankton dynamics by free-drifting icebergs in the NW Weddell Sea', *Deep-Sea Research Part II: Topical Studies in Oceanography*. Elsevier, 58(11–12), pp. 1422–1435. doi: 10.1016/j.dsr2.2010.11.022.
- Vernet, M. *et al.* (2012) 'Islands of ice: Influence of free-drifting Antarctic icebergs on pelagic marine ecosystems', *Oceanography*, 25(3), pp. 38–39. doi: 10.5670/oceanog.2012.72.
- Vinje, T. E. (1980) 'Some Satellite-Tracked Iceberg Drifts in the Antarctic', *Annals of Glaciology*, 1(22), pp. 83–87. doi: 10.3189/s026030550001702x.
- Wagner, T. J. W. *et al.* (2014) 'The "footloose" mechanism: Iceberg decay from hydrostatic stresses', *Geophysical Research Letters*, 41(15), pp. 5522–5529. doi: 10.1002/2014GL060832.
- Wagner, T. J. W., Dell, R. W. and Eisenman, I. (2017) 'An analytical model of iceberg drift', *Journal of Physical Oceanography*, 47(7), pp. 1605–1616. doi: 10.1175/JPO-D-16-0262.1.
- Weeks, W. F. and Campbell, W. J. (1973) 'Icebergs as a fresh-water source: an appraisal', *Journal of Glaciology*, 12(65).
- Wesche, C. and Dierking, W. (2012) 'Iceberg signatures and detection in SAR images in two test regions of the Weddell Sea, Antarctica', *Journal of Glaciology*, 58(208), pp. 325–339. doi: 10.3189/2012JOG11J020.
- Wesche, C. and Dierking, W. (2015) 'Near-coastal circum-Antarctic iceberg size distributions determined from Synthetic Aperture Radar images', *Remote Sensing of Environment*. Elsevier Inc., 156, pp. 561–569. doi: 10.1016/j.rse.2014.10.025.

- Willatt, R. C. *et al.* (2010) 'Field investigations of Ku-band radar penetration into snow cover on antarctic sea ice', *IEEE Transactions on Geoscience and Remote Sensing*. IEEE, 48(1), pp. 365–372. doi: 10.1109/TGRS.2009.2028237.
- Williams, R. and Macdonald, M. (1995) 'An image segmentation technique to infer the outlines of icebergs, depicted in satellite images, from their shadows and bright sunlit surfaces', *ANZIIS 1995 - Proceedings of the 3rd Australian and New Zealand Conference on Intelligent Information Systems*, pp. 76–81. doi: 10.1109/ANZIIS.1995.705718.
- Williams, R. N., Rees, W. G. and Young, N. W. (1999) 'A technique for the identification and analysis of icebergs in synthetic aperture radar images of Antarctica', *International Journal of Remote Sensing*, 20(15–16), pp. 3183–3199. doi: 10.1080/014311699211697.
- Willis, C. J. *et al.* (1996) 'Iceberg detection using ers-1 synthetic aperture radar', *International Journal of Remote Sensing*, 17(9), pp. 1777–1795. doi: 10.1080/01431169608948739.
- Wise, M. G. *et al.* (2017) 'Evidence of marine ice-cliff instability in Pine Island Bay from iceberg-keel plough marks', *Nature*, 550(7677), pp. 506–510. doi: 10.1038/nature24458.
- Wu, S. Y. and Hou, S. (2017) 'Impact of icebergs on net primary productivity in the Southern Ocean', *Cryosphere*, 11(2), pp. 707–722. doi: 10.5194/tc-11-707-2017.
- Young, N. W. *et al.* (1998) 'Near-coastal iceberg distributions in East Antarctica, 50-145°E', *Annals of Glaciology*, 27, pp. 68–74. doi: 10.3189/1998aog27-1-68-74.

# 2

## TRACKING CHANGES IN THE AREA, THICKNESS, AND VOLUME OF THE THWAITES TABULAR ICEBERG "B30" USING SATELLITE ALTIMETRY AND IMAGERY

**This chapter is based on the following paper with small post-viva additions.**

**Citation:** Braakmann-Folgmann, A., Shepherd, A., Ridout, A., 2021. Tracking changes in the area, thickness, and volume of the Thwaites tabular iceberg "B30" using satellite altimetry and imagery. *Cryosphere* 15, 3861–3876. <https://doi.org/10.5194/tc-15-3861-2021>

**Author contributions:** I designed the study together with my supervisor, Andy Shepherd. Andy Ridout provided pre-processed CryoSat elevations. I then computed iceberg freeboard, area, and volume change, calculated the uncertainties, prepared the figures, wrote the manuscript and revised it according to the reviewers' comments. Andy Shepherd supervised the work and suggested edits to the manuscript.

2. Tracking changes in the area, thickness, and volume of the Thwaites tabular iceberg “B30” using satellite altimetry and imagery
- 

## Abstract

Icebergs account for half of all ice loss from Antarctica and, once released, present a hazard to maritime operations. Their melting leads to a redistribution of cold fresh water around the Southern Ocean which, in turn, influences water circulation, promotes sea ice formation, and fosters primary production. In this study, we combine CryoSat-2 satellite altimetry with MODIS and Sentinel-1 satellite imagery and meteorological data to track changes in the area, freeboard, thickness, and volume of the B30 tabular iceberg between 2012 and 2018. We track the iceberg elevation when it was attached to Thwaites Glacier and on a further 106 occasions after it calved using Level 1b CryoSat data, which ensures that measurements recorded in different acquisition modes and within different geographical zones are consistently processed. From these data, we map the iceberg’s freeboard and estimate its thickness taking snowfall and changes in snow and ice density into account. We compute changes in freeboard and thickness relative to the initial average for each overpass and compare these to estimates from precisely located tracks using the satellite imagery. This comparison shows good agreement (correlation coefficient 0.87), and suggests that collocation reduces the freeboard uncertainty by 1.6 m. We also demonstrate that the snow layer has a significant impact on iceberg thickness change. Changes in the iceberg area are measured by tracing its perimeter and we show that alternative estimates based on arc lengths recorded in satellite altimetry profiles and on measurements of the semi-major and semi-minor axes also capture the trend, though with a 48 % overestimate and a 15 % underestimate, respectively. Since it calved, the area of B30 has decreased from  $1500 \pm 60$  to  $426 \pm 27$  km<sup>2</sup>, its mean freeboard has fallen from  $49.0 \pm 4.6$  to  $38.8 \pm 2.2$  m, and its mean thickness has reduced from  $315 \pm 36$  to  $198 \pm 14$  m. The combined loss amounts to an  $80 \pm 16$  % reduction in volume, two thirds ( $69 \pm 14$  %) of which is due to fragmentation and the remainder ( $31 \pm 11$  %) is due to basal melting.

## 2.1. Introduction

Iceberg calving accounts for roughly half of all ice loss from Antarctica (Depoorter *et al.*, 2013; Rignot *et al.*, 2013). At any time, about 50-90 large tabular icebergs are tracked in the Southern Ocean containing 7 000 to 17 000 km<sup>3</sup> of ice in total (Tournadre *et al.*, 2015). For maritime operators it is essential to know the location of icebergs in order to reduce the risk of collision (Power *et al.*, 2001; Eik and Gudmestad, 2010; Bigg *et al.*, 2018). The thickness of an iceberg

2. Tracking changes in the area, thickness, and volume of the Thwaites tabular iceberg “B30” using satellite altimetry and imagery

---

determines if and where it will ground on the seabed, which has implications for maritime operations as well as for marine geophysics. Iceberg thickness also influences a wide range of physical and biological interactions with the Antarctic environment. Grounded icebergs can, for example, alter the local ocean circulation (Grosfeld *et al.*, 2001; Robinson and Williams, 2012), influence melting of the adjacent ice shelves (Robinson and Williams, 2012), and prevent local sea ice from breaking up (Nøst and Østerhus, 1998; Remy *et al.*, 2008). This, in turn, can impact the local primary production (Arrigo *et al.*, 2002; Remy *et al.*, 2008) and pose an obstacle to penguin colonies on their way to their feeding grounds (Kooyman *et al.*, 2007). Temporarily grounded icebergs leave plough marks on the sea floor which can be an important geological record (Wise *et al.*, 2017) but also impact on marine benthic communities (Gutt, 2001; Barnes, 2017). Therefore, iceberg thickness is an important parameter.

Changes in iceberg thickness are also important, because they control the quantity of cold fresh water and terrigenous nutrients released into the ocean as icebergs melt (Gladstone, Bigg and Nicholls, 2001; Silva, Bigg and Nicholls, 2006). The release of relatively cold fresh water facilitates sea ice growth (Bintanja, Van Oldenborgh and Katsman, 2015; Merino *et al.*, 2016), immediately lowers the sea surface temperature (Merino *et al.*, 2016), and has been found to even influence ocean water down to 1500 m depth (Helly *et al.*, 2011) as well as lead to upwelling of deep ocean properties (Jenkins, 1999). In terms of nutrients, icebergs have shown to be the main source of iron in the Southern Ocean (Raiswell *et al.*, 2016; Wu and Hou, 2017; Laufkötter *et al.*, 2018) and therefore foster primary production in the proximity of icebergs (Helly *et al.*, 2011; Biddle *et al.*, 2015; Duprat, Bigg and Wilton, 2016), which in turn increases the abundance of krill and seabirds (Smith *et al.*, 2007; Joiris, 2018) around icebergs. Furthermore, a range of studies have demonstrated that including more realistic iceberg distributions, trajectories, and volumes in climate models leads to a redistribution of fresh water and heat flux, which agrees better with observations than models that only include small icebergs or that treat iceberg discharge as coastal runoff (Jongma *et al.*, 2009; Martin and Adcroft, 2010; Rackow *et al.*, 2017; Schloesser *et al.*, 2019). To investigate each of these processes and interrelations, knowledge of iceberg thickness and volume and their change over time is required (England *et al.*, 2020; Merino *et al.*, 2016). Moreover, monitoring iceberg melting also presents an opportunity to gain insights into the response of glacial ice to warmer environmental conditions, which may develop at ice shelf barriers in the future (Scambos *et al.*, 2008; Shepherd *et al.*, 2019).

The first detailed studies on iceberg melting were performed in the 1970’s and 1980’s, and were mainly based on laboratory experiments or ship-based observations (Huppert and Josberger,

## 2. Tracking changes in the area, thickness, and volume of the Thwaites tabular iceberg “B30” using satellite altimetry and imagery

---

1980; Neshyba and Josberger, 1980; Russell-Head, 1980; Hamley and Budd, 1986). These studies found that iceberg melting, to first order, is proportional to the water temperature and that for large icebergs breakage dominates over melting. More recently, Silva et al. (2006) and Jansen et al. (2007) modelled melting of giant icebergs and the associated fresh water fluxes. The latter found that melting does not only depend on ocean temperature but also on iceberg drift speed and the surrounding ocean currents. Scambos et al. (2008) installed a range of measurement tools including a GPS receiver, a pre-marked accumulation mast and buried bamboo poles observed with a camera on a large Antarctic iceberg to monitor melting. They differentiate between three kinds of mass loss: rift calving, edge wasting, and rapid disintegration. While rift calving can occur at any time within the iceberg life cycle along pre-existing fractures, edge wasting is only observed outside the sea ice edge. Rapid disintegration is caused by surface melting and the formation of surface lakes.

The advent of satellite remote sensing greatly increased our capability to study icebergs – especially the largest ones. A wide range of studies have employed repeat satellite imagery to track changes in iceberg area (Scambos *et al.*, 2008; Bouhier *et al.*, 2018; Budge and Long, 2018; Collares *et al.*, 2018; Li *et al.*, 2018; Han *et al.*, 2019; Mazur, Wåhlin and Kalén, 2019). The most common approach to measure iceberg thickness is using satellite altimeter measurements of their freeboard, which began in the late 1980’s (McIntyre and Cudlip, 1987). Since then, a range of studies have employed laser and radar altimetry to study freeboard change of large tabular icebergs: Jansen et al. (2007) studied the A-38B iceberg in the Weddell and Scotia Sea with a combination of laser and radar altimetry, and Scambos et al. (2008) also included three Ice, Cloud and land Elevation Satellite (ICESat) overpasses over the A22A iceberg to derive its thickness change. Both studies make use of satellite imagery to colocate the altimetry tracks and to compare similar areas in terms of freeboard change. In contrast, Tournadre et al. (2015) employed altimetry measurements from Envisat, Jason1, and Jason2 to analyse freeboard change of the C19A iceberg without any colocation. Bouhier et al. (2018) analysed thickness changes of the B17A and C19A icebergs in open water using altimetry data without colocation. Li et al. (2018) calculated freeboard change of the C28A and C28B icebergs for two years at the intersections of CryoSat-2 overpasses, and Han et al. (2019) also used intersecting CryoSat-2 tracks to calculate freeboard change of the A68 iceberg in the Weddell Sea. When thickness and area changes are combined, it is possible to detect changes in iceberg volume (Tournadre, Girard-Ardhuin and Legrésy, 2012; Bouhier *et al.*, 2018; Han *et al.*, 2019). However, studies to date have

been limited to selected icebergs, have focussed on the Weddell Sea, and have employed a variety of approaches to account for the irregular sampling of altimetry tracks including manual collocation of entire tracks relative to the initial surface (Jansen, Schodlok and Rack, 2007), collocation of intersecting tracks (Li *et al.*, 2018; Han *et al.*, 2019), and with no collocation at all (Tournadre *et al.*, 2015; Bouhier *et al.*, 2018). For smaller icebergs satellite stereo photogrammetry (Enderlin and Hamilton, 2014; Sulak *et al.*, 2017) and interferometry (Dammann *et al.*, 2019) have been employed to measure iceberg thickness and volume as an alternative approach, though in our experience both methods are labour intensive.

In this study, we quantify changes in the area, freeboard, thickness, and volume of the giant tabular B30 iceberg, which has been adrift in the Southern Ocean since it calved from the Thwaites Glacier 8.5 years ago (Budge and Long, 2018; Figure 2.1). The long life-cycle and large drift of the B30 iceberg result in a relatively high number of observations, enabling a detailed study of its evolution. This is also one of the first studies to investigate iceberg thinning in the Southern Ocean around Marie Byrd Land. We assess the agreement between estimates of freeboard change determined relative to the average initial surface and using precise collocation with the aid of near-coincident satellite imagery. Moreover, we develop a methodology to account for snowfall and the evolutions of snow and ice density and examine the influence of snow on the iceberg thickness calculation. The next section introduces the remote sensing data used in this study and explains our methodology; Section 2.3 presents our results on iceberg area, freeboard, thickness, and volume change in turn and discusses our findings. We close with conclusions and a brief outlook in Section 2.4.

## 2.2. Data and methods

To chart the iceberg area change over time we delineate its extent in a sequence of Moderate Resolution Imaging Spectroradiometer (MODIS) optical satellite imagery and Sentinel-1 synthetic aperture radar (SAR) satellite imagery. We then use CryoSat-2 satellite radar altimetry to determine changes in the iceberg freeboard and thickness, assuming that it is floating in hydrostatic equilibrium, and making use of the iceberg orientation relative to its initial position using near-coincident satellite imagery on some occasions. We account for snow accumulation and model variations in snow and ice density when converting iceberg freeboard to thickness. Finally, we combine both data sets to estimate the iceberg’s volume change over time.

2. Tracking changes in the area, thickness, and volume of the Thwaites tabular iceberg “B30” using satellite altimetry and imagery

### 2.2.1. Iceberg location

We use daily archived iceberg positions from the Antarctic Iceberg Tracking (AIT) database version 3.0 provided by the Brigham Young University (Budge and Long, 2018) as a baseline estimate of the B30 iceberg location since it calved in 2012 (Figure 2.1). The AIT database makes use of coarse-resolution passive microwave scatterometer imagery in which icebergs are manually detected and the central position is recorded daily (Stuart and Long, 2011). It includes icebergs longer than 6 km adrift in the Southern Ocean between 1987 and 2019, augmented with estimates of position and the semi minor and major axes lengths of icebergs longer than 18.5 km that are tracked operationally by the U.S. National Ice Center (NIC) using a combination of visible, infrared, and SAR imagery.

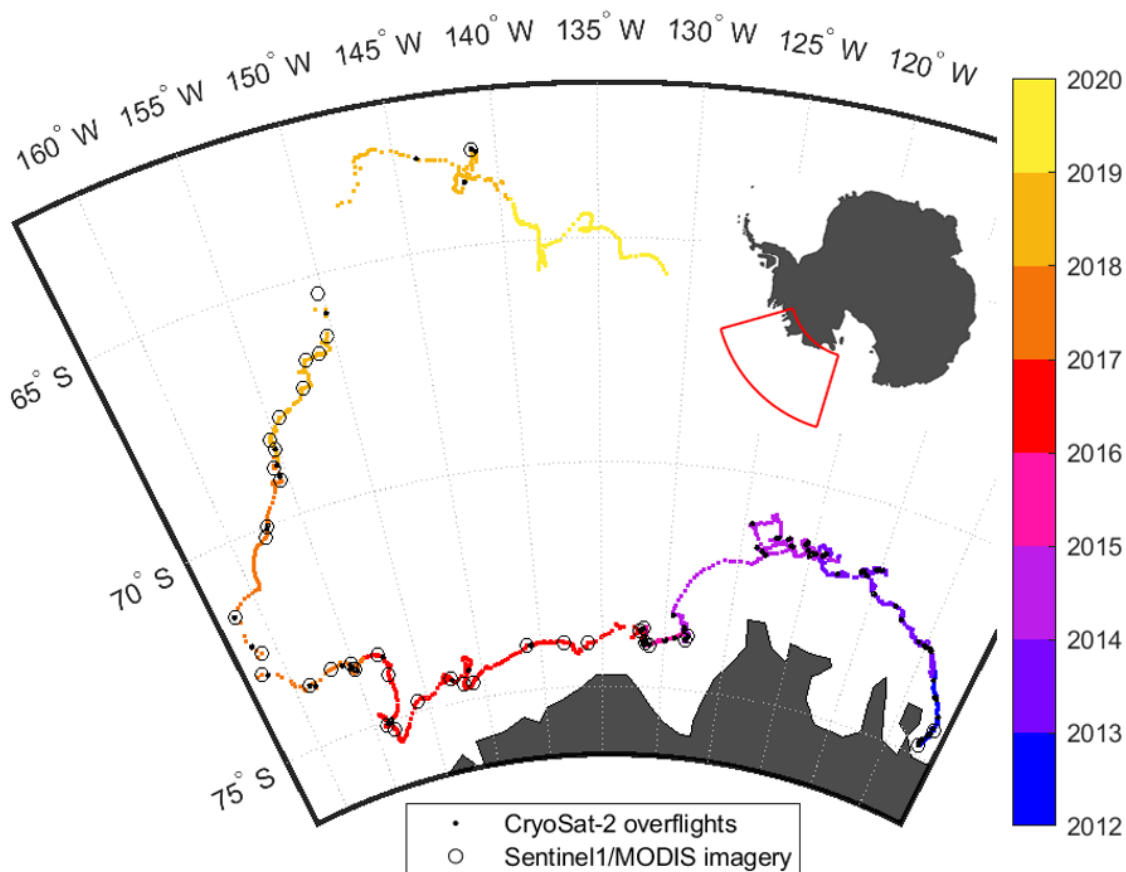


Figure 2.1: Trajectory of the B30 iceberg as recorded by the Antarctic Iceberg Tracking Database (Budge and Long, 2018): After calving from the Thwaites Ice Shelf in 2012, it followed the coastal current westwards, started drifting north in 2017 and eventually disintegrated in 2019. Black dots mark the positions where CryoSat-2 overflights over the iceberg are available, circles depict the positions of the MODIS and Sentinel-1 images used in this study

2. Tracking changes in the area, thickness, and volume of the Thwaites tabular iceberg “B30” using satellite altimetry and imagery
- 

### 2.2.2. Initial iceberg shape, size and calving position

To determine the initial shape, size, and calving position of B30, we use MODIS images acquired before and after the calving event to identify which section of the Thwaites Ice Shelf calved to form the iceberg. MODIS is an instrument on the Terra and Aqua satellites by NASA launched on 18<sup>th</sup> December 1999 and 4<sup>th</sup> May 2002, respectively. The instrument measures radiance in the visible and infrared range with a spatial resolution of 250 m to 1 km and covers the entire Earth in 1-2 days, though cloud occlusions and the absence of daylight reduce data availability for many applications. For this study we use bands 1 (red), 4 (green), and 3 (blue) of the MODIS Level 1B calibrated radiances at 500 m resolution (MOD02HKM). As B30 broke off on 24 May 2012 (Budge and Long, 2018) in Antarctic winter, during darkness, the closest useful MODIS imagery is from the preceding autumn and subsequent spring. We use several MODIS images acquired in the subsequent spring after calving to determine the initial shape, as it is difficult to unambiguously distinguish the berg from clouds and sea ice in a single image. The initial perimeter (Figure 2.2a, 2.3a) was then shifted and rotated to fit the situation before calving to identify the part of the Thwaites ice shelf that formed B30 (Figure 2.4). The initial area (in plan-view) of the iceberg is 1500 km<sup>2</sup> with a long axis of around 59 km (Budge and Long, 2018).

### 2.2.3. Iceberg area

We employ three approaches to estimate the plan-view iceberg area; (i) manual delineation in sequential satellite imagery scenes, (ii) using measurements of the semi-major and semi-minor axes provided by the NIC and assuming an elliptical shape, and (iii) using measurements of their arc lengths recorded in satellite altimetry and assuming a circular shape. While manual delineation provides the most consistent and accurate area estimate, the axes and arc length approaches are much simpler to implement and can be fully automated.

Our main approach to determine iceberg area is manual delineation using a sequence of 32 Sentinel-1 SAR and 8 MODIS optical images. Sentinel-1A and 1B are companion imaging radar satellites launched by the European Space Agency on 3<sup>rd</sup> April 2014 and 25<sup>th</sup> April 2016, respectively. Together, they provide repeat sampling of the Earth’s surface every 6 days. For this study, we use Level 1 Ground Range Detected (GRD) data. Depending on availability, both interferometric wide (IW) and extra wide (EW) swath mode are used, but over the open ocean only EW data are acquired. We employ the Sentinel Application Platform (SNAP) toolbox to apply the orbital and radiometric corrections provided with the imagery. The SAR images were multi-

## 2. Tracking changes in the area, thickness, and volume of the Thwaites tabular iceberg “B30” using satellite altimetry and imagery

looked with a factor of six to reduce speckle and computation time, leading to a spatial resolution of 240 m. Finally, a terrain correction was applied using the GETASSE30 (Global Earth Topography And Sea Surface Elevation at 30 arc second resolution) digital elevation model. The resulting backscatter values are scaled between their 5<sup>th</sup> and 95<sup>th</sup> percentiles. The MODIS optical imagery were required prior to the launch of Sentinel-1A in 2014.

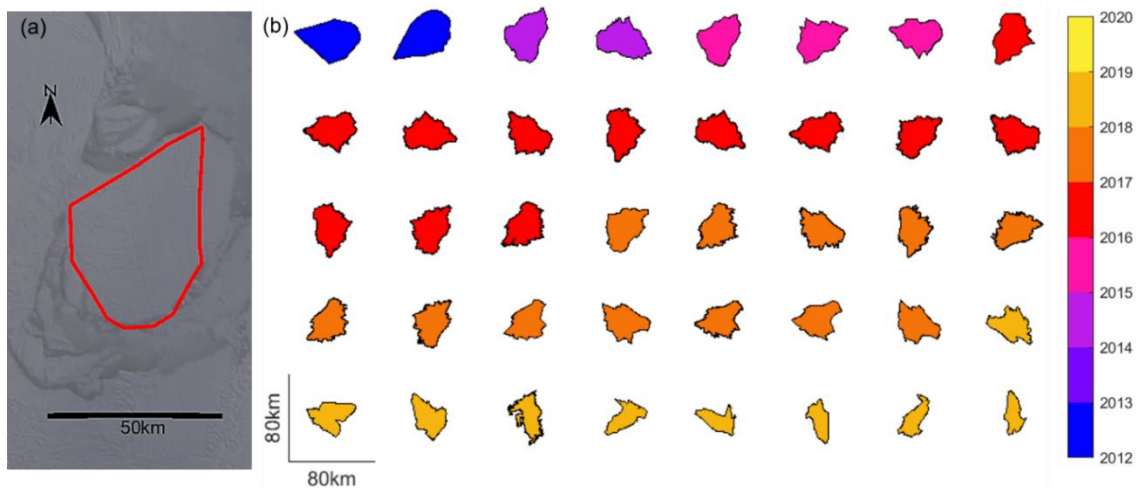


Figure 2.2: Outlines of the B30 iceberg derived from satellite imagery. a) Initial shape (red polygon) of the B30 iceberg determined from MODIS images after calving; the background is a MODIS image on 11 September 2012. b) Polygon outlines derived from further MODIS and Sentinel-1 imagery plotted in polar stereographic projection and used to calculate area change of the B30 iceberg.

To chart changes in the iceberg area over time, we delimit its outline as a polygon in each subsequent image (Figure 2.2, see also Bouhier *et al.*, 2018; Collares *et al.*, 2018; Han *et al.*, 2019). When the iceberg is drifting in open water its outline can be detected automatically using boundary detection techniques (e.g. using matlab’s `bwboundaries` function). However, in the presence of sea ice the iceberg could not be separated using this approach, and so we instead delimit its outline manually on such occasions (Bouhier *et al.*, 2018). If parts of the iceberg are covered by clouds, we again use multiple MODIS images together, so that different parts of the iceberg are obscured by clouds in each image (e.g. Figure 2.3i). Also sea ice frozen to the iceberg is easier to distinguish from its colour and texture, when several images are used together (e.g. Figure 2.3b, c). To estimate the uncertainty of our delineations, we buffer the polygons by the source imagery pixel width (500 m for MODIS images and 240 m for multi-looked Sentinel-1 images) and calculate the resulting difference in area. This gives a mean relative difference of  $3.6 \pm 0.9$  %. Manually, outlines are usually drawn at a resolution where the whole iceberg fits on the screen, so using the native Sentinel-1 resolution instead would reduce this uncertainty insignificantly

## 2. Tracking changes in the area, thickness, and volume of the Thwaites tabular iceberg “B30” using satellite altimetry and imagery

---

within error. For automated approaches, higher resolution improves the uncertainty (e.g. buffering those polygons with 30 m rather than 240 m pixel size reduces the average uncertainty to  $2.2 \pm 1.8 \%$ ), but also increases computation time and requires more resources. As area change is calculated with respect to the first polygon from MODIS, the fragmentation uncertainty is governed by that and we stick to the multi-looked images in this study.

Our second method of estimating the iceberg area is based on 228 measurements of the semi-major and semi-minor axes lengths. Although iceberg area is most accurately calculated from delineation of their full perimeter in satellite images, the downside of this approach is that it requires a high degree of time-consuming manual interaction and clear imagery. This also makes it less reproducible and subject to individual judgement. We take the size of an ellipse calculated from the semi major and minor axis provided by the NIC and compare this with our imagery-based iceberg area calculations. The NIC operationally tracks icebergs longer than 18.5 km using a combination of visible, infrared, and SAR imagery. Observations are made weekly, but especially in the early days longer data gaps exist, and not every estimate of semi axes length is based on a new manual observation, but some are just duplicated from the previous observation. Their estimates of semi axes lengths are also rounded to nautical miles (1.852 km), leading to a step-wise evolution of iceberg area with only 8 different estimates. We base our trend estimate and analysis solely on these 8 estimates, because we are confident that these are unique observations. The uncertainty of this approach is governed by the assumption of an elliptical iceberg shape and the irregular, rounded updates.

Our third and final method of estimating the iceberg area is to make use of 106 CryoSat-2 satellite altimeter overpasses, which are also used to calculate the iceberg’s thickness. We record the arc lengths of the iceberg sampled by these tracks and estimate iceberg area by assuming the iceberg has a circular shape. Depending on the position and relative orientation of the iceberg with respect to each overpass, CryoSat-2 will occasionally sample the long axis but more often a shorter corner. This leads to considerable variations in the area estimates, and in general an underestimation. We employ a ten-point moving mean over time to reduce the variability. The principal uncertainty of this approach is because one-dimensional arc lengths cannot reliably represent a two-dimensional area especially when the shape is evolving and if it is unknown which part of the shape was sampled.

- Tracking changes in the area, thickness, and volume of the Thwaites tabular iceberg “B30” using satellite altimetry and imagery

### 2.2.4. Iceberg orientation

To track the iceberg shape and rotation in later images relative to its initial orientation, we record the iceberg’s orientation in all satellite images that are near-coincident in time with CryoSat-2 overflights (Figure 2.3). To orientate the iceberg, we manually identify the coordinates of one corner of the initial iceberg polygon outline at the time of each new overpass and adjust the rotation angle to align (colocate) all images to a common orientation (Figure 2.8a-l). This allows us to transform the iceberg coordinates at the time of each image acquisition relative to the equivalent position at the time just before it calved.

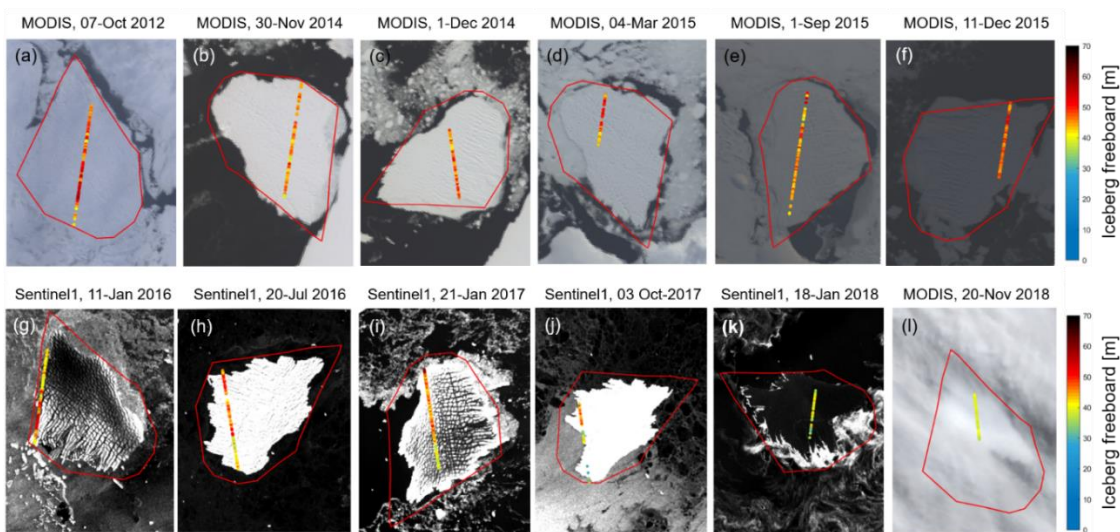


Figure 2.3: Satellite imagery with near-coincident CryoSat-2 tracks of iceberg freeboard and the manually transformed initial polygon shape plotted on top. The initial polygons are used to determine the relative position of each new overpass.

### 2.2.5. Initial iceberg freeboard

We use CryoSat-2 satellite altimetry to determine freeboard and thickness of the B30 iceberg. CryoSat-2 is a satellite radar altimeter that employs SAR processing to achieve along track resolution of 250 m. It was launched by the European Space Agency on 8 April 2010 in a 369-day repeat period with a 30-day sub cycle. We use Level 1B baseline C data from the CryoSat-2 Science server and apply the Centre for Polar Observation and Modelling sea ice processing system (Tilling, Ridout and Shepherd, 2018) to deduce surface height. Specifically, we apply ionospheric, wet and dry tropospheric and inverse barometer corrections and account for the ocean tide, long period tide, ocean loading tide, earth tide and geocentric pole tide (Tilling, Ridout and Shepherd, 2018). For consistency, a common 70 % threshold retracker is applied to measurements acquired in both SAR and SAR interferometric mode and over all surface types. Using Level 1B data is important, because the Level 2 products are generated using different retracker

2. Tracking changes in the area, thickness, and volume of the Thwaites tabular iceberg “B30” using satellite altimetry and imagery

and different biases for different modes and surface types, and so the signals acquired during different parts of the iceberg trajectory are not comparable. Iceberg freeboard is calculated by subtracting the adjacent mean sea surface height from the iceberg surface height.

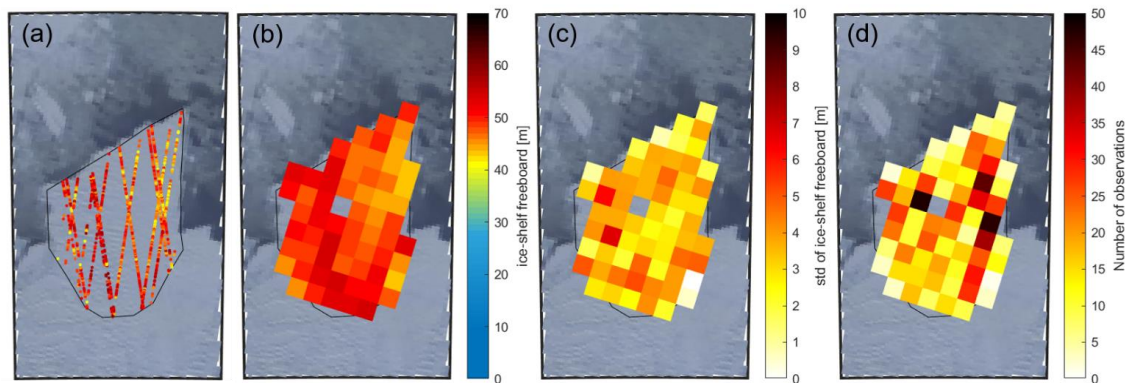


Figure 2.4: Initial freeboard heights of the B30 iceberg overlain on a MODIS image on 19 March 2012 (before calving). a) Filtered CryoSat-2 measurements of 145 days before calving, b) Gridded CryoSat-2 data, c) Standard deviation of the gridding, d) Number of measurements per grid cell

Although satellite altimeters only sample icebergs along 1-dimensional profiles beneath their ground track while they are drifting, it is possible to build up a detailed 2-dimensional picture of their surface over time prior to calving while their movement is relatively modest. To map the initial freeboard height of B30, we combine all CryoSat-2 tracks recorded within almost 5 months (1 January 2012 to 24 May 2012) before it calved (Figure 2.4a). The Thwaites Ice Shelf flows at 3.9 km per year on average (Mouginot, Rignot and Scheuchl, 2019), and so we adjust earlier tracks to account for this movement. Because the Thwaites Ice Shelf has a particularly rugged and crevassed surface topography, the point-of-closest-approach (POCA) varies. To make different overpasses more comparable, we remove outliers by deleting freeboard heights greater than 60 m or below 20 m freeboard (Tournadre *et al.*, 2015), and crevasses by deleting freeboard heights falling either below the median minus one standard deviation or below the 5-point moving mean minus the 5-point moving standard deviation. After outlier removal, the mean initial iceberg freeboard is 45.5 m above the adjacent sea level with a wide spread of 8.1 m standard deviation. When crevasses are excluded, the mean freeboard is 49.0 m with a much lower standard deviation of 4.6 m. Because the resulting freeboard measurements are still quite sparse, we average them within 5 km grid cells to obtain a continuous reference surface (Figure 2.4). The number and standard deviation of the gridded freeboards give an indication of the variance within each grid cell. The mean standard deviation within each grid cell is 3.3 m, the standard deviation across different grid cells is 3.1 m and the overall standard deviation of all

## 2. Tracking changes in the area, thickness, and volume of the Thwaites tabular iceberg “B30” using satellite altimetry and imagery

---

heights within the polygon is 4.6 m. We compare the gridded initial freeboard to measurements from the first CryoSat overpass when the iceberg is adrift, acquired shortly after calving, to check they are consistent, and find a mean difference of -0.4 m. As this value is considerably lower than the iceberg freeboard variability, we conclude that the ice shelf was floating freely prior to calving also, and that the gridded heights are representative of the initial freeboard.

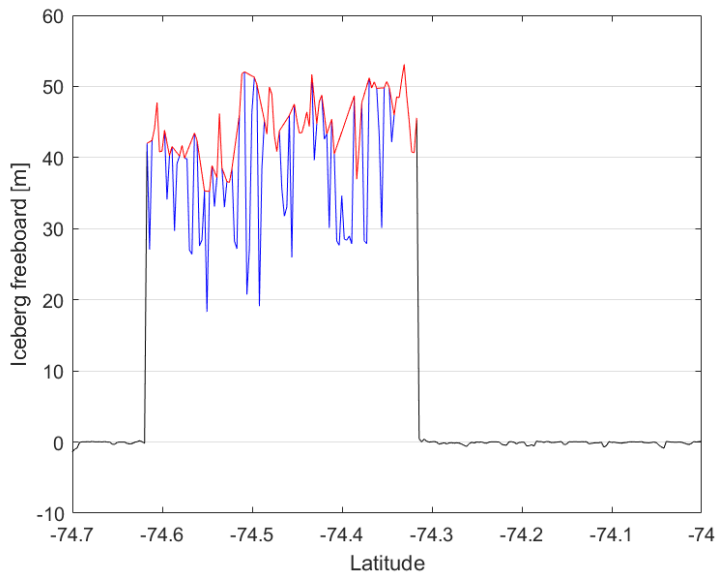


Figure 2.5: Example of CryoSat-2 freeboard measurements along one track. The blue line shows which heights were identified as iceberg and the red line shows the remaining heights after filtering out crevasses.

### 2.2.6. Iceberg freeboard change

When icebergs are adrift, their motion is sufficiently large to mean that they are only sampled in 1-dimensional profiles along satellite altimeter ground tracks (Figure 2.3) and only the largest tabular icebergs are sampled frequently enough to derive changes in their freeboard. We extract surface heights over the B30 iceberg when it is adrift (e.g. Figure 2.5) using the position from the AIT database as an initial estimate of its location. However, because the AIT positions and timings are approximate and the iceberg has a significant extent, we investigate all CryoSat-2 ground tracks that pass within 1-degree latitude and 2-degrees longitude of the database position. We automatically extract measurements sampling the iceberg with the following steps: Track segments are truncated to exclude altimeter echoes from targets where the first or last freeboard height is more than 3 m, to exclude measurements from the nearby continent, and we also exclude tracks that do not contain freeboard measurement between 20 and 60 m, to ensure that they sample the iceberg. We consider all freeboard heights between the first and last echo falling in the range of 20 to 60 m as potential iceberg measurements (Tournadre *et al.*,

2. Tracking changes in the area, thickness, and volume of the Thwaites tabular iceberg “B30” using satellite altimetry and imagery

---

2015). To avoid including adjacent icebergs or berg fragments, we exclude segments with more than 10 measurements of ocean or sea ice, identified as surface heights in the range -3 to +3 m, between potential iceberg measurements. We also remove crevasses and other rugged features using the same editing steps applied to determine the surface height prior to calving. As a final check, we calculate the distance of these remaining heights to the AIT database location, and discard measurements that are further away than half the iceberg length (28 km) to ensure we are tracking B30.

We apply two different techniques to calculate changes in the iceberg freeboard. For 12 tracks we are able to calculate precise changes in freeboard with spatial definition by making use of near-coincident satellite imagery to account for the rotation and translation of the iceberg relative to its initial position prior to calving (Jansen, Schodlok and Rack, 2007) and consider the estimated movement between the time of the nearest satellite image and altimeter acquisitions. At 94 other times, we compute the freeboard height change as the difference of mean freeboard from each new overpass relative to the initial mean surface height. While these observations are of poorer certainty, they provide denser temporal sampling and fill gaps between the colocated measurements. The first collocation method assigns both the initial heights and the new measurements to their closest 5 km grid cell and averages them to ensure that the same locations are compared. We account for the iceberg drift between the times of the satellite acquisitions, allowing a maximum separation of 72 hours (though most overpasses are separated by less than 24 hours). If the image is from a different date than the CryoSat track, we correct the distance travelled based on the daily iceberg locations from the AIT database. In any case, we account for the drift in our uncertainty estimate performing a Monte Carlo simulation with 1000 slightly differently colocated samples per track. These are normally distributed around our estimated translation and rotation with a standard deviation of  $15^\circ$  per day and a drift speed of 3 km per day (Scambos *et al.*, 2008) scaled by the respective time separation. We then calculate the freeboard difference for each of the 1000 slightly differently colocated tracks and use the resulting standard deviation of freeboard change from these samples as the uncertainty of our collocation. This is combined with the standard deviation of the gridded CryoSat-2 freeboard data (of the new track and of the reference) to yield a conservative uncertainty estimate for the colocated tracks. The second method ignores the relative position and orientation of the iceberg at the time of the altimeter overpasses (Tournadre *et al.*, 2015; Bouhier *et al.*, 2018), and simply compares the mean freeboard along each new track to the mean surface height before calving. Although this method is easiest, since it does not rely on additional image data to locate the

## 2. Tracking changes in the area, thickness, and volume of the Thwaites tabular iceberg “B30” using satellite altimetry and imagery

---

track, it cannot account for potential spatial variations in the iceberg freeboard. Because of this, we restrict the new overpasses to those including at least 20 measurements, as tracks sampling only the edges of an iceberg tend to be inaccurate. As uncertainty estimate we combine the standard deviation of each new overpass with the standard deviation of the initial height. As a first check to see if the mean freeboard from a single overpass can be compared to the mean initial height, we calculate the mean height for each of the 15 tracks over the pre-calved iceberg (Figure 2.4a) and find a standard deviation of 2.8 m compared to the mean initial height of  $49.0 \pm 4.6$  m.

### 2.2.7. Iceberg thickness

We compute iceberg thickness  $H$  (freeboard plus draft) from our estimates of iceberg freeboard heights  $h_{fb}$  assuming hydrostatic equilibrium and that CryoSat-2 does not penetrate through the snow layer (Eq. 1; Zwally *et al.*, 2008). Besides these freeboard heights, iceberg thickness also depends on column-average densities of sea-water  $\rho_w$ , ice  $\rho_i$ , and snow  $\rho_s$  as well as snow depth  $h_s$ . Including a snow layer in this equation is important, because the snow layer adds to the observed freeboard and disguises a part of the ice freeboard change. On the other hand the additional load of the snow layer pushes the iceberg downwards. Both effects are taken into consideration. We assume sea-water density to be  $1024 \text{ kg m}^{-3}$  (Fichefet and Morales Maqueda, 1999) and set its uncertainty to  $2 \text{ kg m}^{-3}$ . Due to the long life cycle of the B30 iceberg of 6.5 years and the changing environmental conditions it experiences during this time, we allow the ice and snow densities to evolve with time. Snow depth is also time-varying, and estimates of this and of snow and ice density are introduced successively.

$$H = \frac{\rho_w}{\rho_w - \rho_i} h_{fb} - \frac{(\rho_w - \rho_s)}{\rho_w - \rho_i} h_s \quad (1)$$

At calving, we set snow depth to zero. Already existing snow, which fell on the ice shelf, is accounted for by using the ice density profile of the Thwaites Ice Shelf with lower density at the surface (Figure 2.6a), but we do not call it snow in the following. To estimate the thickness of the snow layer that accumulated since calving, we download hourly ERA5 Reanalysis snowfall, snowmelt, and snow evaporation data (Copernicus Climate Change Service, 2018), accumulate it daily and interpolate it in space and time to the iceberg’s trajectory. Snowmelt and snow evaporation are subtracted from the snowfall (Figure 2.6b). However, this snow estimate does not account for snow being blown off the iceberg or onto the iceberg from the continent (Fedotov, Cherepanov and Tyshko, 1998; Leonard and Maksym, 2011). We refer to the snow layer as all

2. Tracking changes in the area, thickness, and volume of the Thwaites tabular iceberg “B30” using satellite altimetry and imagery

additional snowfall since calving, even if some of it will become firn. To convert snow water equivalent (SWE) to snow depth, we need to know snow density.

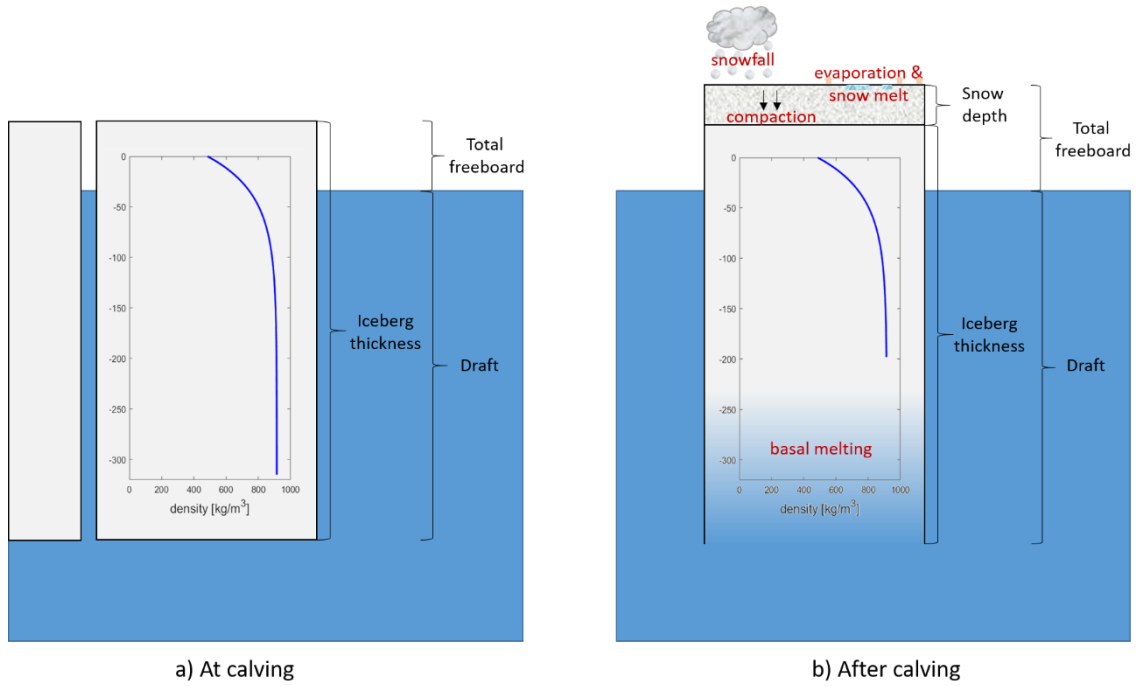


Figure 2.6: Illustration of how iceberg thickness is calculated at calving (a) and after calving (b) with the different processes affecting iceberg thickness that we account for labelled in red. The ice density profile is calculated using Eq. 3 with ice densities of the Thwaites Ice Shelf by Ligtenberg, Helsen and Van Den Broeke (2011).

Snow density is time variable because snow compacts gradually during the iceberg’s life time of several years as a function of snow depth  $h_s$  [m], the mean air temperature  $T$  [°C], and the mean wind speed  $v$  [ $\text{m} \cdot \text{s}^{-1}$ ] (Eq. 2; International Organization for Standardization, 1998). We use hourly ERA5 Reanalysis 2 m air temperature data and calculate wind speed from the ERA5 Reanalysis 10 m eastwards and northwards wind components (Copernicus Climate Change Service, 2018). Both are interpolated to the iceberg’s trajectory and averaged since the day of calving. Because snow density depends on snow depth and snow depth depends on snow density, we calculate both iteratively starting with a snow density of  $300 \text{ kg m}^{-3}$ . We set the uncertainty in snow density to  $50 \text{ kg m}^{-3}$  (Kurtz and Markus, 2012) and the uncertainty in snow depth to 20 % (Kwok and Cunningham, 2008).

$$\rho_s = (90 + 130 \cdot \sqrt{h_s}) \cdot (1.5 + 0.17 \cdot \sqrt[3]{T}) \cdot (1 + 0.1 \cdot \sqrt{v}) \quad (2)$$

To calculate the iceberg’s ice density profile we follow the approach by Tournadre et al. (2015), and determine two parameters  $V$  and  $R$  to fit the surface density and the depths of the critical density levels ( $550 \text{ kg m}^{-3}$  and  $830 \text{ kg m}^{-3}$ ) of the Thwaites Ice Shelf, from which it calved, as given

2. Tracking changes in the area, thickness, and volume of the Thwaites tabular iceberg “B30” using satellite altimetry and imagery
- 

in Ligtenberg, Helsen and Van Den Broeke (2011; Eq. 3).  $\rho_g$  is the density of pure glacial ice (915 kg m<sup>-3</sup>). Since the mean ice density depends on ice thickness and ice thickness depends on the mean ice density, we iterate over both equations. We also account for ice density changes over the iceberg’s life cycle by calculating new mean densities as the iceberg thins (cropping the ice density profile from Figure 2.6a at lower depth as thickness decreases – see Figure 2.6b). This incrementally reduces the average ice density as the densest ice is melted at the bottom. As ice density uncertainty we take 10 kg m<sup>-3</sup> (Dryak and Enderlin, 2020).

$$\rho_i = \frac{1}{H} \int_0^H (\rho_g - V \cdot e^{R \cdot z}) dz \quad (3)$$

## 2.3. Results and discussion

We first assess changes in the B30 iceberg area using boundaries mapped from satellite imagery, and we compare the observed trend to less accurate estimates derived from arc-lengths and semi-major axes. Next, we determine the change in iceberg freeboard and we assess the impact of employing precise collocation using near-coincident satellite imagery. Iceberg thickness changes are then computed from freeboard changes using time-varying estimates of snow accumulation and snow and ice densities derived from atmospheric reanalyses. Finally, iceberg area and thickness changes are combined to derive the change in volume and mass.

### 2.3.1. Iceberg area change

When the B30 iceberg first calved in May 2012, it was  $1500 \pm 60$  km<sup>2</sup>. Over the following 6.5 years it lost  $1075 \pm 66$  km<sup>2</sup> of its extent, which corresponds to a  $72 \pm 11$  % reduction at an average rate of  $149 \pm 5$  km<sup>2</sup> per year (Figure 2.7). However, because deriving iceberg outlines requires a high degree of time-consuming manual interaction, we also evaluate the efficacy of two alternative methods based on measurements of their orthogonal (semi-major and semi-minor) axes by the NIC and on arc lengths recorded in satellite altimetry which are considerably less laborious. Although these approaches also yield progressive reductions in area (Figure 2.7), they exhibit significant positive (138 km<sup>2</sup>, 14%) and negative (-426 km<sup>2</sup>, 45%) biases, respectively, due to under-sampling of the iceberg geometry and the necessary approximation of a regular shape (ellipses and circles, respectively). While an ellipse overestimates the area compared to most shapes with the same axes, arc lengths yield an underestimate because corners are sampled more often than the major axis. One idea for improvement would be to use the maximum or to filter out tracks that only sample one corner, but the main problem remains that a one-dimen-

2. Tracking changes in the area, thickness, and volume of the Thwaites tabular iceberg “B30” using satellite altimetry and imagery

sional length measurement cannot be translated into a reasonable area estimate without knowing the iceberg shape, which changes over time. Nevertheless, both the orthogonal axes and arc-length approaches yield area estimates that are reasonably well correlated ( $r > 0.90$ ) with those determined from our manual delineation. Area trends are overestimated by 16% and underestimated by 48%, respectively. While manual delineation provides the most consistent and most accurate area estimate, tracking iceberg axes or arc lengths yields area and area change estimates that are within 48% and is considerably less time consuming.

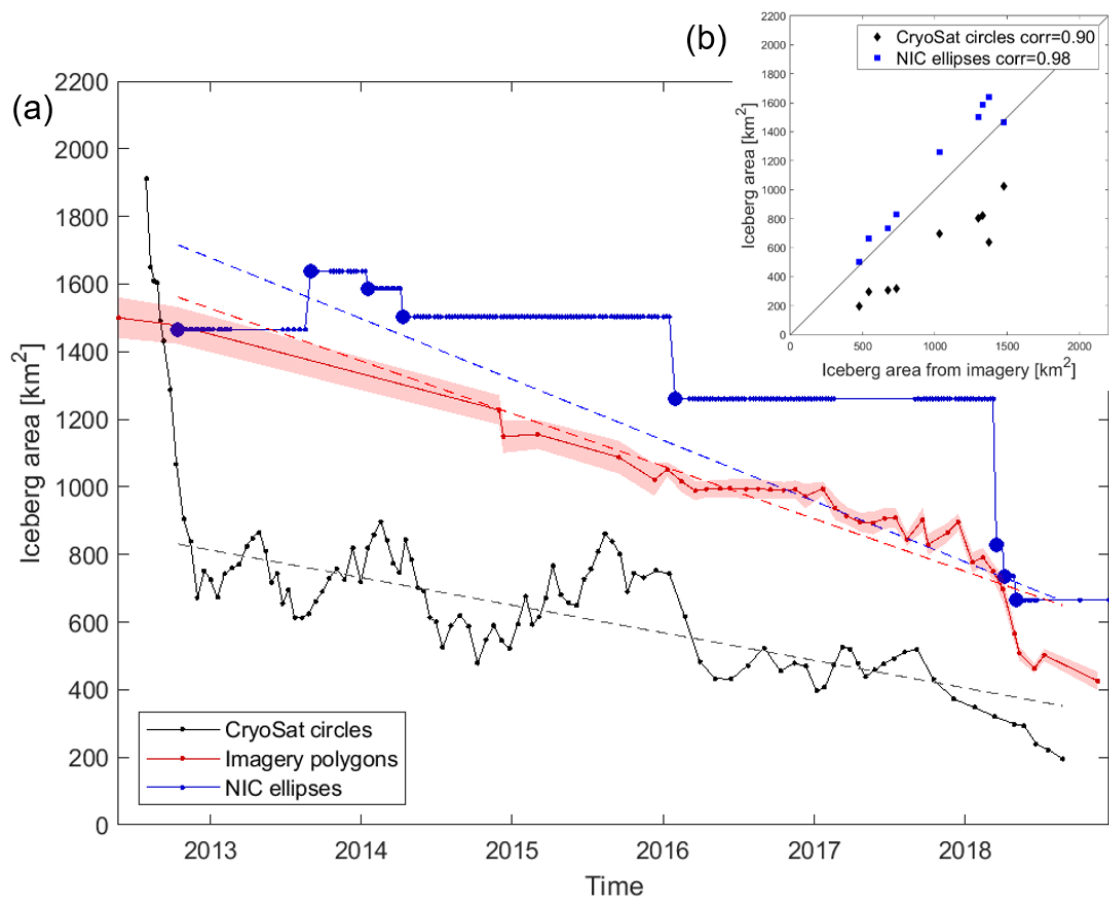


Figure 2.7: Area change of the B30 iceberg from polygons delineated in satellite imagery with their uncertainty (red) and approximations using orthogonal axes provided by the National Ice Center (NIC) assuming an elliptical shape (blue) or using the arc lengths of CryoSat-2 overflights assuming a circular shape (black) over time (a) and as scatter plot (b). To fit the NIC trend line in (a) we only use unique values of orthogonal axes length (thick blue dots). These also define the dates of comparison in (b).

The rate of iceberg area loss from B30 was approximately constant until 2018, after which time it started to lose larger sections more rapidly. Although its area has reduced steadily over time, it is less obvious which sections have been lost during individual calving events. However, by aligning the initial polygon to each subsequent image (Figure 2.3) it is possible to identify when

## 2. Tracking changes in the area, thickness, and volume of the Thwaites tabular iceberg “B30” using satellite altimetry and imagery

---

and where changes occur. The iceberg shape already appears altered on 30<sup>th</sup> November 2014, after bumping into the adjacent ice shelf which likely caused the first chunks to break off. B30 continued to lose smaller sections along its edges over the next year – either through melting at the sides or smaller wastings – when it was drifting along the coastal current. In 2018, bigger sections are lost more rapidly, as the iceberg is drifting northwards in open water. Rift calving can occur at any time within an iceberg life cycle along pre-existing fractures (Scambos *et al.*, 2008), while edge wasting is typically only observed when icebergs are travelling outside the sea ice pack. B30 was heavily crevassed prior to calving (e.g. visible in Figure 2.3g and i), and so even the smaller wastings along its edges could reflect rift calving events rather than edge wastings. The ‘footloose mechanism’ (Wagner *et al.*, 2014) can become a main driver of iceberg decay in warm waters, when wave erosion at the waterline forms a sub-surface foot, creating a buoyancy stress that can lead to calving. Although it is not possible to investigate the effects of wave erosion using satellite data, the effect could in principle have caused the larger break-ups that occurred in 2018.

### 2.3.2. Iceberg freeboard change

To assess the change in freeboard over the survey period, we compare differences between the new overpasses and the initial heights in space and time (Figure 2.8). For the spatial analysis we chart the freeboard difference between each colocated overpass post-calving (Fig. 3) and the gridded initial height pre-calving (Figure 2.4b) at the same relative iceberg position. This comparison shows that the change in freeboard height across the iceberg is relatively homogenous at each epoch (Figure 2.8a-l). We then average these differences per CryoSat-2 track and chart the variation over time alongside the less accurate (but more abundant) estimates determined without collocation (Figure 2.8m). Because the observations without collocation are relatively imprecise, we apply a 10-point moving mean to the data and we also fit a polynomial of 3<sup>rd</sup> order (and starting at zero). Overall, the B30 iceberg freeboard has reduced by  $9.2 \pm 2.2$  m during the 6.5 years since it calved.

To assess the importance of collocation, we compare freeboard changes calculated with and without this step (Figure 2.8n). The estimates are well correlated ( $r=0.87$ ) and the root mean square difference is 1.6 m, which is a measure of the improvement in certainty associated with collocation and equal to the difference in mean uncertainty of colocated tracks (4.7 m) versus tracks without collocation (6.3 m). Also, the temporal variation of freeboard changes computed from observations with and without collocation are in good overall agreement (Figure 2.8m), and

2. Tracking changes in the area, thickness, and volume of the Thwaites tabular iceberg “B30” using satellite altimetry and imagery

we conclude that for this iceberg we can combine the two and make use of the entire set of CryoSat-2 measurements. This finding should hold for other tabular icebergs where the topographic variability is smaller than the observed thinning. The variability of freeboards computed within each 5 km grid cell and across different grid cells are also of the same order (3.3 m and 3.1 m, respectively), and this is likely to have reduced the impact of collocation uncertainties. For other icebergs with more heterogeneous freeboard across the iceberg that are less crevassed (i.e. with lower freeboard variabilities within the same grid cell), collocation might have a larger impact and more icebergs need to be studied to generalise these findings.

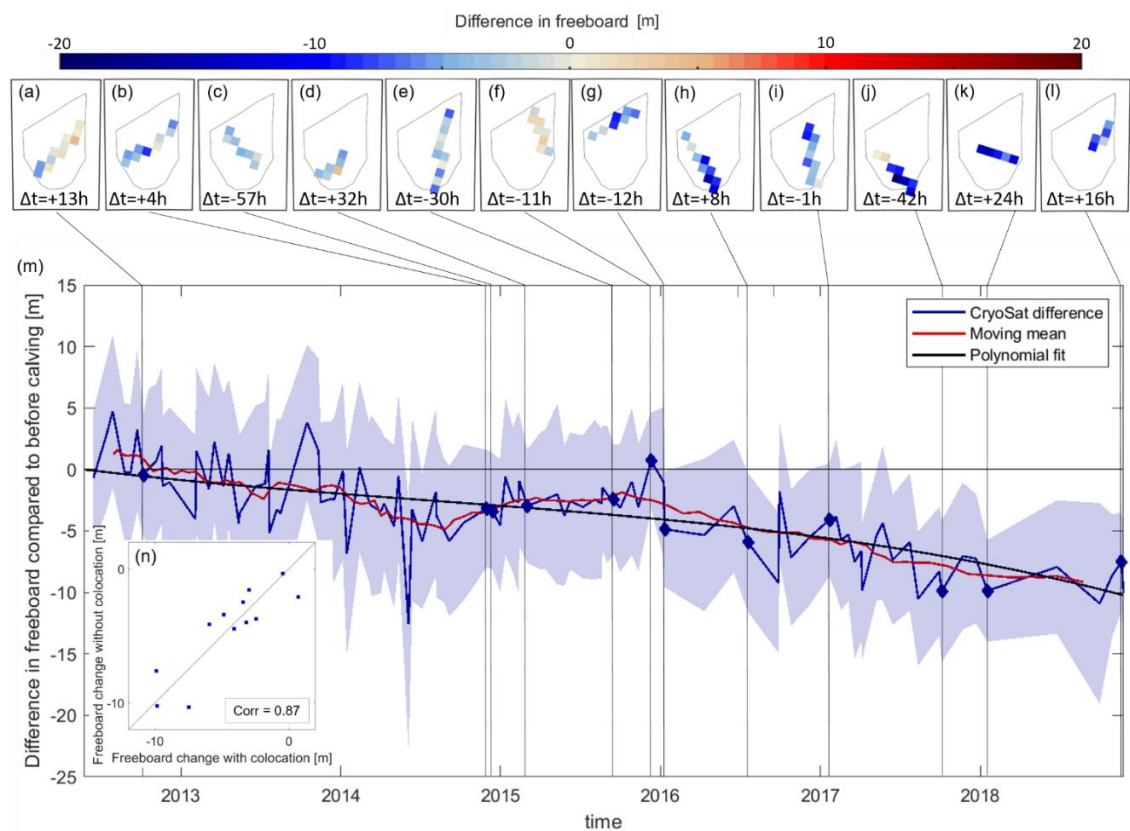


Figure 2.8: Freeboard change of the B30 iceberg. a-l) Freeboard difference in each grid cell sampled by collocated CryoSat-2 overpasses; the  $\Delta t$  values give the time difference between the CryoSat-2 overpass and the corresponding satellite image as an indication of the collocation uncertainty due to iceberg drift; Negative values indicate that the image was taken before the CryoSat overpass. m) mean difference of each new overpass along time. CryoSat-2 tracks that have been collocated are marked with a diamond, but all available CryoSat-2 overpasses have been used to calculate a moving mean and fit a polynomial; The shading shows the standard deviations. n) scatter plot of freeboard change from collocated CryoSat-2 tracks versus the same tracks used without collocation

2. Tracking changes in the area, thickness, and volume of the Thwaites tabular iceberg “B30” using satellite altimetry and imagery
- 

### 2.3.3. Iceberg thickness change

We compute the iceberg thickness from our measurements of its freeboard (using the moving mean, red line in Figure 2.8m) and by assuming that it is floating in hydrostatic equilibrium within the surrounding ocean with a surface snow layer. Accounting for the snow layer is important because it affects the ice freeboard and the iceberg buoyancy, and we take both effects into consideration. Based on hourly snowfall, evaporation and snowmelt derived from ERA5 reanalyses (Copernicus Climate Change Service, 2018), we estimate that the iceberg accumulates 4.6 m of snow water equivalent during the 6.5 year survey period (Figure 2.9). The rate of accumulation is quite linear. The iceberg thickness also depends on densities of the snow layer, the iceberg, and the sea-water and we allow the snow layer and iceberg densities to evolve over time due to the changing environmental conditions it experiences during its long lifecycle. The mean iceberg density reduces from an initial estimate of  $864 \text{ kg m}^{-3}$  to a final value of  $835 \text{ kg m}^{-3}$  as a consequence of basal ice melting (Figure 2.9a). The mean change in height due to firn densification in West Antarctica has been estimated to be 2.79 cm per year on floating ice (Zwally *et al.*, 2005); upscaling this rate gives a total of 18 cm after 6.5 years, which is significantly smaller than the observed freeboard loss of 9.2 m, so we don't apply it. The snow layer compacts over time due to its accumulation and warming, and we estimate that its average density rises from 252 to  $616 \text{ kg m}^{-3}$  which yields a 7.2 m thick layer after 6.5 years (Figure 2.9b). We also investigate the impact of surface thawing; although the iceberg surface does experience temperatures above freezing every summer and for a total of 218 degree hours (number of hours above zero degrees Celsius times the temperature above zero degrees Celsius) since calving (Figure 2.9c), in situ observations (Scambos *et al.*, 2008) suggest that this translates into only 8 to 16 cm of snow melting and this has negligible impact on the iceberg freeboard, so we discard this effect.

We estimate the initial iceberg thickness to be  $315 \pm 36 \text{ m}$ , on average, reducing to  $198 \pm 14 \text{ m}$  after 6.5 years. This amounts to  $117 \pm 38 \text{ m}$  of thinning (Figure 2.9d) at an average rate of  $17.3 \pm 1.8 \text{ m per year}$ . Previous studies have recorded iceberg thinning rates of up to 10 m per year when drifting within the sea ice extent close to the coast (Morgan and Budd, 1978; Jansen, Schodlok and Rack, 2007; Scambos *et al.*, 2008; Li *et al.*, 2018; Han *et al.*, 2019) and much higher rates in excess of 20 m per year when in warmer open water (Morgan and Budd, 1978; Hamley and Budd, 1986; Jansen, Schodlok and Rack, 2007; Scambos *et al.*, 2008; Tournadre *et al.*, 2015; Li *et al.*, 2018). Jacka and Giles (2007) find dissolution rates of 11-18 m per year between 60 and

2. Tracking changes in the area, thickness, and volume of the Thwaites tabular iceberg “B30” using satellite altimetry and imagery

150° E based on shipborne observations over 15 years. Although all these studies were conducted for different regions of the Southern Ocean, our estimated average thinning rate is in line with the melt rates previously reported, given that the B30 iceberg has spent most of its lifetime close to the coast (Figure 2.1). To assess the impact of including a snow layer in the thickness calculation, we also compute thickness change assuming no snow has accumulated since calving (Figure 2.9d); this scenario leads to an estimated  $90 \pm 39$  m reduction in iceberg thickness, 23 % lower than the rate determined when the snow layer is included, which illustrates its importance. We expect the importance of including a snow layer to be highest in phases where the iceberg is melting slowly, as snow accumulation can disguise the thickness change in this instance. Based on the mostly linear snow accumulation, it will also be more important the longer the iceberg survives, as more snow accumulates. Apart from the snow layer, iceberg density is also a significant factor in our thickness change calculation, and while we have attempted to model the evolutions of ice density, snow density, snow accumulation, and surface thawing, their uncertainties are difficult to quantify.

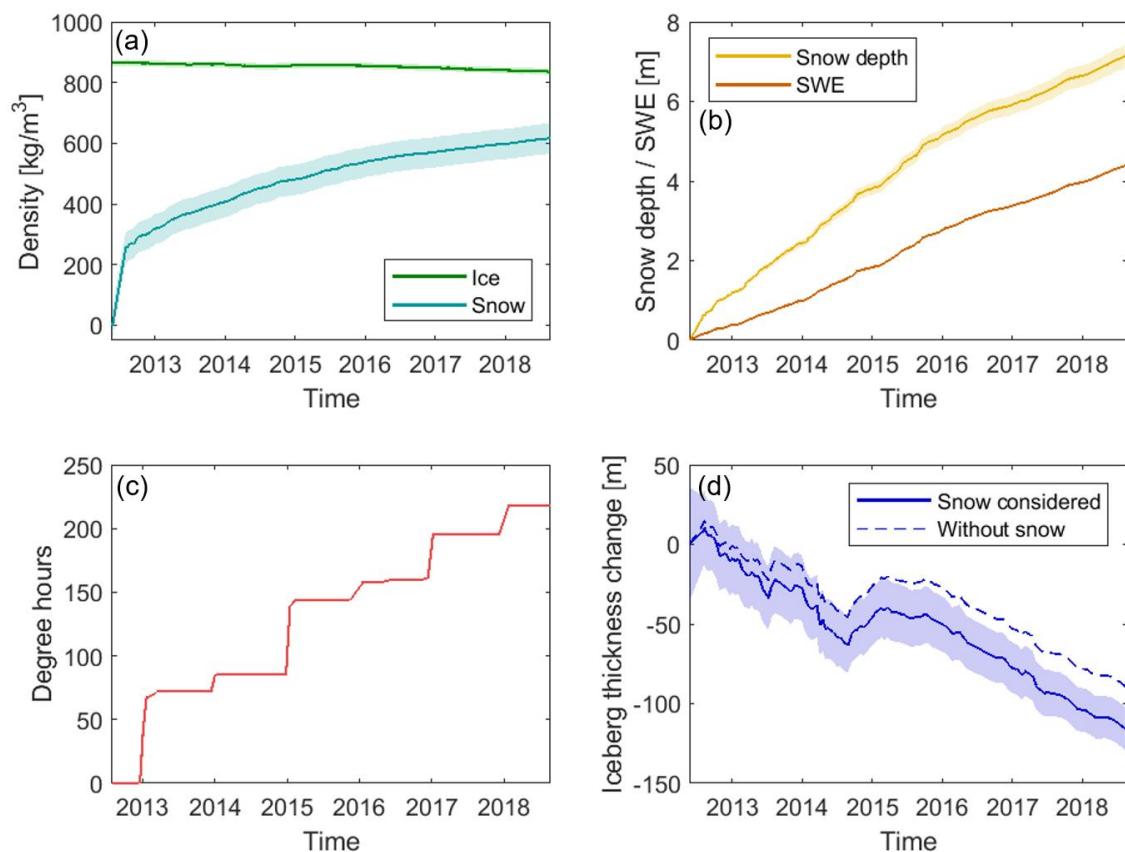


Figure 2.9: Evolution of the B30 iceberg properties: a) Ice density and snow density, b) Snow water equivalent (SWE) and snow depth accumulation on the B30 iceberg, c) Degree hours that the B30 iceberg experienced, and d) Thickness change of the B30 iceberg with snow accumulation taken into consideration or without. Uncertainties are plotted as shaded areas.

## 2. Tracking changes in the area, thickness, and volume of the Thwaites tabular iceberg “B30” using satellite altimetry and imagery

---

Besides the observed thinning, the iceberg also seems to slightly thicken between mid-2014 and early 2015. During this time B30 was very close to the coast (Figure 2.3b-d). Therefore, a range of processes – both physical processes that impact the actual thickness of the iceberg and processes that impact the freeboard measurement – could have caused this gain in thickness: First of all, iceberg thickness can increase through marine ice formation, when the iceberg is surrounded by very cold water. Little *et al.* (2008) found that freezing beneath ice-shelves is concentrated along their western side and B30 was indeed located at the western side of Getz Ice Shelf at this time (Figure 2.1, 2.3b, c). Iceberg thickness can also grow through snow accumulation on the surface, which we account for, but only based on reanalysis data and there might be additional local snowfall or snow accumulation through strong katabatic winds from the nearby continent (Fedotov, Cherepanov and Tyshko, 1998). Furthermore, external forcing from collisions with the adjacent ice-shelf might have led to a deformation (MacAyeal *et al.*, 2008) and hence a compression in some parts. All of these processes can cause a physical increase in iceberg thickness. Apart from that, a short (partial) grounding could lead to higher measured iceberg freeboards (Li *et al.*, 2018). Also surface melting could shift the scattering horizon of CryoSat-2 (Otosaka *et al.*, 2020) and therefore appear like a freeboard increase. Indeed we observe a steep increase in degree hours around the turn of the year 2015. What caused the signal in this instance is hard to disentangle. Most probably, it was a combination of several of the mentioned effects.

### 2.3.4. Iceberg volume and mass change

Having calculated changes in the B30 iceberg thickness associated with snowfall and basal melting and changes in area due to fragmentation, we combine both to determine the overall change in volume (Figure 2.10). To do this, we multiply each thickness estimate with the imagery-based area estimates interpolated to the times of the CryoSat-2 overpasses. Unlike small icebergs, which can take on various shapes (Enderlin and Hamilton, 2014; Sulak *et al.*, 2017), large tabular icebergs inherit their shape from their parent ice shelf and therefore have rather homogenous thickness and near vertical walls (American Meteorological Society, 2012). Deviations from vertical may occur in both directions and we therefore expect them to approximately even out (Orheim, 1987). The larger the length to thickness ratio is, the smaller the impact of tilted side walls on the resulting volume. For the B30 iceberg with an initial length to thickness ratio of 187:1, we therefore conclude that our assumption of vertical walls has negligible impact on the volume. The proportion of the total volume changes associated with melting and fragmentation are calculated by keeping area and thickness constant (and equal to

2. Tracking changes in the area, thickness, and volume of the Thwaites tabular iceberg “B30” using satellite altimetry and imagery

their average), respectively. To compute changes in mass, we multiply the volume change due to fragmentation by the column-average iceberg density at each point in time, because this ice is lost at the sides. In contrast, we multiply the volume change due to basal melting by the density of pure ice ( $915 \text{ kg m}^{-3}$ ), since this ice is lost at the bottom where ice density is highest. The total mass change is the sum of both components. Uncertainties are calculated by propagating the uncertainties of thickness change, area change, and ice density.

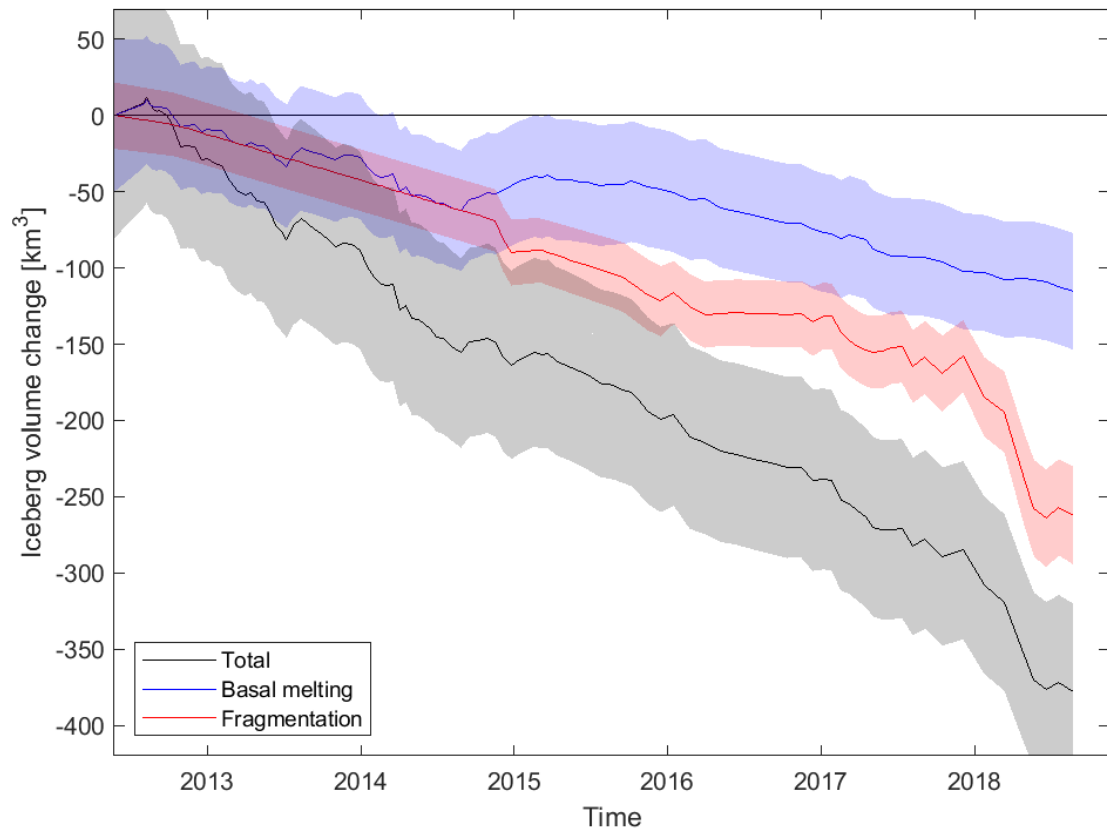


Figure 2.10: Volume change of the B30 iceberg divided into loss due to basal melting (thickness change, blue) and due to fragmentation (area change, red), as well as total volume loss (black).

The initial volume of B30 at the time of its calving was  $472 \pm 57 \text{ km}^3$  and after 6.5 years it has lost  $378 \pm 57 \text{ km}^3$  of ice, corresponding to a  $80 \pm 16 \%$  reduction. Fragmentation accounts for two thirds ( $69 \pm 14 \%$ ) of the total volume loss and basal melting is responsible for the remainder ( $31 \pm 11 \%$ ). Volume changes due to fragmentation become the dominant source of ice loss towards the end of our survey, consistent with previous findings (Bouhier *et al.*, 2018). This is because the main drivers of fragmentation are surface melting, which can lead to a rapid disintegration (Scambos *et al.*, 2008) and wave erosion or wave stress (Wagner *et al.*, 2014). Both increase the further North (i.e. surrounded by open ocean and warmer air temperatures) the iceberg gets. The two icebergs studied by Bouhier *et al.*, (2018) also show similar fractions of ice

## 2. Tracking changes in the area, thickness, and volume of the Thwaites tabular iceberg “B30” using satellite altimetry and imagery

---

loss due to fragmentation (60% for the B17A iceberg and 75% for the C19A iceberg). In terms of mass, the iceberg has lost  $325 \pm 44$  Gt of ice in total at an average rate of  $46 \pm 4$  Gt per year. The loss due to basal melting ( $106 \pm 35$  Gt) can be used as a lower estimate of the freshwater flux from B30. Some of the mass lost due to changes in area - in particular melting at the sides and smaller edge wastings, which will probably melt locally, add to the freshwater flux, but bigger calving events create smaller icebergs, which can survive and travel on their own (Bigg *et al.*, 1997; Martin and Adcroft, 2010; England, Wagner and Eisenman, 2020). To calculate the total freshwater flux, the melting of all fragments has to be considered (Tournadre, Girard-Arduin and Legrésy, 2012; Tournadre *et al.*, 2016).

### 2.4. Conclusions

In this study we have derived changes in the area, freeboard, thickness, and volume of the tabular B30 iceberg using a combination of satellite altimetry and satellite imagery. During the 6.5 years after the iceberg calved in May 2012, its area reduced from  $1500 \pm 60$  km<sup>2</sup> to  $426 \pm 27$  km<sup>2</sup> at an average rate of  $149 \pm 5$  km<sup>2</sup> per year. The iceberg freeboard lowered by  $9.2 \pm 2.2$  m over the same period. Using estimates of the snow accumulation and changes in snow and ice density, we estimate that the iceberg thinned by  $117 \pm 38$  m at a mean rate of  $17.3 \pm 1.8$  m per year. Altogether, the iceberg lost  $378 \pm 57$  km<sup>3</sup> of ice, and this equates to an estimated  $325 \pm 44$  Gt reduction in mass.

We investigated the capability of automated approaches to approximate iceberg area and area change by comparing them to manually-derived estimates. Although the most reliable method of charting iceberg area change is through manual delineation in satellite imagery, we show that less time-consuming estimates derived from measurements of the iceberg’s orthogonal axes or arc-lengths are also able to capture the area and area change over time, albeit with poorer certainty. Orthogonal axes lead to estimates of area and area trends that are 14 % and 16 % higher, respectively, and arc-lengths lead to estimates of area and area trends that are 45 % and 48 % lower, due to the necessary approximate of the iceberg shape.

We also presented a new thorough methodology to investigate iceberg freeboard and thickness change, using a densely sampled time series of consistently processed Level 1 CryoSat data and assessed the importance of collocation. Using a subset of 12 instances with collocation, we find that omitting this step leads to a small deterioration in the certainty of detected freeboard change for the B30 iceberg, but the densely sampled time series is in good agreement with the

## 2. Tracking changes in the area, thickness, and volume of the Thwaites tabular iceberg “B30” using satellite altimetry and imagery

---

colocated tracks. We expect this finding also holds for other large tabular Antarctic icebergs with uniform topography, when the observed freeboard change exceeds the topography and when enough tracks are averaged. In this case, it suggests that the procedure for tracking changes in iceberg thickness could be automated, given reliable estimates of their position (Budge and Long, 2018).

Finally, we developed a methodology to account for snowfall and variations in snow and ice density due to changing environmental conditions that large icebergs experience during their multi-annual drift. We found that the impact of snowfall on the retrieval of iceberg thickness increases over time, and after 6.5 years we estimate that 7.2 metres of snow have accumulated, which leads to a 27 m adjustment to the iceberg thickness change. Iceberg thickness change is also strongly dependent on the ice density profile which we derive from the depths of critical density levels (Ligtenberg, Helsen and Van Den Broeke, 2011), and so in situ observations would help to assess the reliability of this relationship. Likewise, direct measurements of the near-surface firn will help to assess the reliability of our reanalyses-based estimate of snow loading.

More icebergs - including the fragments lost from B30 - need to be studied to generalise the results we have and to constrain both the fresh water flux, which influences water circulation (Jenkins, 1999; Grosfeld *et al.*, 2001) and promotes sea ice formation (Bintanja, Van Oldenborgh and Katsman, 2015; Merino *et al.*, 2016), and input of terrigenous nutrients such as glacial iron into the Southern Ocean, which fosters primary production (Helly *et al.*, 2011; Biddle *et al.*, 2015; Duprat, Bigg and Wilton, 2016). Finally, studying icebergs as they drift through warmer water may give unique insights into the response of glacial ice to environmental conditions which may become commonplace at the ice shelf front in the future (Scambos *et al.*, 2008; Shepherd *et al.*, 2019).

## References

- American Meteorological Society (2012) ‘Tabular iceberg’, *Glossary of Meteorology*. Available at: [https://glossary.ametsoc.org/wiki/Tabular\\_iceberg](https://glossary.ametsoc.org/wiki/Tabular_iceberg).
- Arrigo, K. R. *et al.* (2002) ‘Ecological impact of a large Antarctic iceberg’, *Geophysical Research Letters*, 29(7), pp. 8-1-8-4. doi: 10.1029/2001GL014160.
- Barnes, D. K. A. (2017) ‘Iceberg killing fields limit huge potential for benthic blue carbon in Antarctic shallows’, *Global Change Biology*, 23(7), pp. 2649–2659. doi: 10.1111/gcb.13523.

2. Tracking changes in the area, thickness, and volume of the Thwaites tabular iceberg “B30” using satellite altimetry and imagery
- 

- Biddle, L. C. *et al.* (2015) ‘Ocean glider observations of iceberg-enhanced biological production in the northwestern Weddell Sea’, *Geophysical Research Letters*, 42(2), pp. 459–465. doi: 10.1002/2014GL062850.
- Bigg, G. R. *et al.* (1997) ‘Modelling the dynamics and thermodynamics of icebergs’, *cold regions science and technology*, 26(2), pp. 113–135. doi: 10.1016/S0165-232X(97)00012-8.
- Bigg, G. R. *et al.* (2018) ‘A model for assessing iceberg hazard’, *Natural Hazards*. Springer Netherlands, 92(2), pp. 1113–1136. doi: 10.1007/s11069-018-3243-x.
- Bintanja, R., Van Oldenborgh, G. J. and Katsman, C. A. (2015) ‘The effect of increased fresh water from Antarctic ice shelves on future trends in Antarctic sea ice’, *Annals of Glaciology*, 56(69), pp. 120–126. doi: 10.3189/2015AoG69A001.
- Bouhier, N. *et al.* (2018) ‘Melting and fragmentation laws from the evolution of two large Southern Ocean icebergs estimated from satellite data’, *Cryosphere*, 12(7), pp. 2267–2285. doi: 10.5194/tc-12-2267-2018.
- Budge, J. S. and Long, D. G. (2018) ‘A Comprehensive Database for Antarctic Iceberg Tracking Using Scatterometer Data’, *IEEE Journal of Selected Topics in Applied Earth Observations and Remote Sensing*, 11(2), pp. 434–442. doi: 10.1109/JSTARS.2017.2784186.
- Collares, L. L. *et al.* (2018) ‘Iceberg drift and ocean circulation in the northwestern Weddell Sea, Antarctica’, *Deep-Sea Research Part II: Topical Studies in Oceanography*. Elsevier Ltd, 149(March), pp. 10–24. doi: 10.1016/j.dsr2.2018.02.014.
- Copernicus Climate Change Service (2018) ‘ERA5 hourly data on single levels from 1979 to present’. Copernicus Climate Change Service Climate Data Store (CDS). doi: 10.24381/cds.adbb2d47.
- Dammann, D. O. *et al.* (2019) ‘Iceberg topography and volume classification using TanDEM-X interferometry’, *Cryosphere*, 13(7), pp. 1861–1875. doi: 10.5194/tc-13-1861-2019.
- Depoorter, M. A. *et al.* (2013) ‘Calving fluxes and basal melt rates of Antarctic ice shelves’, *Nature*. Nature Publishing Group, 502(7469), pp. 89–92. doi: 10.1038/nature12567.
- Dryak, M. C. and Enderlin, E. M. (2020) ‘Analysis of Antarctic Peninsula glacier frontal ablation rates with respect to iceberg melt-inferred variability in ocean conditions’, *Journal of Glaciology*, 66(257), pp. 457–470. doi: 10.1017/jog.2020.21.
- Duprat, L. P. A. M., Bigg, G. R. and Wilton, D. J. (2016) ‘Enhanced Southern Ocean marine productivity due to fertilization by giant icebergs’, *Nature Geoscience*, 9(3), pp. 219–221. doi: 10.1038/ngeo2633.

- Tracking changes in the area, thickness, and volume of the Thwaites tabular iceberg “B30” using satellite altimetry and imagery
- 

- Eik, K. and Gudmestad, O. T. (2010) ‘Iceberg management and impact on design of offshore structures’, *Cold Regions Science and Technology*. Elsevier B.V., 63(1–2), pp. 15–28. doi: 10.1016/j.coldregions.2010.04.008.
- Enderlin, E. M. and Hamilton, G. S. (2014) ‘Estimates of iceberg submarine melting from high-resolution digital elevation models: Application to Sermilik Fjord, East Greenland’, *Journal of Glaciology*, 60(224), pp. 1111–1116. doi: 10.3189/2014JoG14J085.
- England, M. R., Wagner, T. J. W. and Eisenman, I. (2020) ‘Modeling the breakup of tabular icebergs’, *Science Advances*, 6(51), pp. 1–9. doi: 10.1126/sciadv.abd1273.
- Fedotov, V. I., Cherepanov, N. V. and Tyshko, K. P. (1998) ‘Some Features of the Growth, Structure and Metamorphism of East Antarctic Landfast Sea Ice’, in Jeffries, M. O. (ed.) *Antarctic Sea Ice: Physical Processes, Interactions and Variability*. Washington DC: American Geophysical Union, pp. 343–354. doi: 10.1029/ar074p0343.
- Fichefet, T. and Morales Maqueda, M. A. (1999) ‘Modelling the influence of snow accumulation and snow-ice formation on the seasonal cycle of the Antarctic sea-ice cover’, *Climate Dynamics*, 15(4), pp. 251–268. doi: 10.1007/s003820050280.
- Gladstone, R. M., Bigg, G. R. and Nicholls, K. W. (2001) ‘Iceberg trajectory modeling and meltwater injection in the Southern Ocean’, *Journal of Geophysical Research: Oceans*, 106(C9), pp. 19903–19915. doi: 10.1029/2000jc000347.
- Grosfeld, K. *et al.* (2001) ‘How iceberg calving and grounding change the circulation and hydrography in the Filchner Ice Shelf–Ocean System’, *Journal of Geophysical Research*, 106(2000), pp. 9039–9055.
- Gutt, J. (2001) ‘On the direct impact of ice on marine benthic communities, a review’, *Polar Biology*, 24(8), pp. 553–564. doi: 10.1007/s003000100262.
- Hamley, T. C. and Budd, W. F. (1986) ‘Antarctic Iceberg Distribution and Dissolution’, *Journal of Glaciology*, 32(111), pp. 242–251. doi: 10.1017/s0022143000015574.
- Han, H. *et al.* (2019) ‘Changes in a giant iceberg created from the collapse of the Larsen C Ice Shelf, Antarctic Peninsula, derived from Sentinel-1 and CryoSat-2 data’, *Remote Sensing*, 11(4), pp. 1–14. doi: 10.3390/rs11040404.
- Helly, J. J. *et al.* (2011) ‘Cooling, dilution and mixing of ocean water by free-drifting icebergs in the Weddell Sea’, *Deep-Sea Research Part II: Topical Studies in Oceanography*. Elsevier, 58(11–12), pp. 1346–1363. doi: 10.1016/j.dsr2.2010.11.010.

2. Tracking changes in the area, thickness, and volume of the Thwaites tabular iceberg “B30” using satellite altimetry and imagery
- 

- Huppert, H. E. and Josberger, E. G. (1980) ‘The Melting of Ice in Cold Stratified water’, *Journal of Physical Oceanography*, 10(6), pp. 953–960. doi: [https://doi.org/10.1175/1520-0485\(1980\)010<0953:TMOIIC>2.0.CO;2](https://doi.org/10.1175/1520-0485(1980)010<0953:TMOIIC>2.0.CO;2).
- International Organization for Standardization (1998) ‘ISO 4355 Bases for design on structures – Determination of snow loads on roofs.’
- Jacka, T. H. and Giles, A. B. (2007) ‘Antarctic iceberg distribution and dissolution from ship-based observations’, *Journal of Glaciology*, 53(182), pp. 341–356. doi: [10.3189/002214307783258521](https://doi.org/10.3189/002214307783258521).
- Jansen, D., Schodlok, M. and Rack, W. (2007) ‘Basal melting of A-38B: A physical model constrained by satellite observations’, *Remote Sensing of Environment*, 111(2), pp. 195–203. doi: [10.1016/j.rse.2007.03.022](https://doi.org/10.1016/j.rse.2007.03.022).
- Jenkins, A. (1999) ‘The impact of melting ice on ocean waters’, *Journal of Physical Oceanography*, 29(9), pp. 2370–2381. doi: [10.1175/1520-0485\(1999\)029<2370:TIOMIO>2.0.CO;2](https://doi.org/10.1175/1520-0485(1999)029<2370:TIOMIO>2.0.CO;2).
- Joiris, C. R. (2018) ‘Seabird hotspots on icebergs in the Amundsen Sea, Antarctica’, *Polar Biology*. Springer Berlin Heidelberg, 41(1), pp. 111–114. doi: [10.1007/s00300-017-2174-4](https://doi.org/10.1007/s00300-017-2174-4).
- Jongma, J. I. *et al.* (2009) ‘The effect of dynamic-thermodynamic icebergs on the Southern Ocean climate in a three-dimensional model’, *Ocean Modelling*. Elsevier Ltd, 26(1–2), pp. 104–113. doi: [10.1016/j.ocemod.2008.09.007](https://doi.org/10.1016/j.ocemod.2008.09.007).
- Kooyman, G. L. *et al.* (2007) ‘Effects of giant icebergs on two emperor penguin colonies in the Ross Sea, Antarctica’, *Antarctic Science*. University of Leeds, 19(1), pp. 31–38. doi: [10.1017/S0954102007000065](https://doi.org/10.1017/S0954102007000065).
- Kurtz, N. T. and Markus, T. (2012) ‘Satellite observations of Antarctic sea ice thickness and volume’, *Journal of Geophysical Research: Oceans*, 117(8), pp. 1–9. doi: [10.1029/2012JC008141](https://doi.org/10.1029/2012JC008141).
- Kwok, R. and Cunningham, G. F. (2008) ‘ICESat over Arctic sea ice: Estimation of snow depth and ice thickness’, *Journal of Geophysical Research: Oceans*, 113(8), pp. 1–17. doi: [10.1029/2008JC004753](https://doi.org/10.1029/2008JC004753).
- Laufkötter, C. *et al.* (2018) ‘Glacial Iron Sources Stimulate the Southern Ocean Carbon Cycle’, *Geophysical Research Letters*, 45(24), pp. 13,377–13,385. doi: [10.1029/2018GL079797](https://doi.org/10.1029/2018GL079797).
- Leonard, K. C. and Maksym, T. (2011) ‘The importance of wind-blown snow redistribution to snow accumulation on Bellingshausen Sea ice’, *Annals of Glaciology*, 52(57 PART 2), pp. 271–278. doi: [10.3189/172756411795931651](https://doi.org/10.3189/172756411795931651).

2. Tracking changes in the area, thickness, and volume of the Thwaites tabular iceberg “B30” using satellite altimetry and imagery

---

- Li, Tian *et al.* (2018) ‘Monitoring the tabular icebergs C28A and C28B calved from the Mertz Ice Tongue using radar remote sensing data’, *Remote Sensing of Environment*. Elsevier, 216(July 2017), pp. 615–625. doi: 10.1016/j.rse.2018.07.028.
- Ligtenberg, S. R. M., Helsen, M. M. and Van Den Broeke, M. R. (2011) ‘An improved semi-empirical model for the densification of Antarctic firn’, *Cryosphere*, 5(4), pp. 809–819. doi: 10.5194/tc-5-809-2011.
- Little, C. M., Gnanadesikan, A. and Hallberg, R. (2008) ‘Large-scale oceanographic constraints on the distribution of melting and freezing under ice shelves’, *Journal of Physical Oceanography*, 38(10), pp. 2242–2255. doi: 10.1175/2008JPO3928.1.
- MacAyeal, D. R. *et al.* (2008) ‘Tabular iceberg collisions within the coastal regime’, *Journal of Glaciology*, 54(185), pp. 371–386. doi: 10.3189/002214308784886180.
- Martin, T. and Adcroft, A. (2010) ‘Parameterizing the fresh-water flux from land ice to ocean with interactive icebergs in a coupled climate model’, *Ocean Modelling*. Elsevier Ltd, 34(3–4), pp. 111–124. doi: 10.1016/j.ocemod.2010.05.001.
- Mazur, A. K., Wåhlin, A. K. and Kalén, O. (2019) ‘The life cycle of small-to medium-sized icebergs in the Amundsen sea embayment’, *Polar Research*, 38, pp. 1–17. doi: 10.33265/polar.v38.3313.
- McIntyre, N. F. and Cudlip, W. (1987) ‘Observation of a giant antarctic tabular iceberg by satellite radar altimetry’, *Polar Record*, 23(145), pp. 458–462. doi: 10.1017/S0032247400007610.
- Merino, N. *et al.* (2016) ‘Antarctic icebergs melt over the Southern Ocean : Climatology and impact on sea ice’, *Ocean Modelling*. Elsevier Ltd, 104, pp. 99–110. doi: 10.1016/j.ocemod.2016.05.001.
- Morgan, V. I. and Budd, W. F. (1978) ‘the Distribution, Movement and Melt Rates of Antarctic Icebergs’, in *Iceberg Utilization*. Iowa State University Research Foundation, pp. 220–228. doi: 10.1016/b978-0-08-022916-4.50025-x.
- Mouginot, J., Rignot, E. and Scheuchl, B. (2019) ‘Continent-Wide, Interferometric SAR Phase, Mapping of Antarctic Ice Velocity’, *Geophysical Research Letters*, 46(16), pp. 9710–9718. doi: 10.1029/2019GL083826.
- Neshyba, S. and Josberger, E. G. (1980) ‘On the estimation of Antarctic iceberg melt rate’, *Journal of Physical Oceanography*, 10(10), pp. 1681–1685. doi: [https://doi.org/10.1175/1520-0485\(1980\)010<1681:OTEOAI>2.0.CO;2](https://doi.org/10.1175/1520-0485(1980)010<1681:OTEOAI>2.0.CO;2).

- Tracking changes in the area, thickness, and volume of the Thwaites tabular iceberg “B30” using satellite altimetry and imagery
- 

- Nøst, O. A. and Østerhus, S. (1998) ‘Impact of Grounded Icebergs on the Hydrographic Conditions Near the Filchner Ice Shelf’, in *Ocean, Ice, and Atmosphere: Interactions at the Antarctic Continental Margin*, pp. 267–284. doi: 10.1029/ar075p0267.
- Orheim, O. (1987) ‘Evolution of under Water Sides of Ice Shelves and Icebergs’, *Annals of Glaciology*, 9, pp. 176–182. doi: doi:10.3189/S0260305500000574.
- Otosaka, I. N. *et al.* (2020) ‘Surface Melting Drives Fluctuations in Airborne Radar Penetration in West Central Greenland’, *Geophysical Research Letters*, 47(17). doi: 10.1029/2020GL088293.
- Power, D. *et al.* (2001) ‘Iceberg detection capabilities of radarsat synthetic aperture radar’, *Canadian Journal of Remote Sensing*, 27(5), pp. 476–486. doi: 10.1080/07038992.2001.10854888.
- Rackow, T. *et al.* (2017) ‘A simulation of small to giant Antarctic iceberg evolution: Differential impact on climatology estimates’, *Journal of Geophysical Research : Oceans*, pp. 3170–3190. doi: 10.1002/2016JC012513.
- Raiswell, R. *et al.* (2016) ‘Potentially bioavailable iron delivery by iceberg-hosted sediments and atmospheric dust to the polar oceans’, *Biogeosciences*, 13(13), pp. 3887–3900. doi: 10.5194/bg-13-3887-2016.
- Remy, J. P. *et al.* (2008) ‘Impact of the B-15 iceberg “stranding event” on the physical and biological properties of sea ice in McMurdo Sound, Ross Sea, Antarctica’, *Antarctic Science*, 20(6), pp. 593–604. doi: 10.1017/S0954102008001284.
- Rignot, E. *et al.* (2013) ‘Ice-shelf melting around Antarctica’, *Science*, 341(6143), pp. 266–270. doi: 10.1126/science.1235798.
- Robinson, N. J. and Williams, M. J. M. (2012) ‘Iceberg-induced changes to polynya operation and regional oceanography in the southern Ross Sea, Antarctica, from in situ observations’, *Antarctic Science*, 24(5), pp. 514–526. doi: 10.1017/S0954102012000296.
- Russell-Head, D. S. (1980) ‘The Melting of Free-Drifting Icebergs’, *Annals of Glaciology*, 1, pp. 119–122. doi: 10.3189/s0260305500017092.
- Scambos, T. *et al.* (2008) ‘Calving and ice-shelf break-up processes investigated by proxy: Antarctic tabular iceberg evolution during northward drift’, *Journal of Glaciology*, 54(187), pp. 579–591. doi: 10.3189/002214308786570836.
- Schloesser, F. *et al.* (2019) ‘Antarctic iceberg impacts on future Southern Hemisphere climate’, *Nature Climate Change*. Springer US, 9(9), pp. 672–677. doi: 10.1038/s41558-019-0546-1.

2. Tracking changes in the area, thickness, and volume of the Thwaites tabular iceberg “B30” using satellite altimetry and imagery

---

- Shepherd, A. *et al.* (2019) ‘Trends in Antarctic Ice Sheet Elevation and Mass’, *Geophysical Research Letters*, 46(14), pp. 8174–8183. doi: 10.1029/2019GL082182.
- Silva, T. A. M., Bigg, G. R. and Nicholls, K. W. (2006) ‘Contribution of giant icebergs to the Southern Ocean freshwater flux’, *Journal of Geophysical Research*, 111(July 2005), pp. 1–8. doi: 10.1029/2004JC002843.
- Smith, K. L. *et al.* (2007) ‘Free-drifting icebergs: Hot spots of chemical and biological enrichment in the Weddell Sea’, *Science*, 317(5837), pp. 478–482. doi: 10.1126/science.1142834.
- Stuart, K. M. and Long, D. G. (2011) ‘Tracking large tabular icebergs using the SeaWinds Ku-band microwave scatterometer’, *Deep-Sea Research Part II: Topical Studies in Oceanography*. Elsevier, 58(11–12), pp. 1285–1300. doi: 10.1016/j.dsr2.2010.11.004.
- Sulak, D. J. *et al.* (2017) ‘Iceberg properties and distributions in three Greenlandic fjords using satellite imagery’, *Annals of Glaciology*, 58(74), pp. 92–106. doi: 10.1017/aog.2017.5.
- Tilling, R. L., Ridout, A. and Shepherd, A. (2018) ‘Estimating Arctic sea ice thickness and volume using CryoSat-2 radar altimeter data’, *Advances in Space Research*. COSPAR, 62(6), pp. 1203–1225. doi: 10.1016/j.asr.2017.10.051.
- Tournadre, J. *et al.* (2015) ‘Large icebergs characteristics from altimeter waveforms analysis’, *Journal of Geophysical Research: Oceans*, 120(3), pp. 2121–2128. doi: <https://doi.org/10.1002/2014JC010502>.
- Tournadre, J. *et al.* (2016) ‘Antarctic icebergs distributions 1992–2014’, *Journal of Geophysical Research: Oceans*. John Wiley & Sons, Ltd, 121(1), pp. 327–349. doi: 10.1002/2015JC011178.
- Tournadre, J., Girard-Ardhuin, F. and Legrésy, B. (2012) ‘Antarctic icebergs distributions, 2002–2010’, *Journal of Geophysical Research: Oceans*, 117(5), pp. 2002–2010. doi: 10.1029/2011JC007441.
- Wagner, T. J. W. *et al.* (2014) ‘The “footloose” mechanism: Iceberg decay from hydrostatic stresses’, *Geophysical Research Letters*, 41(15), pp. 5522–5529. doi: 10.1002/2014GL060832.
- Wise, M. G. *et al.* (2017) ‘Evidence of marine ice-cliff instability in Pine Island Bay from iceberg-keel plough marks’, *Nature*, 550(7677), pp. 506–510. doi: 10.1038/nature24458.
- Wu, S. Y. and Hou, S. (2017) ‘Impact of icebergs on net primary productivity in the Southern Ocean’, *Cryosphere*, 11(2), pp. 707–722. doi: 10.5194/tc-11-707-2017.

2. Tracking changes in the area, thickness, and volume of the Thwaites tabular iceberg “B30” using satellite altimetry and imagery
- 

Zwally, H. J. *et al.* (2005) ‘Mass changes of the Greenland and Antarctic ice sheets and shelves and contributions to sea-level rise: 1992-2002’, *Journal of Glaciology*, 51(175), pp. 509–527. doi: 10.3189/172756505781829007.

Zwally, H. J. *et al.* (2008) ‘ICESat measurements of sea ice freeboard and estimates of sea ice thickness in the Weddell Sea’, *Journal of Geophysical Research: Oceans*, 113(2), pp. 1–17. doi: 10.1029/2007JC004284.

# 3

## OBSERVING THE DISINTEGRATION OF THE A68A ICEBERG FROM SPACE

**This chapter is based on the following paper with small post-viva additions.**

**Citation:** Braakmann-Folgmann, A., Shepherd, A., Gerrish, L., Izzard, J., Ridout, A., 2022. Observing the disintegration of the A68A iceberg from space. *Remote Sens. Environ.* 270, 112855.

<https://doi.org/10.1016/j.rse.2021.112855>

**Author contributions:** I designed the study together with my supervisor, Andy Shepherd. Andy Ridout provided pre-processed CryoSat elevations. Jamie Izzard searched for ICESat-2 tracks sampling the iceberg and pre-processed them during his internship. I took care of all other processing steps and data acquisition to compute iceberg freeboard. Deriving iceberg outlines and calculating iceberg area were split between Laura Gerrish, Jamie Izzard and me. Laura Gerrish also produced Figure 1 in the paper. I calculated iceberg thickness, volume, their changes over time, their corresponding uncertainties and prepared the other figures. I also wrote the manuscript and adjusted it according to the reviewers' comments. Andy Shepherd supervised the work and suggested edits to the manuscript.

## Abstract

Icebergs impact the physical and biological properties of the ocean where they drift, depending on the degree of melting. We use satellite imagery and altimetry to quantify the area, thickness, and volume change of the massive A68A iceberg from its calving off the Larsen-C Ice Shelf in July 2017 until January 2021, when it disintegrated. A68A thinned from  $235 \pm 9$  to  $168 \pm 10$  m, on average, and lost  $802 \pm 34$  Gt of ice in 3.5 years,  $254 \pm 17$  Gt of which was through basal melting (a lower bound for the immediate fresh water input into the ocean). Basal melting peaked at  $7.2 \pm 2.3$  m/month in the Northern Scotia Sea and an estimated  $152 \pm 61$  Gt of freshwater was released off South Georgia, potentially altering the local ocean properties, plankton occurrence and conditions for predators.

### 3.1. Introduction

Icebergs impact and interact with the Antarctic environment through a range of processes. This begins with their calving, which may influence the stability of their parent ice shelf (Rott et al., 1996) and flow of glaciers upstream (Rignot et al., 2004). As they drift, icebergs release cold fresh melt water, altering the local ocean properties (Helly et al., 2011; Jenkins, 1999) and facilitating sea ice growth (Bintanja et al., 2015; Merino et al., 2016). They also carry debris with terrigenous nutrients, which supply the majority of iron input to the Southern Ocean (Wu & Hou, 2017), fostering biological production (Biddle et al., 2015; Duprat et al., 2016; Smith et al., 2007). When icebergs ground, they impact marine benthic communities (Barnes, 2017; Gutt, 2001) and leave plough marks on the sea floor (Wise et al., 2017). Furthermore, large icebergs can act as a barrier disrupting the local ocean circulation (Grosfeld et al., 2001) or blocking access of penguin colonies to their feeding grounds (Kooyman et al., 2007). The response of icebergs to the warmer climates they drift through can also inform predictions on how the Antarctic ice shelves will react to climate change (Scambos et al., 2008; Shepherd et al., 2019).

A68A was the sixth largest iceberg ever recorded in satellite observations (Budge and Long, 2018), and had a significant potential to impact its environment. Indeed when it calved from the Larsen-C Ice Shelf in July 2017, concerns were raised that its loss might trigger a collapse of the entire ice shelf (A. E. Hogg & Gudmundsson, 2017; Jansen et al., 2015). After residing close to its calving position for over a year, A68A started to move northwards through the Weddell Sea (Figure 3.1). It reached the Scotia Sea in early 2020 and approached South Georgia at the end of 2020, where it started to disintegrate. Although this is a common trajectory for icebergs (Figure

3.1 and Tournadre et al., 2016), the sheer size of A68A elevates its potential to impact ecosystems around South Georgia through release of fresh water and nutrients, through blockage and through collision with the benthic habitat (Grimm, 2021; Vernet et al., 2012). Here, we combine satellite imagery and satellite altimetry to chart changes in the A68A iceberg's area, freeboard, thickness, volume and mass over its lifetime to assess its disintegration and melt rate in different environments.

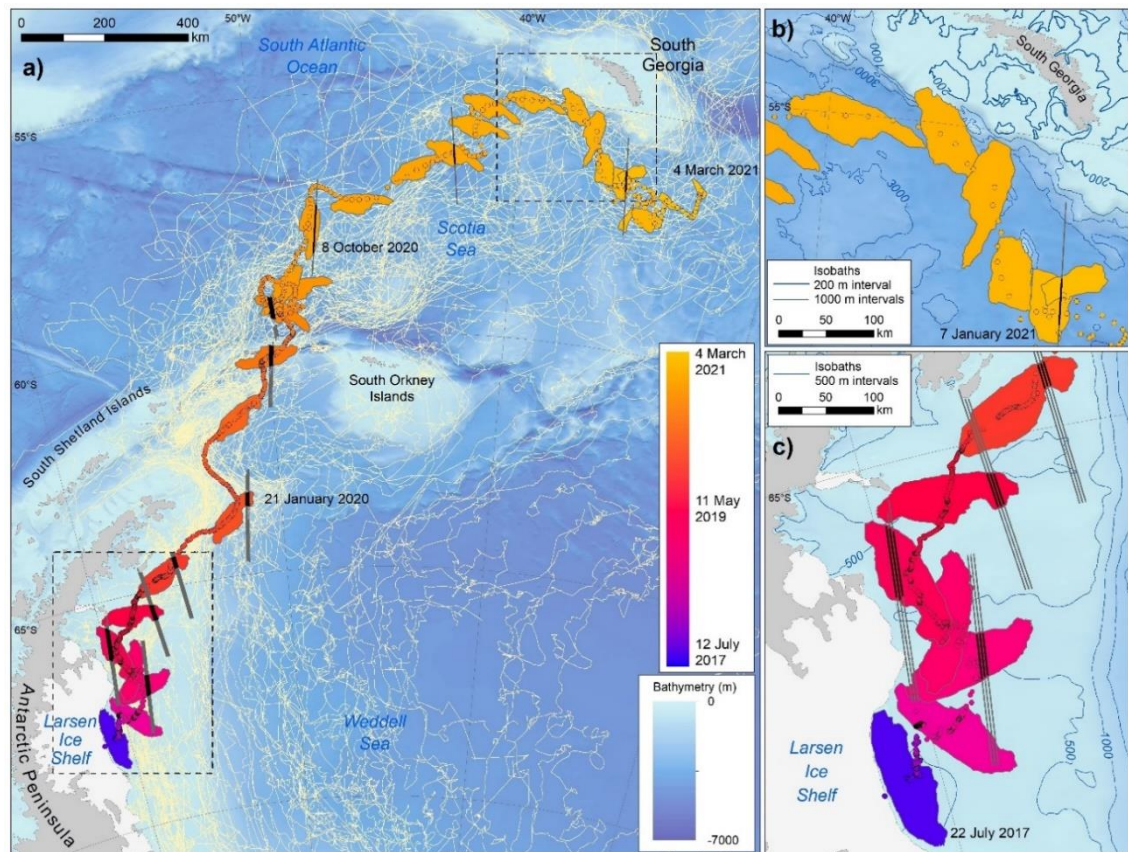


Figure 3.1: Trajectory of A68A (circles colored by date) and historic icebergs (yellow lines, Budge & Long, 2018) overlain on a bathymetric map (GEBCO Compilation Group, 2019; O. Hogg et al., 2016). Selected outlines (date colour coded), altimetry overpasses (grey lines with black marking the parts that sample the iceberg) and key dates are also shown. Panels b and c are zoom regions of interest.

### 3.2. Data and methods

We track the iceberg's area and area change in satellite imagery. In total, 23 Sentinel-1, 18 Moderate Resolution Imaging Spectroradiometer (MODIS) and 14 Sentinel-3 scenes are used to manually delineate the iceberg's outlines using GIS software. While the Sentinel-1 Synthetic Aperture Radar (SAR) imagery offers all-weather capability and higher spatial resolution, MODIS and Sentinel-3 optical imagery have the advantage of a higher temporal resolution, but cannot be used

### 3. Observing the disintegration of the A68A iceberg from space

during the polar night and on cloudy days. In optical imagery the spatial resolution is slightly lower and it is harder to distinguish sea ice from icebergs or clouds, which is the main error source. Therefore, we rely on Sentinel-1 data, if available close to the altimetry overpasses and use MODIS or Sentinel-3 data on the other occasions. To estimate the accuracy of our delineations we buffer the polygon outlines by two pixels and calculate the resulting difference in area. This gives a mean relative difference of 3.2 %.

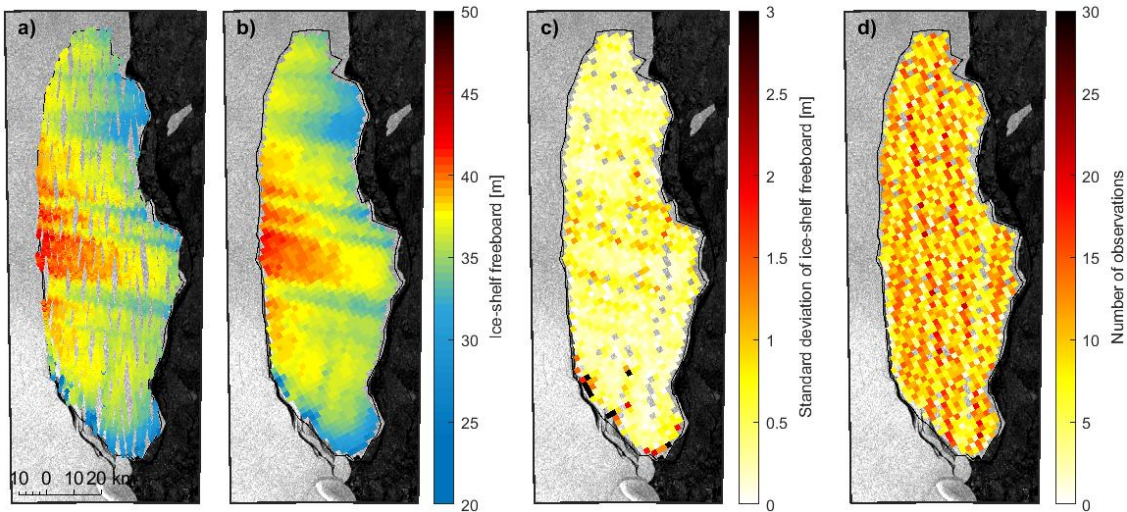


Figure 3.2: Calculation of initial iceberg freeboard map: (a) CryoSat tracks over the Larsen-C Ice Shelf over 1 year (12 July 2016 - 11 July 2017) before the iceberg calved, cut to the area that later formed the iceberg. (b) The same measurements gridded at 2 km and empty grid cells filled with linear interpolation. (c) Standard deviation within each grid cell. (d) Number of observations averaged per grid cell. The background shows a Sentinel-1 image on 10 July 2017

Changes in the iceberg's freeboard and thickness are derived from CryoSat-2 and ICESat-2 satellite altimetry. To generate a complete map of the initial iceberg freeboard and thickness, we collect all CryoSat-2 tracks over the part of the Larsen-C Ice Shelf that formed the A68A iceberg between 12 July 2016 and 11 July 2017 (Figure 3.2), correcting for the mean ice motion of 696 m/year (Mouginot et al., 2019). To track changes in the iceberg freeboard while it is drifting, we collocate 15 overpasses from ICESat-2 and 9 overpasses from CryoSat-2 with the initial freeboard map, post them on a common 2-km grid, and difference them. For this collocation to the initial iceberg reference system, we digitize the iceberg outline in a near-coincident image using 7 Sentinel-1 and 17 MODIS scenes. We then transform this outline to maximize the overlapping area with respect to the outline of the previous overpass by automatically searching for the optimal translation and rotation parameters (Figure 3.3). The rough translation is known from differencing the centroids of both polygons, greatly reducing the search radius. This iterative procedure then yields the optimal rotation and translation parameters with respect to the initial

outline and hence initial thickness map, too. At least for icebergs like A68A that are non-symmetric and when the general shape is preserved it allows us to determine where the new overpass samples the iceberg and which part of the initial freeboard map this corresponds to automatically. Grid cells of the initial map that are not covered by any track are filled using linear interpolation.

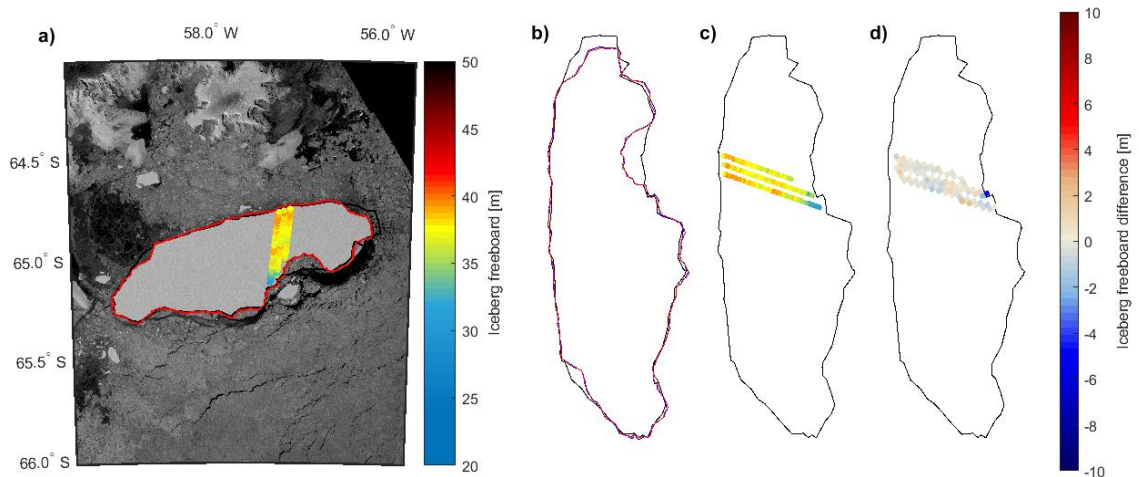


Figure 3.3: Collocation of a sample ICESat-2 track and the corresponding Sentinel-1 image on 18 September 2019: For each altimetry overpass a near-coincident image is used to derive the iceberg’s outline at the time of the new overpass (red, panel a). The new outline is transformed to maximize the overlapping area with the previous outline (blue, panel b). This is done iteratively, so we know the transformation of the previous polygon with respect to the initial polygon (black) and can transform the new overpass to the initial situation (panel c). We then grid the new track on the same grid as the initial freeboard measurements and difference it with these initial heights (panel d)

The CryoSat-2 data are processed from Level 1B baseline D using the Centre for Polar Observation and Modelling sea ice processing system (Tilling et al., 2018). For consistency, a common threshold retracker is applied to measurements acquired in both SAR and SAR interferometric mode and over all surface types. Iceberg freeboard is calculated by subtracting the adjacent mean sea surface height from the iceberg surface height. For ICESat-2 we use Level 2A, ATL03 photon data as a primary product, because iceberg heights are filtered out in the higher level products. For each track, we analyze the three strong beams separately and discard the weak beams. Low confidence flagged photons (2 and below) are filtered out and 150 photons each are averaged along-track, to reduce noise. We then extract the mean sea surface height, ocean tides and inverted barometer effect from Level 3A version 3 ATL07 data, interpolated to the ATL03 locations. These are subtracted from the photon heights, yielding sea surface heights that agree with the ATL07 sea surface heights, and to derive iceberg freeboard. Finally, we dis-

### 3. Observing the disintegration of the A68A iceberg from space

---

card freeboard measurements from both altimeters below 20 and above 100 m and measurements outside the iceberg polygon derived from the near-coincident satellite imagery. To make the higher resolution ICESat-2 data comparable to the initial heights derived from CryoSat-2, we also filter out crevasses searching for local minima with a prominence of 3 or more and reject the outer 2 km at the edges.

Uncertainty estimates are a combination of the freeboard standard deviations and the impact of the colocation uncertainty. The colocation uncertainty is mainly caused by the time separation between the altimetry overpass and the corresponding image. We perform a Monte Carlo simulation using 1000 samples that are normally distributed around the estimated translation and rotation assuming a maximum (3 sigma) daily rotation of 15 degrees and a maximum translation based on the drift speed of the iceberg scaled by the time separation. The drift speed is calculated as the path distance (Greene et al., 2017) from the locations given in the Antarctic Iceberg Tracking database (Budge and Long, 2018). We then calculate the freeboard difference for each of the 1000 slightly differently colocated samples and take their standard deviation as an estimate of the impact of erroneous colocation. This colocation uncertainty is combined with the standard deviations of the initial freeboard and of the new overpass using uncertainty propagation. The freeboard standard deviations are calculated within each grid cell. When the whole track is averaged to derive the mean freeboard change at one point in time, the uncertainties of the involved grid cells are propagated. Rather than assume that our freeboard measurement errors are not correlated in space or time, we employ a more conservative approach and propagate the uncertainties using a full covariance matrix to account for their correlation (Storto et al., 2019). In the absence of independent freeboard measurements for verification, we assume that altimeter-derived freeboards recorded along the same track are 60 % correlated and that the initial freeboards, which are derived from measurements acquired along several independent tracks, are 30% correlated. The mean standard deviation of the calculated freeboard change is 0.45 m, with colocation contributing 22 %, the initial freeboard contributing 29 % and the new track contributing 49 %.

Iceberg thickness  $H$  is derived from iceberg freeboard  $h_{fb}$  assuming hydrostatic equilibrium (Eq. 1). We treat ICESat-2 and CryoSat-2 measurements in the same way, presuming neither penetrates the snow layer. Because the iceberg survives for several years and travels a long distance passing through varying environmental conditions, we model the evolution of the snow layer and iceberg density based on ERA5 Reanalysis data (Copernicus Climate Change Service, 2018) of air temperature, wind speed and snow accumulation (Figure 3.4, Braakmann-Folgmann et al., 2021). The iceberg's column-average density  $\rho_i$  reduces from 868 to 848 kg m<sup>-3</sup> during its

drift (Ligtenberg et al., 2011), because the densest, pure glacial ice is melted from the bottom. We estimate the uncertainty in the column average and basal ice densities to be  $10 \text{ kg m}^{-3}$  (Dryak and Enderlin, 2020) and  $2 \text{ kg m}^{-3}$ , respectively. The density of the surface snow layer  $\rho_s$  reaches  $465 \text{ kg m}^{-3}$  after 3.5 years (International Organization for Standardization, 1998) and snow depth  $h_s$  increases by 3.3 m. We estimate the snow density and depth uncertainties to be  $50 \text{ kg m}^{-3}$  (Kurtz and Markus, 2012) and 20 % (Kwok and Cunningham, 2008), respectively. As sea water density  $\rho_w$  we use  $1024 \text{ kg m}^{-3}$  (Fichefet and Morales Maqueda, 1999) with an uncertainty of  $2 \text{ kg m}^{-3}$ . Altogether, the mean uncertainty in thickness change is 5.3 m, with ice density uncertainty being the largest factor. To obtain a continuous representation of iceberg thickness in space and time, we fit a third order polynomial function of latitude, longitude and time to our observations of thickness change and combine this with the initial thickness map ([supplementary animation](#), Braakmann-Folgmann et al., 2022).

$$H = \frac{\rho_w}{\rho_w - \rho_i} h_{fb} - \frac{(\rho_w - \rho_s)}{\rho_w - \rho_i} h_s \quad (1)$$

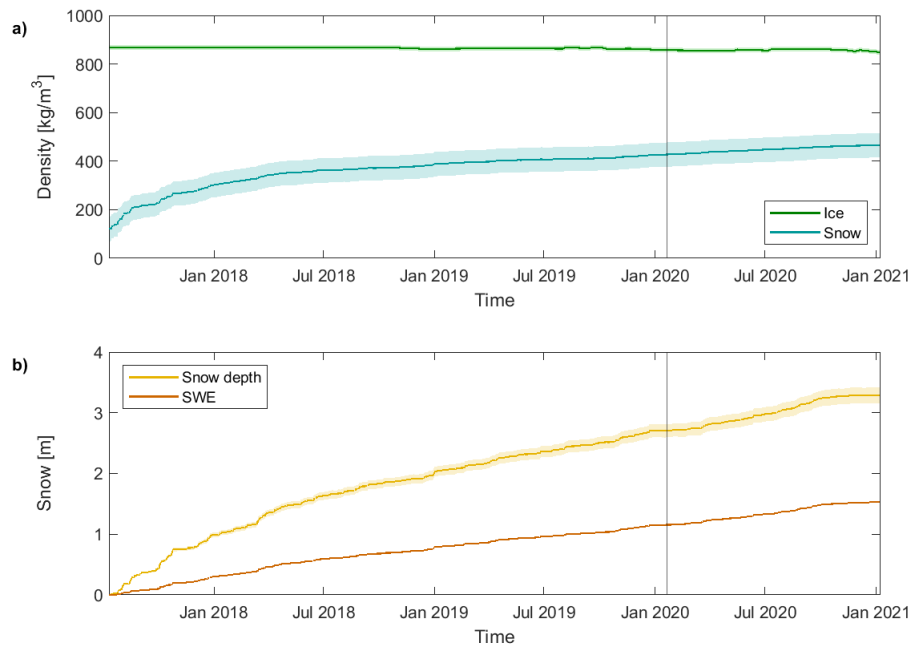


Figure 3.4: Evolution of iceberg properties based on ERA-5 Reanalysis data (Copernicus Climate Change Service, 2018): (a) Iceberg density and snow density; (b) snow depth and snow water equivalent (SWE)

Iceberg volume is determined by multiplying iceberg thickness and area, interpolated to the times of the altimetry overpasses. Changes in the volume of the mother iceberg are then calculated by differencing each volume estimate to the initial value. We differentiate between volume loss through fragmentation (area loss) and volume loss through basal melting (thickness change) by keeping either thickness or area constant. To convert volume change to mass change,

we multiply the loss due to fragmentation by the column-average ice density at each point in time, and we multiply the basal thickness change by the density of pure glacial ice. Summing both components gives the total iceberg mass change. Uncertainties are propagated, and we find that the uncertainties in area and thickness change contribute 45 % and 55 %, respectively, to the uncertainty of volume change.

### 3.3. Results

The initial area of the A68A iceberg was  $5719 \pm 77 \text{ km}^2$ . Since A68A and A68B separated just after calving (Budge & Long, 2018, Figure 3.5a), our initial polygon shows the outline of the A68A iceberg and all our results relate to A68A. During its lifetime, the iceberg's area gradually reduced both through larger break-ups and continuous processes (Figure 3.1 and Figure 3.6a). A larger break-up took place between 2018 and 2019 and another large piece, A68C, was lost in April 2020. In December 2020, the A68A iceberg gave birth to several children icebergs, named A68D-A68F (Budge and Long, 2018), rapidly reducing the area of the remaining largest part. Apart from these sudden losses, iceberg area also reduced gradually through side melting and smaller edge-wastings. Overall, the iceberg lost  $3206 \pm 78 \text{ km}^2$  up to 7 January 2021, when our last thickness measurement is, and  $5052 \pm 106 \text{ km}^2$  by 4 March 2021 - a  $56 \pm 8 \%$  and  $88 \pm 4 \%$  reduction in area of the mother iceberg, respectively. We find distinct patterns of area change according to the iceberg's geographical location (Figure 3.6a), with a mean loss rate of  $200 \pm 82 \text{ km}^2$  per year in the Weddell Sea and a more than ten times higher loss rate of  $2807 \pm 199 \text{ km}^2$  per year in the Scotia Sea until 7 January 2021, when the iceberg is drifting in open ocean.

The maps of initial iceberg freeboard and thickness (Figure 3.2 and Figure 3.5a) reveal the iceberg's topography. The mean gridded initial freeboard is  $36.0 \pm 0.2 \text{ m}$  and the mean estimated initial iceberg thickness is  $235 \pm 9 \text{ m}$ . The iceberg was thicker on the side facing the Antarctic Peninsula and thinnest on the Southern tip, where the crack which separated the iceberg from the ice shelf started (Jansen et al., 2015), and in the North. Moreover, the iceberg is covered by longitudinal surface structures in the former ice shelf flow direction of a few meters depth, which extend across the iceberg's full width and are a few kilometers wide, widening towards the sea. These are not visible in optical or radar imagery, but revealed by the thickness. One of these features coincides with a suture zone (Jansen et al., 2013). Owing to the undulating topography, gridded freeboard heights range from 22.1 to 42.6 m, and this motivates our collocation of subsequent altimetry tracks to improve confidence in estimates of freeboard and thickness change.

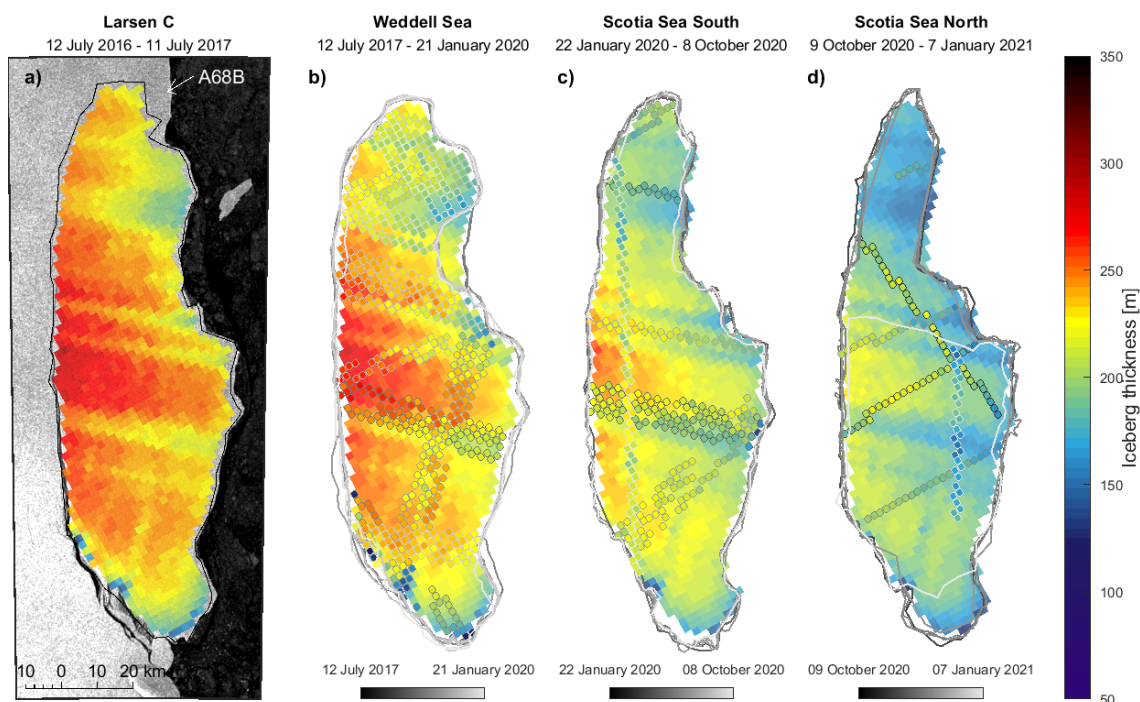


Figure 3.5: Maps of the A68A iceberg thickness when it was still part of the Larsen-C Ice Shelf (a) and at later dates as it drifted through the Weddell and Scotia Seas (b-d). The initial thickness is superimposed on a Sentinel-1 image acquired on 10 July 2017, and the region from which A68B was formed is also indicated. On later dates, the iceberg thickness is computed at colocated altimetry overpasses (outlined gridcells, shaded according to date relative to the interval start) and modelled at the mid-point of each interval elsewhere

The iceberg freeboard stays almost constant while in the Weddell Sea with a mean freeboard loss of  $0.2 \pm 0.1$  m/year (Figure 3.6b), but starts to rapidly decrease once it enters the Scotia Sea, where the mean rate of freeboard lowering is  $5.7 \pm 0.4$  m/year. Marking the location of each track, we observe that the initially southern part of the iceberg is the most resilient to melting. This explains the positive outliers in the time series, which all stem from the southern part. For thickness change (Figure 3.5, Figure 3.6c and [supplementary animation](#)) we record a total reduction of  $67 \pm 5$  m, leaving the iceberg with a mean thickness of  $168 \pm 10$  m close to South Georgia. The mean melt rates are  $7.8 \pm 2.1$  m/year in the Weddell Sea and  $49.5 \pm 6.5$  m/year in the Scotia Sea ( $3.0 \pm 0.8$  m/month in the Southern and  $7.2 \pm 2.3$  m/month in the Northern Scotia Sea). We find good agreement (average RMSE 10 m, maximum RMSE 22 m) between our observed iceberg thickness and the model fit (Figure 3.5). Another finding from our study is that CryoSat-2 and ICESat-2 freeboard and thickness measurements over the iceberg are comparable and can be merged into a consistent time series (see Figure 3.6b, c - especially the tracks on 5 and 16 May 2020, which are close in time).

### 3. Observing the disintegration of the A68A iceberg from space

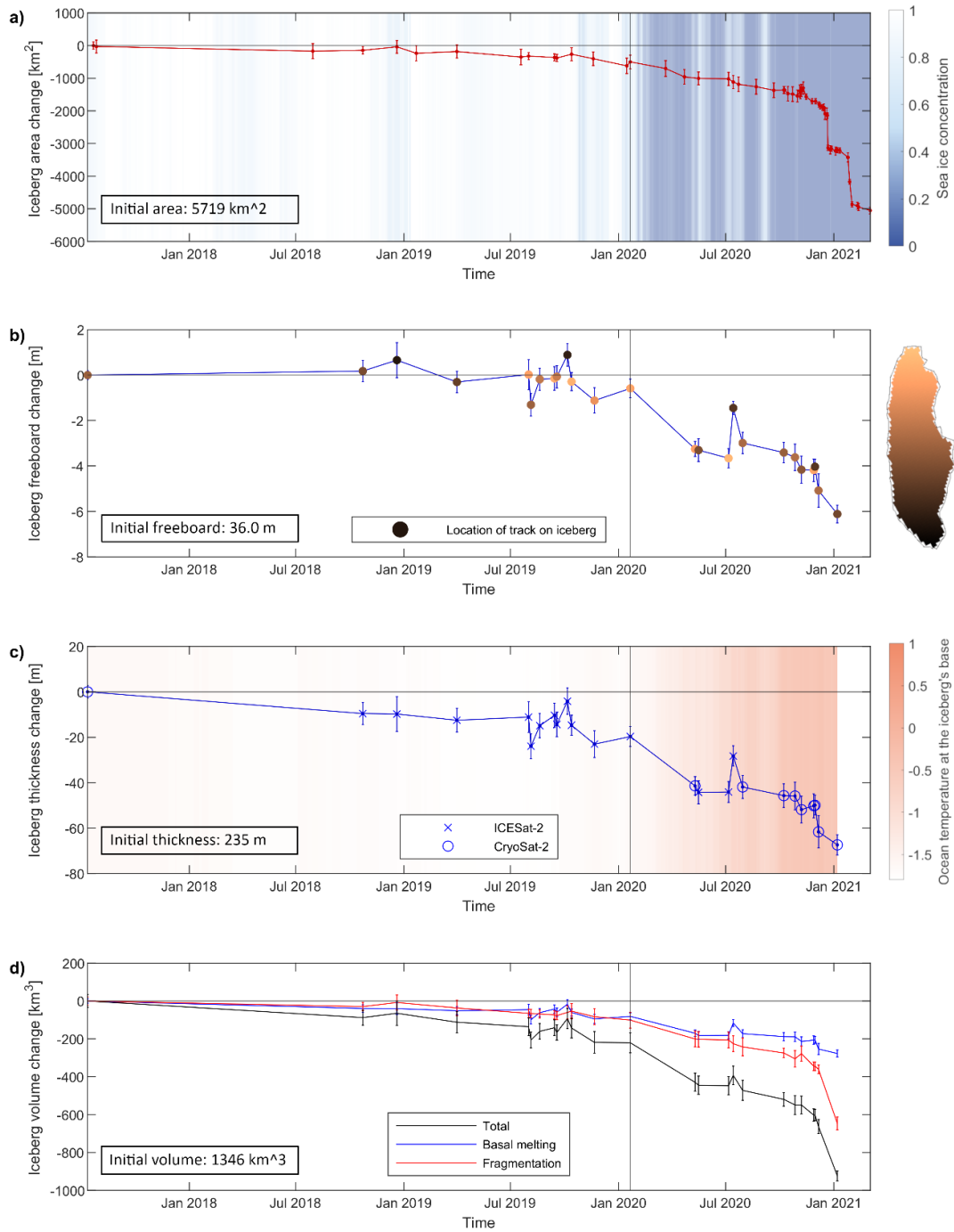


Figure 3.6: Time series of changes in the A68A iceberg area (a), freeboard (b), thickness (c) and volume (d). The vertical line marks 21 January 2020, when the iceberg moved from the Weddell to the Scotia Sea (see Figure 3.1). In panel (a) the background shading indicates sea ice concentration around the iceberg (OSI SAF, 2021) and in panel (c) the background shading indicates ocean temperature at the iceberg's base (Boyer et al., 2018)

The A68A iceberg's initial volume was  $1346 \pm 53 \text{ km}^3$ . After 3.5 years, the volume of the mother iceberg had reduced by  $924 \pm 27 \text{ km}^3$  (Figure 3.6d), which is  $69 \pm 3 \%$  of its initial value. Converted to mass loss this corresponds to  $802 \pm 34 \text{ Gt}$  lost from the mother iceberg. Fragmentation makes

up for  $68 \pm 5$  % of the total mass loss and basal melting accounts for the remaining  $32 \pm 3$  %. While both processes contribute roughly equally in the Weddell Sea and increase as the iceberg drifts northwards, fragmentation becomes the dominant wastage factor as the iceberg falls apart and forms numerous children icebergs in the Northern Scotia Sea (Figure 3.6d, Table 3.1). The total loss through basal melting ( $277 \pm 19$  km<sup>3</sup> or  $254 \pm 17$  Gt) can be considered as a lower estimate of the immediate freshwater flux along the iceberg's trajectory. However, smaller edge wastings will add to this and also larger children icebergs will eventually melt, but not necessarily at the location where they are lost.

**Table 3.1: Annual change in the A68A iceberg area, thickness and volume in different regions along its trajectory.**

Annual loss rate	Weddell Sea	Scotia Sea	Scotia Sea South	Scotia Sea North
Area [km <sup>2</sup> /year]	$-200 \pm 82$	$-2807 \pm 199$	$-1205 \pm 286$	$-7400 \pm 298$
Thickness [m/year]	$-7.8 \pm 2.1$	$-49.5 \pm 6.5$	$-36.4 \pm 9.5$	$-86.9 \pm 27.4$
Volume [km <sup>3</sup> /year]	$-87.3 \pm 21.0$	$-729.4 \pm 50.4$	$-418.3 \pm 75.7$	$-1621.7 \pm 116.0$
..through fragmen- tation	$-44.7 \pm 18.5$	$-538.3 \pm 47.0$	$-244.1 \pm 59.2$	$-1323.0 \pm 90.9$
..through melting	$-42.6 \pm 11.3$	$-191.2 \pm 25.9$	$-174.2 \pm 46.0$	$-298.7 \pm 94.5$

### 3.4. Discussion

Our findings compare well with previous studies of the Larsen-C Ice Shelf and of icebergs that followed similar trajectories. For example, our initial iceberg density of  $868 \text{ kg m}^{-3}$  is consistent with the estimated  $\sim 15$  m firn air content derived from airborne observations (Holland et al., 2011) and our estimates and spatial distribution of initial iceberg thickness and freeboard agree very well with ice drafts derived from the same airborne campaign (Holland et al., 2009) and from in situ measurements collected along the suture zone (Jansen et al., 2013). Lopez-Lopez et al. (2021) estimated the area of A68A between 22 July 2017 and 26 January 2019 using a largely automated approach, and found a decrease of  $\sim 210 \text{ km}^2$ , which is close to our estimate of  $236 \text{ km}^2$  over a similar period (22 July 2017 to 22 January 2019). Scambos et al. (2008) identified three types of breakup for the A22A iceberg, which took a similar path: rift calvings, edge wastings and rapid disintegration. The breakups of A68B and A68C were probably rift calvings along pre-existing fractures; the breakup of numerous children icebergs in the last few months of our survey were rapid disintegration likely caused by surface melting, and edge-wasting and side-melting are likely the reason for the remaining area reductions (Figure 3.6a).

Previous studies have also reported similar rates of iceberg freeboard and thickness change. Scambos et al. (2008) recorded no change in freeboard ( $0 \pm 1.3$  m) for the A22A iceberg over 17 months until it reached the tip of the Antarctic Peninsula and a reduction by  $11.7 \pm 2.3$  m/year during its passage to South Georgia; we find similar rates for A68A of  $0.2 \pm 0.1$  m/year and  $5.7 \pm 0.4$  m/year in the same locations. This comparison also shows that our collocation improves the melt rate accuracy with respect to using tracks that only sample similar parts of the iceberg. Han et al. (2019) estimated the rate of thickness change of A68A to be  $12.89 \pm 3.34$  m/year between February and November 2018 at sparse crossing points of CryoSat-2 ground tracks. Although we do not have measurements for the same period, interpolation of our collocated estimates suggests a value of  $7.0 \pm 0.8$  m which is in reasonable agreement. In the Weddell Sea, Jansen et al. (2007) report melt rates in the range 0 to 12 m per year for the A38B iceberg, in good agreement with our estimate of  $7.8 \pm 2.1$  m/year for A68A. Iceberg melting increases significantly in the Scotia Sea, and our estimate of  $49.5 \pm 6.5$  m/year for A68A is almost identical to the value of  $\sim 48$  m/year found by Jansen et al. (2007) for A38B. Bouhier et al. (2018) recorded melt rates for the B17A iceberg of 68.4 m/year in Scotia Sea South and 180 m/year in the Scotia Sea North. These values are approximately double the melt rates we have calculated for A68A in the same location (Table 3.1). A possible explanation could be that B17A started out with significantly higher freeboard of around 50 m, which means that its draft was exposed to ocean currents at a greater depth, where the water temperature is higher (Boyer et al., 2018). Concerning the contributions of melting and breakage, Tournadre et al. (2015) found that melting contributes only 18 % over the whole life cycle of all large Antarctic icebergs – which is a slightly lower estimate than the 32 % which we find for A68A during our study period. However, previous studies (Bouhier et al., 2018; Scambos et al., 2008) found that fragmentation becomes the dominant factor towards the end, which is also apparent from our data (Figure 3.6d, Table 3.1), and calculating volume loss until e.g. March 2021 (when our area change time series ends) would have likely increased the share of fragmentation.

The very distinct melt rates in the Weddell and Scotia Sea can be explained by the different environmental conditions: First of all, icebergs experience significantly higher water and air temperatures in the Scotia Sea compared to the Weddell Sea (Scambos et al., 2008; see also Figure 3.6c and 3.7b). Based on our four averaged data points, we find high correlation (0.99) between the ocean temperature at the iceberg's base and iceberg thinning rates (Figure 3.7b). Secondly, icebergs drifting freely in the Scotia Sea (Schodlok et al., 2006) are no longer sheltered by sea ice (Figure 3.6a, 3.7a), exposing them to wave erosion at the sides, forming a subsurface 'foot', which leads to calving owing to buoyancy stress (the so-called 'footloose mechanism'; Wagner

et al., 2014). Apart from wave erosion at the waterline, ocean swell also induces strain on the iceberg, which can lead to crevasse and rift propagation (Li et al., 2018). The correlation between sea ice concentration and iceberg fragmentation is lower (-0.71), but still significant (Figure 3.7a). Our observation that the initially southern part of the iceberg seems more stable (Figure 3.6b) could be explained by the fact that this part is thinner (Figure 3.2a and Figure 3.5a) and therefore comes into contact with ocean water of a different temperature or current speed, as these are the two main drivers of iceberg melting (Bigg et al., 1997). In principle the iceberg could also have tilted to adjust its balance after break-offs from the northern part. Interestingly, we observe a notable thickness change in the Weddell Sea, although hardly any freeboard change was observed. This is because freeboard loss associated with basal melting and freeboard gain due to snow accumulation even out and hence a slow basal melting process can only be observed, when a snow layer is included in the calculations (Braakmann-Folgmann et al., 2021).

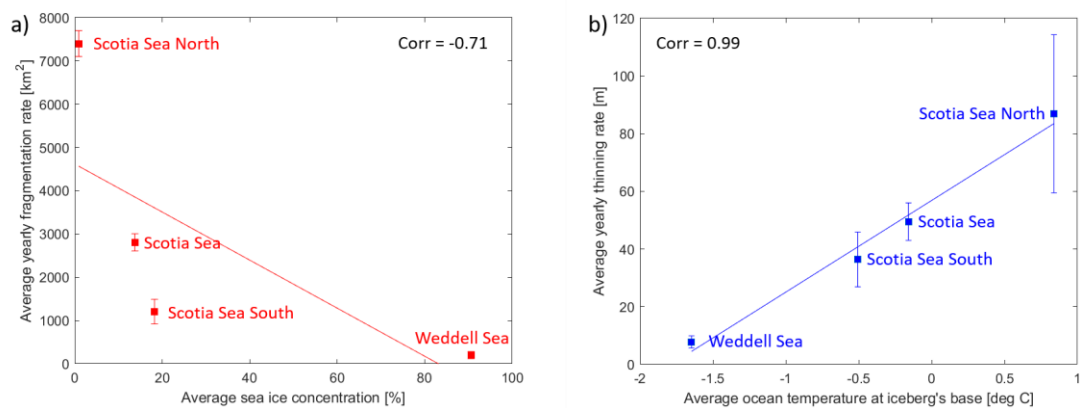


Figure 3.7: Scatter plots linking the iceberg decay processes to the environmental conditions: Fragmentation rate compared to sea ice concentration (a) and thinning rate compared to ocean temperature (b) in different regions along the trajectory

To constrain the intrusion of fresh water and nutrients, it is essential to determine where and by how much icebergs are melting (Silva et al., 2006). While volume loss due to basal melting serves as a lower bound estimate of freshwater and nutrient input, some of the area loss due to sidewall melting and edge-wastings also contribute, but are difficult to quantify in satellite observations. Children icebergs and larger edge-wastings, which form in larger calving events, travel further and take more time to melt (Tournadre et al., 2016). How quickly these melt depends on their size and the surrounding ocean conditions (Rackow et al., 2017; Stern et al., 2016); along the A68A trajectory, for example, melt rates vary from 10 to 100 m/year (Table 3.1) and ocean temperature at the iceberg's base increases from -1.8°C to just over +1°C (Figure 3.6c). Children icebergs of sufficient length will also fragment further (England et al., 2020). And

unlike large tabular icebergs, smaller icebergs with lengths similar to their thickness frequently roll over (Hamley and Budd, 1986). To track the entire freshwater and nutrient input, the trajectories and melting of all fragmented pieces would have to be considered. Furthermore, the amount of bioavailable iron and nutrients delivered by icebergs also depends on the amount of sediments contained in the iceberg (Raiswell et al., 2016).

Despite these unknowns, our observations allow for an initial assessment of A68A's impact on the ecosystem around South Georgia through scouring, melting and blockage. The closest recorded distance to the island was 62 km on 15 December 2020 with a mean draft of  $141 \pm 11$  m. Seafloor bathymetry reveals a couple of shallower features within a distance of 52-65 km to the southern coastline (Figure 3.1), where the iceberg could have grounded and where other icebergs may do so in future. Although A68A did not ground, it likely hit one of these features while turning (Figure 3.1b). The shallowest bathymetry beneath the iceberg locations captured in satellite imagery is 150 m (O. Hogg et al., 2016). Although any scouring on the sea bed destroys the local benthic fauna (Barnes, 2017; Gutt, 2001), A68A's turn will have affected only a small area. As it fragmented into smaller pieces, the risk of blockage to foraging grounds (Kooyman et al., 2007) for the millions of penguins and seals, raising their offspring on South Georgia (Clarke et al., 2012; Joiris et al., 2015), was largely averted. For future icebergs, this scenario is most likely at the western tip of the island, where icebergs of similar draft can approach up to a few kilometers. However, birds, seals and whales that regularly feed in the highly productive waters surrounding South Georgia (Atkinson et al., 2001; Joiris et al., 2015) could also be influenced by the large amount of melt water and nutrients released by icebergs as they drift near to the island, altering the ocean properties and plankton occurrence (Arrigo et al., 2002; Smith et al., 2013; Vernet et al., 2012). Overall, A68A spent at least 96 days (28 November 2020 to 4 March 2021, when our observations end) within 300 km off the coastline. Assuming its children icebergs melted at the same rate of  $0.43 \pm 0.17$  m per day, we estimate that  $152 \pm 61$  Gt of fresh water mixed with nutrients was released during this time. More research should be conducted to study the impact of this alteration on the marine life around South Georgia. As this is a common iceberg trajectory, our results could also help to predict the disintegration of other large tabular icebergs and to include their impact in ocean models (England et al., 2020; Martin and Adcroft, 2010; Rackow et al., 2017).

### 3.5. Conclusions

We have characterized the evolution of the A68A iceberg from its calving off the Larsen-C Ice Shelf in July 2017 to its disintegration close to South Georgia in early-2021. Although the iceberg was tabular, it had significant undulations in topography across its surface. Thus, accurate collocation of the iceberg's orientation is required to derive reliable estimates of its freeboard and thickness change over time from satellite altimetry. We estimate that the average iceberg thickness reduced from  $235 \pm 9$  m at calving to  $168 \pm 10$  m near South Georgia. Combined with observations of its area change determined from satellite imagery, we estimate an initial volume of  $1346 \pm 53$  km<sup>3</sup> and  $802 \pm 34$  Gt of ice loss from the main iceberg in 3.5 years. Around one third ( $254 \pm 17$  Gt) of the mass loss was through basal melting, which provides a lower bound estimate of the direct freshwater input along the iceberg's trajectory. Losses due to side melting and break-offs of smaller pieces will add to the immediate freshwater flux, and larger children icebergs will also contribute as they melt. Near South Georgia we estimate a fresh water input of  $152 \pm 61$  Gt over  $\sim 3$  months, potentially impacting the island's rich ecosystem. We confirm that the distinct environmental conditions in the Weddell and Scotia Sea lead to rapidly increasing rates of melting and fragmentation once icebergs travel north of the Antarctic Peninsula. Our detailed maps of the A68A iceberg thickness change (Braakmann-Folgmann et al., 2022) will be useful for investigations of the impact of this calving event on the stability of the Larsen-C Ice Shelf, and for more detailed studies on the effects of meltwater and nutrients released in the vicinity of South Georgia. As this is a common iceberg trajectory, our results could also help to model the disintegration of other large tabular icebergs that take a similar path and to include their impact in ocean models.

### References

- Arrigo, K.R., Van Dijken, G.L., Ainley, D.G., Fahnestock, M.A., Markus, T., 2002. Ecological impact of a large Antarctic iceberg. *Geophys. Res. Lett.* 29, 8-1-8-4. <https://doi.org/10.1029/2001GL014160>
- Atkinson, A., Whitehouse, M.J., Priddle, J., Cripps, G.C., Ward, P., Brandon, M.A., 2001. South Georgia, Antarctica: A productive, cold water, pelagic ecosystem. *Mar. Ecol. Prog. Ser.* 216, 279–308. <https://doi.org/10.3354/meps216279>
- Barnes, D.K.A., 2017. Iceberg killing fields limit huge potential for benthic blue carbon in Antarctic shallows. *Glob. Chang. Biol.* 23, 2649–2659. <https://doi.org/10.1111/gcb.13523>

### 3. Observing the disintegration of the A68A iceberg from space

---

- Biddle, L.C., Kaiser, J., Heywood, K.J., Thompson, A.F., Jenkins, A., 2015. Ocean glider observations of iceberg-enhanced biological production in the northwestern Weddell Sea. *Geophys. Res. Lett.* 42, 459–465. <https://doi.org/10.1002/2014GL062850>
- Bigg, G.R., Wadley, M.R., Stevens, D.P., Johnson, J.A., 1997. Modelling the dynamics and thermodynamics of icebergs. *cold Reg. Sci. Technol.* 26, 113–135. [https://doi.org/10.1016/S0165-232X\(97\)00012-8](https://doi.org/10.1016/S0165-232X(97)00012-8)
- Bintanja, R., Van Oldenborgh, G.J., Katsman, C.A., 2015. The effect of increased fresh water from Antarctic ice shelves on future trends in Antarctic sea ice. *Ann. Glaciol.* 56, 120–126. <https://doi.org/10.3189/2015AoG69A001>
- Bouhler, N., Tournadre, J., Rémy, F., Gourves-Cousin, R., 2018. Melting and fragmentation laws from the evolution of two large Southern Ocean icebergs estimated from satellite data. *Cryosphere* 12, 2267–2285. <https://doi.org/10.5194/tc-12-2267-2018>
- Boyer, T.P., Garcia, Hernan E. Locarnini, Ricardo A. Zweng, Melissa M. Mishonov, Alexey V. Reagan, James R. Weathers, Katharine A. Baranova, Olga K. Seidov, D., Smolyar, I. V., 2018. *World Ocean Atlas 2018*.
- Braakmann-Folgmann, A., Shepherd, A., Gerrish, L., Izzard, J., Ridout, A., 2022. A68A iceberg thickness maps (Jul 2017-Jan 2021). <https://doi.org/10.17632/26dg4fwkhhb.1>
- Braakmann-Folgmann, A., Shepherd, A., Ridout, A., 2021. Changes in the Area, Thickness, and Volume of the Thwaites ‘B30’ Iceberg Observed by Satellite Altimetry and Imagery. *Cryosph. Discuss.* 1–27.
- Budge, J.S., Long, D.G., 2018. A Comprehensive Database for Antarctic Iceberg Tracking Using Scatterometer Data. *IEEE J. Sel. Top. Appl. Earth Obs. Remote Sens.* 11, 434–442. <https://doi.org/10.1109/JSTARS.2017.2784186>
- Clarke, A., Croxall, J.P., Poncet, S., Martin, A.R., Burton, R., 2012. Important bird areas: South Georgia. *Br. Birds* 105, 118–144.
- Copernicus Climate Change Service, 2018. ERA5 hourly data on single levels from 1979 to present. <https://doi.org/10.24381/cds.adbb2d47>
- Dryak, M.C., Enderlin, E.M., 2020. Analysis of Antarctic Peninsula glacier frontal ablation rates with respect to iceberg melt-inferred variability in ocean conditions. *J. Glaciol.* 66, 457–470. <https://doi.org/10.1017/jog.2020.21>
- Duprat, L.P.A.M., Bigg, G.R., Wilton, D.J., 2016. Enhanced Southern Ocean marine productivity due to fertilization by giant icebergs. *Nat. Geosci.* 9, 219–221. <https://doi.org/10.1038/ngeo2633>

- England, M.R., Wagner, T.J.W., Eisenman, I., 2020. Modeling the breakup of tabular icebergs. *Sci. Adv.* 6, 1–9. <https://doi.org/10.1126/sciadv.abd1273>
- Fichefet, T., Morales Maqueda, M.A., 1999. Modelling the influence of snow accumulation and snow-ice formation on the seasonal cycle of the Antarctic sea-ice cover. *Clim. Dyn.* 15, 251–268. <https://doi.org/10.1007/s003820050280>
- GEBCO Compilation Group, 2019. GEBCO 2019 Grid. <https://doi.org/10.5285/836f016a-33be-6ddc-e053-6c86abc0788e>
- Greene, C.A., Gwyther, D.E., Blankenship, D.D., 2017. Antarctic Mapping Tools for MATLAB. *Comput. Geosci.* 104, 151–157. <https://doi.org/10.1016/j.cageo.2016.08.003>
- Grimm, I., 2021. Assessing effects of iceberg A-68a on the Weddell Sea and South Georgia ecosystems.
- Grosfeld, K., Schröder, M., Fahrbach, E., Gerdes, R., Mackensen, A., 2001. How iceberg calving and grounding change the circulation and hydrography in the Filchner Ice Shelf–Ocean System. *J. Geophys. Res.* 106, 9039–9055.
- Gutt, J., 2001. On the direct impact of ice on marine benthic communities, a review. *Polar Biol.* 24, 553–564. <https://doi.org/10.1007/s003000100262>
- Hamley, T.C., Budd, W.F., 1986. Antarctic Iceberg Distribution and Dissolution. *J. Glaciol.* 32, 242–251. <https://doi.org/10.1017/s0022143000015574>
- Han, H., Lee, S., Kim, J.I., Kim, S.H., Kim, H.C., 2019. Changes in a giant iceberg created from the collapse of the Larsen C Ice Shelf, Antarctic Peninsula, derived from Sentinel-1 and CryoSat-2 data. *Remote Sens.* 11, 1–14. <https://doi.org/10.3390/rs11040404>
- Helly, J.J., Kaufmann, R.S., Stephenson, G.R., Vernet, M., 2011. Cooling, dilution and mixing of ocean water by free-drifting icebergs in the Weddell Sea. *Deep. Res. Part II Top. Stud. Oceanogr.* 58, 1346–1363. <https://doi.org/10.1016/j.dsr2.2010.11.010>
- Hogg, A.E., Gudmundsson, G.H., 2017. Commentary: Impacts of the Larsen-C Ice Shelf calving event. *Nat. Clim. Chang.* 7, 540–542. <https://doi.org/10.1038/nclimate3359>
- Hogg, O., Huvenne, V.A., Griffiths, H.J., Dorschel, B., Linse, K., 2016. A Bathymetric Compilation of South Georgia, 1985–2015. <https://doi.org/10.5285/ce8bf6be-4b5f-454c-9165-73ab4c3baf23>
- Holland, P.R., Corr, H.F.J., Pritchard, H.D., Vaughan, D.G., Arthern, R.J., Jenkins, A., Tedesco, M., 2011. The air content of Larsen Ice Shelf. *Geophys. Res. Lett.* 38, 1–6. <https://doi.org/10.1029/2011GL047245>
- Holland, P.R., Corr, H.F.J., Vaughan, D.G., Jenkins, A., Skvarca, P., 2009. Marine ice in Larsen Ice Shelf. *Geophys. Res. Lett.* 36, 1–6. <https://doi.org/10.1029/2009GL038162>

- International Organization for Standardization, 1998. ISO 4355 Bases for design on structures – Determination of snow loads on roofs.
- Jansen, D., Luckman, A., Cook, A., Bevan, S., Kulesa, B., Hubbard, B., Holland, P.R., 2015. Brief Communication: Newly developing rift in Larsen C Ice Shelf presents significant risk to stability. *Cryosphere* 9, 1223–1227. <https://doi.org/10.5194/tc-9-1223-2015>
- Jansen, D., Luckman, A., Kulesa, B., Holland, P.R., King, E.C., 2013. Marine ice formation in a suture zone on the Larsen C Ice Shelf and its influence on ice shelf dynamics. *J. Geophys. Res. Earth Surf.* 118, 1628–1640. <https://doi.org/10.1002/jgrf.20120>
- Jansen, D., Schodlok, M., Rack, W., 2007. Basal melting of A-38B: A physical model constrained by satellite observations. *Remote Sens. Environ.* 111, 195–203. <https://doi.org/10.1016/j.rse.2007.03.022>
- Jenkins, A., 1999. The impact of melting ice on ocean waters. *J. Phys. Oceanogr.* 29, 2370–2381. [https://doi.org/10.1175/1520-0485\(1999\)029<2370:TIOMIO>2.0.CO;2](https://doi.org/10.1175/1520-0485(1999)029<2370:TIOMIO>2.0.CO;2)
- Joiris, C.R., Humphries, G.R.W., D’Hert, D., Robert, H., Beudels-Jamar, R.C., 2015. Major hotspots detected along the Scotia Ridge in autumn for southern right whales *Eubalaena australis*, Antarctic fur seals *Arctocephalus gazella* and Antarctic prions *Pachyptila desolata*. *Adv. Polar Sci.* 26, 282–291. <https://doi.org/10.13679/j.advps.2015.4.00282>
- Kooyman, G.L., Ainley, D.G., Ballard, G., Ponganis, P.J., 2007. Effects of giant icebergs on two emperor penguin colonies in the Ross Sea, Antarctica. *Antarct. Sci.* 19, 31–38. <https://doi.org/10.1017/S0954102007000065>
- Kurtz, N.T., Markus, T., 2012. Satellite observations of Antarctic sea ice thickness and volume. *J. Geophys. Res. Ocean.* 117, 1–9. <https://doi.org/10.1029/2012JC008141>
- Kwok, R., Cunningham, G.F., 2008. ICESat over Arctic sea ice: Estimation of snow depth and ice thickness. *J. Geophys. Res. Ocean.* 113, 1–17. <https://doi.org/10.1029/2008JC004753>
- Li, Tian, Shokr, M., Liu, Y., Cheng, X., Li, Teng, Wang, F., Hui, F., 2018. Monitoring the tabular icebergs C28A and C28B calved from the Mertz Ice Tongue using radar remote sensing data. *Remote Sens. Environ.* 216, 615–625. <https://doi.org/10.1016/j.rse.2018.07.028>
- Ligtenberg, S.R.M., Helsen, M.M., Van Den Broeke, M.R., 2011. An improved semi-empirical model for the densification of Antarctic firn. *Cryosphere* 5, 809–819. <https://doi.org/10.5194/tc-5-809-2011>
- Lopez-Lopez, L., Parmiggiani, F., Moctezuma-Flores, M., Guerrieri, L., 2021. On the detection and long-term path visualisation of a-68 iceberg. *Remote Sens.* 13, 1–13. <https://doi.org/10.3390/rs13030460>

- Martin, T., Adcroft, A., 2010. Parameterizing the fresh-water flux from land ice to ocean with interactive icebergs in a coupled climate model. *Ocean Model.* 34, 111–124. <https://doi.org/10.1016/j.ocemod.2010.05.001>
- Merino, N., Le Sommer, J., Durand, G., Jourdain, N.C., Madec, G., Mathiot, P., Tournadre, J., 2016. Antarctic icebergs melt over the Southern Ocean : Climatology and impact on sea ice. *Ocean Model.* 104, 99–110. <https://doi.org/10.1016/j.ocemod.2016.05.001>
- Mouginot, J., Rignot, E., Scheuchl, B., 2019. Continent-Wide, Interferometric SAR Phase, Mapping of Antarctic Ice Velocity. *Geophys. Res. Lett.* 46, 9710–9718. <https://doi.org/10.1029/2019GL083826>
- OSI SAF, 2021. AMSR-2 sea ice concentration product of the EUMETSAT Ocean and Sea Ice Satellite Application Facility.
- Rackow, T., Wesche, C., Timmermann, R., Hellmer, H.H., Juricke, S., Jung, T., 2017. A simulation of small to giant Antarctic iceberg evolution: Differential impact on climatology estimates. *J. Geophys. Res. Ocean.* 3170–3190. <https://doi.org/10.1002/2016JC012513>
- Raiswell, R., Hawkings, J.R., Benning, L.G., Baker, A.R., Death, R., Albani, S., Mahowald, N., Krom, M.D., Poulton, S.W., Wadham, J., Tranter, M., 2016. Potentially bioavailable iron delivery by iceberg-hosted sediments and atmospheric dust to the polar oceans. *Biogeosciences* 13, 3887–3900. <https://doi.org/10.5194/bg-13-3887-2016>
- Rignot, E., Casassa, G., Gogineni, P., Krabill, W., Rivera, A., Thomas, R., 2004. Accelerated ice discharge from the Antarctic Peninsula following the collapse of Larsen B ice shelf. *Geophys. Res. Lett.* 31, 2–5. <https://doi.org/10.1029/2004GL020697>
- Rott, H., Skvarca, P., Nagler, T., 1996. Rapid collapse of northern Larsen Ice Shelf, Antarctica. *Science (80-. )*. 271, 788–792. <https://doi.org/10.1126/science.271.5250.788>
- Scambos, T., Ross, R., Bauer, R., Yermolin, Y., Skvarca, P., Long, D., Bohlander, J., Haran, T., 2008. Calving and ice-shelf break-up processes investigated by proxy: Antarctic tabular iceberg evolution during northward drift. *J. Glaciol.* 54, 579–591. <https://doi.org/10.3189/002214308786570836>
- Schodlok, M.P., Hellmer, H.H., Rohardt, G., Fahrbach, E., 2006. Weddell Sea iceberg drift: Five years of observations. *J. Geophys. Res. Ocean.* 111, 1–14. <https://doi.org/10.1029/2004JC002661>
- Shepherd, A., Gilbert, L., Muir, A.S., Konrad, H., McMillan, M., Slater, T., Briggs, K.H., Sundal, A. V., Hogg, A.E., Engdahl, M.E., 2019. Trends in Antarctic Ice Sheet Elevation and Mass. *Geophys. Res. Lett.* 46, 8174–8183. <https://doi.org/10.1029/2019GL082182>

### 3. Observing the disintegration of the A68A iceberg from space

---

- Silva, T.A.M., Bigg, G.R., Nicholls, K.W., 2006. Contribution of giant icebergs to the Southern Ocean freshwater flux. *J. Geophys. Res.* 111, 1–8. <https://doi.org/10.1029/2004JC002843>
- Smith, K.L., Robison, B.H., Helly, J.J., Kaufmann, R.S., Ruhl, H.A., Shaw, T.J., Twining, B.S., Vernet, M., 2007. Free-drifting icebergs: Hot spots of chemical and biological enrichment in the Weddell Sea. *Science* (80-. ). 317, 478–482. <https://doi.org/10.1126/science.1142834>
- Smith, K.L., Sherman, A.D., Shaw, T.J., Sprintall, J., 2013. Icebergs as unique lagrangian ecosystems in polar seas. *Ann. Rev. Mar. Sci.* 5, 269–287. <https://doi.org/10.1146/annurev-marine-121211-172317>
- Stern, A.A., Adcroft, A., Sergienko, O., 2016. The effects of Antarctic iceberg calving-size distribution in a global climate model. *J. Geophys. Res. Ocean.* 1–14. <https://doi.org/10.1002/2016JC011835>
- Storto, A., Oddo, P., Cozzani, E., Coelho, E.F., 2019. Introducing along-track error correlations for altimetry data in a regional ocean prediction system. *J. Atmos. Ocean. Technol.* 36, 1657–1674. <https://doi.org/10.1175/JTECH-D-18-0213.1>
- Tilling, R.L., Ridout, A., Shepherd, A., 2018. Estimating Arctic sea ice thickness and volume using CryoSat-2 radar altimeter data. *Adv. Sp. Res.* 62, 1203–1225. <https://doi.org/10.1016/j.asr.2017.10.051>
- Tournadre, J., Bouhier, N., Girard-Ardhuin, F., Remy, F., 2015. Large icebergs characteristics from altimeter waveforms analysis. *J. Geophys. Res. Ocean.* 120, 2121–2128. <https://doi.org/https://doi.org/10.1002/2014JC010502>
- Tournadre, J., Bouhier, N., Girard-Ardhuin, F., Rémy, F., 2016. Antarctic icebergs distributions 1992–2014. *J. Geophys. Res. Ocean.* 121, 327–349. <https://doi.org/10.1002/2015JC011178>
- Vernet, M., Smith, K.L., Cefarelli, A.O., Helly, J.J., Kaufmann, R.S., Lin, H., Long, D.G., Murray, A.E., Robison, B.H., Ruhl, H.A., Shaw, T.J., Sherman, A.D., Sprintall, J., Stephenson, G.R., Stuart, K.M., Twining, B.S., 2012. Islands of ice: Influence of free-drifting Antarctic icebergs on pelagic marine ecosystems. *Oceanography* 25, 38–39. <https://doi.org/10.5670/oceanog.2012.72>
- Wagner, T.J.W., Wadhams, P., Bates, R., Elosegui, P., Stern, A., Vella, D., Abrahamsen, E.P., Crawford, A., Nicholls, K.W., 2014. The “footloose” mechanism: Iceberg decay from hydrostatic stresses. *Geophys. Res. Lett.* 41, 5522–5529. <https://doi.org/10.1002/2014GL060832>

Wise, M.G., Dowdeswell, J.A., Jakobsson, M., Larter, R.D., 2017. Evidence of marine ice-cliff instability in Pine Island Bay from iceberg-keel plough marks. *Nature* 550, 506–510. <https://doi.org/10.1038/nature24458>

Wu, S.Y., Hou, S., 2017. Impact of icebergs on net primary productivity in the Southern Ocean. *Cryosphere* 11, 707–722. <https://doi.org/10.5194/tc-11-707-2017>

### 3. Observing the disintegration of the A68A iceberg from space

---

# 4

## MAPPING THE EXTENT OF GIANT ANTARCTIC ICEBERGS WITH DEEP LEARNING

**This chapter is based on the following paper with small post-viva additions.**

**Citation:** Braakmann-Folgmann, A., Shepherd, A., Hogg, D., Redmond, E., 2023 . Mapping the extent of giant Antarctic icebergs with Deep Learning. EGU sphere [preprint], <https://doi.org/10.5194/egusphere-2023-858>

**Author contributions:** I designed the study together with my supervisors Andy Shepherd and David Hogg. Ella Redmond clicked most of the iceberg outlines, which are used as training data, during her internship, supervised by me. I also generated some of the outlines. I then designed and implemented the U-net architecture, implemented the comparison methods, plotted the figures and wrote the manuscript. Andy Shepherd and David Hogg supervised the work and suggested edits to the manuscript.

### Abstract

Icebergs release cold, fresh meltwater and terrigenous nutrients as they drift and melt, influencing the local ocean properties and encouraging sea ice formation and biological production. To locate and quantify the fresh water flux from Antarctic icebergs, changes in their area and thickness have to be monitored along their trajectories. While the locations of large icebergs are tracked operationally by manual inspection, delineation of their extent is not. Here, we propose a U-net approach to automatically map the extent of giant icebergs in Sentinel-1 imagery. This greatly improves the efficiency compared to manual delineations, reducing the time for each outline from several minutes to less than 0.01 sec. We evaluate the performance of our U-net and two state-of-the-art segmentation algorithms on 191 images. For icebergs, larger than covered by the training data, we find that U-net tends to miss parts. Otherwise, U-net is more robust to scenes with complex backgrounds, ignoring sea ice, smaller patches of nearby coast or other icebergs and outperforms the other two techniques achieving an  $F_1$  score of 0.84 and an absolute median deviation in iceberg area of 4.1 %.

### 4.1. Introduction

Icebergs influence the environment along their trajectory through the release of cold fresh water mixed with terrigenous nutrients (Duprat et al., 2016; Helly et al., 2011; Jenkins, 1999; Merino et al., 2016; Smith et al., 2007; Vernet et al., 2012). The more they melt, the higher the impact. However, this melting is not linear, but depends on the surrounding ocean temperature, current speed and many other variables that are hard to model or observe (Bigg et al., 1997; Bouhier et al., 2018; England et al., 2020; Jansen et al., 2007; Silva et al., 2006). Calculating fresh water input from satellite observations is possible and can partially be automated, but requires manual delineations of the iceberg outlines to calculate changes in iceberg area and to collocate altimetry tracks with a map of initial iceberg thickness to estimate basal melting (Braakmann-Folgmann et al., 2022, 2021). Here, we present an automated approach using a U-net (Ronneberger et al., 2015) to segment giant Antarctic icebergs in Sentinel-1 images and hence to derive their outline and area.

A number of methods have been proposed to automatically detect and segment icebergs in satellite radar imagery. Early work by Willis et al. (1996) was based on a simple thresholding technique and limited to certain iceberg sizes of a few hundred meters and certain wind conditions. Later, the Constant False Alarm Rate (CFAR) thresholding technique has been applied to detect icebergs in the Arctic (Frost et al., 2016; Gill, 2001; Power et al., 2001). Wesche and

Dierking (2012) also used a threshold based on a K-distribution fitted to observed backscatter coefficients of icebergs, sea ice and open ocean followed by morphological operations. Mazur et al. (2017) developed an algorithm for iceberg detection in the Weddell Sea based on thresholds for brightness, shape, size, etc. at five scale levels applied to ENVISAT ASAR data. Apart from thresholding, edge-detection techniques have been applied: Williams et al. (1999) used a standard edge-detection technique followed by pixel bonding (Sephton et al., 1994) applied to ERS-1 images during austral winter to detect and segment icebergs in East Antarctica. Silva and Bigg (2005) extended this to ENVISAT images and improved the algorithm by using a slightly more sophisticated edge detection technique followed by a watershed segmentation and a classification step that takes area and shape into consideration, but also requires manual interventions. Collares et al. (2018) use the k-means algorithm (Macqueen, 1967) to segment icebergs, which are then manually tracked. Koo et al. (2021) employ a built-in segmentation technique similar to k-means using Google Earth Engine to segment Sentinel-1 images and then apply an incidence angle-dependent brightness threshold to find icebergs. Calculating the similarity of the distance to centroid histograms of all detected icebergs, they then track one specific giant iceberg (B43). The most elaborate algorithm has been proposed by Barbat et al. (2019) using a graph-based segmentation and Ensemble Forest Committee classification algorithm with a range of hand-crafted features.

Despite the quantity and variety of previous approaches, a range of limitations has so far hindered the operational application of an automated iceberg segmentation algorithm. Overall, previous studies have focused on smaller icebergs and perform worse for larger ones or are not even applicable there (Mazur et al., 2017; Wesche and Dierking, 2012; Willis et al., 1996). Our work extends previous studies with the goal is to delineate specific giant icebergs. Giant icebergs make up a very small part of the total iceberg population, but hold the majority of the total ice volume (Tournadre et al., 2016), which makes them the most relevant for freshwater fluxes. Apart from iceberg size, there are many remaining challenges, resulting from the variable appearance of icebergs as well as the surrounding ocean or sea ice in SAR imagery (Ulaby and Long., 2014). Some of the existing techniques are therefore limited to austral winter images and still require manual intervention (Silva and Bigg, 2005; Williams et al., 1999). Dark icebergs remain a problem for all existing methods using SAR images. Many studies also report degrading accuracies in high wind conditions (Frost et al., 2016; Mazur et al., 2017; Willis et al., 1996). Deformed sea ice or sea ice in general is also mentioned to lead to false detections (Koo et al., 2021; Mazur et al., 2017; Silva and Bigg, 2005; Wesche and Dierking, 2012; Willis et al., 1996). And finally clusters of several bergs and berg fragments too close to each other have been found

to pose a problem (Barbat et al., 2019a; Frost et al., 2016; Koo et al., 2021; Williams et al., 1999). Our work aims to delineate icebergs in a variety of environmental conditions as accurately as possible using a deep learning technique.

Deep neural networks can encode the most meaningful features themselves and are able to learn more complex non-linear relationships. They therefore outperform classic machine learning techniques in most tasks (LeCun et al., 2015; Schmidhuber, 2015). U-net is a neural network that was originally developed for biomedical image segmentation (Ronneberger et al., 2015). It has since been applied to many other domains including satellite images and polar science (Andersson et al., 2021; Baumhoer et al., 2019; Dirscherl et al., 2021; Mohajerani et al., 2021, 2019; Poliyapram et al., 2019; Singh et al., 2020; Stokholm et al., 2022; Surawy-Stepney et al., 2023; Zhang et al., 2019). U-net works well with few training examples, trains quickly and still achieves very good results (Ronneberger et al., 2015). A comparison between three network architectures (DeepLab, DenseNet and U-net) for river ice segmentation found that U-net provided the best balance between quantitative performance and good generalization (Singh et al., 2020). Baumhoer et al. (2019) used a U-net architecture to automatically delineate ice shelf fronts in Sentinel-1 images with good success (108 m average deviation). As the calving front to ocean boundary looks very similar to an iceberg to ocean boundary and both goals have to deal with comparable problems like near-by sea ice and varying appearance of the ice, ocean and sea ice surfaces, we decided to also employ a U-net.

## 4.2. Data and methods

This section describes the Sentinel-1 input data, generation of the manually derived outlines for training, validation and testing, the implementation of two standard segmentation methods and our U-net architecture. The goal is to derive the outlines of Antarctic icebergs, which are large enough to receive a name and to be tracked operationally. Therefore, we aim to generate a binary segmentation map, where the biggest iceberg present is selected and everything else – including smaller icebergs, iceberg fragments and adjacent land ice – is considered as background. This approach differs from most previous work, where the goal has been to find all icebergs and is targeted to monitor changes in area of these large bergs, but also to track how the icebergs rotate and to use their outline to automatically collocate altimetry overpasses (Braakmann-Folgmann et al., 2022).

### 4.2.1. Sentinel-1 input imagery

The Sentinel-1 satellites measure the backscatter of the surface beneath them using Synthetic Aperture Radar (SAR). In contrast to optical imagery, SAR provides data throughout the polar night and independent of cloud cover (Ulaby and Long., 2014), which is frequent over the Southern Ocean. The Sentinel satellites are an operational satellite system with free data availability (Torres et al., 2012). Sentinel-1a (2014-present) and Sentinel-1b (2016-2022) had a combined repeat cycle of 6 days (Torres et al., 2012), but the polar regions are sampled more frequently. We use the Level 1 Ground Range Detected (GRD) data. Depending on the geographic location around Antarctica, data are collected in either interferometric wide (IW) or extra wide (EW) swath mode. IW is a 250 km wide swath with 5 x 20 m native spatial resolution and EW is a 400 km wide swath with 20 x 40 m native resolution. We use both modes depending on availability. While HH (horizontal transmit and horizontal receive) polarised data are available across the Southern Ocean, HV (horizontal transmit and vertical receive) data are only available in some parts. As icebergs drift across these acquisition masks and HH has been found to give the best results for iceberg detection (Sandven et al., 2007), we use the HH polarised data only. Should both modes become available across the Southern Ocean in the future, their collective use might be advantageous as icebergs and their surrounding cause different changes in polarisation, which could be exploited using e.g. the HH/HV ratio.

We pre-process and crop the Sentinel-1 images before applying the segmentation techniques. First, we apply the precise orbit file, remove thermal noise and apply a radiometric calibration. We also multilook the data with a factor of six to reduce speckle and image size, yielding a spatial resolution of 240 m. Then we apply a terrain correction using the GETASSE30 (Global Earth Topography And Sea Surface Elevation at 30 arc second resolution) digital elevation model and project the output on a polar stereographic map with true latitude of 71°S. These pre-processing steps are conducted in the Sentinel Application Platform (SNAP). All icebergs that are longer than 18.5 km (10 nautical miles) or that encompass an area of at least 68.6 km<sup>2</sup> (20 square nautical miles) are named and tracked operationally every week by the National Ice Center (NIC). Also slightly smaller icebergs (longer than 6 km) are tracked by the Brigham Young University (Budge and Long, 2018), who release daily positions every few years. Therefore, we have a good estimate of where each of these giant icebergs should be and cannot only download targeted Sentinel-1 images containing these icebergs, but also crop the images around the estimated central position to a size of 256 x 256 pixels. Hence, every input image contains a giant target iceberg. Some images contain several icebergs and in this case, we are only interested in the largest one. To ensure that the largest bergs fit within the image, we rescale images of icebergs

#### 4. Mapping the extent of giant Antarctic icebergs with Deep Learning

with a major axis longer than 37 km (20 nautical miles). As the NIC also provides estimates of the semi major axes lengths, we apply the rescaling based on this. The rescaled images have a pixel resolution of 480 m instead. For all input images, we scale the backscatter between the 1<sup>st</sup> and 99<sup>th</sup> percentile to enhance the contrast. In this step, we also replace pixels outside the satellite scene coverage with ones, and create a mask to discard the same pixels from the predictions.

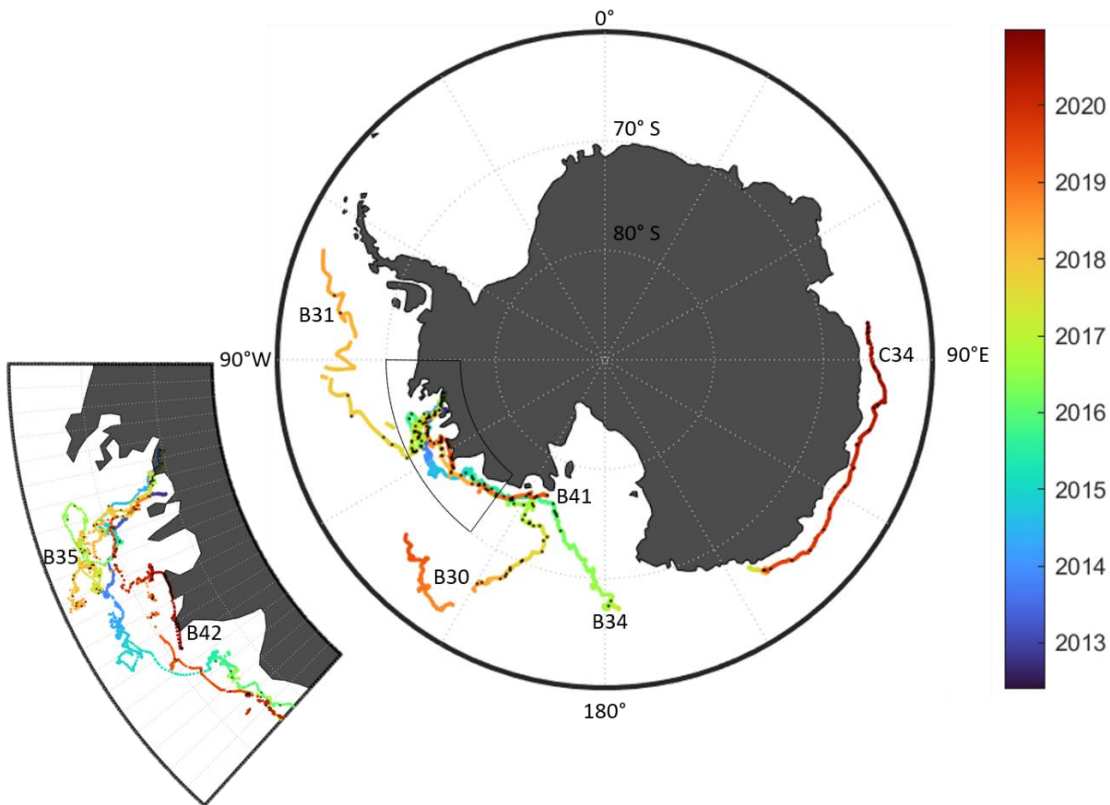


Figure 4.1: Spatial and temporal coverage of our dataset: The trajectories (by Budge and Long, 2018) of the seven selected icebergs are colour-coded according to time and black squares indicate the locations of the images used in this study.

The overall dataset consists of 191 images, showing seven giant icebergs: B30, B31, B34, B35, B41, B42 and C34. These are between 54 and 1052 km<sup>2</sup> in size. B30 is the only iceberg that is initially longer than 37 km, so we rescale the first 27 images, until its length drops below 37 km. A further two images of this iceberg are then used at normal resolution. Spatially, we cover different parts of the Southern Ocean including the Pacific and Indian Ocean side with a focus on the Amundsen Sea (see Figure 4.1). Temporally, our images span the years 2014-2020 and are scattered across all seasons. For each iceberg, the individual images are roughly one month apart. Far higher temporal sampling would be possible in terms of satellite image availability, but we aim to cover a wide range of environmental conditions, seasons and iceberg shapes and

sizes. As these are highly correlated in subsequent images, we decided to use only one image per month.

#### 4.2.2. Grouping of input images according to environmental conditions

The appearance of icebergs versus the surrounding ocean or sea ice depends on their roughness, the dielectric properties (e.g. moisture of the ice) and the angle of satellite overpass (Figure 4.2). While calm ocean appears as a dark surface in SAR images, wind roughened sea appears brighter depending on the relative wind direction versus the satellite viewing angle (Young et al., 1998). Thin sea ice has a similar backscatter to calm sea (Young et al., 1998), but rougher first-year ice already exhibits higher backscatter and multi-year ice can reach backscatter values overlapping with the range of typical iceberg backscatter (Drinkwater, 1998). Icebergs with dry, compact snow are usually bright targets in SAR images (Mazur et al., 2017; Wesche and Dierking, 2012; Young et al., 1998). However, surface thawing can reduce the iceberg backscatter significantly (Young and Hyland, 1997), meaning that those icebergs have the same or lower backscatter than the surrounding ocean and sea ice, and appear as dark objects (Wesche and Dierking, 2012; see our Figure 4.2, last column). Furthermore, giant tabular icebergs can exhibit a gradient (Barbat et al., 2019b) due to variations in backscatter with the viewing angle (Wesche and Dierking, 2012) or appear heterogeneous due to crevasses, (see Figure 4.2, third and last column), which also complicates segmentation and differentiation from the surrounding ocean and sea ice.

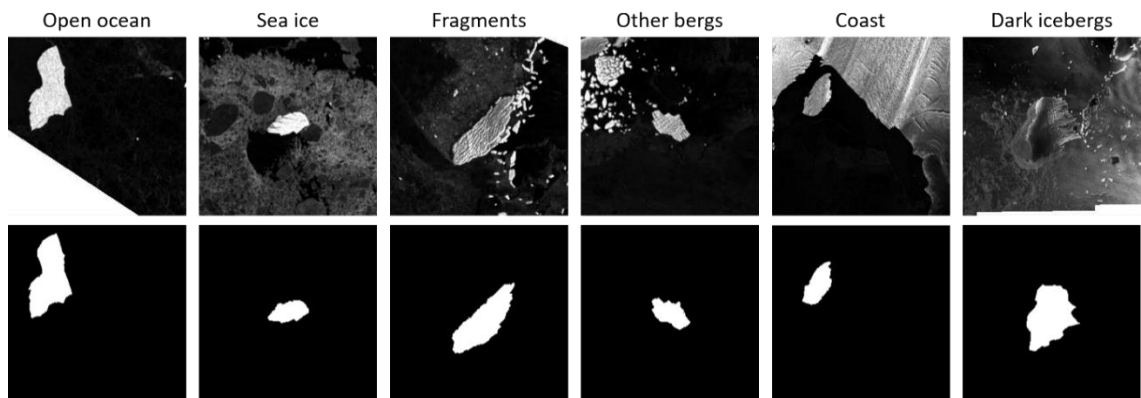


Figure 4.2: Examples of input images (top row) and segmentation maps based on manually derived delineations (bottom row) in different environmental conditions. From left to right these are B31 in open ocean, B41 surrounded by sea ice, B42 with nearby fragments, C34 and another similar sized iceberg, B41 close to the coast and B30 appearing dark.

We visually group all input images into different categories to assess the performance in different potentially challenging conditions. These groups are *open ocean*, *sea ice*, *fragments*, *other bergs*, *coast* and *dark icebergs* (Figure 4.2 shows one example each). We class an image as *dark iceberg*, if the iceberg appears as dark or does not stand out from the background, because both

have a similar intensity of grey, making it hard to pick out the berg (Wesche and Dierking, 2012). Images that contain *coast* (i.e. nearby ice shelves or glaciers on the Antarctic continent) are grouped into this category. Due to very similar physical conditions, ice-shelves and icebergs are hard to differentiate. In some cases, several giant icebergs drift very close to each other and both are (partially) visible in our cropped images. If another berg of similar size is present, the algorithms might pick the wrong berg and therefore we introduce one group of *other bergs*. There is also one case where a bigger iceberg is partially visible, but we are aiming to segment the largest berg that is fully visible (e.g. Figure 4.4h). *Fragments* occur frequently in the vicinity of icebergs, as icebergs regularly calve smaller bits and pieces around their edges. We assign images to this category if the fragments pose a challenge because they are so close to the iceberg, that they are easily grouped together (Koo et al., 2021). The last challenge is *sea ice*. Young and flat sea ice usually appears homogenous and dark and does not pose a problem. However, older, ridged sea ice and other cases where the background appears grey rather than black with significant structure (Mazur et al., 2017) are grouped into this category. If the sea ice is not visually apparent (i.e. young and flat) and the background appears as dark and relatively homogenous or only contains fragments that are further away from the iceberg and hence there is no obvious challenge apparent to us, we class these images as *open ocean*. If several challenges are present (e.g. if *coast* and *sea ice* are visible), we assign the image to the most relevant group.

### 4.2.3. Manual delineation of iceberg perimeters

Although the goal is to develop an automated segmentation technique, we require manual delineations of iceberg extent for training and evaluation. We manually click the iceberg perimeter in GIS software to yield a polygon. The accuracy of such manual delineations is estimated to be 2-4 % of the iceberg area (Bouhier et al., 2018; Braakmann-Folgmann et al., 2022, 2021). We then create a binary map of the same size as the input image, where pixels within the manually derived polygon are defined as iceberg and everything else as background to allow a rapid evaluation of performance. Some examples of input images and their corresponding segmentation maps based on the manual outlines are shown in Figure 4.2. We regard the manually derived outlines as the most accurate and use these binary maps to train our neural network and to evaluate all automated segmentation techniques. When the area deviation of our automated segmentation techniques drops below 2-4 %, their prediction might be more accurate than the manual delineation. In any case, automated approaches are advantageous over manual delineations – especially when rolled out for numerous icebergs or in operational applications, as each outline takes several minutes to click manually.

#### 4.2.4. Iceberg segmentation with k-means and Otsu

We implement two standard segmentation techniques as a baseline: Otsu thresholding and k-means. In both cases, we mask out the areas that had no satellite scene coverage by setting them to zero (black). For the first segmentation technique, we smooth the input image with a 5x5 Gaussian kernel. Then we apply the Otsu threshold (Otsu, 1979) yielding a binary image. The Otsu threshold is determined automatically based on the image's greyscale histogram so that the within-class variance is minimised. To find an iceberg, we apply connected component analysis to the binary image and select the largest component. We also experimented with other thresholding techniques including adaptive mean and adaptive Gaussian thresholding, but found that the Otsu threshold gave the best results. Although different thresholding techniques have been proposed for iceberg detection (Frost et al., 2016; Mazur et al., 2017; Power et al., 2001; Wesche and Dierking, 2012; Willis et al., 1996), to our knowledge none of them have used the Otsu method. The second technique is k-means (Macqueen, 1967) with  $k=2$ . We use random centre initialisation and run the algorithm for 20 iterations. We repeat this 50 times with different initialisations and take the result with the best compactness. Afterwards, we also perform a connected component analysis and select the largest one. Both our standard segmentation techniques are implemented using the OpenCV library (Bradski, 2000) for Python. K-means and a variation of it have also been applied to track selected icebergs by Collares et al. (2018) and Koo et al. (2021) respectively.

#### 4.2.5. Iceberg segmentation with U-net

We suggest a U-net architecture to segment Sentinel-1 input images into the largest iceberg and background, which is based on the original U-net (Ronneberger et al., 2015) with some modifications. The input images are 256 x 256 one-channel backscatter images (as described in Section 4.2.1 and shown in Figure 4.2). The U-net is composed of an encoder that produces a compressed representation of the input image followed by a decoder that constructs a segmentation map from the compressed encoding with the same spatial resolution as the input (Figure 4.3). The encoder uses a number of convolutional layers and downsampling to generate feature maps at increasing levels of abstraction and spatial scale. The decoder uses further convolutional layers and upsampling to construct the required segmentation map. Cross-links convey feature maps from different spatial scales in the encoder to the respective decoder stage, where they are combined with contextual feature maps from the decoder layer below. This allows U-net to produce accurate segmentations whilst also considering contextual features. We use same padding in the convolutions and pooling operations, so that the feature maps remain the same size

at each level. We also use depth-wise separable convolutions (Chollet, 2017), which are more efficient. Furthermore, we added dropout of 0.3 in between the two convolutions per level to avoid over-fitting (Srivastava et al., 2014) and residual connections to aid the learning process and increase the accuracy (He et al., 2016). The outputs are one-channel 256 x 256 greyscale images, representing the probability that each pixel belongs to the iceberg class. During training these greyscale output maps are compared with the segmentation maps from our manually derived outlines to alter the network parameters accordingly. When evaluating the validation and test data output, we convert the greyscale probability map to a binary output, where 1 corresponds to the iceberg class and 0 to background (everything else), by thresholding it at 0.5. We find that the exact threshold has very little impact, as thresholds between 0.1-0.8 reduce the  $F_1$  score by only 0.02 or less. The optimal threshold is 0.3-0.5. As we are only interested in the largest iceberg and would like to discard other smaller icebergs and iceberg fragments around, we also apply a connected component analysis and select the largest one (Figure 4.3).

We train and evaluate the network using cross-validation. This means that we train seven different neural networks and always retain the images of one iceberg for testing as an independent dataset. The exact number of test images varies, as we have between 15 and 46 images per iceberg (Table 4.2). Although the images are roughly one month apart and cover a wide range of seasons and surroundings overall (e.g. near the calving front, surrounded by sea ice and within open ocean), we find that consecutive images of the same iceberg are often similar – both concerning iceberg shape, size and appearance as well as the surrounding. Therefore, we do not mix training and test data. On the other hand, and for the same reason, we find that it stabilises the training process, if we draw training and validation data from the same set of icebergs. 24 images are taken as validation data, which is used to set the best performing hyperparameters (i.e. network architecture, number of layers, optimizer, learning rate, loss function and batch size). It also determines when we stop the learning process to avoid overfitting. Depending on which iceberg was picked for testing, this leaves between 121-152 images for training. We also tried to augment the data by flipping the training images vertically and horizontally, leading to a tripling of the training data, but we found slightly degraded performance ( $F_1$  score for the B42 iceberg used as test data reduces from 0.88 to 0.79). We believe that this is because consecutive images already show a similar iceberg shape and size in similar conditions, but with varying rotation and translation through the natural drift. Therefore, in this case data augmentation does not help but rather lead to overfitting. We train the network end-to-end using a binary cross entropy loss function and a batch size of one. Higher batch sizes had little impact on the performance and run time. The Adam optimizer (Kingma and Ba, 2015) is employed with an initial

#### 4. Mapping the extent of giant Antarctic icebergs with Deep Learning

learning rate of 0.001. The learning rate is halved when the validation loss has not decreased for eight consecutive epochs. Training is stopped when the validation loss has not improved for twenty epochs. In practice, this means that the networks are trained for 57-193 epochs. The implementation is done in Python using Keras (Chollet and Others, 2015). Training takes up to 20 minutes on a Tesla P100 GPU with 25 GB RAM (Google Colab Pro). The prediction for 24 images takes 0.2 seconds.

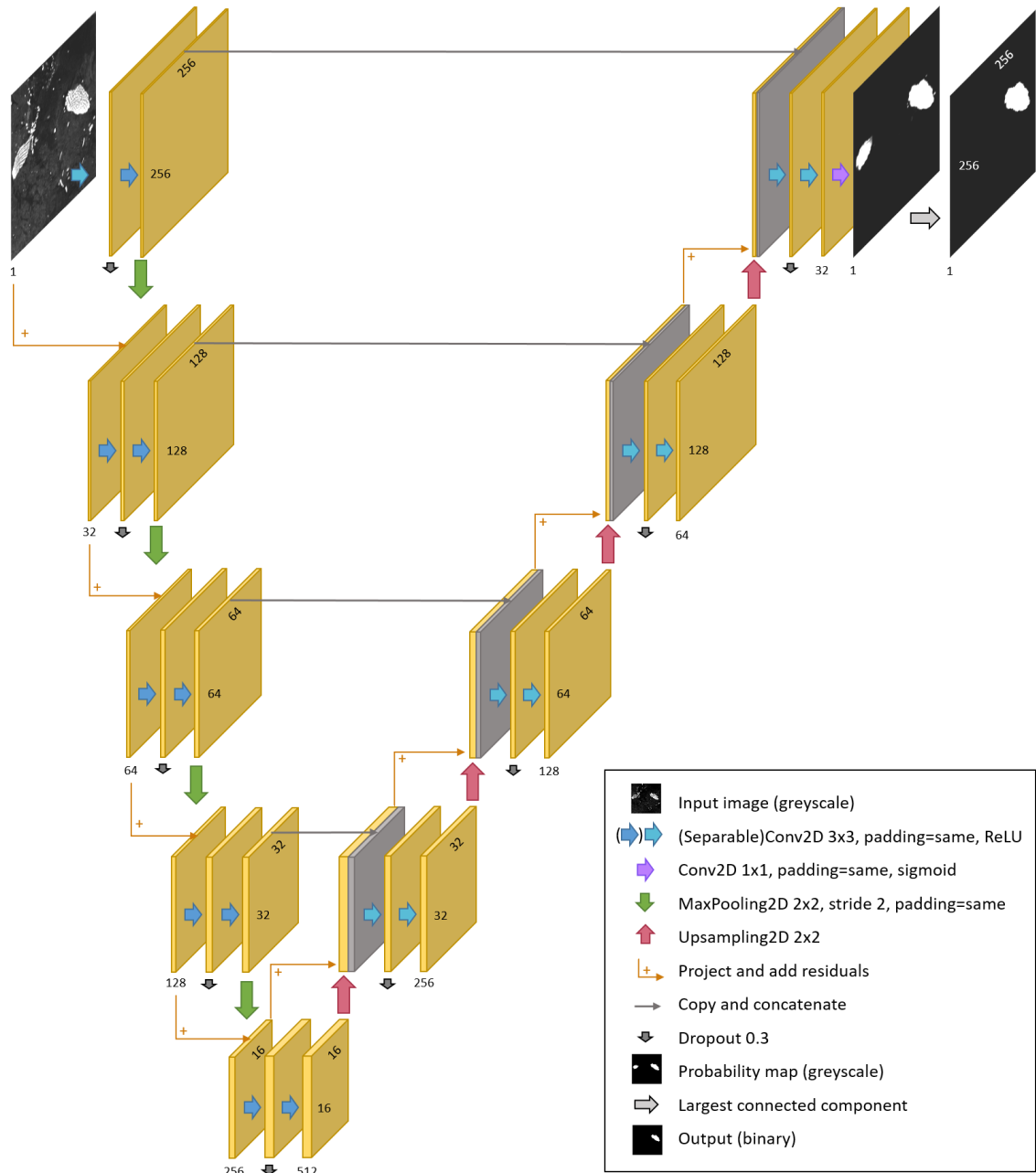


Figure 4.3: Modified U-net architecture as used in this paper

### 4.3. Results and discussion

In this section, we present and discuss the results from the three different approaches (U-net, Otsu and k-means). After an overall analysis, we assess the performance for each iceberg and evaluate the impact of iceberg size and different challenging environments. Finally, we compare our results to previous studies.

#### 4.3.1. Performance of the three methods

We evaluate the performance of the three methods compared to the manual delineations using a range of metrics. True positives (TP) are all correctly classified iceberg pixels and true negatives (TN) are all correctly classified background pixels. False positives (FP) are pixels that were classified as iceberg, but belong to the background according to manual delineations and false negatives (FN) are iceberg pixels in the manually derived segmentation map, which the algorithm has missed and erroneously classified as background. These are the basis for most evaluation metrics including the overall accuracy, the  $F_1$  score (also known as dice coefficient), misses (also known as false negative rate) and false alarms (also known as false positive rate). The detection rate is equal to the iceberg class accuracy and can be derived from 1-misses; hence, we do not list it separately. In the case of a large class imbalance, the  $F_1$  score is much more meaningful than the overall accuracy. The iceberg class makes up only 5 % of all pixels, so we focus on the  $F_1$  score, but list the overall accuracy for completeness. Except the  $F_1$  score, all measures are given in percent. In addition to these metrics commonly used to evaluate segmentation algorithms, we also examine the accuracy of the resulting area estimates  $a_i$ . We calculate the mean absolute error (MAE) in area, the mean error (area bias) and the median absolute deviation (MAD) in area. We focus on the MAD, as it is robust to a few complete failures. However, some previous studies have reported the MAE in area, but most have reported the area bias, so we also list these for completeness. Areas  $a_i$  and  $\alpha_i$  are calculated as the sum of all iceberg pixels in the prediction and manually derived segmentation map respectively multiplied by the pixel area. All area deviations are relative deviations and given in percent compared to the iceberg area in the manually derived segmentation map. We also calculate the standard deviation for each metric. Only the MAD is given with the 25 % and 75 % quantiles instead.

$$F_1 = \frac{2 TP}{2TP+FN+FP} \quad (1)$$

$$\text{Overall accuracy} = \frac{TN+TP}{TN+TP+FN+FP} \quad (2)$$

$$\text{Misses} = \frac{FN}{FN+TP} \quad (3)$$

$$\text{False alarms} = \frac{FP}{FP+TN} \quad (4)$$

$$\text{MAE} = \frac{1}{n} \sum_{i=1}^n \frac{|a_i - \alpha_i|}{\alpha_i} \quad (5)$$

$$\text{Area bias} = \frac{1}{n} \sum_{i=1}^n \frac{a_i - \alpha_i}{\alpha_i} \quad (6)$$

$$\text{MAD} = \text{median} \left( \frac{|a_i - \alpha_i|}{\alpha_i} \right) \quad (7)$$

Comparing the performance of all three techniques, we find that U-net outperforms Otsu and k-means in most metrics. It achieves a significantly higher  $F_1$  score (0.84 compared to 0.62, Table 4.1) and generates a lot less false alarms (0.4 % instead of 4.7 and 5.2 %). On the other hand, both standard segmentation methods have fewer misses than U-net (9 % and 13 % compared to 21 %). On this metric Otsu scores best. In terms of iceberg area, the predictions by U-net are much closer to the manually derived outlines in terms of MAE and bias. Otsu and k-means clearly suffer from a few total failures with over 100 % deviation, which bias these metrics in their cases. The MAD, which is less sensitive to such outliers, is similar for the three methods, with Otsu scoring best (3.6 %), followed by U-net (4.1 %) and k-means (5.1 %). The 25 %-quantiles are very similar for all three methods (2.0, 2.1 and 2.2 % respectively). On the 75 %-quantiles, U-net achieves slightly better results (12.1 % area deviation, compared to 13.8 % and 14.9 % for k-means and Otsu). This means that 75 % of all U-net predictions deviate from the manually derived area by 12.1 % or less. Overall, U-net scores better in most categories, but tends to miss parts and misclassify iceberg as background.

Table 4.1: Performance metrics with standard deviations of U-net, Otsu and k-means across all test data sets (191 images). The median absolute area deviation (MAD) is given with 25 % and 75 % quantiles instead of standard deviation. Except the  $F_1$  score, all measures are percentages. Arrows indicate whether high (up) or low (down) numbers are desirable. The best score per metric is highlighted in bold.

	$F_1$ score $\uparrow$	Overall accuracy [%] $\uparrow$	Misses [%] $\downarrow$	False Alarms [%] $\downarrow$	MAE in area [%] $\downarrow$	Area bias [%] $\downarrow$	MAD in area [%] $\downarrow$
<b>U-net</b>	<b>0.84 <math>\pm</math> 0.30</b>	<b>99 <math>\pm</math> 2</b>	21 $\pm$ 32	<b>0.4 <math>\pm</math> 0.3</b>	<b>15 <math>\pm</math> 26</b>	<b>-5 <math>\pm</math> 29</b>	4.1 [2.1 – <b>12.1</b> ]
<b>Otsu</b>	0.62 $\pm$ 0.34	95 $\pm$ 13	<b>9 <math>\pm</math> 28</b>	5.2 $\pm$ 0.3	170 $\pm$ 490	170 $\pm$ 490	<b>3.6</b> [ <b>2.0</b> - 14.9]
<b>k-means</b>	0.62 $\pm$ 0.33	95 $\pm$ 12	13 $\pm$ 28	4.7 $\pm$ 0.3	150 $\pm$ 460	150 $\pm$ 460	5.1 [2.2 – 13.8]

### 4.3.2. Impact of iceberg size and different environmental conditions

Next, we evaluate how U-net performs for each of the seven different giant icebergs (Table 4.2, shaded in grey), to assess the impact of the chosen test data set and different iceberg sizes. Here, we find that B34 gives the best results. The dataset for this iceberg is the smallest (15 images), meaning that there are more images left for training and the background is usually not

too challenging. B41 gives the lowest  $F_1$  score. This dataset is the largest one, containing 46 images, and hence leaves the least images for training. Furthermore, B41 stays very close to its calving position for a while, which means that the first 13 images contain a significant amount of coast – often directly next to the iceberg (see Figure 4.2 and Figure 4.4j). In these cases all techniques pick the coast rather than the iceberg (see following sections). The highest MAD and miss rate occur for iceberg B31. Because the images of B30 – our largest berg – are resized, this means that B31 appears largest in the images. Therefore, we believe that the large size of the berg, which U-net has not seen in the training data, cause U-net to miss parts of the iceberg (e.g. Figure 4.4b, f). In general, we find quite variable performance depending on which iceberg is retained as test data. This is because the same challenges (e.g. iceberg size, shape, surrounding) occur in subsequent images of the same iceberg, even when they are one month apart. It is also the reason why we decided to evaluate the methods using cross-validation, as this makes the analysis less sensitive to the choice of a single iceberg as test data.

Table 4.2: Performance of the three methods for each test data set (iceberg). The number of images per iceberg and their minimum and maximum size is also given. Note that most images of B30 are rescaled, so it appears smaller in the images. Except the  $F_1$  score, all measures are percentages. Arrows indicate whether high (up) or low (down) numbers are desirable. The best score per iceberg and metric are highlighted in bold.

		$F_1$ score $\uparrow$	Misses [%] $\downarrow$	False Alarms [%] $\downarrow$	MAD in area [%] $\downarrow$
<b>B30</b> 29 images 463-1052 km <sup>2</sup>	U-net	<b>0.90</b>	15	<b>0.3</b>	3.3
	Otsu	0.77	<b>9</b>	3.2	2.7
	k-means	0.79	12	2.4	<b>2.4</b>
<b>B31</b> 32 images 79-518 km <sup>2</sup>	U-net	0.79	34	<b>0.2</b>	13.6
	Otsu	0.91	<b>5</b>	1.6	3.0
	k-means	<b>0.93</b>	6	1.0	<b>1.9</b>
<b>B34</b> 15 images 97-241 km <sup>2</sup>	U-net	<b>0.97</b>	2	<b>0.2</b>	2.1
	Otsu	0.83	<b>1</b>	1.7	<b>1.2</b>
	k-means	0.80	8	1.6	8.3
<b>B35</b> 21 images 62-158 km <sup>2</sup>	U-net	<b>0.94</b>	<b>2</b>	<b>0.3</b>	6.9
	Otsu	0.66	9	2.3	7.4
	k-means	0.63	10	2.5	<b>4.0</b>
<b>B41</b> 46 images 54-116 km <sup>2</sup>	U-net	<b>0.68</b>	33	<b>0.7</b>	<b>3.5</b>
	Otsu	0.27	13	10.5	3.8
	k-means	0.29	<b>11</b>	10.1	5.6
<b>B42</b> 24 images 142-235 km <sup>2</sup>	U-net	<b>0.88</b>	13	<b>0.6</b>	<b>5.4</b>
	Otsu	0.84	<b>6</b>	1.7	8.9
	k-means	0.76	28	1.0	18.7
<b>C34</b> 24 images 61-101 km <sup>2</sup>	U-net	<b>0.81</b>	<b>20</b>	<b>0.4</b>	<b>3.7</b>
	Otsu	0.20	36	10.1	4.3
	k-means	0.23	32	9.1	5.2

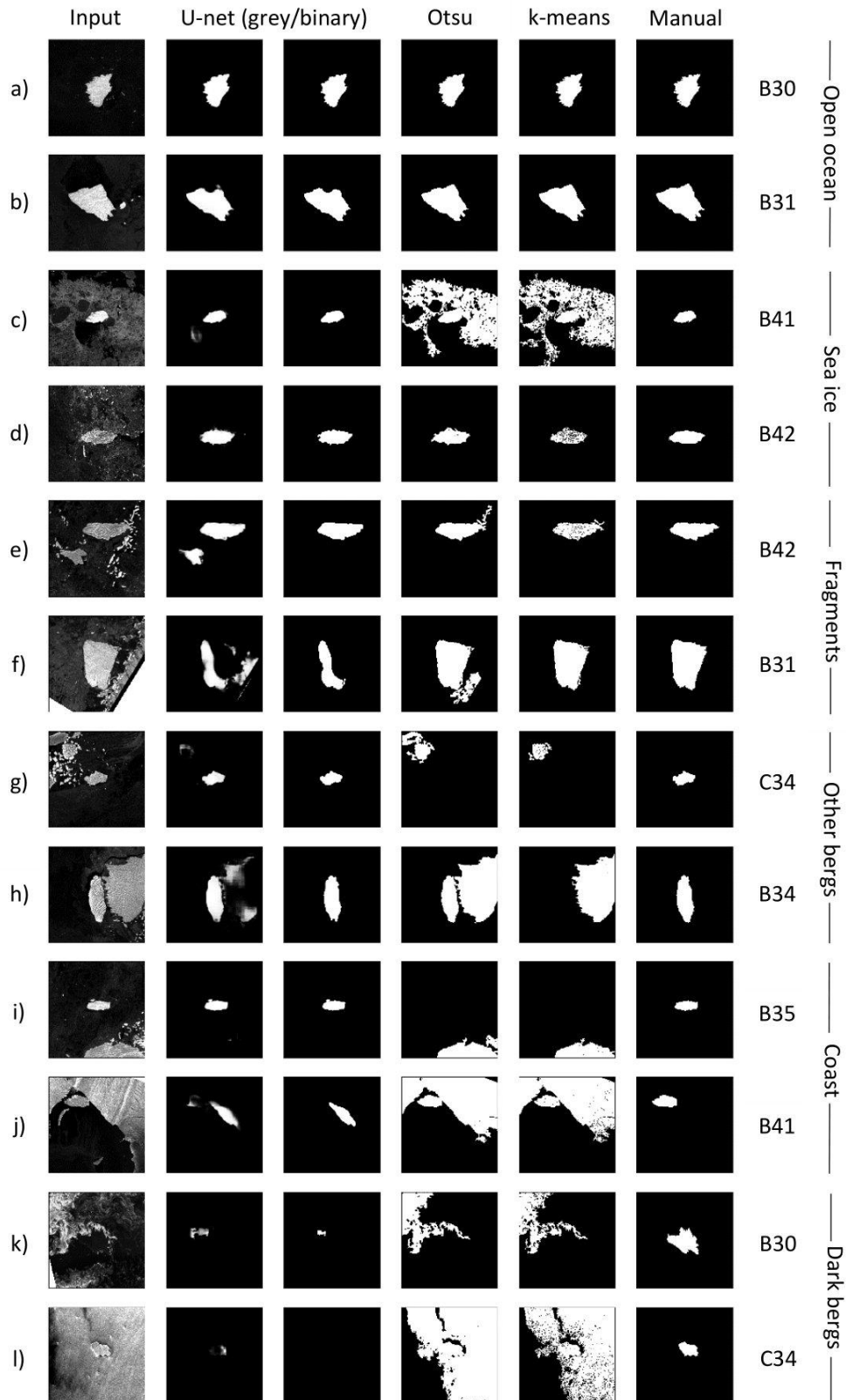


Figure 4.4: Examples of input images (first column) and segmentation maps generated by U-net (second and third column showing the probability map and final segmentation map respectively), Otsu (fourth column), k-means (fifth column), and from manual delineations (last column). We picked these images for illustration to cover each category of environmental conditions twice and to include all icebergs (labelled on the right).

Also for Otsu and k-means the performance varies a lot depending on which iceberg is chosen as test data. The  $F_1$  scores for Otsu range from 0.20 – 0.91, being lowest for C34 and highest for B31. Similarly, k-means also reaches the lowest  $F_1$  score of 0.23 for C34 and the highest for B31 of 0.93. Compared to that, U-net is more consistent reaching  $F_1$  scores between 0.68 – 0.97, but still exhibits significant variability. The fact that Otsu and k-means score so well for B31, also indicates that this data set is not hard per se. We rather suspect that we are challenging U-net too much when the iceberg in the test data is bigger than any iceberg in the training data. Neural networks are known to struggle with a domain-shift, where the test data are from a shifted version of the training data distribution and even more with out-of-domain samples from outside the training data distribution (Gawlikowski et al., 2021). Both are caused by insufficient training data, not or barely covering these examples. Therefore, we recommend expanding the training data, before applying U-net operationally or to icebergs larger than covered by the current training data set. In contrast, iceberg B41, where U-net reaches the lowest  $F_1$  score, poses an even greater problem to the other algorithms, meaning that this dataset is actually challenging. Finally, we observe that U-net achieves the lowest false alarm rate on each iceberg. Otsu generates most false alarms (highest rate for six out of seven icebergs), but also achieves the lowest miss rate for four out of seven icebergs. Except for B31, U-net consistently achieves the highest  $F_1$  score. In terms of MAD in area, k-means and U-net score best on three out of the seven icebergs each.

Grouping the images according to the surrounding environmental conditions (see Section 4.2.2) allows us to judge how well each method can deal with the respective challenge (Figure 4.4, Table 4.3). Open ocean makes up most of the images (46 %) and all methods perform very well with  $F_1$  scores of 0.93-0.95 and MAD in area of 2.4-3.2 %. The Otsu threshold performs best, but the differences between the methods are very small. The two sample images (Figure 4.4a, b) also illustrate that the only problem in this category is rather that U-net generally tends to miss parts of B31 than open ocean in itself posing a problem.

Sea ice occurs in 14 % of our images and overall U-net achieves the best  $F_1$  score (0.88 compared to 0.72 and 0.74), but the Otsu threshold gives a slightly better MAD in area (4.3 % rather than 4.8 % and 5.4 %). Visually, the U-net predictions seem to be the most robust, as sea ice is discarded reliably. In contrast, the two other methods sometimes connect patches of sea ice to the iceberg (Figure 4.4c), but also work fine in other cases (Figure 4.4d).

Iceberg fragments drifting in the direct proximity of the target iceberg were found in 24 % of our images. Overall, k-means scores best in this category with a MAD of 5.7 % compared to 5.9 %

and 6.9 %. In terms of  $F_1$  score, Otsu and k-means both reach 0.94, whereas U-net only reaches 0.85. Visually, there are a few instances where Otsu connects more fragments to the iceberg than k-means and U-net (Figure 4.4e, f). This might be due to the Gaussian smoothing that we apply before the thresholding. We do not apply this step before k-means, and find that k-means tends to rather oversegment images, leaving small holes in the inside (Figure 4.4d, e). In the case of fragments, however, this turns out to be beneficial, as it allows k-means to reliably separate fragments from icebergs, even when they are very close by. The problem for U-net does not seem to be the actual fragments itself, as it rarely connects any fragments to the iceberg (Figure 4.4e, f). However, the images containing fragments are mostly from the large B31 and B42 icebergs, where U-net struggles due to their large extent. This can also be seen from the fact that U-net and k-means both generate only 0.4 % false alarms (fragments erroneously connected to the iceberg), but U-net has a much higher miss rate.

In 3 % of all images, another similar sized or bigger berg is (partially) visible. U-net scores best in all categories with a large margin, yielding an  $F_1$  score of 0.96 compared to 0.12 and 0.11 and MAD in area of 5.9 % compared to 11 % and 110 %. Also visually, it becomes clear that U-net reliably picks the target iceberg and discards any other ice, while Otsu and k-means often pick the wrong berg or connect both with each other (Figure 4.4g, h). Considering iceberg shape and size in a tracking scenario could help mitigate this phenomenon, though (Barbat et al., 2021; Collares et al., 2018; Koo et al., 2021).

Coast is present in 8 % of all images and U-net outperforms the other techniques, but also struggles in some cases. The  $F_1$  score is 0.34 for U-net and 0.12 and 0.11 for Otsu and k-means respectively. While U-net achieves a MAD of 18 %, the other methods yield over 1000 % each. Figure 4.4j illustrates what is happening in these cases: If too much coast is present, all algorithms pick the coast rather than the iceberg (and this is much larger than the iceberg, hence 1000 % deviation). However, U-net discards smaller parts of the coast around the image edges (Figure 4.4i). This is on the one hand because of the sliding convolution window and on the other hand, because U-net learns that the iceberg is usually in the centre (as we crop the images around the estimated position from operational iceberg tracking databases). Hence, U-net is able to correctly pick out the iceberg if not too much coast is present. For the same reason, it is easier for U-net to discard other bergs at the image edges. Interestingly, even when a lot of coast is present, U-net does not pick the full coast, but predicts either nothing or a small – almost iceberg shaped – part of the coast (Figure 4.4j). This could indicate that U-net even learns that only ice that is fully surrounded by water is an iceberg. A possible strategy to avoid misclassifications due to large amounts of coast would be the inclusion of a land mask (Barbat et al., 2019;

#### 4. Mapping the extent of giant Antarctic icebergs with Deep Learning

Collares et al., 2018; Frost et al., 2016; Mazur et al., 2017; Silva and Bigg, 2005). However, ice shelves and glaciers advance and retreat regularly and especially the calving of icebergs themselves significantly alters the land mask. Thus, just after calving, the iceberg itself would be within the former land mask and could not be picked up.

The last category of dark icebergs is the hardest and makes up 5 % of the overall data set. In these cases, all methods fail with  $F_1$  scores of 0.11-0.12 and the lowest MAD in area of 96 %. Again, it is interesting that U-net predicts either very small patches or nothing at all in these cases (Figure 4.4k, l), while the other two methods segment large areas of brighter looking ocean. Potentially, U-net could learn to segment dark icebergs with a lot more training examples, but we only had ten such images in our overall data set. Finally, we would like to stress that the occurrence of these different environmental conditions will vary and our data set is not necessarily representative of all icebergs. We also find that the influence of iceberg size and environmental conditions cannot always be disentangled, as subsequent images of the same iceberg are often similar and the different environmental conditions are not spread equally across the different test data sets (individual icebergs).

Table 4.3: Performance of the three methods in different environmental conditions. The first column also indicates how often these conditions occur in our data set. Except the  $F_1$  score, all measures are percentages. Arrows indicate whether high (up) or low (down) numbers are desirable. The best values per category and metric are highlighted in bold.

		$F_1$ score $\uparrow$	Misses [%] $\downarrow$	False Alarms [%] $\downarrow$	MAD in area [%] $\downarrow$
<b>Open ocean</b> (46 %)	U-net	0.93	11	<b>0.1</b>	2.8
	Otsu	<b>0.95</b>	<b>2</b>	0.4	<b>2.4</b>
	k-means	<b>0.95</b>	4	0.3	3.2
<b>Sea ice</b> (14 %)	U-net	<b>0.88</b>	14	<b>0.3</b>	4.8
	Otsu	0.72	<b>3</b>	2.4	<b>4.3</b>
	k-means	0.74	11	1.7	5.4
<b>Fragments</b> (24 %)	U-net	0.85	21	<b>0.4</b>	6.9
	Otsu	<b>0.94</b>	<b>2</b>	0.7	5.9
	k-means	<b>0.94</b>	7	<b>0.4</b>	<b>5.7</b>
<b>Other bergs</b> (3 %)	U-net	<b>0.96</b>	<b>6</b>	<b>0.0</b>	<b>5.9</b>
	Otsu	0.18	66	7.7	110
	k-means	0.10	86	5.7	11
<b>Coast</b> (8 %)	U-net	<b>0.34</b>	68	<b>1.8</b>	<b>18</b>
	Otsu	0.12	<b>38</b>	29.5	1200
	k-means	0.11	44	28.6	1200
<b>Dark bergs</b> (5 %)	U-net	<b>0.12</b>	92	<b>1.1</b>	<b>96</b>
	Otsu	<b>0.12</b>	<b>54</b>	34.3	450
	k-means	0.11	62	30.5	460

### 4.3.3. Comparison to previous studies

Previous studies state different accuracy measures and due to the slightly different goal to detect all icebergs in a scene rather than finding one giant iceberg and accurately predicting its outline and area, they are not straightforward to compare. Two studies employ the k-means algorithm (Collares et al., 2018) or a variation of it (Koo et al., 2021), so we have indirectly compared U-net to them. None of them report any of our accuracy measures, though. Many of the previous approaches rely on some form of thresholding (Frost et al., 2016; Gill, 2001; Mazur et al., 2017; Power et al., 2001; Wesche and Dierking, 2012; Willis et al., 1996). We somehow covered these methods by comparing U-net to the Otsu threshold, but the exact approaches vary and none of them have applied the Otsu threshold. Two of the threshold-based methods report estimates for their area deviations. Wesche and Dierking (2012) state that iceberg area was overestimated by  $10 \pm 21$  % with their approach. In a following study, they find that for the correctly detected icebergs 13.3 % of the total area was missing (Wesche and Dierking, 2015), meaning a bias in the opposite direction. Mazur et al. (2017) find positive and negative area deviations of  $\pm 25$  % on average. For edge-detection based algorithms, Williams et al. (1999) find an overestimation of iceberg area by 20 % and Silva and Bigg (2005)'s approach yields an underestimation of iceberg area by 10-13 %. These are biases again and both approaches are limited to winter images. For U-net, we find a bias of  $-5.0 \pm 29.1$  %, which is lower than previous studies, but comes with a relatively high standard deviation due to some complete failures where the iceberg is not found at all. Previous studies only compare iceberg areas where icebergs were detected successfully. Barbat et al. (2019) report the lowest false positive (2.3 %) and false negative (3.3 %) rates, and the highest overall accuracy (97.5 %) of all previous studies. While their false negative rate is lower than our false negative rate (21 %), U-net achieves a lower false positive rate of 0.4 % and higher overall accuracy of 99 %. In a second study, Barbat et al. (2021) also analyse the area deviation of the detected icebergs and find average area deviations of  $10 \pm 4$  %, which is also the best score reported so far. They only consider correctly detected icebergs in this metric, though. We find a MAE of  $15 \pm 26$  % for U-net, which is slightly higher, but contains images where the iceberg was not found at all. These cases are not included in Barbat et al. (2021)'s estimates. Our MAD, which is less sensitive to such outliers, is 4.1 %, with 25 % and 75 % quantiles of 2.1 % and 12.1 %. These metrics compare favourably to all previous studies. We also demonstrate in our study, that the performance varies depending on the chosen test data set and therefore, all measures and comparisons can only give an indication of the real performance. Judging from the data we have and comparing our results on this to previous studies as good as possible, U-net proves to be a very promising approach.

Qualitatively, previous studies have found degraded accuracies in challenging environmental conditions or excluded these from their datasets. Some studies report false detections due to sea ice (Koo et al., 2021; Mazur et al., 2017; Wesche and Dierking, 2012) or only applied their algorithm to sea-ice free conditions (Willis et al., 1996). Moreover, several previous studies have also encountered problems with clusters of several bergs and berg fragments too close to each other (Barbat et al., 2019b; Frost et al., 2016; Koo et al., 2021; Williams et al., 1999). Also U-net shows slightly degraded performance in these situations (4.8 and 6.9 % MAD in area compared to 2.8 % in open ocean and  $F_1$  scores of 0.88 and 0.85 compared to 0.93), but still achieves satisfying results in most of these cases. The challenge of other big bergs does not occur in previous studies, since they were looking for all icebergs anyway. In terms of coast, many previous studies have employed a land mask (e.g. Barbat et al., 2019; Collares et al., 2018; Frost et al., 2016; Mazur et al., 2017; Silva and Bigg, 2005), but might miss newly calved bergs due to that. Finally, the problem of dark icebergs has been described in several papers (Mazur et al., 2017; Wesche and Dierking, 2012; Williams et al., 1999), but was rarely mentioned in the evaluation. This is likely because most previous studies use visual inspection to identify misses and false alarms (e.g. Barbat et al., 2019; Frost et al., 2016; Mazur et al., 2017; Wesche and Dierking, 2012; Williams et al., 1999). However, dark icebergs are hard to spot in SAR images even for humans, so they might be missed by the visual inspection, too, unless in our case we know that there must be an iceberg of a certain size and shape that we are looking for. Others limit their method to winter images, when dark icebergs do not occur (Silva and Bigg, 2005; Williams et al., 1999; Young et al., 1998).

### 4.4. Conclusions

We have developed a novel algorithm to segment giant Antarctic icebergs in Sentinel-1 images automatically. It is the first study to apply a deep neural network for iceberg segmentation. Furthermore, it is also the first study specifically targeting giant icebergs. Comparing U-net to two state-of-the-art segmentation techniques (Otsu thresholding and k-means), we find that U-net outperforms them in most metrics. Across all 191 images, U-net achieves an  $F_1$  score of 0.84 and a median absolute area deviation of 4.1 %. Only the miss rate of Otsu and k-means is lower than for U-net, as we find that U-net overlooks parts of the largest iceberg in our dataset. We believe that this issue could be resolved with a larger training data set. U-net can reliably handle a variety of challenging environmental conditions including sea ice, nearby iceberg fragments, other bergs and small patches of nearby coast. It fails when too much coast is visible and when icebergs appear dark, though. In these cases, all existing algorithms fail, but such obvious errors

could easily be picked out in a tracking scenario. Also compared to previous studies, we regard our results as promising. For an operational application, on the short-term further post-processing could be implemented to filter outliers, but on the long run, we would suggest to enlarge the training data set.

## References

- Andersson, T.R., Hosking, J.S., Pérez-Ortiz, M., Paige, B., Elliott, A., Russell, C., Law, S., Jones, D.C., Wilkinson, J., Phillips, T., Byrne, J., Tietsche, S., Sarojini, B.B., Blanchard-Wrigglesworth, E., Aksenov, Y., Downie, R., Shuckburgh, E., 2021. Seasonal Arctic sea ice forecasting with probabilistic deep learning. *Nat. Commun.* 12, 1–12. <https://doi.org/10.1038/s41467-021-25257-4>
- Barbat, M.M., Rackow, T., Hellmer, H.H., Wesche, C., Mata, M.M., 2019a. Three Years of Near-Coastal Antarctic Iceberg Distribution From a Machine Learning Approach Applied to SAR Imagery. *J. Geophys. Res. Ocean.* 124, 6658–6672. <https://doi.org/10.1029/2019JC015205>
- Barbat, M.M., Rackow, T., Wesche, C., Hellmer, H.H., Mata, M.M., 2021. Automated iceberg tracking with a machine learning approach applied to SAR imagery : A Weddell sea case study. *ISPRS J. Photogramm. Remote Sens.* 172, 189–206. <https://doi.org/10.1016/j.isprsjprs.2020.12.006>
- Barbat, M.M., Wesche, C., Werhli, A. V., Mata, M.M., 2019b. An adaptive machine learning approach to improve automatic iceberg detection from SAR images. *ISPRS J. Photogramm. Remote Sens.* 156, 247–259. <https://doi.org/10.1016/j.isprsjprs.2019.08.015>
- Baumhoer, C.A., Dietz, A.J., Kneisel, C., Kuenzer, C., 2019. Automated extraction of antarctic glacier and ice shelf fronts from Sentinel-1 imagery using deep learning. *Remote Sens.* 11, 1–22. <https://doi.org/10.3390/rs11212529>
- Bigg, G.R., Wadley, M.R., Stevens, D.P., Johnson, J.A., 1997. Modelling the dynamics and thermodynamics of icebergs. *cold Reg. Sci. Technol.* 26, 113–135. [https://doi.org/10.1016/S0165-232X\(97\)00012-8](https://doi.org/10.1016/S0165-232X(97)00012-8)
- Bouhier, N., Tournadre, J., Rémy, F., Gourves-Cousin, R., 2018. Melting and fragmentation laws from the evolution of two large Southern Ocean icebergs estimated from satellite data. *Cryosphere* 12, 2267–2285. <https://doi.org/10.5194/tc-12-2267-2018>
- Braakmann-Folgmann, A., Shepherd, A., Gerrish, L., Izzard, J., Ridout, A., 2022. Observing the disintegration of the A68A iceberg from space. *Remote Sens. Environ.* 270, 112855. <https://doi.org/10.1016/j.rse.2021.112855>

#### 4. Mapping the extent of giant Antarctic icebergs with Deep Learning

---

- Braakmann-Folgmann, A., Shepherd, A., Ridout, A., 2021. Tracking changes in the area, thickness, and volume of the Thwaites tabular iceberg “B30” using satellite altimetry and imagery. *Cryosphere* 15, 3861–3876. <https://doi.org/10.5194/tc-15-3861-2021>
- Bradski, G., 2000. The OpenCV Library. Dr. Dobb’s J. Softw. Tools.
- Budge, J.S., Long, D.G., 2018. A Comprehensive Database for Antarctic Iceberg Tracking Using Scatterometer Data. *IEEE J. Sel. Top. Appl. Earth Obs. Remote Sens.* 11, 434–442. <https://doi.org/10.1109/JSTARS.2017.2784186>
- Chollet, F., 2017. Xception: Deep learning with depthwise separable convolutions. *Proc. - 30th IEEE Conf. Comput. Vis. Pattern Recognition, CVPR 2017* 1800–1807. <https://doi.org/10.1109/CVPR.2017.195>
- Chollet, F., Others, &, 2015. Keras.
- Collares, L.L., Mata, M.M., Kerr, R., Arigony-Neto, J., Barbat, M.M., 2018. Iceberg drift and ocean circulation in the northwestern Weddell Sea, Antarctica. *Deep. Res. Part II Top. Stud. Oceanogr.* 149, 10–24. <https://doi.org/10.1016/j.dsr2.2018.02.014>
- Dirscherl, M., Dietz, A.J., Kneisel, C., Kuenzer, C., 2021. A novel method for automated supraglacial lake mapping in antarctica using sentinel-1 sar imagery and deep learning. *Remote Sens.* 13, 1–27. <https://doi.org/10.3390/rs13020197>
- Drinkwater, M.R., 1998. Satellite Microwave Radar Observations of Antarctic Sea Ice. *Anal. SAR Data Polar Ocean.* 145–187. [https://doi.org/10.1007/978-3-642-60282-5\\_8](https://doi.org/10.1007/978-3-642-60282-5_8)
- Duprat, L.P.A.M., Bigg, G.R., Wilton, D.J., 2016. Enhanced Southern Ocean marine productivity due to fertilization by giant icebergs. *Nat. Geosci.* 9, 219–221. <https://doi.org/10.1038/ngeo2633>
- England, M.R., Wagner, T.J.W., Eisenman, I., 2020. Modeling the breakup of tabular icebergs. *Sci. Adv.* 6, 1–9. <https://doi.org/10.1126/sciadv.abd1273>
- Frost, A., Ressel, R., Lehner, S., 2016. Automated iceberg detection using high resolution X - band SAR images. *Can. J. Remote Sens.* 42. <https://doi.org/https://doi.org/10.1080/07038992.2016.1177451>
- Gawlikowski, J., Tassi, C.R.N., Ali, M., Lee, J., Humt, M., Feng, J., Kruspe, A., Triebel, R., Jung, P., Roscher, R., Shahzad, M., Yang, W., Bamler, R., Zhu, X.X., 2021. A Survey of Uncertainty in Deep Neural Networks 1–41.
- Gill, R.S., 2001. Operational detection of sea ice edges and icebergs using SAR. *Can. J. Remote Sens.* 27, 411–432. <https://doi.org/10.1080/07038992.2001.10854884>
- Greene, C.A., Gwyther, D.E., Blankenship, D.D., 2017. Antarctic Mapping Tools for MATLAB. *Comput. Geosci.* 104, 151–157. <https://doi.org/10.1016/j.cageo.2016.08.003>

- He, K., Zhang, X., Ren, S., Sun, J., 2016. Deep residual learning for image recognition. *Proc. IEEE Comput. Soc. Conf. Comput. Vis. Pattern Recognit.* 2016-Decem, 770–778. <https://doi.org/10.1109/CVPR.2016.90>
- Helly, J.J., Kaufmann, R.S., Stephenson, G.R., Vernet, M., 2011. Cooling, dilution and mixing of ocean water by free-drifting icebergs in the Weddell Sea. *Deep. Res. Part II Top. Stud. Oceanogr.* 58, 1346–1363. <https://doi.org/10.1016/j.dsr2.2010.11.010>
- Jansen, D., Schodlok, M., Rack, W., 2007. Basal melting of A-38B: A physical model constrained by satellite observations. *Remote Sens. Environ.* 111, 195–203. <https://doi.org/10.1016/j.rse.2007.03.022>
- Jenkins, A., 1999. The impact of melting ice on ocean waters. *J. Phys. Oceanogr.* 29, 2370–2381. [https://doi.org/10.1175/1520-0485\(1999\)029<2370:TIOMIO>2.0.CO;2](https://doi.org/10.1175/1520-0485(1999)029<2370:TIOMIO>2.0.CO;2)
- Kingma, D.P., Ba, J.L., 2015. Adam: A method for stochastic optimization. 3rd Int. Conf. Learn. Represent. ICLR 2015 - Conf. Track Proc. 1–15.
- Koo, Y., Xie, H., Ackley, S.F., Mestas-Nunez, A.M., Macdonald, G.J., Hyun, C.-U., 2021. Semi-automated tracking of iceberg B43 using Sentinel-1 SAR images via Google Earth Engine. *Cryosph.* 15, 4727–4744. <https://doi.org/https://doi.org/10.5194/tc-15-4727-2021>
- LeCun, Y., Bengio, Y., Hinton, G., 2015. Deep learning. *Nature* 521, 436–444. <https://doi.org/10.1038/nature14539>
- Macqueen, J., 1967. SOME METHODS FOR CLASSIFICATION AND ANALYSIS OF MULTIVARIATE OBSERVATIONS, in: *Proceedings of the Fifth Berkeley Symposium on Mathematical Statistics and Probability*. California: University of California Press., pp. 281–297.
- Mazur, A.K., Wählín, A.K., Krężel, A., 2017. An object-based SAR image iceberg detection algorithm applied to the Amundsen Sea. *Remote Sens. Environ.* 189, 67–83. <https://doi.org/10.1016/j.rse.2016.11.013>
- Merino, N., Le Sommer, J., Durand, G., Jourdain, N.C., Madec, G., Mathiot, P., Tournadre, J., 2016. Antarctic icebergs melt over the Southern Ocean : Climatology and impact on sea ice. *Ocean Model.* 104, 99–110. <https://doi.org/10.1016/j.ocemod.2016.05.001>
- Mohajerani, Y., Jeong, S., Scheuchl, B., Velicogna, I., Rignot, E., Milillo, P., 2021. Automatic delineation of glacier grounding lines in differential interferometric synthetic-aperture radar data using deep learning. *Sci. Rep.* 11, 1–10. <https://doi.org/10.1038/s41598-021-84309-3>
- Mohajerani, Y., Wood, M., Velicogna, I., Rignot, E., 2019. Detection of glacier calving margins with convolutional neural networks: A case study. *Remote Sens.* 11, 1–13. <https://doi.org/10.3390/rs11010074>

- Otsu, N., 1979. A Threshold Selection Method from Gray-Level Histograms. *IEEE Trans. Syst. Man. Cybern. C*, 62–66.
- Poliyapram, V., Imamoglu, N., Nakamura, R., 2019. DEEP LEARNING MODEL FOR WATER / ICE / LAND CLASSIFICATION USING LARGE-SCALE MEDIUM RESOLUTION SATELLITE IMAGES. *IGARSS 2019 - 2019 IEEE Int. Geosci. Remote Sens. Symp.* 3884–3887.
- Power, D., Youden, J., Lane, K., Randell, C., Flett, D., 2001. Iceberg detection capabilities of radarsat synthetic aperture radar. *Can. J. Remote Sens.* 27, 476–486. <https://doi.org/10.1080/07038992.2001.10854888>
- Ronneberger, O., Fischer, P., Brox, T., 2015. U-net: Convolutional networks for biomedical image segmentation. *Lect. Notes Comput. Sci. (including Subser. Lect. Notes Artif. Intell. Lect. Notes Bioinformatics)* 9351, 234–241. [https://doi.org/10.1007/978-3-319-24574-4\\_28](https://doi.org/10.1007/978-3-319-24574-4_28)
- Sandven, S., Babiker, M., Kloster, K., 2007. Iceberg observations in the barents sea by radar and optical satellite images, in: *Proceedings of the Envisat Symposium*.
- Schmidhuber, J., 2015. Deep Learning in neural networks: An overview. *Neural Networks* 61, 85–117. <https://doi.org/10.1016/j.neunet.2014.09.003>
- Sephton, A.J., Brown, L.M., Macklin, J.T., Partington, K.C., Veck, N.J., Rees, W.G., 1994. Segmentation of synthetic-aperture radar imagery of sea ice. *Int. J. Remote Sens.* 15, 803–825. <https://doi.org/10.1080/01431169408954118>
- Silva, T.A.M., Bigg, G.R., 2005. Computer-based identification and tracking of Antarctic icebergs in SAR Computer-based identification and tracking of Antarctic icebergs in SAR images. <https://doi.org/10.1016/j.rse.2004.10.002>
- Silva, T.A.M., Bigg, G.R., Nicholls, K.W., 2006. Contribution of giant icebergs to the Southern Ocean freshwater flux. *J. Geophys. Res.* 111, 1–8. <https://doi.org/10.1029/2004JC002843>
- Singh, A., Kalke, H., Loewen, M., Ray, N., 2020. River Ice Segmentation with Deep Learning. *IEEE Trans. Geosci. Remote Sens.* 58. <https://doi.org/10.1109/TGRS.2020.2981082>
- Smith, K.L., Robison, B.H., Helly, J.J., Kaufmann, R.S., Ruhl, H.A., Shaw, T.J., Twining, B.S., Vernet, M., 2007. Free-drifting icebergs: Hot spots of chemical and biological enrichment in the Weddell Sea. *Science (80-. )*. 317, 478–482. <https://doi.org/10.1126/science.1142834>
- Srivastava, N., Hinton, G., Krizhevsky, A., Sutskever, I., Salakhutdinov, R., 2014. Dropout: A simple way to prevent neural networks from overfitting. *J. Mach. Learn. Res.* 15, 1929–1958.
- Stokholm, A., Wulf, T., Kucik, A., Saldo, R., Buus-Hinkler, J., Hvidegaard, S.M., 2022. AI4SeaIce: Toward Solving Ambiguous SAR Textures in Convolutional Neural Networks for Automatic

- Sea Ice Concentration Charting. *IEEE Trans. Geosci. Remote Sens.* 60. <https://doi.org/10.1109/TGRS.2022.3149323>
- Surawy-Stepney, T., Hogg, A.E., Cornford, S.L., Davison, B.J., 2023. Episodic dynamic change linked to damage on the thwaites glacier ice tongue. *Nat. Geosci.* 16, 37–43. <https://doi.org/10.1038/s41561-022-01097-9>
- Torres, R., Snoeij, P., Geudtner, D., Bibby, D., Davidson, M., Attema, E., Potin, P., Rommen, B., Floury, N., Brown, M., Navas, I., Deghaye, P., Duesmann, B., Rosich, B., Miranda, N., Bruno, C., Abbate, M.L., Croci, R., Pietropaolo, A., Huchler, M., Rostan, F., 2012. GMES Sentinel-1 mission. *Remote Sens. Environ.* 120, 9–24. <https://doi.org/10.1016/j.rse.2011.05.028>
- Tournadre, J., Bouhier, N., Girard-Arduin, F., Rémy, F., 2016. Antarctic icebergs distributions 1992–2014. *J. Geophys. Res. Ocean.* 121, 327–349. <https://doi.org/10.1002/2015JC011178>
- Ulaby, F.T., Long, D.G., 2014. Microwave radar and radiometric remote sensing. The University of Michigan Press.
- Vernet, M., Smith, K.L., Cefarelli, A.O., Helly, J.J., Kaufmann, R.S., Lin, H., Long, D.G., Murray, A.E., Robison, B.H., Ruhl, H.A., Shaw, T.J., Sherman, A.D., Sprintall, J., Stephenson, G.R., Stuart, K.M., Twining, B.S., 2012. Islands of ice: Influence of free-drifting Antarctic icebergs on pelagic marine ecosystems. *Oceanography* 25, 38–39. <https://doi.org/10.5670/oceanog.2012.72>
- Wesche, C., Dierking, W., 2015. Near-coastal circum-Antarctic iceberg size distributions determined from Synthetic Aperture Radar images. *Remote Sens. Environ.* 156, 561–569. <https://doi.org/10.1016/j.rse.2014.10.025>
- Wesche, C., Dierking, W., 2012. Iceberg signatures and detection in SAR images in two test regions of the Weddell Sea, Antarctica. *J. Glaciol.* 58, 325–339. <https://doi.org/10.3189/2012JOG11J020>
- Williams, R.N., Rees, W.G., Young, N.W., 1999. A technique for the identification and analysis of icebergs in synthetic aperture radar images of Antarctica. *Int. J. Remote Sens.* 20, 3183–3199. <https://doi.org/10.1080/014311699211697>
- Willis, C.J., Macklin, J.T., Partington, K.C., Teleki, K.A., Rees, W.G., Williams, G., 1996. Iceberg detection using ers-1 synthetic aperture radar. *Int. J. Remote Sens.* 17, 1777–1795. <https://doi.org/10.1080/01431169608948739>
- Young, N.W., Hyland, G., 1997. Applications of time series of microwave backscatter over the Antarctic region, in: *Proceedings of the Third ERS Scientific Symposium, 17-21 March 1997, Florence, Italy. Frascati, Italy: European Space Agency, SP-414, pp. 1007–1014.*

#### 4. Mapping the extent of giant Antarctic icebergs with Deep Learning

---

Young, N.W., Turner, D., Hyland, G., Williams, R.N., 1998. Near-coastal iceberg distributions in East Antarctica, 50-145°E. *Ann. Glaciol.* 27, 68–74. <https://doi.org/10.3189/1998aog27-1-68-74>

Zhang, E., Liu, L., Huang, L., 2019. Automatically delineating the calving front of Jakobshavn Isbræ from multitemporal TerraSAR-X images: A deep learning approach. *Cryosphere* 13, 1729–1741. <https://doi.org/10.5194/tc-13-1729-2019>

# 5

## CONCLUSION, SYNTHESIS AND FUTURE WORK

5.1.	Summary of main results .....	124
5.1.1.	Tracking changes in the area, thickness, and volume of the Thwaites tabular iceberg “B30” using satellite altimetry and imagery .....	125
5.1.2.	Observing the disintegration of the A68A iceberg from space.....	128
5.1.3.	Mapping the extent of giant Antarctic icebergs with Deep Learning .....	130
5.2.	Synthesis of principle findings .....	133
5.2.1.	New datasets of giant iceberg decay .....	133
5.2.2.	Methodological advances to derive iceberg thickness .....	135
5.2.3.	Methodological advances to derive iceberg area.....	137
5.3.	Recommendations for future work .....	138
5.3.1.	Investigating snow on icebergs and its impact on radar penetration .....	138
5.3.2.	Improving U-net iceberg segmentation with more data .....	141
5.3.3.	Towards tracking freshwater input from giant icebergs operationally .....	143
5.4.	Concluding remarks .....	146
	References .....	147

The aim set out in the beginning of this thesis was to develop novel methodology and datasets from satellite remote sensing observations to quantify the freshwater flux from giant Antarctic icebergs as accurately and efficiently as possible. In the preceding three chapters, I have met this aim by improving and automating several parts of the methodology to derive iceberg freshwater flux from satellite remote sensing. By applying the improved method to two giant icebergs, I also created new datasets of iceberg area, freeboard, thickness, volume and mass change. In Chapter 2, I have implemented the basic methodology to derive area, thickness and volume changes of a giant iceberg from satellite altimetry and imagery observations. I noticed the importance of using consistently processed CryoSat-2 data to detect changes in iceberg freeboard due to melting. Then, I developed a method to account for the evolution of ice and snow density over the iceberg lifecycle when converting freeboard measurements to thickness estimates. In addition, I have investigated the impact of certain processing steps (iceberg area estimates, collocation of altimetry tracks and considering snowfall) on the accuracy. In Chapter 3, I extended the use of satellite altimetry to include measurements from ICESat-2 and made the method more efficient by automatically collocating the altimetry observations. In Chapter 4, I addressed the main remaining labour intensive step of deriving iceberg outlines. In this chapter, I suggest a neural network approach to map the extent of giant icebergs in SAR imagery and compare the results to two standard-segmentation methods, finding improved skill.

In this chapter, I will explain how this thesis has met the aim and objectives in more detail by first summarising the key findings from each of the previous results chapters, then providing a synthesis of them and finally outlining future work that has emerged from my findings.

### 5.1. Summary of main results

In this section, I summarise the novel datasets and methodological advances developed in this thesis. The novel datasets are time series and maps of changes in iceberg area, freeboard, thickness, volume and mass of the B30 and A68A icebergs from calving until they became too small to be tracked. Together with my intern Ella Redmond, I also generated a time series of iceberg outlines for six further icebergs (B31, B34, B35, B41, B42 and C34), which were used to train the neural network and to evaluate different segmentation techniques. The main methodological advances to derive iceberg melting from satellite observations are the use of consistently processed CryoSat-2 data, an efficient collocation technique to compare altimetry tracks over the same part of the iceberg and taking the evolution of snow and ice density into account. All of these steps are necessary to detect changes in iceberg thickness associated with

basal melting. Another major advance and novelty is the deployment of a deep neural network to map iceberg extent. The neural network is more efficient than manual delineation and yields more accurate outlines than other automated techniques.

### 5.1.1. Tracking changes in the area, thickness, and volume of the Thwaites tabular iceberg “B30” using satellite altimetry and imagery

In Chapter 2, I analysed the decay of the B30 iceberg, focussing on methodological advances and investigations, which comprise the

- Use of consistently processed elevation data
- Colocation of altimetry tracks
- Consideration of the evolution of snow density
- Consideration of the evolution of ice density
- Comparison of different approaches to estimate iceberg area.

With these advances, I calculated changes in area, freeboard, thickness, volume and mass of the B30 iceberg over 6.5 years. The estimated area change was  $1075 \pm 66 \text{ km}^2$ . Freeboard reduced by  $9.2 \pm 2.2 \text{ m}$  over the same period and this corresponds to an overall thinning of  $117 \pm 38 \text{ m}$  at a mean rate of  $17.3 \pm 1.8 \text{ m per year}$ . Overall, B30 lost  $378 \pm 57 \text{ km}^3$  of ice.  $69 \% \pm 14 \%$  were due to basal melting and hence direct freshwater input into the ocean and the remaining  $31 \% \pm 11 \%$  were due to a combination of sidewall melting and fragmentation. The total mass loss was  $325 \pm 44 \text{ Gt}$ .

Although previous studies have used similar techniques to derive changes in iceberg area, thickness and volume, this study contributed a number of methodological advances and I investigated each step extensively, comparing different approaches and quantifying the impact of certain approximations. The first improvement from this study is the use of consistently processed elevations from CryoSat-2. When using Level-2 data, I noticed that different retrackers and biases are applied in different acquisition modes and within different geographical zones. When building the reference map of initial iceberg freeboard pre-calving, the iceberg was still attached to the ice shelf and within the *continental ice* mask, where CryoSat-2 operates in SAR interferometric (SARIn) mode. A few months after calving, B30 left the area defined as *continental ice* and reached the area defined as *open ocean* in the Level 2 product, but stayed within the SARIn acquisition mask, which also covers the near-coastal areas around Antarctica. Once it drifted further from the continent, it then reached the area where CryoSat-2 operates in SAR mode. This means that three different retrackers and biases are applied across

the iceberg life time and I found that these lead to jumps in freeboard heights. Therefore, I used consistently processed elevation data, instead.

Secondly, I analysed and quantified the impact of collocating altimetry tracks over the floating iceberg with a map of initial iceberg freeboard pre-calving versus simply comparing freeboard measurements regardless of where they sample the iceberg. Overall, I found good agreement between measurements with and without collocation (correlation coefficient 0.87). For the B30 iceberg, the collocation step reduced freeboard uncertainty by 1.6 m. The impact depends on the initial topography of the iceberg, though. For icebergs where the across-grid variation significantly exceeds the variation within each grid cell, the impact will be larger. B30 was a specifically crevassed iceberg, meaning that the variance of freeboard heights within each grid cell was in the same order of magnitude as across different grid cells (3.3 m and 3.1 m, respectively).

The third investigation and improvement is the consideration of snow on the iceberg. Before, only Han *et al.* (2019) used snowfall reanalysis data when converting freeboard observations to iceberg thickness and assume a constant snow density of  $300 \text{ kg m}^{-3}$ . In contrast to their 1.5-year study period, I monitored changes in the B30 iceberg over 6.5 years, where 4.6 m of snow water equivalent accumulated and this snow evolved with time (Figure 5.1). Therefore, I developed a method to account for changes in snow density as a function of air temperature, wind speed and snow depth. This yielded an increase in the average snow density from 252 to  $616 \text{ kg m}^{-3}$  and a 7.2 m thick snow layer after 6.5 years. Accounting for the snowfall over this multi-annual drift resulted in a 27 m or 23 % adjustment to the iceberg thickness change after 6.5 years (Figure 5.1c), which demonstrates its importance – particularly when the iceberg survives for a long time and when melting is rather slow.

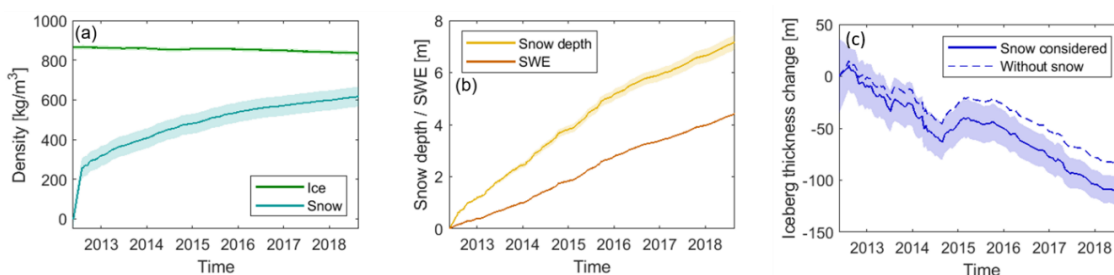


Figure 5.1: Evolution of ice and snow density (a), snow water equivalent (SWE) and snow depth (b), and iceberg thickness with and without considering a snow layer (c) over the lifetime of the B30 iceberg

Similarly, I improved the accuracy of ice density by modelling the ice density profile and accounting for an evolving average ice density during iceberg drift. Just like snow on icebergs,

iceberg density has not received much attention yet, but is a crucial parameter in the conversion of freeboard to thickness, contributing the majority in the uncertainty budget. Here, I decided to model the iceberg's ice density profile from the depths of critical density levels (Ligtenberg, Helsen and Van Den Broeke, 2011) of the Thwaites Ice Shelf, where B30 calved from. I then updated the average ice density over time, by integrating to evolving lower depths, as the iceberg melted from below. The average ice density therefore reduced from  $864 \text{ kg m}^{-3}$  at calving to  $835 \text{ kg m}^{-3}$  after 6.5 years (Figure 5.1a).

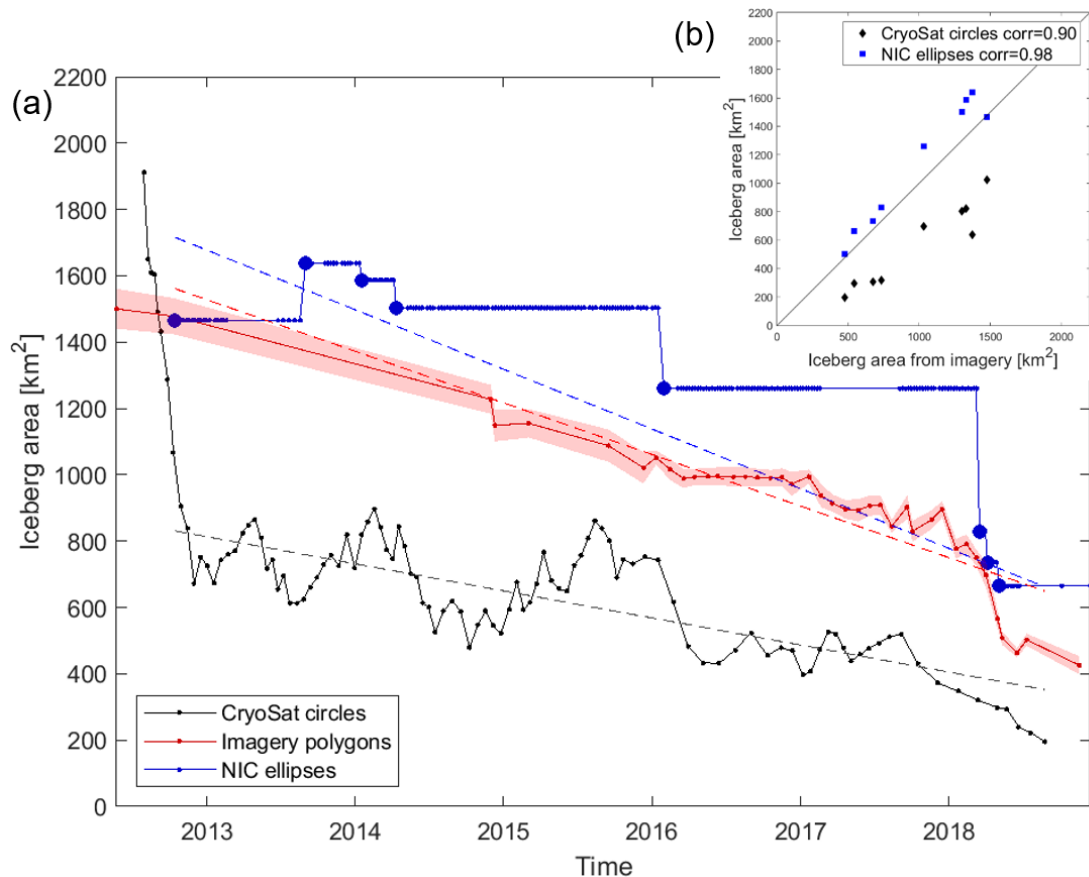


Figure 5.2: Area estimates for the B30 iceberg over time based on manual delineation (red), compared to arc-lengths of altimetry overflights assuming a circular iceberg shape (black) and semi axes lengths provided by NIC assuming an elliptical iceberg shape (blue). Unique observations of semi axes are marked with thick blue dots and determine the times of correlation in (b).

Finally, I considered two simple approaches to automate the calculation of iceberg area and to make the manual derivation of iceberg outlines redundant. Here, I examined whether estimates of the iceberg's orthogonal axes, which are measured operationally by NIC and provided together with the tracks (Budge and Long, 2018), or the arc-lengths of altimetry overpasses can approximate iceberg area. I found that both methods are able to capture the area and area change over time, but with lower accuracy. Compared to the most accurate manually derived

outlines, orthogonal axes lead to estimates of area and area trends that are 14 % and 16 % higher, respectively, and arc-lengths lead to estimates of area and area trends that are 45 % and 48 % lower. This is because iceberg shape is approximated as a circle or ellipse, which does not represent the actual iceberg shape accurately. Another problem with the major axes estimates by NIC is that they are rounded to nautical miles and are only updated occasionally, leading to only eight unique observations (Figure 5.2).

### 5.1.2. Observing the disintegration of the A68A iceberg from space

In Chapter 3, I applied the methodology from Chapter 2 to the famous A68A iceberg and added

- ICESat-2 data
- An automatic collocation of altimetry tracks
- A more advanced uncertainty estimation
- The analysis of scouring, melting and blockage near South Georgia

With these improvements, I calculated changes in area, freeboard, thickness, volume and mass of the A68A iceberg over 3.5 years. As it approached the islands of South Georgia up to 62 km and stayed within 300 km off the coast for 3 months, I also calculated the freshwater input near the island, which likely affected the rich ecosystem there. The estimated area change was  $3206 \pm 78 \text{ km}^2$  over 3.5 years. Thickness reduced by  $67 \pm 5 \text{ m}$  over the same time. Overall, A68A lost  $924 \pm 27 \text{ km}^3$  of ice, which is equivalent to  $802 \pm 34 \text{ Gt}$  of mass.  $32 \pm 3 \%$  were due to basal melting and hence direct freshwater input into the ocean and the remaining  $68 \pm 5 \%$  were due to sidewall melting and fragmentation. Near South Georgia, I estimated a freshwater input of  $152 \pm 61 \text{ Gt}$  over three months through basal melting alone.

The addition of ICESat-2 laser altimetry brings several advantages: It increases the data availability and offers greater coverage due to the three beams and the smaller spatial resolution. Furthermore, laser altimeters scatter from the snow-air interface (Kwok *et al.*, 2007), while radar altimetry is assumed to scatter from the snow-ice interface in sea ice applications (Beaven *et al.*, 1995; Laxon, Peacock and Smith, 2003). However, several studies have suggested that CryoSat-2 might scatter from within the snow layer in certain conditions (Giles, Laxon and Worby, 2008; Willatt *et al.*, 2010) and it is unlikely to penetrate a several meter thick snow layer, which is several years old and might have melted in between. Therefore, I decided to assume that CryoSat-2 is also scattered from the snow-air interface. A comparison of the respective thickness estimates from CryoSat-2 and ICESat-2 supports this assumption, as both agree well and yield a consistent time series.

The second improvement – both in terms of accuracy and efficiency is the automated collocation of altimetry tracks. Although the results from Chapter 2 indicated that the collocation step did not have too much influence for B30, in the case of A68A, I found significant undulations in topography across the initial thickness map, indicating that in this case an accurate collocation is crucial. That is why, I developed an automated collocation. Using the iceberg outline from a near-coincident image, I maximise the overlapping area with respect to the previous outline. This iterative procedure accounts for the evolving shape of the iceberg and smaller parts breaking off as it evolves and yields the optimal rotation and translation parameters (Figure 5.3). For A68A it has proven useful and reliable, but would not work with symmetric outlines and might fail if the shape changes too much between two observations.

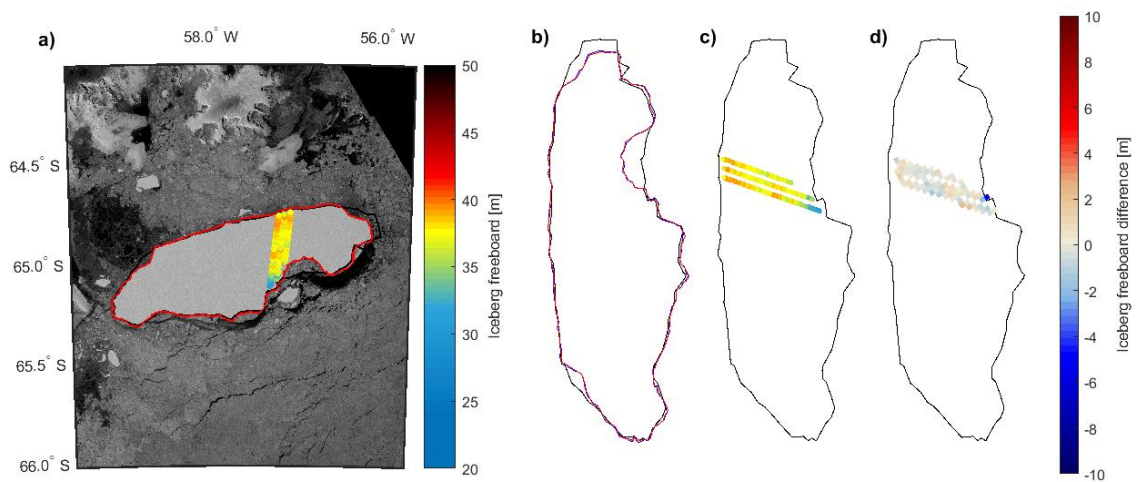


Figure 5.3: Automated collocation of altimetry tracks over the floating iceberg with respect to the initial iceberg outline. The new outline (red) is derived from a near-coincident image (a) and the overlapping area to the previous outline (blue) is maximised (b). This iterative procedure yields the translation and rotation with respect to the initial outline (black, b) and allows us to transform the altimetry track accordingly (c). The new track is then gridded on the same grid as the initial freeboard and subtracted from it (d).

The last methodological advance is a more detailed investigation of the uncertainty budget. Here, I added correlations between freeboard measurements, assuming that measurements from the same track are 60 % correlated and measurements forming the initial freeboard map, which stem from several tracks, are 30 % correlated. I also investigated the contributions from different components to the overall uncertainty budget. With the correlations being taken into account, the uncertainty from the new track dominates the uncertainty of freeboard change, contributing 49 %, while the initial freeboard contributes 29 % and collocation is only responsible for 22 % of the uncertainty. For ice thickness, the uncertainty in ice density has most impact. Overall, I found that the estimates of thickness and area change contribute similarly (55 % and 45 %).

Apart from the methodological advances, the main added contribution of this paper is the analysis of scouring, melting and blockage near South Georgia, which was of wider environmental interest. I measured the distance of the iceberg to the island and compared the iceberg draft at that time to a map of seafloor bathymetry. I found that A68A approached South Georgia up to 62 km and that it had a mean draft of  $141 \pm 11$  m at that time. The shallowest bathymetry beneath the iceberg locations captured in satellite imagery is 150 m (O. Hogg et al., 2016). The fact that the iceberg turned slightly after and a smaller piece broke off, indicate that it briefly scoured the seafloor, but did not ground. This was lucky for the benthic fauna (Gutt, 2001; Barnes, 2017) and nearby colonies of seals and penguins, who could have experienced blockage to their feeding grounds if A68A had grounded for a longer time and in its full size (Kooyman *et al.*, 2007; Clarke *et al.*, 2012; Joiris *et al.*, 2015). The wildlife is also affected by changes in oceanographic conditions and food availability through the release of huge amounts of meltwater within a short time and area (Arrigo *et al.*, 2002; Vernet *et al.*, 2012; Smith *et al.*, 2013). I estimated that A68A and its children icebergs that broke off near the island, released  $152 \pm 61$  Gt of freshwater through basal melting within 300 km offshore and 3 months.

### 5.1.3. Mapping the extent of giant Antarctic icebergs with Deep Learning

In Chapter 4, I address the need for an efficient and accurate method to map iceberg extent in Sentinel-1 imagery by

- Developing a deep neural network
- Comparing its performance to two standard segmentation techniques
- Investigating the impact of iceberg size
- Analysing the performance in different challenging environmental conditions

The neural network was trained and evaluated in a cross-validation fashion using 191 Sentinel-1 images and corresponding manual delineations of iceberg outline. The images contain seven giant Antarctic icebergs between 2014-2020, where individual images of the same iceberg are roughly one month apart and include all seasons. Spatially, they cover different parts of the Southern Ocean and different environmental conditions like open ocean, sea ice, nearby coast, iceberg fragments, other bergs and surface thawing. I also applied two standard segmentation methods (Otsu thresholding and k-means) to the same images and compared the performance of each of the automated techniques with manually derived outlines.

A main novelty of this work is the development of a deep neural network, as it is the first study to employ a deep neural network to iceberg segmentation. Deep neural networks decide on the

most meaningful features themselves, can encode complex non-linear relationships and are able to consider the wider image context. They therefore outperform classic machine learning techniques in most tasks (LeCun, Bengio and Hinton, 2015; Schmidhuber, 2015). U-net was developed for biomedical image segmentation (Ronneberger, Fischer and Brox, 2015), but has become popular in many domains including polar remote sensing (Baumhoer *et al.*, 2019; Mohajerani *et al.*, 2019, 2021; Poliyapram, Imamoglu and Nakamura, 2019; Zhang, Liu and Huang, 2019; Singh *et al.*, 2020; Andersson *et al.*, 2021; Dirscherl *et al.*, 2021; Stokholm *et al.*, 2022; Surawy-Stepney *et al.*, 2023). In Chapter 4, I slightly modified the original U-net architecture to segment Sentinel-1 images of giant Antarctic icebergs and found improved skill compared to other machine learning techniques.

By comparing U-net to k-means and Otsu thresholding, which are two standard segmentation techniques, I showed that U-net outperforms them in most metrics. Mainly, U-net achieves a significantly higher  $F_1$  score (0.84 compared to 0.62). As the iceberg class only cover 5 % of all pixels across the whole data set, the  $F_1$  score is the most reliable metric. U-net very rarely mistakes background (e.g. sea ice, iceberg fragments or coast) for iceberg (0.4 % false alarm rate), which is a considerable improvement compared to Otsu and k-means (5.2 % and 4.7 % false alarm rates). This was the case regardless of which iceberg was chosen as test data and across all environmental conditions. I also found that Otsu scores worst in this category across six out of seven icebergs and across all environmental conditions. I suspect that this is a consequence of the Gaussian smoothing, which was applied before the threshold. On the other hand, U-net tends to miss parts – especially of the largest icebergs, scoring lowest on the miss rate (21 % compared to 9 % and 13 %). While the median absolute deviation in iceberg area is similar for all three methods (3.6 - 5.1 %), the mean (absolute) deviation reveals that both Otsu and k-means generate a few complete failures with over 100 % area deviation.

Investigating the metrics for each of the seven icebergs kept as test data, I analysed the impact of iceberg size and the sensitivity to the choice of test data. I found high variability across the different test data sets (icebergs) for all the methods with  $F_1$  scores ranging from 0.20 – 0.91 for Otsu, 0.23 - 0.93 for k-means and 0.68 - 0.97 for U-net. This clearly demonstrates the sensitivity of any approach to the chosen test data set and that images from the same iceberg are highly correlated, exhibiting the same challenges in terms of iceberg size, shape and background, even when individual images are one month apart. It is also the reason, why I chose to use cross-validation. When all techniques showed decreased skill for a certain iceberg (e.g. B41), I concluded that the background of this iceberg is particularly challenging. In contrast, U-net specifically struggles with B31, but the other two techniques achieve their highest  $F_1$  scores on

this berg. In this case, the dataset itself is not challenging per se. B31, rather appears largest in the images (as images of B30, which is largest, were rescaled). This means that U-net has to predict larger outlines for the test data than in any of the training data, which can be considered a domain-shift or even an out-of-domain sample. Ideally, the training data, should therefore be extended to cover more icebergs of various sizes.

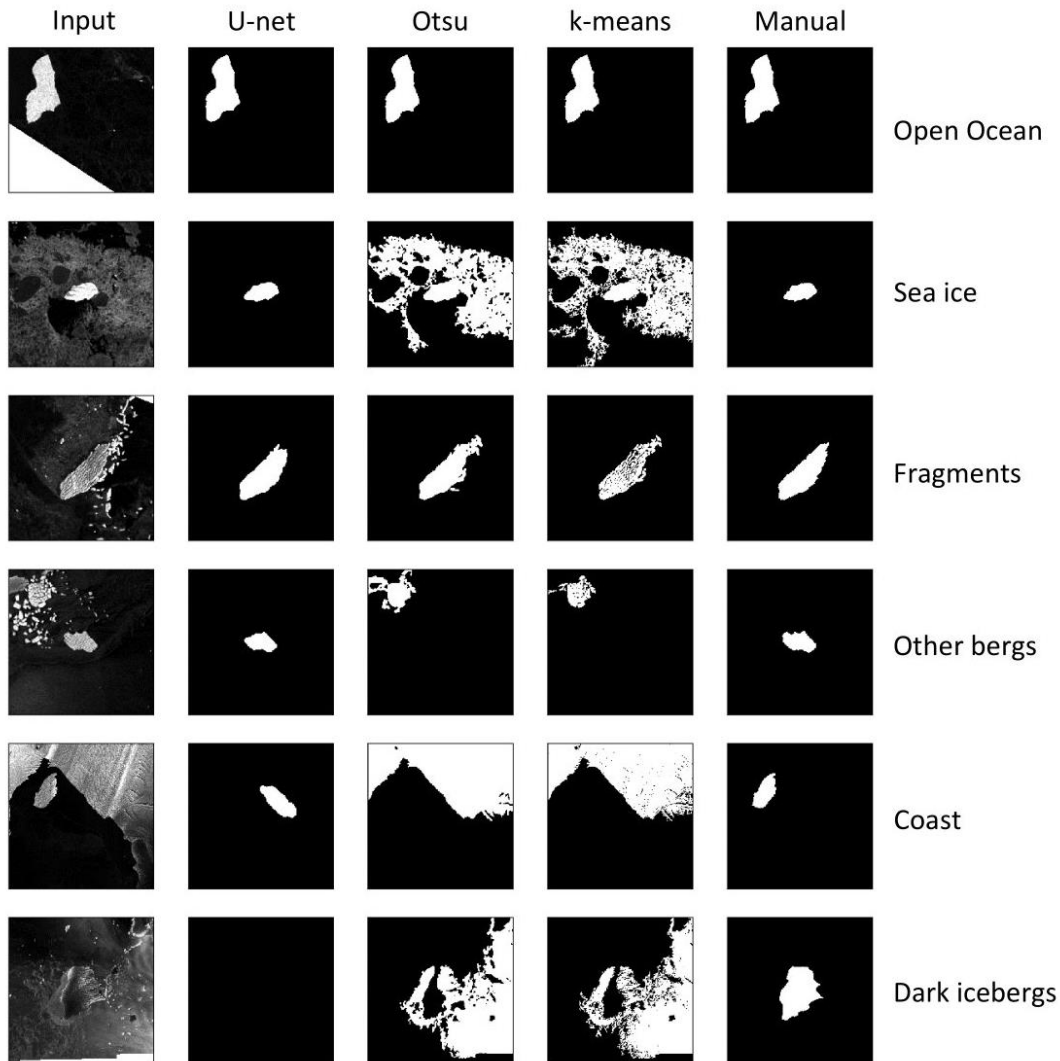


Figure 5.4: Impact of different environmental conditions on the skill of automated methods to segment Sentinel-1 images into the largest iceberg and background. The first column shows Sentinel-1 input images in different conditions (as labelled on the right), and the following columns show the segmentation maps produced by U-net, Otsu, k-means and manual delineation

The final analysis targeted different environmental conditions. Here, I found that all methods achieve very good results in open ocean. U-net is more robust to busy backgrounds like deformed sea ice (achieving an  $F_1$  score of 0.88 compared to 0.72 and 0.74 for Otsu and k-means). When iceberg fragments are drifting close to the iceberg, they can easily be connected

to the berg by error. Although, U-net achieves a lower  $F_1$  score in this category (0.85 instead of 0.95 for Otsu and k-means), it achieves the same low false alarm rate as k-means (0.4 instead of 0.7 for Otsu). This indicates, that U-net does not actually struggle with erroneously connecting the fragments to the iceberg, but rather misses bits of the iceberg and a good amount of images with fragments stem from B31, where U-net misses large parts of the berg due to its size. When another iceberg is present, U-net reliably picks the largest target iceberg ( $F_1$  score 0.96) – potentially also learning that it tends to be in the centre of the image. Otsu and k-means in contrast pick another iceberg in most of these cases ( $F_1$  scores 0.18 and 0.10). For images containing coast, I found that U-net discards smaller patches of coast reliably, but fails if too much coast is present. In these cases, it predicts almost nothing, though, while the other methods find the whole coast instead of the iceberg. If the iceberg appears dark due to surface thawing, all methods fail (see Figure 5.4 for one example each).

## 5.2. Synthesis of principal findings

In this thesis, I have developed novel methods and datasets from satellite remote sensing observations to quantify the freshwater flux from giant Antarctic icebergs as accurately and efficiently as possible. Several methodological investigations and advances have formed a consolidated method to calculate iceberg freeboard, thickness and basal melting with higher accuracy. Novel methodology to map iceberg extent and outlines automatically, reduces the required amount of manual intervention significantly. Together, my results advance our understanding of iceberg decay, will contribute to the improvement of models and pave the way for an accurate and efficient operational monitoring of freshwater flux from giant icebergs using satellite remote sensing and artificial intelligence.

### 5.2.1. New datasets of giant iceberg decay

Throughout this thesis, I have generated new extensive datasets of changes in iceberg area, freeboard, thickness, volume and mass. In Chapters 2 and 3, I calculated all of these quantities for the B30 and A68A icebergs from their calving to their disintegration (Figure 5.5a). Chapter 4 contributes a dataset of iceberg imagery and the corresponding outlines, from which changes in iceberg area of six further icebergs (B31, B34, B35, B41, B42 and C34) can be calculated over several years (Figure 5.6). These datasets add to the literature, where other specific giant icebergs had been studied or in the case of A68A extend existing studies by another two years. Since especially the manual outlines are tedious to generate, previous studies have focussed on one or two giant icebergs and adding further observations of giant iceberg decay is a valuable

contribution in itself. As discussed in Chapter 1, models are currently not able to represent giant iceberg disintegration adequately, so I expect that additional observations aid our understanding of iceberg decay and contribute to the improvement of models.

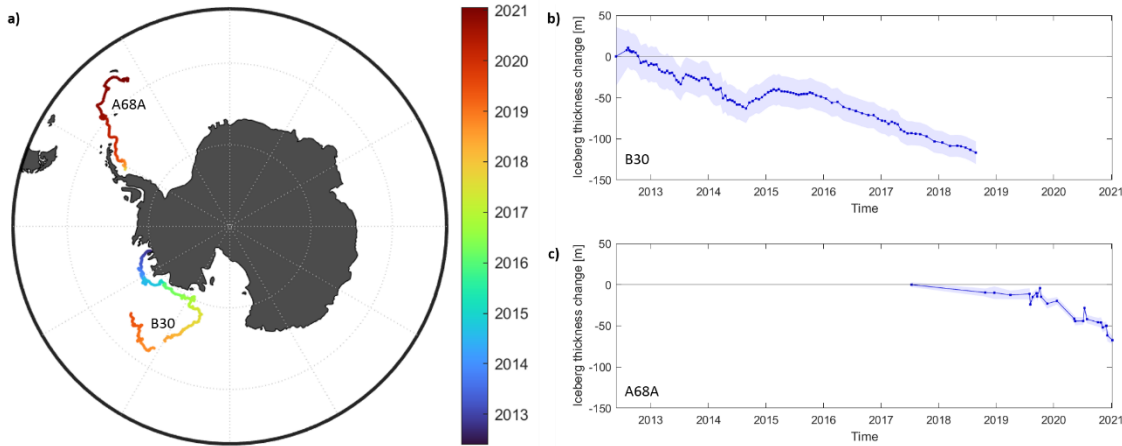


Figure 5.5: Trajectories (a) and thickness change of B30 (b) and A68A (c) icebergs on common axes

Comparing my findings on the B30 and A68A icebergs (Chapters 2 and 3), there are some differences, but also many similarities with respect to their decay. Both bergs calved from different areas of Antarctica and took distinct paths (Figure 5.5a). B30 calved from the Thwaites Ice Shelf in the Amundsen Sea and followed the coastal current for almost five years, before turning North near the Ross Sea. A68A calved from the Larsen-C Ice Shelf and moved slowly within the first 2.5 years, while surrounded by thick sea ice in the western Weddell Sea. It then passed the tip of the Antarctic Peninsula and took the ‘iceberg alley’ to approach South Georgia eleven months later, where it disintegrated. Despite their different origins and trajectories, their disintegration exhibits several similarities: The average melt rate is 17.3 m/year for B30 and 19.3 m/year for A68A (Figure 5.5b, c). B30 stayed close to the coast for longer and A68A reached lower latitudes, which explain the slightly higher average melt rate of A68A. I found that the contribution of melting to the overall mass loss is very similar for both bergs, too: 33 % for B30 and 32 % for A68A. Also in both cases, fragmentation became the main driver towards the end.

Despite the similarities in method, Chapters 2 and 3 had a different focus. My main goal in Chapter 2 was to investigate and compare existing methodology, to quantify the impact of certain processing steps, where different approaches had been suggested in the literature, to improve the accuracy and to automate the processing where possible. The B30 iceberg was a good sample iceberg for this purpose, because it survived and drifted for 6.5 years, offering many satellite overpasses and hence observations, which enabled a detailed analysis across a

range of surroundings. In contrast, the focus of Chapter 3 was more on the application, analysing the iceberg's interaction and impact on its environment. A68A was the biggest iceberg at that time and the sixth largest since the satellite record (Budge and Long, 2018). Together with its drift trajectory, approaching South Georgia closely and almost intact (with little fragmentation before), it had the potential to have a significant environmental impact. This also made A68A a star in the media, a concern for biologists and of huge interest to oceanographers and glaciologists (Tarling, 2022). For me, A68A offered the opportunity to study a giant iceberg that was of broader interest and where the freshwater input was of immediate significance. Therefore, Chapter 3 focussed more on the iceberg's behaviour and impact near South Georgia and the links to the environment. Near South Georgia, I quantified the freshwater input and investigated scouring or grounding based on my estimates of iceberg thickness at that time. Also along the full trajectory, I plotted area loss together with sea ice concentration and thickness change together with ocean temperature, showing their interconnection (Figure 3.6).

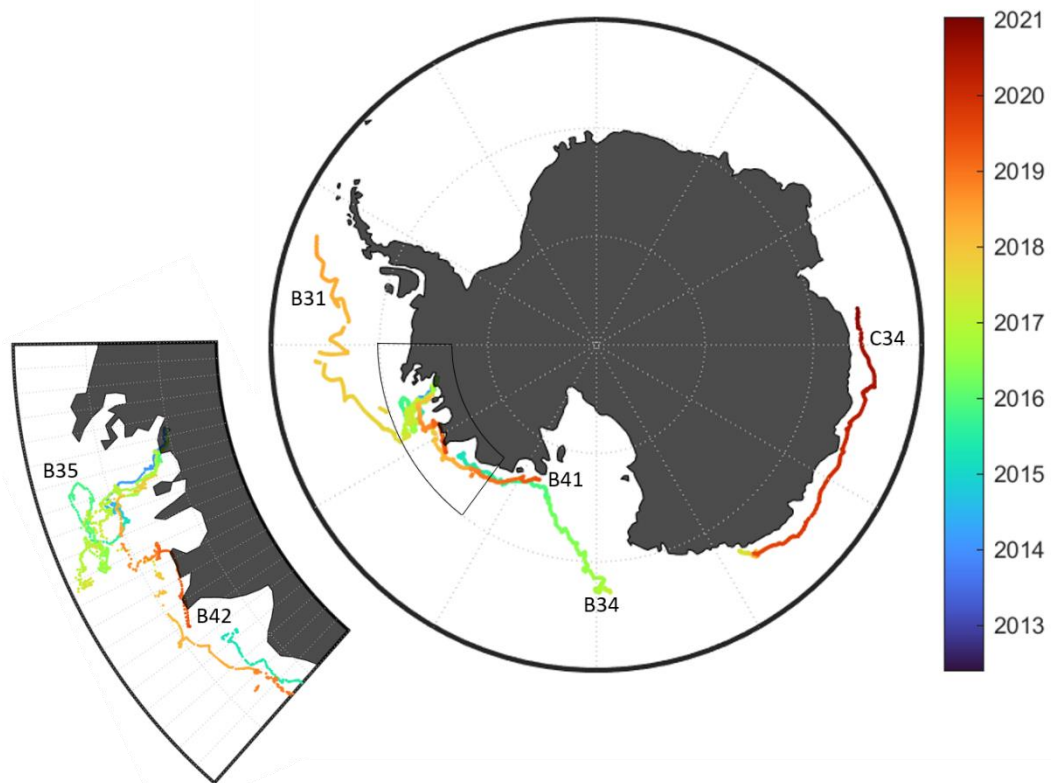


Figure 5.6: Trajectories of further icebergs, where datasets of iceberg imagery and outlines have been generated

### 5.2.2. Methodological advances to derive iceberg thickness

Generally, I used the same method to derive changes in iceberg thickness for both the B30 and A68A iceberg. Particularly, I applied the same method to account for the evolution of snow and

ice density, as developed in Chapter 2, to the A68A iceberg in Chapter 3. Also here, this yielded realistic values for snow accumulation (3.3 m after 3.5 years), snow density (465 kg m<sup>-3</sup> after 3.5 years) and ice density (decreasing from 868 to 848 kg m<sup>-3</sup> as the densest ice melted from below). I verified the initial iceberg density of A68A with firn air content derived from airborne observations over the Larsen-C ice shelf (Holland *et al.*, 2011), and found that these are consistent. These findings from Chapter 3 support the methodology developed in Chapter 2. Furthermore, I illustrated the importance of including a snow layer in the calculation of iceberg thickness in Chapter 2, showing that an omission would miss 27 m of iceberg thinning. Similarly, in Chapter 3 I found a notable thickness change in the Weddell Sea, although hardly any freeboard change was observed. Here, the freeboard loss associated with basal melting and freeboard gain due to snow accumulation evened out, confirming that a slow basal melting process is only detectable, when snow is included in the calculations. Overall, the methodological advances developed for B30 proved applicable and relevant for A68A, too.

Only the impact of collocating altimetry tracks was different for both icebergs, as it depends on the iceberg's topography. For B30 and A68A, I found large differences in topography, due to their different calving origin (Thwaites versus Larsen-C) and iceberg size (1500 km<sup>3</sup> versus 5719 km<sup>3</sup>). While in Chapter 2, I suggested to use altimetry tracks without collocation to make some manual intervention redundant, I found that collocation is essential for A68A and therefore developed an automated collocation step in Chapter 3. The B30 iceberg was relatively flat, but particularly crevassed, so the mean standard deviation within each grid cell was 3.3 m and the standard deviation across different grid cells was 3.1 m. This reduced the impact of collocation drastically. In contrast, A68A was a lot larger and less crevassed. Here, the gridded freeboard heights ranged from 22.1 to 42.6 m, with higher freeboard on the side facing the Antarctic Peninsula and lower freeboard on the side facing the ocean. The standard deviation within each grid cell was mostly below 1 m and the map of initial iceberg freeboard appears a lot smoother than that of B30 (Figure 5.7). Both factors increase the impact of collocation. So, from these two examples I conclude that if the overall topography is comparable to within grid cell variations, altimetry observations can be used without collocation, which is the easiest and fastest approach, requiring no manual interaction (as suggested in Chapter 2). However, if the across grid cell variations exceed the within grid cell variations, I suggest employing the automated collocation developed in Chapter 3 with automatically derived outlines using the U-net developed in Chapter 4.

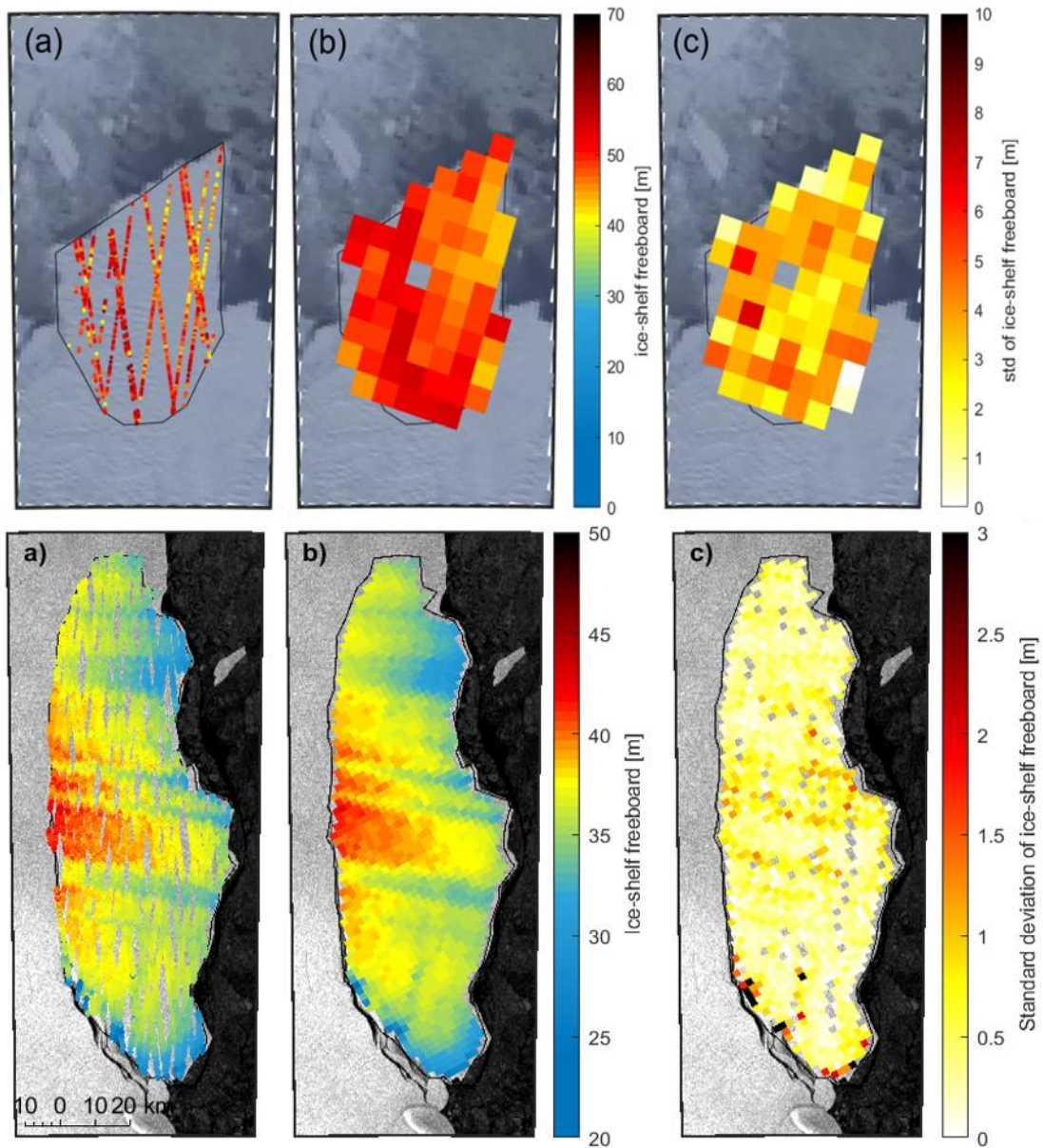


Figure 5.7: Maps of initial iceberg freeboard from individual tracks (a), gridded (b), and their standard deviation (c) of the B30 iceberg (top row) and the A68A iceberg (bottom row)

### 5.2.3. Methodological advances to derive iceberg area

In both Chapter 2 and 4, I evaluated different approaches to derive estimates of iceberg area automatically. In Chapter 2, I first investigated two simple approaches: Here, I assumed a circular iceberg shape and employed arc-lengths of altimetry overflights as diameter or I assumed an elliptical iceberg shape using the orthogonal axes lengths provided by NIC. In both cases, I found degraded accuracy by 45 % and 14 % respectively. Another disadvantage of the second, more accurate, approach is that NIC only provides eight unique estimates over 6.5 years, limiting the number of observations. In between the observations, the area deviation is more than 14 %. In

Chapter 3, I calculated that the uncertainty in iceberg area contributes 45 % to the overall uncertainty in iceberg volume change, making the accuracy of iceberg area an important factor. Furthermore, none of those techniques yields iceberg outlines, which are needed to collocate the altimetry tracks. Therefore, I examined more advanced approaches to derive iceberg area and outlines in Chapter 4, as this is the main remaining task that requires manual intervention and a significant contributor to uncertainty. Here, I applied the k-means segmentation algorithm (Macqueen, 1967) and the Otsu thresholding technique (Otsu, 1979) and developed a deep neural network to segment satellite images of giant icebergs. I found that the neural network improves the skill in most cases. The implementation from Chapter 4 also ensures that only the largest iceberg in each image is segmented, yielding iceberg outlines and estimates of iceberg area, that could directly be incorporated into the processing scheme from Chapters 2 and 3.

### 5.3. Recommendations for future work

In this section, I outline some remaining challenges and directions of future research that have emerged from the findings in my thesis. Firstly, based on my findings from Chapter 2 and 3, I suggest investigating the characteristics of snow on icebergs and its impact on the scattering horizon of radar altimeters with novel datasets that have been acquired since. Secondly, I recommend improving the accuracy and transferability of the U-net suggested in Chapter 4 further, by greatly extending the training data set. Finally, I propose to combine the methods developed across this thesis and to apply them on a larger scale, building an operational system to track freshwater input from giant icebergs.

#### 5.3.1. Investigating snow on icebergs and its impact on radar penetration

The first remaining challenge is to understand how deep radar altimetry penetrates snow on icebergs and whether snow depth on icebergs can be calculated from differences in penetration depth of altimeters or ERA-5 reanalysis data. Good estimates of penetration depth and snow on icebergs are essential to calculate accurate iceberg thickness from measurements of iceberg freeboard. To address this aim, I suggest comparing coincident satellite and airborne measurements of laser and radar freeboard to determine the penetration depth. Differences in penetration depth could then be compared with airborne snow radar measurements and snow depth derived from ERA-5 reanalysis, to assess whether one of them yields good estimates of snow depth on icebergs.

Snow on icebergs and the scattering horizon of radar altimeters over icebergs have barely received any attention so far. Only Scambos *et al.* (2008) made in-situ measurements of snow

depth on a tabular iceberg, installing pre-marked poles observed with a camera to track accumulation and ablation. During the installation, they also dug a snow pit and made measurements of firn temperature and density. They found fresh snow with  $450 \text{ kg m}^{-3}$  density on the surface and denser firn with melt layers of  $650 \text{ kg m}^{-3}$  density lower down. The study by Han *et al.* (2019) has been the only one accounting for snowfall during iceberg drift when converting iceberg freeboard to thickness. In Chapter 2, I have developed a method to account for the evolution of snow density during iceberg drift and assume that CryoSat-2 does not penetrate a several years old snow layer. This assumption is supported by a quick comparison of CryoSat-2 and ICESat-2 freeboard heights in Chapter 3, but a more extensive verification would be needed. In the meantime, many useful data have been acquired, which enable such an extensive analysis.

In Chapter 2, I found that giant tabular icebergs accumulate a thick snow layer over their multi-annual drift. B30 gathered 7.2 m of snow within the 6.5 years of observations. Therefore, I assume that CryoSat-2 does not penetrate this thick, old snow layer and is rather scattered from the air-snow interface. For sea ice applications, CryoSat-2 is mostly assumed to scatter from the snow-ice interface (Beaven *et al.*, 1995; Laxon, Peacock and Smith, 2003), but this only holds true for fresh, dry snow. On Antarctic sea ice, observations indicate that CryoSat-2 rather scatters from within the snowpack (Giles, Laxon and Worby, 2008; Willatt *et al.*, 2010). In Chapter 3, I then added ICESat-2 laser altimetry observations over the A68A iceberg and found that the time series of combined CryoSat-2 and ICESat-2 observations was in good agreement. Two of the tracks from CryoSat-2 and ICESat-2 are close in time, but sample different parts of the iceberg. This analysis supports my assumption that CryoSat-2 is rather scattered from the snow-air interface, but I was not able to investigate this in more detail due to the lack of coincident data.

In July 2020, ESA and NASA launched the CRYO2ICE campaign with the goal to yield laser and radar altimetry measurements over the same areas close in time. First, the orbit of CryoSat-2 was adjusted to receive coincident tracks over the Arctic and since June 2022, CryoSat-2 and ICESat-2 sample the same regions in the Antarctic every 19 orbits (roughly 31 hours). This is the ideal opportunity to assess the scattering horizon of CryoSat-2 compared to ICESat-2 over large tabular Antarctic icebergs and hence to also learn more about the properties of snow on icebergs. In addition to the satellite data, airborne observations will greatly benefit this analysis. In December 2022, airborne measurements were collected over sea ice in the Weddell Sea during the CRYOVEX/DEFIANT campaign. During the many aircraft flights, multiple tabular icebergs were also overflown. These measurements include lidar measurements, radar altimetry

measurements in Ka- and Ku-band, where Ku-band is the same frequency as CryoSat-2 and S/C-band (2-8 GHz) radar measurements, which are used to derive snow depth (Arnold *et al.*, 2020). Once all the data have been pre-processed and are available, I suggest exploiting satellite and airborne data together to first draw conclusions about radar penetration over tabular Antarctic icebergs and then also to investigate and potentially improve estimates of snow depth on icebergs. To achieve this, I propose to conduct several comparisons (Figure 5.8). The coincident CRYO2ICE tracks will allow for a direct comparison of satellite lidar and radar altimetry measurements over Antarctic icebergs. They will reveal whether CryoSat-2 and ICESat-2 measure comparable freeboard heights or whether CryoSat-2 freeboard is systematically lower as it penetrates (a part of) the snowpack (Figure 5.8a). These tracks will also indicate how much the agreement varies spatially and temporally, as – in contrast to the airborne data – several CRYO2ICE tracks will sample giant icebergs in different locations and seasons. Next, a similar comparison could analyse airborne lidar and radar measurements over the icebergs that were sampled during the campaign with higher spatial resolution (Figure 5.8b). This comparison allows crosschecking the results from airborne and satellite-borne measurements. Then, it would also be interesting to compare airborne freeboard measurements in Ku- and Ka-band (Figure 5.8c), again investigating the difference in radar penetration. This analysis would be useful in preparation for the future CRISTAL satellite mission, which will measure radar freeboard in Ka- and Ku-band.

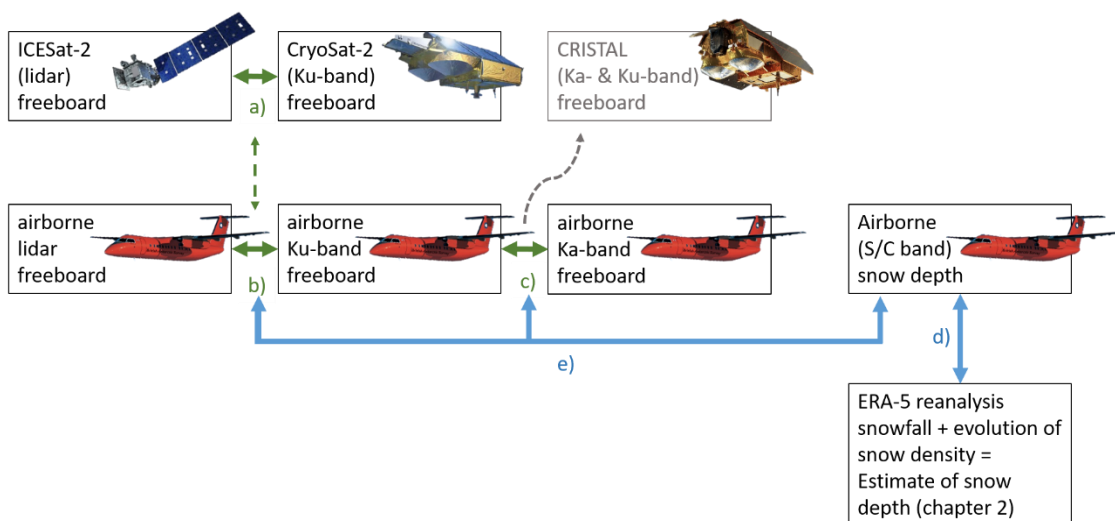


Figure 5.8: Schematic overview of acquired/future data (black/grey boxes) and useful comparisons to investigate differences in penetration depth (green arrows) and snow depth (blue arrows) over an iceberg. Copyright of satellite and airplane icons: NASA, ESA, Airbus and BAS

In a next step, I then propose to focus on snow depth. From the airborne S/C band data, snow depth can be derived (Kwok *et al.*, 2011; Newman *et al.*, 2014) and would be regarded as the best estimate. Using ERA-5 reanalysis data over the same iceberg and accounting for snow compaction as a function of snow depth, air temperature and wind speed, as I suggested in Chapter 2, the resulting snow depth could be verified with the airborne data (Figure 5.8d). Furthermore, if consistent differences in the scattering horizon between lidar, Ku- and Ka-band radar have been found (Figure 5.8a-c), these could then also be compared to the snow depth (Figure 5.8e) to investigate whether any difference of (future) satellite freeboard measurement yields snow depth on icebergs. In an optimal scenario, all these remote sensing data would be complemented with in situ observations on the iceberg, but such data have not been collected during the last CRYOVEX/DEFIANT campaign.

### 5.3.2. Improving U-net iceberg segmentation with more data

The main remaining challenge for an efficient mapping of iceberg extent and outlines in Sentinel-1 images is that the U-net suggested in Chapter 3 misses parts of icebergs that appear larger than those contained in the training data. Therefore, I suggest extending the training data set to a wider range of iceberg sizes. The main obstacle is the generation of manual outlines for training. To overcome this problem, either a crowd-sourcing platform could be used or the neural network could be trained in a semi-supervised fashion.

My work in Chapter 4 has demonstrated the capability of a deep neural network to segment Sentinel-1 images of giant icebergs, showing that the proposed U-net already outperforms standard segmentation algorithms in most metrics and conditions. However, the current U-net tends to miss parts of the largest icebergs. I believe that this happens, because when the iceberg appearing largest in the images is retained as test data, the training data set only contains smaller icebergs. Therefore, enlarging the training data set and including more icebergs of different sizes, would benefit the performance of the neural network and make it more robust and transferable to a range of iceberg sizes and conditions.

The acquisition of a large amount of training data is usually the biggest hurdle, but also an essential step when training machine learning algorithms and neural networks. The amount of input data (i.e. Sentinel-1 images of giant Antarctic icebergs) could be increased easily, as there are many more icebergs tracked by the NIC and BYU and the sampling interval for each iceberg could be increased to a week or a few days rather than taking only one image per month. The challenge is that icebergs are moving targets and different areas have to be searched as they drift. So far, my intern Ella Redmond and I searched for the satellite images manually by drawing

a box around the expected position for each month and iceberg based on positions provided by BYU and then downloaded a dedicated image. This step could be automated with a script, but different areas would have to be searched at different times for each iceberg.

Manually drawing iceberg outlines, which are used for training and evaluation, is the most tedious task. There are two possible solutions, when the training data are increased to a multitude. One way would be to use the crowdsourcing platform Amazon Mechanical Turk. Here, users can upload a batch of images – in this case, the cropped Sentinel-1 input images, and people around the world click the outlines of the iceberg for a small remuneration. This approach would allow the generation of many outlines in a relatively short time. As non-experts are commissioned with this task, a scientist should check the resulting outlines afterwards. Alternatively or additionally, several users could be tasked with the same outlines to crosscheck the consistency.

The second possibility would be to use semi-supervised learning. In semi-supervised learning, a small amount of labelled data are used together with a larger amount of unlabelled data (Qi and Luo, 2022). The advantage is that less manual labelling is needed, but the training data set can be largely increased and cover a wider range of scenarios. Therefore, semi-supervised learning was found to outperform supervised learning (using only labelled data for training) in previous studies (Khaleghian *et al.*, 2021; Marszalek *et al.*, 2022). There are various approaches on how exactly the labelled and unlabelled data are used (Qi and Luo, 2022). In many cases unsupervised (i.e. relying on unlabelled data only) neural network architectures are used first. These extract useful information and yield a good, compressed representation of the unlabelled input images (Huang, Pan and Lei, 2017; Qi and Luo, 2022). In a second step, the labelled data are then used for fine-tuning and adaption to the actual task. However, in other cases the labelled data are used first and unlabelled data are added later, or both are used together (Qi and Luo, 2022). As plenty of different approaches exist, here I only suggest one approach that seems promising, but would like to stress that there are almost endless options of how exactly semi-supervised learning can be implemented.

Similar to unsupervised learning, in self-supervised learning no labels are needed. Here, the network is first given an auxiliary task that can be performed without labels to extract the main statistics of the data and yield a useful data representation (Dhere and Sivaswamy, 2021; Hoyer *et al.*, 2021). In a second step, this representation is then used and the network is fine-tuned for the actual task using the labelled data. Again, there are various creative approaches of what this auxiliary task can be. For me, a promising idea is to learn the motion (optical flow) between

consecutive images. Pathak *et al.* (2017) suggest to segment images in a video based on areas that move together in consecutive frames. This can be done without labels and the segments are then used as *pseudo ground truth* to train a network that can segment single images. Robitaille *et al.* (2022) apply a similar approach to microscopy imagery of cells, leveraging the fact that cells move more than the background. While these algorithms focus on one moving object, in the case of icebergs, also the sea ice and iceberg fragments are moving, so it is not directly transferable to our task. However, also in autonomous driving, where several objects (cars, pedestrians, etc.) are moving, optical flow is often calculated together with segmentation, as both tasks benefit from similar features and good overall scene understanding (Chen *et al.*, 2019; Hoyer *et al.*, 2021; Jiao, Tran and Shi, 2021). Hoyer *et al.*, (2021) calculate a depth map (distance to objects) as auxiliary task before segmenting RGB images in autonomous driving. And Rashed *et al.* (2019) have shown that using optical flow together with RGB images improves the segmentation for autonomous driving.

Therefore, I suggest estimating optical flow from consecutive SAR images of the same iceberg as an auxiliary task using the magnitude of additional unlabelled images first. In this case, I expect that denser temporal sampling would be advantageous, as consecutive scenes would be more similar and optical flow would be less ambiguous. This should encourage the network to learn a good representation of the images, understand the overall statistics and learn to group iceberg pixels together, as they move coherently. In a second step, this encoded representation can then be used in a supervised training with the few labelled data that we already have to generate segmentation maps. I expect that the resulting neural network would be more robust than the current U-net, as it would be trained with much more data.

### **5.3.3. Towards tracking freshwater input from giant icebergs operationally**

Ultimately, the main remaining challenge is to build an operational system to track freshwater input from all giant Antarctic icebergs along their trajectories. To achieve this, I propose to combine the methods from this thesis – and ideally using an improved version of the U-net as proposed in the previous section. Instead of an improved U-net, for now a few simple post-processing steps could be applied after the automated iceberg segmentation to further boost the accuracy. Finally, a few remaining manual steps to calculate iceberg thickness should be automated when applied on a larger scale.

Across this thesis, I developed the methods to track freshwater input from giant Antarctic icebergs with improved accuracy and efficiency compared to previous work. Chapter 2 forms

the baseline, providing a consolidated and improved pipeline to calculate iceberg melting, fragmentation and freshwater input together with their uncertainties. Chapter 3 contributes the automated collocation of altimetry tracks (where needed) and a revised estimation of the uncertainty budget. In Chapter 4, I developed a U-net that enables automated mapping of iceberg extent and is more robust to challenging environmental conditions than previously existing methods. An improved version trained with a greater amount and variability of training data (as suggested in Section 5.3.2) would further boost the accuracy. Alternatively, a few simple post-processing steps could be employed to exclude outliers from a time series of iceberg area.

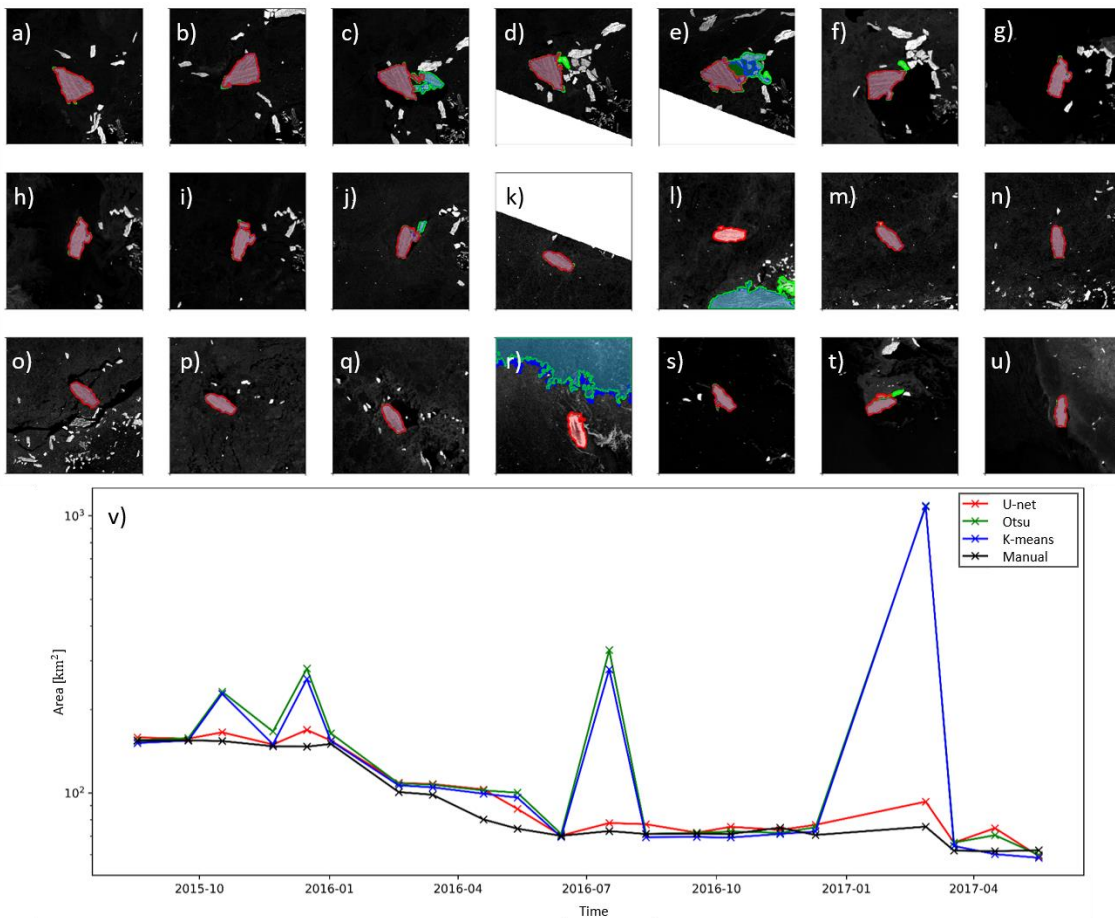


Figure 5.9: Time series of predicted outlines for the B35 iceberg. Outlines are derived from the binary segmentation maps using OpenCV’s findContours function. a-u) shows the outlines of the different methods overlain on the input images and shaded in the respective colour. v) shows the resulting area estimates over time on a log scale

To illustrate how automatically derived outlines can be used to track changes in iceberg area, I plotted time series of iceberg outlines and derived iceberg areas for the B35 iceberg as an example (Figure 5.9). Overall, U-net yields area estimates that agree with those from manually derived outlines, tracking area reductions, where they occur. Only in a few cases, iceberg area is slightly overestimated, because nearby fragments are erroneously added to the iceberg area

(Figure 5.9c, e-j and t). Compared to the standard-segmentation techniques (Otsu and k-means), the outlines from U-net are closer to the manually derived outlines in most cases. Apart from the fragments, the other two methods also generate two complete failures, picking the adjacent coast (Figure 5.9l) or a relatively busy background (Figure 5.9r) instead of the iceberg. U-net, in contrast, does not get distracted by those.

To calculate reliable freshwater input from changes in iceberg area, area deviations below 10 % - ideally around 5 % would be needed. Manual delineations are usually estimated to have a standard deviation of 2-4 % (Bouhier *et al.*, 2018; Braakmann-Folgmann, Shepherd and Ridout, 2021; Braakmann-Folgmann *et al.*, 2022). Therefore, once area deviation drops below this, it is not clear, whether U-net or the manual delineation is more accurate. In any case, an automated approach would certainly be advantageous over manual delineations – especially when rolled out for numerous icebergs or in operational applications, as it greatly reduces the time required to derive each outline. Without further post-processing or improvement, the current U-net achieves a mean absolute deviation of 15 %, a median absolute deviation of 4.1 % and 75 % of all images can be segmented with an area deviation of 12 % or less (Chapter 4).

In a tracking scenario, obvious failures could be picked out and discarded quite easily (Figure 5.9v). Such post-processing could for example compare the estimated iceberg area, length, or shape to previous estimates (Collares *et al.*, 2018; Barbat *et al.*, 2021; Koo *et al.*, 2021). Alternatively, manual inspections can be used to discard erroneous predictions (Silva and Bigg, 2005; Wesche and Dierking, 2015; Koo *et al.*, 2021). Cases where U-net does not predict anything e.g. for large areas of coast or dark icebergs, could easily be excluded from a time series, too and would simply leave gaps. Also including a land mask (Barbat *et al.*, 2019; Collares *et al.*, 2018; Frost *et al.*, 2016; Mazur *et al.*, 2017; Silva and Bigg, 2005) would be a simple step to limit false predictions at the cost of losing data just after calving or when the iceberg is too close to the coast and hence within the land mask. Therefore, with some extra post-processing or manual intervention, iceberg area estimates could be improved further. Before applying U-net operationally, I would however, suggest expanding the training data set to mitigate the remaining problem that U-net misses parts of large icebergs. I anticipate that this would further boost the overall performance – potentially making such post-processing steps redundant – and eventually yield an accurate fully automated method for giant iceberg segmentation.

From these early results, I conclude that applying the U-net from Chapter 4 and some post-processing, or ideally an improved U-net as suggested in Section 5.3.2, would greatly simplify the processing from Chapters 2 and 3, allowing it to be rolled out for more giant icebergs in the

future. Ultimately, it would be desirable to automate the whole processing chain and to build an operational system that tracks freshwater input from all giant icebergs along their trajectory. My method from Chapter 2 searches and processes altimetry tracks over the iceberg automatically. In Section 5.3.2 I suggested searching iceberg imagery automatically and together with the U-net, this would allow a completely automated calculation of changes in iceberg area. This leaves only a few, relatively quick steps requiring human intervention: The main remaining task is to find out where exactly the iceberg calved from to build the initial freeboard and thickness map. Given an initial polygon from U-net and comparing ice front geometry pre- and post-calving, the user has to shift and rotate this polygon onto the bit of the ice-shelf that calved. Potentially, this step could be automated similar to my automated collocation of tracks over the floating iceberg (Chapter 3). Apart from that, different bits of code would have to be combined into one pipeline, the downloading of ERA-5 data has to be automated, and extracting ice densities from a map by Ligtenberg, Helsen and Van Den Broeke (2011) still requires human intervention at the moment. Finally, I should mention that the processing relies on iceberg positions from the Antarctic Iceberg Tracking Database (Budge and Long, 2018) and consistently processed CryoSat-2 elevations. Overall, I believe that this thesis has contributed the main steps towards tracking freshwater input from giant icebergs operationally and that such a system would be a very valuable achievement.

### 5.4. Concluding remarks

Icebergs are a vital part of the polar environments, affecting their environment through their calving, potential grounding, and especially through the release of freshwater and nutrients along their drift trajectories (Rignot *et al.*, 2004; Helly *et al.*, 2011; Vernet *et al.*, 2012; Smith *et al.*, 2013; Bigg, 2015; Jansen *et al.*, 2015; Barnes, 2017). As the biggest tabular icebergs from Antarctica hold most freshwater, their impact is largest (Silva, Bigg and Nicholls, 2006; Tournadre *et al.*, 2016; Barbat *et al.*, 2021). Satellite observations have enabled us to track changes in freeboard and area of selected giant icebergs (Jansen, Schodlok and Rack, 2007; Bouhier *et al.*, 2018; Li *et al.*, 2018; Han *et al.*, 2019). With this thesis, I contributed additional datasets and methodological advances to quantify the freshwater flux from giant Antarctic icebergs with improved accuracy and higher efficiency using satellite remote sensing data and artificial intelligence. Besides other methodological advances, I improved the representation of snow on icebergs. Novel datasets – both from satellites and airborne surveys – have been acquired since, and could be exploited to further improve our understanding of snow on icebergs and the resulting scattering horizon of radar altimetry. I also developed a deep neural

network to map the extent of giant icebergs in Sentinel-1 imagery automatically. With this, I found improved performance compared to standard segmentation techniques, but the network misses parts of the largest icebergs due to limited training data. A multiplication of the training data and the use of a crowd-sourcing platform to label these or rather the use of semi-supervised learning would further boost the performance. Finally, the (improved) neural network could be used to track changes in area of all giant Antarctic icebergs automatically. Combined with the improved and more efficient calculation of iceberg thickness, which I developed in this thesis, freshwater flux could eventually be tracked on an operational basis.

## References

- Andersson, T. R. *et al.* (2021) 'Seasonal Arctic sea ice forecasting with probabilistic deep learning', *Nature Communications*. Springer US, 12(1), pp. 1–12. doi: 10.1038/s41467-021-25257-4.
- Arnold, E. *et al.* (2020) 'CReSIS airborne radars and platforms for ice and snow sounding', *Annals of Glaciology*, 61(81), pp. 58–67. doi: 10.1017/aog.2019.37.
- Arrigo, K. R. *et al.* (2002) 'Ecological impact of a large Antarctic iceberg', *Geophysical Research Letters*, 29(7), pp. 8-1-8–4. doi: 10.1029/2001GL014160.
- Barbat, M. M. *et al.* (2019) 'An adaptive machine learning approach to improve automatic iceberg detection from SAR images', *ISPRS Journal of Photogrammetry and Remote Sensing*. Elsevier, 156(August), pp. 247–259. doi: 10.1016/j.isprsjprs.2019.08.015.
- Barbat, M. M. *et al.* (2021) 'Automated iceberg tracking with a machine learning approach applied to SAR imagery : A Weddell sea case study', *ISPRS Journal of Photogrammetry and Remote Sensing*. Elsevier B.V., 172(December 2020), pp. 189–206. doi: 10.1016/j.isprsjprs.2020.12.006.
- Barnes, D. K. A. (2017) 'Iceberg killing fields limit huge potential for benthic blue carbon in Antarctic shallows', *Global Change Biology*, 23(7), pp. 2649–2659. doi: 10.1111/gcb.13523.
- Baumhoer, C. A. *et al.* (2019) 'Automated extraction of antarctic glacier and ice shelf fronts from Sentinel-1 imagery using deep learning', *Remote Sensing*, 11(21), pp. 1–22. doi: 10.3390/rs11212529.
- Beaven, S. G. *et al.* (1995) 'Laboratory measurements of radar backscatter from bare and snow-covered saline ice sheets', *International Journal of Remote Sensing*, 16(5), pp. 851–876. doi: 10.1080/01431169508954448.

- Bigg, G. (2015) *Icebergs: Their Science and Links to Global Change*. Cambridge University Press. doi: doi:10.1017/CBO9781107589278.
- Bouhier, N. *et al.* (2018) 'Melting and fragmentation laws from the evolution of two large Southern Ocean icebergs estimated from satellite data', *Cryosphere*, 12(7), pp. 2267–2285. doi: 10.5194/tc-12-2267-2018.
- Braakmann-Folgmann, A. *et al.* (2022) 'Observing the disintegration of the A68A iceberg from space', *Remote Sensing of Environment*. Elsevier Inc., 270, p. 112855. doi: 10.1016/j.rse.2021.112855.
- Braakmann-Folgmann, A., Shepherd, A. and Ridout, A. (2021) 'Tracking changes in the area, thickness, and volume of the Thwaites tabular iceberg "B30" using satellite altimetry and imagery', *Cryosphere*, 15(8), pp. 3861–3876. doi: 10.5194/tc-15-3861-2021.
- Budge, J. S. and Long, D. G. (2018) 'A Comprehensive Database for Antarctic Iceberg Tracking Using Scatterometer Data', *IEEE Journal of Selected Topics in Applied Earth Observations and Remote Sensing*, 11(2), pp. 434–442. doi: 10.1109/JSTARS.2017.2784186.
- Chen, Y. *et al.* (2019) 'Learning on-road visual control for self-driving vehicles with auxiliary tasks', *Proceedings - 2019 IEEE Winter Conference on Applications of Computer Vision, WACV 2019*, pp. 331–338. doi: 10.1109/WACV.2019.00041.
- Clarke, A. *et al.* (2012) 'Important bird areas: South Georgia.', *British Birds*, 105(3), pp. 118–144. Available at: <http://www.britishbirds.co.uk/articles/important-bird-areas-south-georgia>.
- Collares, L. L. *et al.* (2018) 'Iceberg drift and ocean circulation in the northwestern Weddell Sea, Antarctica', *Deep-Sea Research Part II: Topical Studies in Oceanography*. Elsevier Ltd, 149(March), pp. 10–24. doi: 10.1016/j.dsr2.2018.02.014.
- Dhere, A. and Sivaswamy, J. (2021) 'Self-Supervised Learning for Segmentation', *arXiv*, pp. 1–4. Available at: <http://arxiv.org/abs/2101.05456>.
- Dirscherl, M. *et al.* (2021) 'A novel method for automated supraglacial lake mapping in antarctica using sentinel-1 sar imagery and deep learning', *Remote Sensing*, 13(2), pp. 1–27. doi: 10.3390/rs13020197.
- Frost, A., Ressel, R. and Lehner, S. (2016) 'Automated iceberg detection using high resolution X - band SAR images', *Canadian Journal of Remote Sensing*, 42(4). doi: <https://doi.org/10.1080/07038992.2016.1177451>.
- Giles, K. A., Laxon, S. W. and Worby, A. P. (2008) 'Antarctic sea ice elevation from satellite radar altimetry', *Geophysical Research Letters*, 35(3), pp. 1–5. doi: 10.1029/2007GL031572.

- Gutt, J. (2001) 'On the direct impact of ice on marine benthic communities, a review', *Polar Biology*, 24(8), pp. 553–564. doi: 10.1007/s003000100262.
- Han, H. *et al.* (2019) 'Changes in a giant iceberg created from the collapse of the Larsen C Ice Shelf, Antarctic Peninsula, derived from Sentinel-1 and CryoSat-2 data', *Remote Sensing*, 11(4), pp. 1–14. doi: 10.3390/rs11040404.
- Helly, J. J. *et al.* (2011) 'Cooling, dilution and mixing of ocean water by free-drifting icebergs in the Weddell Sea', *Deep-Sea Research Part II: Topical Studies in Oceanography*. Elsevier, 58(11–12), pp. 1346–1363. doi: 10.1016/j.dsr2.2010.11.010.
- Hogg, O. *et al.* (2016) 'A Bathymetric Compilation of South Georgia, 1985–2015'. Polar Data Centre, British Antarctic Survey, NERC, Cambridge, UK. doi: 10.5285/ce8bf6be-4b5f-454c-9165-73ab4c3baf23.
- Holland, P. R. *et al.* (2011) 'The air content of Larsen Ice Shelf', *Geophysical Research Letters*, 38(10), pp. 1–6. doi: 10.1029/2011GL047245.
- Hoyer, L. *et al.* (2021) 'Three Ways to Improve Semantic Segmentation with Self-Supervised Depth Estimation', *Proceedings of the IEEE Computer Society Conference on Computer Vision and Pattern Recognition*, pp. 11125–11135. doi: 10.1109/CVPR46437.2021.01098.
- Huang, Z., Pan, Z. and Lei, B. (2017) 'Transfer learning with deep convolutional neural network for SAR target classification with limited labeled data', *Remote Sensing*, 9(9), pp. 1–21. doi: 10.3390/rs9090907.
- Jansen, D. *et al.* (2015) 'Brief Communication: Newly developing rift in Larsen C Ice Shelf presents significant risk to stability', *Cryosphere*, 9(3), pp. 1223–1227. doi: 10.5194/tc-9-1223-2015.
- Jansen, D., Schodlok, M. and Rack, W. (2007) 'Basal melting of A-38B: A physical model constrained by satellite observations', *Remote Sensing of Environment*, 111(2), pp. 195–203. doi: 10.1016/j.rse.2007.03.022.
- Jiao, Y., Tran, T. D. and Shi, G. (2021) 'Effiscene: Efficient Per-Pixel Rigidity Inference for Unsupervised Joint Learning of Optical Flow, Depth, Camera Pose and Motion Segmentation', *Proceedings of the IEEE Computer Society Conference on Computer Vision and Pattern Recognition*, 1, pp. 5534–5543. doi: 10.1109/CVPR46437.2021.00549.
- Joiris, C. R. *et al.* (2015) 'Major hotspots detected along the Scotia Ridge in autumn for southern right whales *Eubalaena australis*, Antarctic fur seals *Arctocephalus gazella* and Antarctic prions *Pachyptila desolata*', *Advances in Polar Science*, 26(4), pp. 282–291. doi: 10.13679/j.advps.2015.4.00282.

- Khaleghian, S. *et al.* (2021) 'Deep Semisupervised Teacher-Student Model Based on Label Propagation for Sea Ice Classification', *IEEE Journal of Selected Topics in Applied Earth Observations and Remote Sensing*, 14, pp. 10761–10772. doi: 10.1109/JSTARS.2021.3119485.
- Koo, Y. *et al.* (2021) 'Semi-automated tracking of iceberg B43 using Sentinel-1 SAR images via Google Earth Engine', *The Cryosphere*, 15(May), pp. 4727–4744. doi: <https://doi.org/10.5194/tc-15-4727-2021>.
- Kooyman, G. L. *et al.* (2007) 'Effects of giant icebergs on two emperor penguin colonies in the Ross Sea, Antarctica', *Antarctic Science*. University of Leeds, 19(1), pp. 31–38. doi: 10.1017/S0954102007000065.
- Kwok, R. *et al.* (2007) 'Ice, Cloud, and land Elevation Satellite (ICESat) over Arctic sea ice: Retrieval of freeboard', *Journal of Geophysical Research*, 112. doi: <https://doi.org/10.1029/2006JC003978>.
- Kwok, R. *et al.* (2011) 'Airborne surveys of snow depth over Arctic sea ice', *Journal of Geophysical Research: Oceans*, 116(11), pp. 1–16. doi: 10.1029/2011JC007371.
- Laxon, S., Peacock, H. and Smith, D. (2003) 'High interannual variability of sea ice thickness in the Arctic region', *Nature*, 425(6961), pp. 947–950. doi: 10.1038/nature02050.
- LeCun, Y., Bengio, Y. and Hinton, G. (2015) 'Deep learning', *Nature*, 521(7553), pp. 436–444. doi: 10.1038/nature14539.
- Li, Tian *et al.* (2018) 'Monitoring the tabular icebergs C28A and C28B calved from the Mertz Ice Tongue using radar remote sensing data', *Remote Sensing of Environment*. Elsevier, 216(July 2017), pp. 615–625. doi: 10.1016/j.rse.2018.07.028.
- Ligtenberg, S. R. M., Helsen, M. M. and Van Den Broeke, M. R. (2011) 'An improved semi-empirical model for the densification of Antarctic firn', *Cryosphere*, 5(4), pp. 809–819. doi: 10.5194/tc-5-809-2011.
- Macqueen, J. (1967) 'SOME METHODS FOR CLASSIFICATION AND ANALYSIS OF MULTIVARIATE OBSERVATIONS', in *Proceedings of the fifth Berkeley symposium on mathematical statistics and probability*. California: University of California Press., pp. 281–297.
- Marszalek, M. L. *et al.* (2022) 'Self-Supervised Learning - a Way To Minimize Time and Effort for Precision Agriculture?', *International Archives of the Photogrammetry, Remote Sensing and Spatial Information Sciences - ISPRS Archives*, 43(B3-2022), pp. 1327–1333. doi: 10.5194/isprs-archives-XLIII-B3-2022-1327-2022.

- Mazur, A. K., Wählín, A. K. and Krężel, A. (2017) 'An object-based SAR image iceberg detection algorithm applied to the Amundsen Sea', *Remote Sensing of Environment*, 189, pp. 67–83. doi: 10.1016/j.rse.2016.11.013.
- Mohajerani, Y. *et al.* (2019) 'Detection of glacier calving margins with convolutional neural networks: A case study', *Remote Sensing*, 11(1), pp. 1–13. doi: 10.3390/rs11010074.
- Mohajerani, Y. *et al.* (2021) 'Automatic delineation of glacier grounding lines in differential interferometric synthetic-aperture radar data using deep learning', *Scientific Reports*. Nature Publishing Group UK, 11(1), pp. 1–10. doi: 10.1038/s41598-021-84309-3.
- Newman, T. *et al.* (2014) 'Assessment of radar-derived snow depth over Arctic sea ice', *Journal of Geophysical Research: Oceans*, (119), pp. 3868–3882. doi: 10.1002/2014JC010284.
- Otsu, N. (1979) 'A Threshold Selection Method from Gray-Level Histograms', *IEEE Transactions on Systems, Man, and Cybernetics*, C(1), pp. 62–66.
- Pathak, D. *et al.* (2017) 'Learning features by watching objects move', *Proceedings - 30th IEEE Conference on Computer Vision and Pattern Recognition, CVPR 2017*, 2017-Janua, pp. 6024–6033. doi: 10.1109/CVPR.2017.638.
- Poliyapram, V., Imamoglu, N. and Nakamura, R. (2019) 'DEEP LEARNING MODEL FOR WATER / ICE / LAND CLASSIFICATION USING LARGE-SCALE MEDIUM RESOLUTION SATELLITE IMAGES', *IGARSS 2019 - 2019 IEEE International Geoscience and Remote Sensing Symposium*. IEEE, (d), pp. 3884–3887.
- Qi, G. J. and Luo, J. (2022) 'Small Data Challenges in Big Data Era: A Survey of Recent Progress on Unsupervised and Semi-Supervised Methods', *IEEE Transactions on Pattern Analysis and Machine Intelligence*. IEEE, 44(4), pp. 2168–2187. doi: 10.1109/TPAMI.2020.3031898.
- Rashed, H. *et al.* (2019) 'Depth Augmented Semantic Segmentation Networks for Automated Driving', *Communications in Computer and Information Science*, 1019 CCIS, pp. 1–13. doi: 10.1007/978-981-15-1387-9\_1.
- Rignot, E. *et al.* (2004) 'Accelerated ice discharge from the Antarctic Peninsula following the collapse of Larsen B ice shelf', *Geophysical Research Letters*, 31(18), pp. 2–5. doi: 10.1029/2004GL020697.
- Ronneberger, O., Fischer, P. and Brox, T. (2015) 'U-net: Convolutional networks for biomedical image segmentation', *Lecture Notes in Computer Science (including subseries Lecture Notes in Artificial Intelligence and Lecture Notes in Bioinformatics)*, 9351, pp. 234–241. doi: 10.1007/978-3-319-24574-4\_28.

- Scambos, T. *et al.* (2008) 'Calving and ice-shelf break-up processes investigated by proxy: Antarctic tabular iceberg evolution during northward drift', *Journal of Glaciology*, 54(187), pp. 579–591. doi: 10.3189/002214308786570836.
- Schmidhuber, J. (2015) 'Deep Learning in neural networks: An overview', *Neural Networks*. Elsevier Ltd, 61, pp. 85–117. doi: 10.1016/j.neunet.2014.09.003.
- Silva, T. A. M. and Bigg, G. R. (2005) 'Computer-based identification and tracking of Antarctic icebergs in SAR Computer-based identification and tracking of Antarctic icebergs in SAR images', (May 2018). doi: 10.1016/j.rse.2004.10.002.
- Silva, T. A. M., Bigg, G. R. and Nicholls, K. W. (2006) 'Contribution of giant icebergs to the Southern Ocean freshwater flux', *Journal of Geophysical Research*, 111(July 2005), pp. 1–8. doi: 10.1029/2004JC002843.
- Singh, A. *et al.* (2020) 'River Ice Segmentation with Deep Learning', *IEEE Transactions on Geoscience and Remote Sensing*, 58(11). doi: 10.1109/TGRS.2020.2981082.
- Smith, K. L. *et al.* (2013) 'Icebergs as unique lagrangian ecosystems in polar seas', *Annual Review of Marine Science*, 5(August 2012), pp. 269–287. doi: 10.1146/annurev-marine-121211-172317.
- Stokholm, A. *et al.* (2022) 'AI4Sealce: Toward Solving Ambiguous SAR Textures in Convolutional Neural Networks for Automatic Sea Ice Concentration Charting', *IEEE Transactions on Geoscience and Remote Sensing*, 60. doi: 10.1109/TGRS.2022.3149323.
- Surawy-Stepney, T. *et al.* (2023) 'Episodic dynamic change linked to damage on the thwaites glacier ice tongue', *Nature Geoscience*. Springer US, 16(1), pp. 37–43. doi: 10.1038/s41561-022-01097-9.
- Tarling, G. (2022) 'The birth and death of "megaberg" A68', *The Marine Biologist*, (April), pp. 20–21.
- Tournadre, J. *et al.* (2016) 'Antarctic icebergs distributions 1992–2014', *Journal of Geophysical Research: Oceans*. John Wiley & Sons, Ltd, 121(1), pp. 327–349. doi: 10.1002/2015JC011178.
- Vernet, M. *et al.* (2012) 'Islands of ice: Influence of free-drifting Antarctic icebergs on pelagic marine ecosystems', *Oceanography*, 25(3), pp. 38–39. doi: 10.5670/oceanog.2012.72.
- Wesche, C. and Dierking, W. (2015) 'Near-coastal circum-Antarctic iceberg size distributions determined from Synthetic Aperture Radar images', *Remote Sensing of Environment*. Elsevier Inc., 156, pp. 561–569. doi: 10.1016/j.rse.2014.10.025.

Willatt, R. C. *et al.* (2010) 'Field investigations of Ku-band radar penetration into snow cover on antarctic sea ice', *IEEE Transactions on Geoscience and Remote Sensing*. IEEE, 48(1), pp. 365–372. doi: 10.1109/TGRS.2009.2028237.

Zhang, E., Liu, L. and Huang, L. (2019) 'Automatically delineating the calving front of Jakobshavn Isbræ from multitemporal TerraSAR-X images: A deep learning approach', *Cryosphere*, 13(6), pp. 1729–1741. doi: 10.5194/tc-13-1729-2019.



# APPENDIX A

## TRACKING CHANGES IN THE AREA, THICKNESS, AND VOLUME OF THE THWAITES TABULAR ICEBERG "B30" USING SATELLITE ALTIMETRY AND IMAGERY



# Tracking changes in the area, thickness, and volume of the Thwaites tabular iceberg “B30” using satellite altimetry and imagery

Anne Braakmann-Folgmann<sup>1</sup>, Andrew Shepherd<sup>1</sup>, and Andy Ridout<sup>2</sup>

<sup>1</sup>Centre for Polar Observation and Modelling (CPOM), University of Leeds, Leeds, LS2 9JT, UK

<sup>2</sup>Centre for Polar Observation and Modelling (CPOM), University College London, London, WC1E 6BT, UK

**Correspondence:** Anne Braakmann-Folgmann (eeabr@leeds.ac.uk)

Received: 13 January 2021 – Discussion started: 5 March 2021

Revised: 8 June 2021 – Accepted: 11 July 2021 – Published: 19 August 2021

**Abstract.** Icebergs account for half of all ice loss from Antarctica and, once released, present a hazard to maritime operations. Their melting leads to a redistribution of cold fresh water around the Southern Ocean which, in turn, influences water circulation, promotes sea ice formation, and fosters primary production. In this study, we combine CryoSat-2 satellite altimetry with MODIS and Sentinel-1 satellite imagery and meteorological data to track changes in the area, freeboard, thickness, and volume of the B30 tabular iceberg between 2012 and 2018. We track the iceberg elevation when it was attached to Thwaites Glacier and on a further 106 occasions after it calved using Level 1b CryoSat data, which ensures that measurements recorded in different acquisition modes and within different geographical zones are consistently processed. From these data, we map the iceberg’s freeboard and estimate its thickness taking snowfall and changes in snow and ice density into account. We compute changes in freeboard and thickness relative to the initial average for each overpass and compare these to estimates from precisely located tracks using the satellite imagery. This comparison shows good agreement (correlation coefficient 0.87) and suggests that collocation reduces the freeboard uncertainty by 1.6 m. We also demonstrate that the snow layer has a significant impact on iceberg thickness change. Changes in the iceberg area are measured by tracing its perimeter, and we show that alternative estimates based on arc lengths recorded in satellite altimetry profiles and on measurements of the semi-major and semi-minor axes also capture the trend, though with a 48 % overestimate and a 15 % underestimate, respectively. Since it calved, the area of B30 has decreased from  $1500 \pm 60$  to  $426 \pm 27$  km<sup>2</sup>, its mean freeboard has fallen from  $49.0 \pm 4.6$  to  $38.8 \pm 2.2$  m, and its mean thickness has

reduced from  $315 \pm 36$  to  $198 \pm 14$  m. The combined loss amounts to an  $80 \% \pm 16 \%$  reduction in volume, two thirds ( $69 \% \pm 14 \%$ ) of which is due to fragmentation and the remainder ( $31 \% \pm 11 \%$ ) of which is due to basal melting.

## 1 Introduction

Iceberg calving accounts for roughly half of all ice loss from Antarctica (Depoorter et al., 2013; Rignot et al., 2013). At any time, about 50–90 large tabular icebergs are tracked in the Southern Ocean containing 7000 to 17 000 km<sup>3</sup> of ice in total (Tournadre et al., 2015). For maritime operators it is essential to know the location of icebergs in order to reduce the risk of collision (Bigg et al., 2018; Eik and Gudmestad, 2010; Power et al., 2001). The thickness of an iceberg determines if and where it will ground on the seabed, which has implications for maritime operations, as well as for marine geophysics. Iceberg thickness also influences a wide range of physical and biological interactions with the Antarctic environment. Grounded icebergs can, for example, alter the local ocean circulation (Grosfeld et al., 2001; Robinson and Williams, 2012), influence melting of the adjacent ice shelves (Robinson and Williams, 2012), and prevent local sea ice from breaking up (Nøst and Østerhus, 1998; Remy et al., 2008). This, in turn, can impact the local primary production (Arrigo et al., 2002; Remy et al., 2008) and pose an obstacle to penguin colonies on their way to their feeding grounds (Kooyman et al., 2007). Temporarily grounded icebergs leave plough marks on the sea floor which can be an important geological record (Wise et al., 2017) but also impact on marine

benthic communities (Barnes, 2017; Gutt, 2001). Therefore, iceberg thickness is an important parameter.

Changes in iceberg thickness are also important because they control the quantity of cold fresh water and terrigenous nutrients released into the ocean as icebergs melt (Gladstone et al., 2001; Silva et al., 2006). The release of relatively cold fresh water facilitates sea ice growth (Bintanja et al., 2015; Merino et al., 2016), immediately lowers the sea surface temperature (Merino et al., 2016), and has been found to even influence ocean water down to 1500 m depth (Helly et al., 2011), as well as lead to upwelling of deep ocean properties (Jenkins, 1999). In terms of nutrients, icebergs have been shown to be the main source of iron in the Southern Ocean (Laufkötter et al., 2018; Raiswell et al., 2016; Wu and Hou, 2017) and therefore foster primary production in the proximity of icebergs (Biddle et al., 2015; Duprat et al., 2016; Helly et al., 2011), which in turn increases the abundance of krill and seabirds (Joiris, 2018; Smith et al., 2007) around icebergs. Furthermore, a range of studies have demonstrated that including more realistic iceberg distributions, trajectories, and volumes in climate models leads to a redistribution of fresh water and heat flux, which agrees better with observations than models that only include small icebergs or that treat iceberg discharge as coastal runoff (Jongma et al., 2009; Martin and Adcroft, 2010; Rackow et al., 2013; Schloesser et al., 2019). To investigate each of these processes and interrelations, knowledge of iceberg thickness and volume and their change over time is required (England et al., 2020; Merino et al., 2016). Moreover, monitoring iceberg melting also presents an opportunity to gain insights into the response of glacial ice to warmer environmental conditions which may develop at ice shelf barriers in the future (Scambos et al., 2008; Shepherd et al., 2019).

The first detailed studies on iceberg melting were performed in the 1970s and 1980s, and were mainly based on laboratory experiments or ship-based observations (Hamley and Budd, 1986; Huppert and Josberger, 1980; Neshyba and Josberger, 1980; Russell-Head, 1980). These studies found that iceberg melting, to first order, is proportional to the water temperature and that for large icebergs breakage dominates over melting. More recently, Silva et al. (2006) and Jansen et al. (2007) modelled melting of giant icebergs and the associated fresh water fluxes. The latter found that melting does not only depend on ocean temperature but also on iceberg drift speed and the surrounding ocean currents. Scambos et al. (2008) installed a range of measurement tools including a GPS receiver, a pre-marked accumulation mast, and buried bamboo poles observed with a camera on a large Antarctic iceberg to monitor melting. They differentiate between three kinds of mass loss: rift calving, edge wasting, and rapid disintegration. While rift calving can occur at any time within the iceberg life cycle along pre-existing fractures, edge wasting is only observed outside the sea ice edge. Rapid disintegration is caused by surface melting and the formation of surface lakes.

The advent of satellite remote sensing greatly increased our capability to study icebergs – especially the largest ones. A wide range of studies have employed repeat satellite imagery to track changes in iceberg area (Bouhier et al., 2018; Budge and Long, 2018; Collares et al., 2018; Han et al., 2019; Li et al., 2018; Mazur et al., 2019; Scambos et al., 2008). The most common approach to measure iceberg thickness is using satellite altimeter measurements of their freeboard, which began in the late 1980s (McIntyre and Cudlip, 1987). Since then, a range of studies have employed laser and radar altimetry to study freeboard change in large tabular icebergs: Jansen et al. (2007) studied the A-38B iceberg in the Weddell and Scotia seas with a combination of laser and radar altimetry, and Scambos et al. (2008) also included three Ice, Cloud, and land Elevation Satellite (ICESat) overpasses over the A22A iceberg to derive its thickness change. Both studies make use of satellite imagery to collocate the altimetry tracks and to compare similar areas in terms of freeboard change. In contrast, Tournadre et al. (2015) employed altimetry measurements from Envisat, Jason1, and Jason2 to analyse freeboard change in the C19A iceberg without any collocation. Bouhier et al. (2018) analysed thickness changes in the B17A and C19A icebergs in open water using altimetry data without collocation. Li et al. (2018) calculated freeboard change in the C28A and C28B icebergs for 2 years at the intersections of CryoSat-2 overpasses, and Han et al. (2019) also used intersecting CryoSat-2 tracks to calculate freeboard change in the A68 iceberg in the Weddell Sea. When thickness and area changes are combined, it is possible to detect changes in iceberg volume (Bouhier et al., 2018; Han et al., 2019; Tournadre et al., 2012). However, studies to date have been limited to selected icebergs, have focussed on the Weddell Sea, and have employed a variety of approaches to account for the irregular sampling of altimetry tracks including manual collocation of entire tracks relative to the initial surface (Jansen et al., 2007), collocation of intersecting tracks (Han et al., 2019; Li et al., 2018), and no collocation at all (Bouhier et al., 2018; Tournadre et al., 2015). For smaller icebergs satellite stereo photogrammetry (Enderlin and Hamilton, 2014; Sulak et al., 2017) and interferometry (Dammann et al., 2019) have been employed to measure iceberg thickness and volume as an alternative approach, though in our experience both methods are labour intensive.

In this study, we quantify changes in the area, freeboard, thickness, and volume of the giant tabular B30 iceberg which has been adrift in the Southern Ocean since it calved from the Thwaites Glacier 8.5 years ago (Budge and Long, 2018; Fig. 1). The long life cycle and large drift of the B30 iceberg result in a relatively high number of observations, enabling a detailed study of its evolution. This is also one of the first studies to investigate iceberg thinning in the Southern Ocean around Marie Byrd Land. We assess the agreement between estimates of freeboard change determined relative to the average initial surface and using precise collocation with the aid of near-coincident satellite imagery. Moreover, we de-

velop a methodology to account for snowfall and the evolutions of snow and ice density and examine the influence of snow on the iceberg thickness calculation. The next section introduces the remote sensing data used in this study and explains our methodology; Sect. 3 presents our results on iceberg area, freeboard, thickness, and volume change in turn and discusses our findings. We close with conclusions and a brief outlook in Sect. 4.

## 2 Data and methods

To chart the iceberg area change over time we delineate its extent in a sequence of Moderate Resolution Imaging Spectroradiometer (MODIS) optical satellite imagery and Sentinel-1 synthetic aperture radar (SAR) satellite imagery. We then use CryoSat-2 satellite radar altimetry to determine changes in the iceberg freeboard and thickness, assuming that it is floating in hydrostatic equilibrium and making use of the iceberg orientation relative to its initial position using near-coincident satellite imagery on some occasions. We account for snow accumulation and model variations in snow and ice density when converting iceberg freeboard to thickness. Finally, we combine both data sets to estimate the iceberg's volume change over time.

### 2.1 Iceberg location

We use daily archived iceberg positions from the Antarctic Iceberg Tracking (AIT) database version 3.0 provided by Brigham Young University (Budge and Long, 2018) as a baseline estimate of the B30 iceberg location since it calved in 2012 (Fig. 1). The AIT database makes use of coarse-resolution passive microwave scatterometer imagery in which icebergs are manually detected and the central position is recorded daily (Stuart and Long, 2011). It includes icebergs longer than 6 km adrift in the Southern Ocean between 1987 and 2019, augmented with estimates of position and the semi-minor and semi-major axis lengths of icebergs longer than 18.5 km that are tracked operationally by the US National Ice Center (NIC) using a combination of visible, infrared, and SAR imagery.

### 2.2 Initial iceberg shape, size, and calving position

To determine the initial shape, size, and calving position of B30, we use MODIS images acquired before and after the calving event to identify which section of the Thwaites Ice Shelf calved to form the iceberg. MODIS is an instrument on the Terra and Aqua satellites of NASA launched on 18 December 1999 and 4 May 2002, respectively. The instrument measures radiance in the visible and infrared range with a spatial resolution of 250 m to 1 km and covers the entire Earth in 1–2 d, though cloud occlusions and the absence of daylight reduce data availability for many applications. For this study we use bands 1 (red), 4 (green), and 3 (blue) of

the MODIS Level 1B calibrated radiances at 500 m resolution (MOD02HKM). As B30 broke off on 24 May 2012 (Budge and Long, 2018) in Antarctic winter, during darkness, the closest useful MODIS imagery is from the preceding autumn and subsequent spring. We use several MODIS images acquired in the subsequent spring after calving to determine the initial shape as it is difficult to unambiguously distinguish the berg from clouds and sea ice in a single image. The initial perimeter (Figs. 2a and 3a) was then shifted and rotated to fit the situation before calving to identify the part of the Thwaites ice shelf that formed B30 (Fig. 4). The initial area (in plan view) of the iceberg is 1500 km<sup>2</sup> with a long axis of around 59 km (Budge and Long, 2018).

### 2.3 Iceberg area

We employ three approaches to estimate the plan-view iceberg area; (i) manual delineation in sequential satellite imagery scenes, (ii) using measurements of the semi-major and semi-minor axes provided by the NIC and assuming an elliptical shape, and (iii) using measurements of the arc lengths recorded in satellite altimetry and assuming a circular shape. While manual delineation provides the most consistent and accurate area estimate, the axis and arc-length approaches are much simpler to implement and can be fully automated.

Our main approach to determine iceberg area is manual delineation using a sequence of 32 Sentinel-1 SAR and 8 MODIS optical images. Sentinel-1A and Sentinel-1B are companion imaging radar satellites launched by the European Space Agency on 3 April 2014 and 25 April 2016, respectively. Together, they provide repeat sampling of the Earth's surface every 6 d. For this study, we use Level 1 Ground Range Detected (GRD) data. Depending on availability, both interferometric wide (IW) and extra wide (EW) swath modes are used, but over the open ocean only EW data are acquired. We employ the Sentinel Application Platform (SNAP) toolbox to apply the orbital and radiometric corrections provided with the imagery. The SAR images were multi-looked with a factor of 6 to reduce speckle and computation time, leading to a spatial resolution of 240 m. Finally, a terrain correction was applied using the GETASSE30 (Global Earth Topography And Sea Surface Elevation at 30 arc second resolution) digital elevation model. The resulting backscatter values are scaled between their 5th and 95th percentiles. The MODIS optical imagery was required prior to the launch of Sentinel-1A in 2014.

To chart changes in the iceberg area over time, we delimit its outline as a polygon in each subsequent image (Fig. 2, see also Bouhier et al., 2018; Collares et al., 2018; Han et al., 2019). When the iceberg is drifting in open water its outline can be detected automatically using boundary detection techniques (e.g. using MATLAB's `bwboundaries` function). However, in the presence of sea ice the iceberg could not be separated using this approach, and so we instead delimit its outline manually on such occasions (Bouhier et al., 2018). If

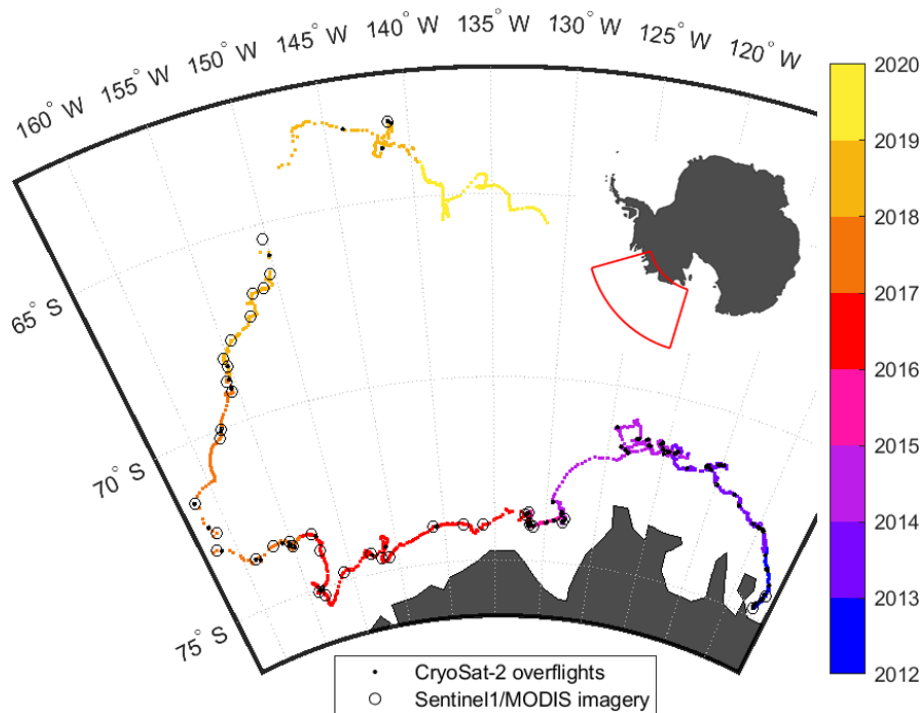


**Figure 1.** Trajectory of the B30 iceberg as recorded by the Antarctic Iceberg Tracking database (Budge and Long, 2018). After calving from the Thwaites Ice Shelf in 2012, it followed the coastal current westwards, started drifting north in 2017, and eventually disintegrated in 2019. Black dots mark the positions where CryoSat-2 overflights over the iceberg are available, and circles depict the positions of the MODIS and Sentinel-1 images used in this study.

parts of the iceberg are covered by clouds, we again use multiple MODIS images together, so that different parts of the iceberg are obscured by clouds in each image (e.g. Fig. 3l). Also sea ice frozen to the iceberg is easier to distinguish from its colour and texture when several images are used together (e.g. Fig. 3b and c). To estimate the uncertainty of our delineations, we buffer the polygons by the source imagery pixel width (500 m for MODIS images and 240 m for multi-looked Sentinel-1 images) and calculate the resulting difference in area. This gives a mean relative difference of  $3.6\% \pm 0.9\%$ .

Our second method of estimating the iceberg area is based on 228 measurements of the semi-major and semi-minor axis lengths. Although iceberg area is most accurately calculated from delineation of their full perimeter in satellite images, the downside of this approach is that it requires a high degree of time-consuming manual interaction and clear imagery. This also makes it less reproducible and subject to individual judgement. We take the size of an ellipse calculated from the semi-major and semi-minor axes provided by the NIC and compare this with our imagery-based iceberg area calculations. The NIC operationally tracks icebergs longer than 18.5 km using a combination of visible, infrared, and SAR imagery. Observations are made weekly, but especially in the early days longer data gaps exist, and not every estimate of semi-axis length is based on a new manual observation, but some are just duplicated from the previous observa-

tion. Their estimates of semi-axis lengths are also rounded to nautical miles (1.852 km), leading to a stepwise evolution of iceberg area with only eight different estimates. We base our trend estimate and analysis solely on these eight estimates because we are confident that these are unique observations. The uncertainty of this approach is governed by the assumption of an elliptical iceberg shape and the irregular, rounded updates.

Our third and final method of estimating the iceberg area is to make use of 106 CryoSat-2 satellite altimeter overpasses, which are also used to calculate the iceberg's thickness. We record the arc lengths of the iceberg sampled by these tracks and estimate iceberg area by assuming the iceberg has a circular shape. Depending on the position and relative orientation of the iceberg with respect to each overpass, CryoSat-2 will occasionally sample the long axis but more often a shorter corner. This leads to considerable variations in the area estimates and in general an underestimation. We employ a 10-point moving mean over time to reduce the variability. The principal uncertainty of this approach is because one-dimensional arc lengths cannot reliably represent a two-dimensional area especially when the shape is evolving and if it is unknown which part of the shape was sampled.

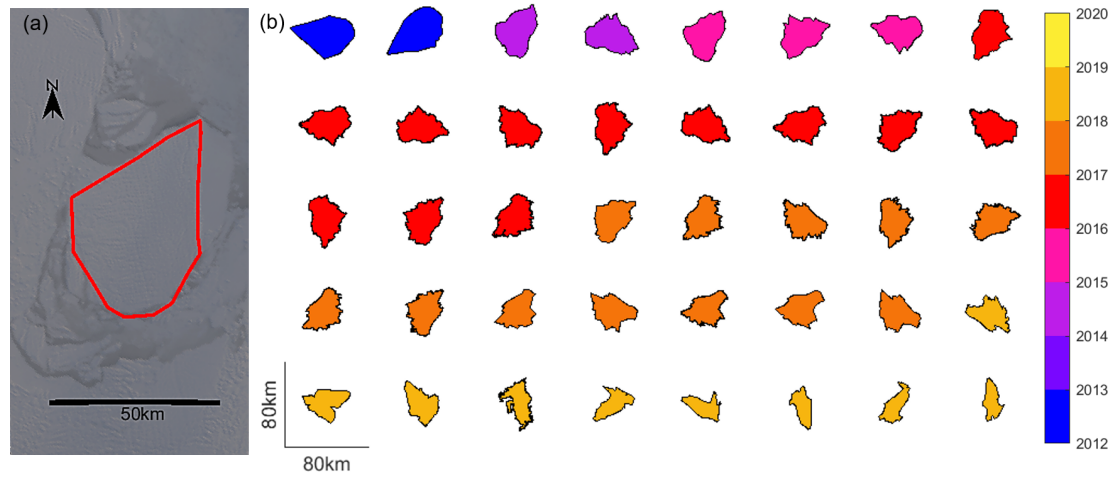


**Figure 2.** Outlines of the B30 iceberg derived from satellite imagery. (a) Initial shape (red polygon) of the B30 iceberg determined from MODIS images after calving; the background is a MODIS image on 11 September 2012. (b) Polygon outlines derived from further MODIS and Sentinel-1 imagery plotted in polar stereographic projection and used to calculate area change in the B30 iceberg.

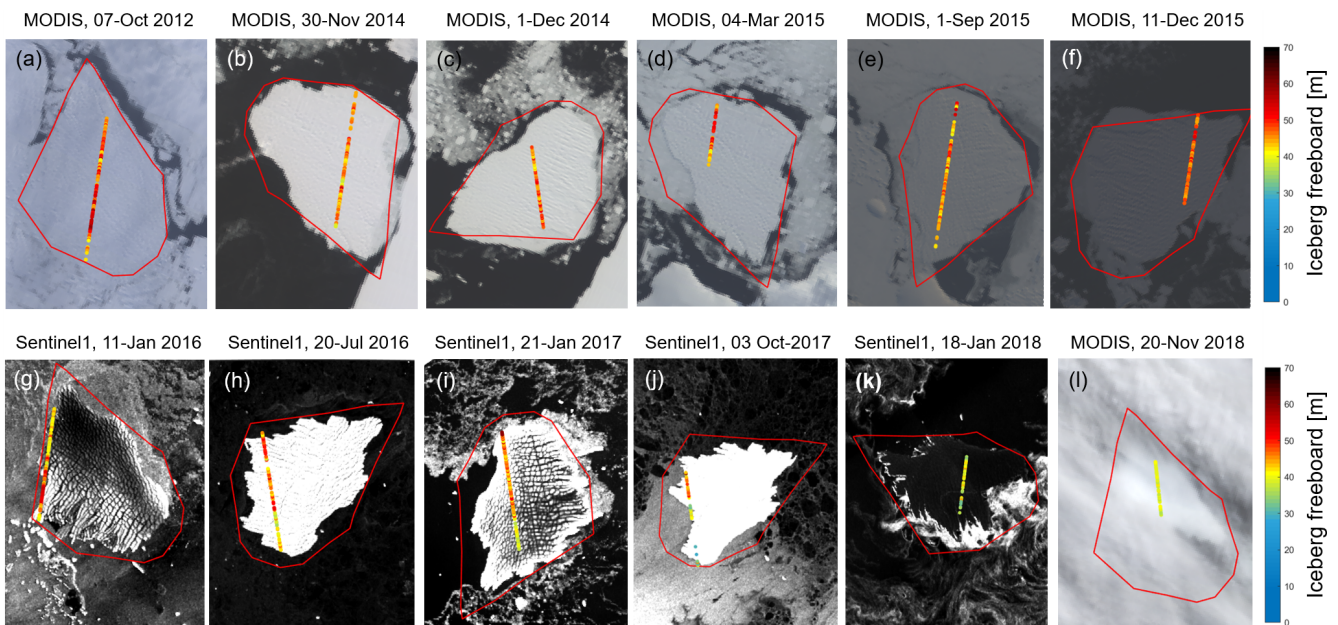


**Figure 3.** Satellite imagery with near-coincident CryoSat-2 tracks of iceberg freeboard and the manually transformed initial polygon shape plotted on top. The initial polygons are used to determine the relative position of each new overpass.

## 2.4 Iceberg orientation

To track the iceberg shape and rotation in later images relative to its initial orientation, we record the iceberg’s orientation in all satellite images that are near-coincident in time with CryoSat-2 overflights (Fig. 3). To orientate the iceberg, we manually identify the coordinates of one corner of the initial iceberg polygon outline at the time of each new overpass and adjust the rotation angle to align (colocate) all images to a common orientation (Fig. 7a–l). This allows us to transform the iceberg coordinates at the time of each image acquisition

relative to the equivalent position at the time just before it calved.

## 2.5 Initial iceberg freeboard

We use CryoSat-2 satellite altimetry to determine freeboard and thickness of the B30 iceberg. CryoSat-2 is a satellite radar altimeter that employs SAR processing to achieve an along-track resolution of 250 m. It was launched by the European Space Agency on 8 April 2010 in a 369 d repeat period with a 30 d sub-cycle. We use Level 1B baseline C data from

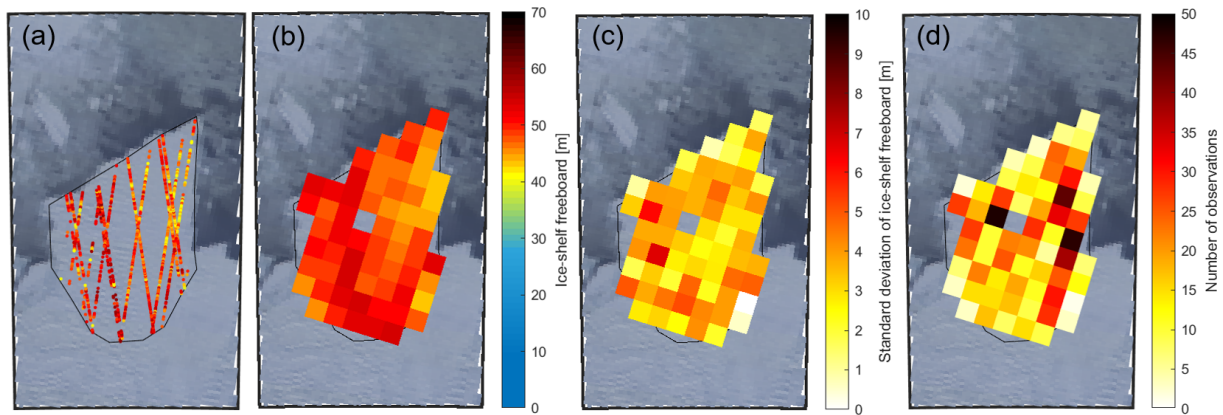


**Figure 4.** Initial freeboard heights of the B30 iceberg overlain on a MODIS image on 19 March 2012 (before calving). (a) Filtered CryoSat-2 measurements of 145 d before calving, (b) gridded CryoSat-2 data, (c) standard deviation of the gridding, and (d) number of measurements per grid cell.

the CryoSat-2 Science server and apply the Centre for Polar Observation and Modelling sea ice processing system (Tilling et al., 2018) to deduce surface height. For consistency, a common threshold retracker is applied to measurements acquired in both SAR and SAR interferometric mode and over all surface types. Using Level 1B data is important because the Level 2 products are generated using different retracker and different biases for different modes and surface types, and so the signals acquired during different parts of the iceberg trajectory are not comparable. Iceberg freeboard is calculated by subtracting the adjacent mean sea surface height from the iceberg surface height.

Although satellite altimeters only sample icebergs along one-dimensional profiles beneath their ground track while they are drifting, it is possible to build up a detailed two-dimensional picture of their surface over time prior to calving while their movement is relatively modest. To map the initial freeboard height of B30, we combine all CryoSat-2 tracks recorded within almost 5 months (1 January 2012 to 24 May 2012) before it calved (Fig. 4a). The Thwaites Ice Shelf flows at  $3.9 \text{ km yr}^{-1}$  on average (Mouginot et al., 2019), and so we adjust earlier tracks to account for this movement. Because the Thwaites Ice Shelf has a particularly rugged and crevassed surface topography, the point-of-closest-approach (POCA) varies. To make different overpasses more comparable, we remove outliers by deleting freeboard heights greater than 60 m or below 20 m freeboard (Tournadre et al., 2015), as well as crevasses by deleting freeboard heights falling either below the median minus 1 standard deviation or below the 5-point moving mean minus the 5-point moving standard deviation. After outlier removal, the mean initial iceberg freeboard is 45.5 m above the adjacent sea level with a wide spread of 8.1 m standard deviation. When crevasses are excluded, the mean freeboard is 49.0 m with a much lower standard deviation of 4.6 m. Because the resulting freeboard measurements are still quite sparse, we average them within 5 km

grid cells to obtain a continuous reference surface (Fig. 4). The number and standard deviation of the gridded freeboards give an indication of the variance within each grid cell. The mean standard deviation within each grid cell is 3.3 m, the standard deviation across different grid cells is 3.1 m, and the overall standard deviation of all heights within the polygon is 4.6 m. We compare the gridded initial freeboard to measurements from the first CryoSat overpass when the iceberg is adrift, acquired shortly after calving, to check they are consistent and find a mean difference of  $-0.4 \text{ m}$ . As this value is considerably lower than the iceberg freeboard variability, we conclude that the ice shelf was floating freely prior to calving also and that the gridded heights are representative of the initial freeboard.

## 2.6 Iceberg freeboard change

When icebergs are adrift, their motion is sufficiently large to mean that they are only sampled in one-dimensional profiles along satellite altimeter ground tracks (Fig. 3) and that only the largest tabular icebergs are sampled frequently enough to derive changes in their freeboard. We extract surface heights over the B30 iceberg when it is adrift (e.g. Fig. 5) using the position from the AIT database as an initial estimate of its location. However, because the AIT positions and timings are approximate and the iceberg has a significant extent, we investigate all CryoSat-2 ground tracks that pass within  $1^\circ$  latitude and  $2^\circ$  longitude of the database position. We automatically extract measurements sampling the iceberg with the following steps: track segments are truncated to exclude altimeter echoes from targets where the first or last freeboard height is more than 3 m to exclude measurements from the nearby continent, and we also exclude tracks that do not contain freeboard measurements between 20 and 60 m to ensure that they sample the iceberg. We consider all freeboard heights between the first and last echo falling in the range

of 20 to 60 m as potential iceberg measurements (Tournadre et al., 2015). To avoid including adjacent icebergs or berg fragments, we exclude segments with more than 10 measurements of ocean or sea ice, identified as surface heights in the range of  $-3$  to  $+3$  m, between potential iceberg measurements. We also remove crevasses and other rugged features using the same editing steps applied to determine the surface height prior to calving. As a final check, we calculate the distance of these remaining heights to the AIT database location and discard measurements that are further away than half the iceberg length (28 km) to ensure we are tracking B30.

We apply two different techniques to calculate changes in the iceberg freeboard. For 12 tracks we are able to calculate precise changes in freeboard with spatial definition by making use of near-coincident satellite imagery to account for the rotation and translation of the iceberg relative to its initial position prior to calving (Jansen et al., 2007) and consider the estimated movement between the time of the nearest satellite image and altimeter acquisitions. At 94 other times, we compute the freeboard height change as the difference of mean freeboard from each new overpass relative to the initial mean surface height. While these observations are of poorer certainty, they provide denser temporal sampling and fill gaps between the colocated measurements. The first collocation method assigns both the initial heights and the new measurements to their closest 5 km grid cell and averages them to ensure that the same locations are compared. We account for the iceberg drift between the times of the satellite acquisitions, allowing a maximum separation of 72 h (though most overpasses are separated by less than 24 h). If the image is from a different date than the CryoSat track, we correct the distance travelled based on the daily iceberg locations from the AIT database. In any case, we account for the drift in our uncertainty estimate performing a Monte Carlo simulation with 1000 slightly differently colocated samples per track. These are normally distributed around our estimated translation and rotation with a standard deviation of  $15^\circ \text{d}^{-1}$  and a drift speed of  $3 \text{ km d}^{-1}$  (Scambos et al., 2008) scaled by the respective time separation. We then calculate the freeboard difference for each of the 1000 slightly differently colocated tracks and use the resulting standard deviation of freeboard change from these samples as the uncertainty of our collocation. This is combined with the standard deviation of the gridded CryoSat-2 freeboard data (of the new track and of the reference) to yield a conservative uncertainty estimate for the colocated tracks. The second method ignores the relative position and orientation of the iceberg at the time of the altimeter overpasses (Bouhier et al., 2018; Tournadre et al., 2015) and simply compares the mean freeboard along each new track to the mean surface height before calving. Although this method is easiest since it does not rely on additional image data to locate the track, it cannot account for potential spatial variations in the iceberg freeboard. Because of this, we restrict the new overpasses to those including at least 20 measurements as tracks sampling only the edges of

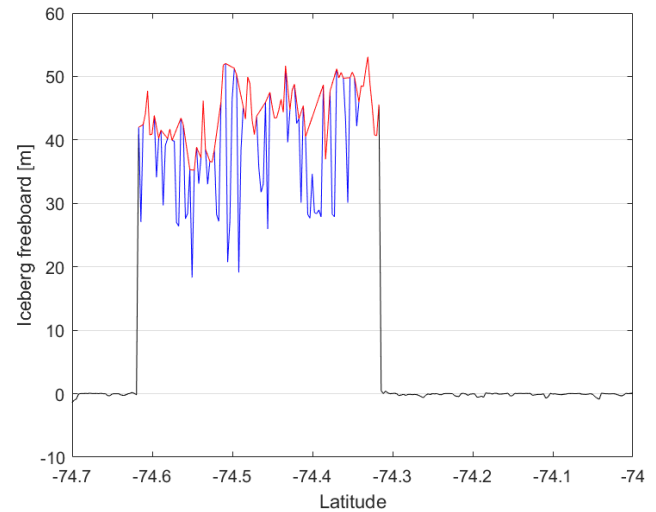


**Figure 5.** Example of CryoSat-2 freeboard measurements along one track. The blue line shows which heights were identified as iceberg, and the red line shows the remaining heights after filtering out crevasses.

an iceberg tend to be inaccurate. As uncertainty estimate we combine the standard deviation of each new overpass with the standard deviation of the initial height. As a first check to see if the mean freeboard from a single overpass can be compared to the mean initial height, we calculate the mean height for each of the 15 tracks over the pre-calved iceberg (Fig. 4a) and find a standard deviation of 2.8 m compared to the mean initial height of  $49.0 \pm 4.6$  m.

## 2.7 Iceberg thickness

We compute iceberg thickness  $H$  (freeboard plus draft) from our estimates of iceberg freeboard heights  $h_{\text{fb}}$  assuming hydrostatic equilibrium and that CryoSat-2 does not penetrate through the snow layer (Eq. 1; Moon et al., 2018). Besides these freeboard heights, iceberg thickness also depends on column-average densities of seawater  $\rho_w$ , ice  $\rho_i$ , and snow  $\rho_s$ , as well as snow depth  $h_s$ . Including a snow layer in this equation is important because the snow layer adds to the observed freeboard and disguises a part of the ice freeboard change. On the other hand the additional load of the snow layer pushes the iceberg downwards. Both effects are taken into consideration. We assume seawater density to be  $1024 \text{ kg m}^{-3}$  (Fichefet and Morales Maqueda, 1999) and set its uncertainty to  $2 \text{ kg m}^{-3}$ . Due to the long life cycle of the B30 iceberg of 6.5 years and the changing environmental conditions it experiences during this time, we allow the ice and snow densities to evolve with time. Snow depth is also time-varying, and estimates of this and of snow and ice density are introduced successively.

$$H = \frac{\rho_w}{\rho_w - \rho_i} h_{\text{fb}} - \frac{(\rho_w - \rho_s)}{\rho_w - \rho_i} h_s \quad (1)$$

To estimate the thickness of the snow layer, we download hourly ERA5 Reanalysis snowfall, snowmelt, and snow evaporation data (Copernicus Climate Change Service, 2018), accumulate it daily, and interpolate it in space and time to the iceberg's trajectory. Snowmelt and snow evaporation are subtracted from the snowfall to retrieve the additional snow accumulation since calving. However, this snow estimate does not account for snow being blown off the iceberg or onto the iceberg from the continent (Fedotov et al., 1998; Leonard and Maksym, 2011). To convert snow water equivalent (SWE) to snow depth, we need to know snow density.

Snow density is time variable because snow compacts gradually during the iceberg's life time of several years as a function of snow depth  $h_s$  (m), the mean air temperature  $T$  ( $^{\circ}\text{C}$ ), and the mean wind speed  $v$  ( $\text{m s}^{-1}$ ) (Eq. 2; International Organization for Standardization, 1998). We use hourly ERA5 Reanalysis 2 m air temperature data and calculate wind speed from the ERA5 Reanalysis 10 m eastwards and northwards wind components (Copernicus Climate Change Service, 2018). Both are interpolated to the iceberg's trajectory and averaged since the day of calving. Because snow density depends on snow depth and snow depth depends on snow density, we calculate both iteratively starting with a snow density of  $300 \text{ kg m}^{-3}$ . We set the uncertainty in snow density to  $50 \text{ kg m}^{-3}$  (Kurtz and Markus, 2012) and the uncertainty in snow depth to 20 % (Kwok and Cunningham, 2008).

$$\rho_s = \left(90 + 130 \cdot \sqrt{h_s}\right) \cdot \left(1.5 + 0.17 \cdot \sqrt[3]{T}\right) \cdot (1 + 0.1 \cdot \sqrt{v}) \quad (2)$$

To calculate the iceberg's ice density profile we follow the approach by Tournadre et al. (2015) and determine two parameters  $V$  and  $R$  to fit the surface density and the depths of the critical density levels ( $550$  and  $830 \text{ kg m}^{-3}$ ) of the Thwaites Ice Shelf, from which it calved, as given in Ligtenberg et al. (2011; Eq. 3);  $\rho_g$  is the density of pure glacial ice ( $915 \text{ kg m}^{-3}$ ). Since the mean ice density depends on ice thickness and ice thickness depends on the mean ice density, we iterate over both equations. We also account for ice density changes over the iceberg's life cycle by calculating new mean densities as the iceberg thins. This incrementally reduces the average ice density as the densest ice is melted at the bottom. As ice density uncertainty we take  $10 \text{ kg m}^{-3}$  (Dryak and Enderlin, 2020).

$$\rho_i = \frac{1}{H} \int_0^H (\rho_g - V \cdot e^{R \cdot z}) dz \quad (3)$$

### 3 Results and discussion

We first assess changes in the B30 iceberg area using boundaries mapped from satellite imagery, and we compare the observed trend to less accurate estimates derived from

arc lengths and semi-major axes. Next, we determine the change in iceberg freeboard, and we assess the impact of employing precise collocation using near-coincident satellite imagery. Iceberg thickness changes are then computed from freeboard changes using time-varying estimates of snow accumulation and snow and ice densities derived from atmospheric reanalyses. Finally, iceberg area and thickness changes are combined to derive the change in volume and mass.

#### 3.1 Iceberg area change

When the B30 iceberg first calved in May 2012, it was  $1500 \pm 60 \text{ km}^2$ . Over the following 6.5 years it lost  $1075 \pm 66 \text{ km}^2$  of its extent, which corresponds to a  $72 \% \pm 11 \%$  reduction at an average rate of  $149 \pm 5 \text{ km}^2$  per year (Fig. 6). However, because deriving iceberg outlines requires a high degree of time-consuming manual interaction, we also evaluate the efficacy of two alternative methods based on measurements of their orthogonal (semi-major and semi-minor) axes by the NIC and on arc lengths recorded in satellite altimetry which are considerably less laborious. Although these approaches also yield progressive reductions in area (Fig. 6), they exhibit significant positive ( $138 \text{ km}^2$ , 14 %) and negative ( $-426 \text{ km}^2$ , 45 %) biases, respectively, due to under-sampling of the iceberg geometry and the necessary approximation of a regular shape (ellipses and circles, respectively). While an ellipse overestimates the area compared to most shapes with the same axes, arc lengths yield an underestimate because corners are sampled more often than the major axis. One idea for improvement would be to use the maximum or to filter out tracks that only sample one corner, but the main problem remains that a one-dimensional length measurement cannot be translated into a reasonable area estimate without knowing the iceberg shape, which changes over time. Nevertheless, both the orthogonal axes and arc-length approaches yield area estimates that are reasonably well correlated ( $r > 0.90$ ) with those determined from our manual delineation. Area trends are overestimated by 16 % and underestimated by 48 %, respectively. While manual delineation provides the most consistent and most accurate area estimate, tracking iceberg axes or arc lengths yields area and area change estimates that are within 48 % and is considerably less time consuming.

The rate of iceberg area loss from B30 was approximately constant until 2018, after which time it started to lose larger sections more rapidly. Although its area has reduced steadily over time, it is less obvious which sections have been lost during individual calving events. However, by aligning the initial polygon to each subsequent image (Fig. 3) it is possible to identify when and where changes occur. The iceberg shape already appears altered on 30 November 2014 after bumping into the adjacent ice shelf which likely caused the first chunks to break off. B30 continued to lose smaller sections along its edges over the next year – either through

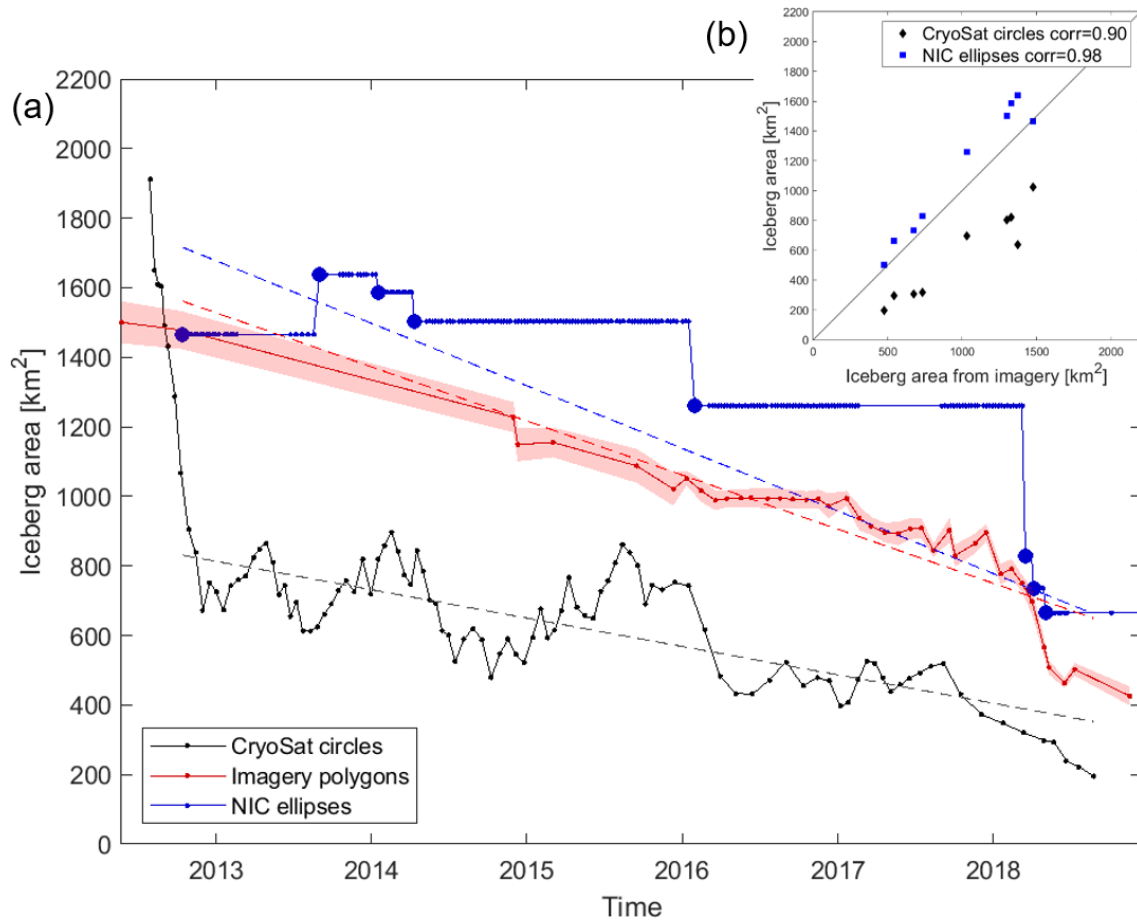


**Figure 6.** Area change in the B30 iceberg from polygons delineated in satellite imagery with their uncertainty (red) and approximations using orthogonal axes provided by the National Ice Center (NIC) assuming an elliptical shape (blue) or using the arc lengths of CryoSat-2 overflights assuming a circular shape (black) over time (a) and as scatter plot (b). To fit the NIC trend line in (a) we only use unique values of orthogonal axis length (thick blue dots). These also define the dates of comparison in (b).

melting at the sides or smaller wastings – when it was drifting along the coastal current. In 2018, bigger sections are lost more rapidly as the iceberg is drifting northwards in open water. Rift calving can occur at any time within an iceberg life cycle along pre-existing fractures (Scambos et al., 2008), while edge wasting is typically only observed when icebergs are travelling outside the sea ice pack. B30 was heavily crevassed prior to calving (e.g. visible in Fig. 3g and i), and so even the smaller wastings along its edges could reflect rift calving events rather than edge wastings. The “foot-loose mechanism” (Wagner et al., 2014) can become a main driver of iceberg decay in warm waters when wave erosion at the waterline forms a sub-surface foot, creating a buoyancy stress that can lead to calving. Although it is not possible to investigate the effects of wave erosion using satellite data, the effect could in principle have caused the larger break-ups that occurred in 2018.

### 3.2 Iceberg freeboard change

To assess the change in freeboard over the survey period, we compare differences between the new overpasses and the initial heights in space and time (Fig. 7). For the spatial analysis we chart the freeboard difference between each collocated overpass post-calving (Fig. 3) and the gridded initial height pre-calving (Fig. 4b) at the same relative iceberg position. This comparison shows that the change in freeboard height across the iceberg is relatively homogenous at each epoch (Fig. 7a–l). We then average these differences per CryoSat-2 track and chart the variation over time alongside the less accurate (but more abundant) estimates determined without collocation (Fig. 7m). Because the observations without collocation are relatively imprecise, we apply a 10-point moving mean to the data, and we also fit a polynomial of 3rd order (and starting at zero). Overall, the B30 iceberg freeboard has reduced by  $9.2 \pm 2.2$  m during the 6.5 years since it calved.

To assess the importance of collocation, we compare freeboard changes calculated with and without this step (Fig. 7n).

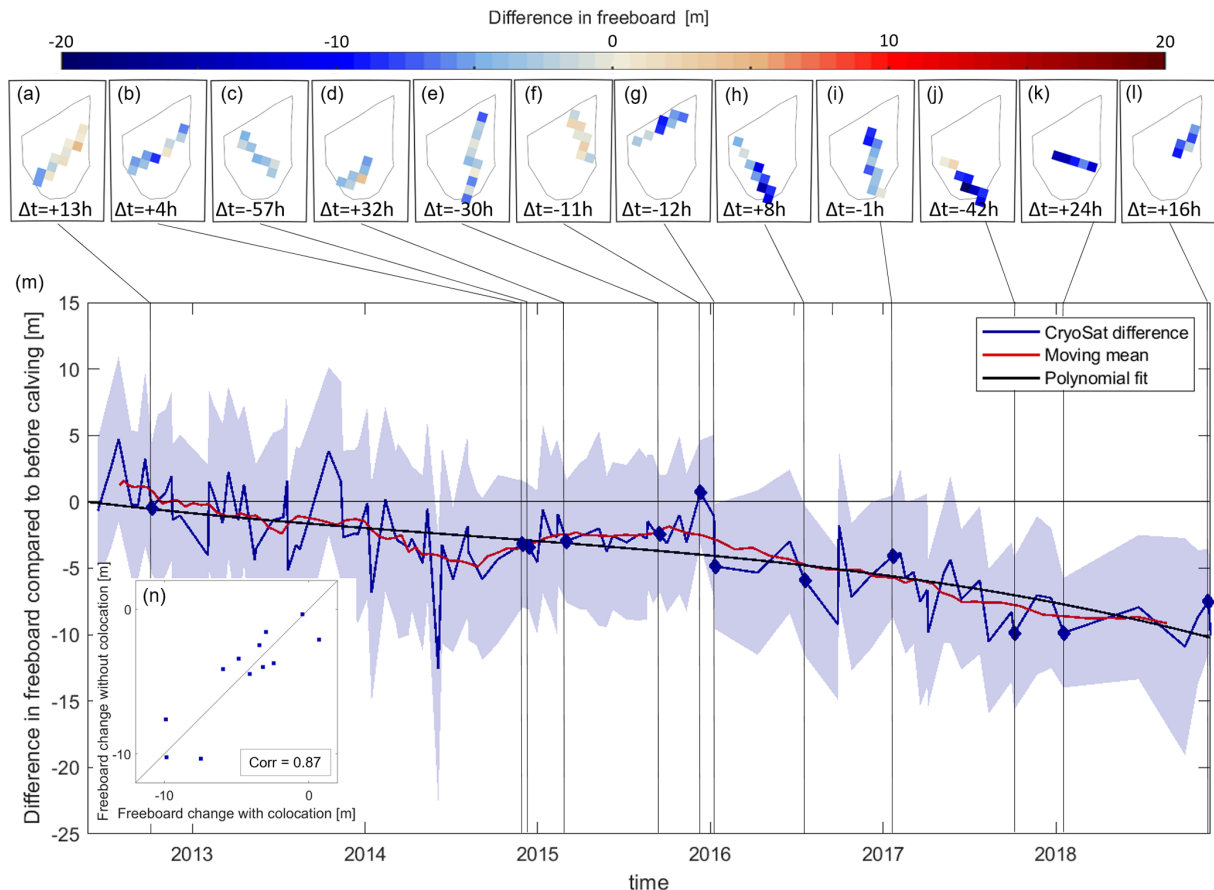


**Figure 7.** Freeboard change in the B30 iceberg. (a–l) Freeboard difference in each grid cell sampled by colocated CryoSat-2 overpasses; the  $\Delta t$  values give the time difference between the CryoSat-2 overpass and the corresponding satellite image as an indication of the collocation uncertainty due to iceberg drift. Negative values indicate that the image was taken before the CryoSat overpass. (m) Mean difference of each new overpass through time. CryoSat-2 tracks that have been colocated are marked with a diamond, but all available CryoSat-2 overpasses have been used to calculate a moving mean and fit a polynomial; the shading shows the standard deviations. (n) Scatter plot of freeboard change from colocated CryoSat-2 tracks versus the same tracks used without collocation.

The estimates are well correlated ( $r = 0.87$ ), and the root mean square difference is 1.6 m, which is a measure of the improvement in certainty associated with collocation and equal to the difference in mean uncertainty of colocated tracks (4.7 m) versus tracks without collocation (6.3 m). Also, the temporal variation of freeboard changes computed from observations with and without collocation are in good overall agreement (Fig. 7m), and we conclude that for this iceberg we can combine the two and make use of the entire set of CryoSat-2 measurements. This finding should hold for other tabular icebergs where the topographic variability is smaller than the observed thinning. The variability of freeboards computed within each 5 km grid cell and across different grid cells are also of the same order (3.3 and 3.1 m, respectively), and this is likely to have reduced the impact of collocation uncertainties. For other icebergs with more heterogeneous freeboard across the iceberg that are less crevassed (i.e. with lower freeboard variabilities within the same grid cell), colo-

cation might have a larger impact, and more icebergs need to be studied to generalise these findings.

### 3.3 Iceberg thickness change

We compute the iceberg thickness from our measurements of its freeboard (using the moving mean, red line in Fig. 7m) and by assuming that it is floating in hydrostatic equilibrium within the surrounding ocean with a surface snow layer. Accounting for the snow layer is important because it affects the ice freeboard and the iceberg buoyancy, and we take both effects into consideration. Based on hourly snowfall, evaporation, and snowmelt derived from ERA5 reanalyses (Copernicus Climate Change Service, 2018), we estimate that the iceberg accumulates 4.6 m of snow water equivalent during the 6.5 year survey period (Fig. 8). The rate of accumulation is quite linear. The iceberg thickness also depends on densities of the snow layer, the iceberg, and the seawater, and we allow the snow layer and iceberg densities to evolve

over time due to the changing environmental conditions it experiences during its long life cycle. The mean iceberg density reduces from an initial estimate of  $864 \text{ kg m}^{-3}$  to a final value of  $835 \text{ kg m}^{-3}$  as a consequence of basal ice melting (Fig. 8a). The mean change in height due to firn densification in West Antarctica has been estimated to be 2.79 cm per year on floating ice (Zwally et al., 2005); upscaling this rate gives a total of 18 cm after 6.5 years, which is significantly smaller than the observed freeboard loss of 9.2 m, so we do not apply it. The snow layer compacts over time due to its accumulation and warming, and we estimate that its average density rises from  $252$  to  $616 \text{ kg m}^{-3}$ , which yields a 7.2 m thick layer after 6.5 years (Fig. 8b). We also investigate the impact of surface thawing; although the iceberg surface does experience temperatures above freezing every summer and for a total of 218 degree hours (number of hours above  $0^\circ\text{C}$  times the temperature above  $0^\circ\text{C}$ ) since calving (Fig. 8c), in situ observations (Scambos et al., 2008) suggest that this translates into only 8 to 16 cm of snow melting, and this has a negligible impact on the iceberg freeboard, so we discard this effect.

We estimate the initial iceberg thickness to be  $315 \pm 36$  m, on average, reducing to  $198 \pm 14$  m after 6.5 years. This amounts to  $117 \pm 38$  m of thinning (Fig. 8d) at an average rate of  $17.3 \pm 1.8$  m per year. Previous studies have recorded iceberg thinning rates of up to 10 m per year when drifting within the sea ice extent close to the coast (Han et al., 2019; Jansen et al., 2007; Li et al., 2018; Morgan and Budd, 1978; Scambos et al., 2008) and much higher rates in excess of 20 m per year when in warmer open water (Hamley and Budd, 1986; Jansen et al., 2007; Li et al., 2018; Morgan and Budd, 1978; Scambos et al., 2008; Tournadre et al., 2015). Jacka and Giles (2007) find dissolution rates of 11–18 m per year between  $60$  and  $150^\circ\text{E}$  based on shipborne observations over 15 years. Although all these studies were conducted for different regions of the Southern Ocean, our estimated average thinning rate is in line with the melt rates previously reported given that the B30 iceberg has spent most of its lifetime close to the coast (Fig. 1). To assess the impact of including a snow layer in the thickness calculation, we also compute thickness change assuming no snow has accumulated since calving (Fig. 8d); this scenario leads to an estimated  $90 \pm 39$  m reduction in iceberg thickness, 23 % lower than the rate determined when the snow layer is included, which illustrates its importance. We expect the importance of including a snow layer to be highest in phases when the iceberg is melting slowly as snow accumulation can disguise the thickness change in this instance. Based on the mostly linear snow accumulation, it will also be more important the longer the iceberg survives as more snow accumulates. Apart from the snow layer, iceberg density is also a significant factor in our thickness change calculation, and while we have attempted to model the evolutions of ice density, snow density, snow accumulation, and surface thawing, their uncertainties are difficult to quantify.

Besides the observed thinning, the iceberg also seems to slightly thicken between mid-2014 and early 2015. During this time B30 was very close to the coast (Fig. 3b–d). Therefore, a range of processes – both physical processes that impact the actual thickness of the iceberg and processes that impact the freeboard measurement – could have caused this gain in thickness. First of all, iceberg thickness can increase through marine ice formation when the iceberg is surrounded by very cold water. Little et al. (2008) found that freezing beneath ice shelves is concentrated along their western side, and B30 was indeed located at the western side of Getz Ice Shelf at this time (Figs. 1 and 3b and c). Iceberg thickness can also grow through snow accumulation on the surface, which we account for, but only based on reanalysis data, and there might be additional local snowfall or snow accumulation through strong katabatic winds from the nearby continent (Fedotov et al., 1998). Furthermore, external forcing from collisions with the adjacent ice shelf might have led to a deformation (MacAyeal et al., 2008) and hence a compression in some parts. All of these processes can cause a physical increase in iceberg thickness. Apart from that, a short (partial) grounding could lead to higher measured iceberg freeboards (Li et al., 2018). Also surface melting could shift the scattering horizon of CryoSat-2 (Otosaka et al., 2020) and therefore appear like a freeboard increase. Indeed we observe a steep increase in degree hours around the turn of the year 2015. What caused the signal in this instance is hard to disentangle. Most probably, it was a combination of several of the mentioned effects.

### 3.4 Iceberg volume and mass change

Having calculated changes in the B30 iceberg thickness associated with snowfall and basal melting and changes in area due to fragmentation, we combine both to determine the overall change in volume (Fig. 9). To do this, we multiply each thickness estimate with the imagery-based area estimates interpolated to the times of the CryoSat-2 overpasses. Unlike small icebergs, which can take on various shapes (Enderlin and Hamilton, 2014; Sulak et al., 2017), large tabular icebergs inherit their shape from their parent ice shelf and therefore have rather homogenous thickness and near vertical walls (American Meteorological Society, 2012). Deviations from vertical may occur in both directions, and we therefore expect them to approximately even out (Orheim, 1987). The larger the length to thickness ratio is, the smaller the impact of tilted side walls on the resulting volume. For the B30 iceberg with an initial length to thickness ratio of 187 : 1, we therefore conclude that our assumption of vertical walls has negligible impact on the volume. The proportion of the total volume changes associated with melting and fragmentation is calculated by keeping area and thickness constant (and equal to their average), respectively. To compute changes in mass, we multiply the volume change due to fragmentation by the column-average iceberg density at each point in time

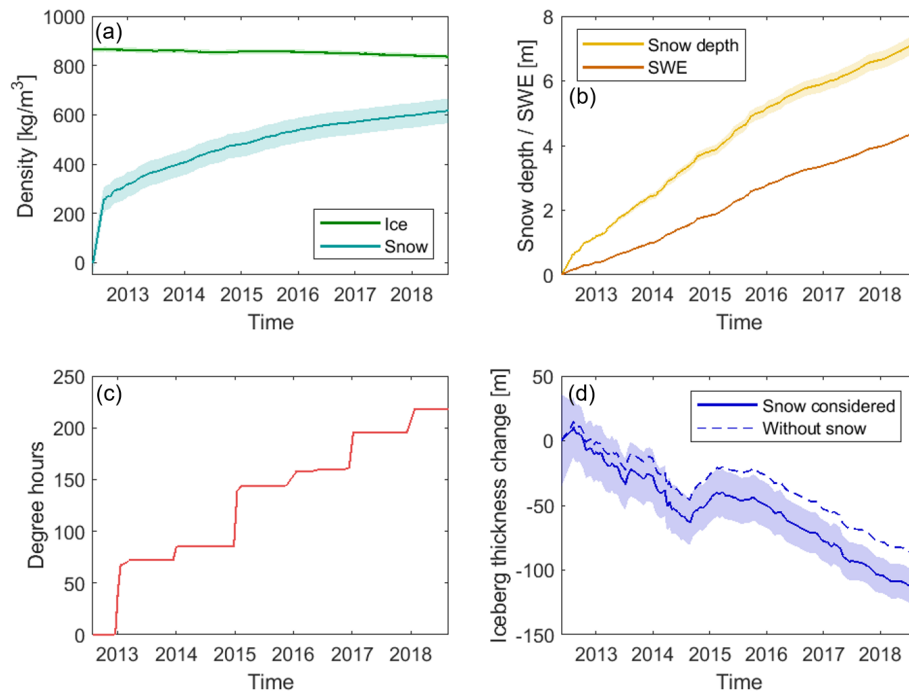


**Figure 8.** Evolution of the B30 iceberg properties: (a) ice density and snow density, (b) snow water equivalent (SWE) and snow depth accumulation on the B30 iceberg, (c) degree hours that the B30 iceberg experienced, and (d) thickness change in the B30 iceberg with and without snow accumulation taken into consideration. Uncertainties are plotted as shaded areas.

because this ice is lost at the sides. In contrast, we multiply the volume change due to basal melting by the density of pure ice ( $915 \text{ kg m}^{-3}$ ) since this ice is lost at the bottom where ice density is highest. The total mass change is the sum of both components. Uncertainties are calculated by propagating the uncertainties of thickness change, area change, and ice density.

The initial volume of B30 at the time of its calving was  $472 \pm 57 \text{ km}^3$ , and after 6.5 years it had lost  $378 \pm 57 \text{ km}^3$  of ice, corresponding to a  $80\% \pm 16\%$  reduction. Fragmentation accounts for two thirds ( $69\% \pm 14\%$ ) of the total volume loss, and basal melting is responsible for the remainder ( $31\% \pm 11\%$ ). Volume changes due to fragmentation become the dominant source of ice loss towards the end of our survey, consistent with previous findings (Bouhier et al., 2018). This is because the main drivers of fragmentation are surface melting, which can lead to a rapid disintegration (Scambos et al., 2008), and wave erosion or wave stress (Wagner et al., 2014). Both increase the further north (i.e. surrounded by open ocean and warmer air temperatures) the iceberg gets. The two icebergs studied by Bouhier et al. (2018) also show similar fractions of ice loss due to fragmentation (60% for the B17A iceberg and 75% for the C19A iceberg). In terms of mass, the iceberg lost  $325 \pm 44 \text{ Gt}$  of ice in total at an average rate of  $46 \pm 4 \text{ Gt}$  per year. The loss due to basal melting ( $106 \pm 35 \text{ Gt}$ ) can be used as a lower estimate of the freshwater flux from B30. Some of the mass lost due to changes in area – in particular melting at the sides and smaller edge

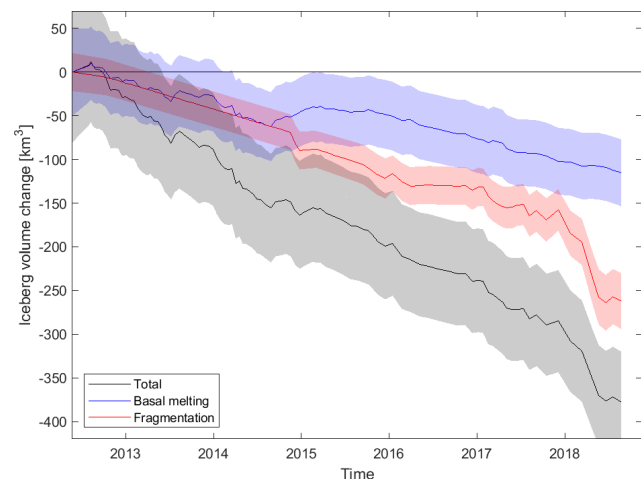


**Figure 9.** Volume change in the B30 iceberg divided into loss due to basal melting (thickness change, blue) and due to fragmentation (area change, red), as well as total volume loss (black).

wastings, which will probably melt locally – adds to the freshwater flux, but bigger calving events create smaller icebergs, which can survive and travel on their own (Bigg et al., 1997; England et al., 2020; Martin and Adcroft, 2010). To calculate the total freshwater flux, the melting of all fragments has to be considered (Tournadre et al., 2012, 2016).

## 4 Conclusions

In this study we have derived changes in the area, freeboard, thickness, and volume of the tabular B30 iceberg using a combination of satellite altimetry and satellite imagery. During the 6.5 years after the iceberg calved in May 2012, its area reduced from  $1500 \pm 60$  to  $426 \pm 27$  km<sup>2</sup> at an average rate of  $149 \pm 5$  km<sup>2</sup> per year. The iceberg freeboard lowered by  $9.2 \pm 2.2$  m over the same period. Using estimates of the snow accumulation and changes in snow and ice density, we estimate that the iceberg thinned by  $117 \pm 38$  m at a mean rate of  $17.3 \pm 1.8$  m yr<sup>-1</sup>. Altogether, the iceberg lost  $378 \pm 57$  km<sup>3</sup> of ice, and this equates to an estimated  $325 \pm 44$  Gt reduction in mass.

We investigated the capability of automated approaches to approximate iceberg area and area change by comparing them to manually derived estimates. Although the most reliable method of charting iceberg area change is through manual delineation in satellite imagery, we show that less time-consuming estimates derived from measurements of the iceberg's orthogonal axes or arc lengths are also able to capture the area and area change over time, albeit with poorer certainty. Orthogonal axes lead to estimates of area and area trends that are 14 % and 16 % higher, respectively, and arc lengths lead to estimates of area and area trends that are 45 % and 48 % lower due to the necessary approximation of the iceberg shape.

We also presented a new thorough methodology to investigate iceberg freeboard and thickness change using a densely sampled time series of consistently processed Level 1 CryoSat data and assessed the importance of collocation. Using a subset of 12 instances with collocation, we find that omitting this step leads to a small deterioration in the certainty of detected freeboard change for the B30 iceberg, but the densely sampled time series is in good agreement with the colocated tracks. We expect this finding also holds for other large tabular Antarctic icebergs with uniform topography when the observed freeboard change exceeds the topography and when enough tracks are averaged. In this case, it suggests that the procedure for tracking changes in iceberg thickness could be automated given reliable estimates of their position (Budge and Long, 2018).

Finally, we developed a methodology to account for snowfall and variations in snow and ice density due to changing environmental conditions that large icebergs experience during their multi-annual drift. We found that the impact of snowfall on the retrieval of iceberg thickness increases over time, and after 6.5 years we estimate that 7.2 metres of snow have accumulated, which leads to a 27 m adjustment to the iceberg thickness change. Iceberg thickness change is also strongly dependent on the ice density profile which we derive from the depths of critical density levels (Ligtenberg et al., 2011), and so in situ observations would help to assess the reliability of this relationship. Likewise, direct measure-

ments of the near-surface firm will help to assess the reliability of our reanalysis-based estimate of snow loading.

More icebergs – including the fragments lost from B30 – need to be studied to generalise the results we have and to constrain both the fresh water flux, which influences water circulation (Grosfeld et al., 2001; Jenkins, 1999) and promotes sea ice formation (Bintanja et al., 2015; Merino et al., 2016), and input of terrigenous nutrients such as glacial iron into the Southern Ocean, which fosters primary production (Biddle et al., 2015; Duprat et al., 2016; Helly et al., 2011). Finally, studying icebergs as they drift through warmer water may give unique insights into the response of glacial ice to environmental conditions which may become commonplace at the ice shelf front in the future (Scambos et al., 2008; Shepherd et al., 2019).

*Code availability.* The code (mostly written in MATLAB) is available from the authors upon reasonable request.

*Data availability.* All data used in this study are freely available. The iceberg trajectory data are available from <https://www.scp.byu.edu/data/iceberg/> (Budge and Long, 2019), CryoSat-2 data are available from <https://science-pds.cryosat.esa.int/> (ESA, 2019), Sentinel-1 data are available from <https://scihub.copernicus.eu/dhus/> (ESA, 2020), MODIS data are available from <https://ladsweb.modaps.eosdis.nasa.gov/search/order/1/MOD02HKM--61> (NASA, 2020), and the ERA-5 reanalysis data are available from <https://cds.climate.copernicus.eu/cdsapp#!/dataset/reanalysis-era5-single-levels> (Copernicus Climate Change Service, 2018).

*Author contributions.* ABF and AS designed the study, AR processed the CryoSat elevations, ABF computed freeboard, area, and volume change and prepared the figures, and AS supervised the work. All authors contributed to the writing.

*Competing interests.* The authors declare that they have no conflict of interest.

*Disclaimer.* Publisher's note: Copernicus Publications remains neutral with regard to jurisdictional claims in published maps and institutional affiliations.

*Acknowledgements.* The Antarctic Mapping Toolbox (Greene et al., 2017) was used to convert geographic coordinates to polar stereographic coordinates and vice versa and to calculate distances. We thank the editor, the reviewers, and Xuying Liu for their comments, which all helped to improve the manuscript.

*Financial support.* This research has been supported by the Natural Environment Research Council (grant no. epom300001) and Barry Slavin.

*Review statement.* This paper was edited by Johannes J. Furst and reviewed by Jessica Scheick and one anonymous referee.

## References

- American Meteorological Society: Tabular iceberg, Gloss. Meteorology, available at: [https://glossary.ametsoc.org/wiki/Tabular\\_iceberg](https://glossary.ametsoc.org/wiki/Tabular_iceberg) (last access: 8 June 2021), 2012.
- Arrigo, K. R., Van Dijken, G. L., Ainley, D. G., Fahnestock, M. A., and Markus, T.: Ecological impact of a large Antarctic iceberg, *Geophys. Res. Lett.*, 29, 8–1–8–4, <https://doi.org/10.1029/2001GL014160>, 2002.
- Barnes, D. K. A.: Iceberg killing fields limit huge potential for benthic blue carbon in Antarctic shallows, *Glob. Change Biol.*, 23, 2649–2659, <https://doi.org/10.1111/gcb.13523>, 2017.
- Biddle, L. C., Kaiser, J., Heywood, K. J., Thompson, A. F., and Jenkins, A.: Ocean glider observations of iceberg-enhanced biological production in the northwestern Weddell Sea, *Geophys. Res. Lett.*, 42, 459–465, <https://doi.org/10.1002/2014GL062850>, 2015.
- Bigg, G. R., Wadley, M. R., Stevens, D. P., and Johnson, J. A.: Modelling the dynamics and thermodynamics of icebergs, *Cold Reg. Sci. Technol.*, 26, 113–135, [https://doi.org/10.1016/S0165-232X\(97\)00012-8](https://doi.org/10.1016/S0165-232X(97)00012-8), 1997.
- Bigg, G. R., Cropper, T. E., O'Neill, C. K., Arnold, A. K., Fleming, A. H., Marsh, R., Ivchenko, V., Fournier, N., Osborne, M., and Stephens, R.: A model for assessing iceberg hazard, *Nat. Hazards*, 92, 1113–1136, <https://doi.org/10.1007/s11069-018-3243-x>, 2018.
- Bintanja, R., Van Oldenborgh, G. J., and Katsman, C. A.: The effect of increased fresh water from Antarctic ice shelves on future trends in Antarctic sea ice, *Ann. Glaciol.*, 56, 120–126, <https://doi.org/10.3189/2015AoG69A001>, 2015.
- Bouhier, N., Tournadre, J., Remy, F., and Gourves-Cousin, R.: Melting and fragmentation laws from the evolution of two large Southern Ocean icebergs estimated from satellite data, *The Cryosphere*, 12, 2267–2285, <https://doi.org/10.5194/tc-12-2267-2018>, 2018.
- Budge, J. S. and Long, D. G.: A Comprehensive Database for Antarctic Iceberg Tracking Using Scatterometer Data, *IEEE J. Sel. Top. Appl.*, 11, 434–442, <https://doi.org/10.1109/JSTARS.2017.2784186>, 2018.
- Budge, J. and Long, D. G.: The Antarctic Iceberg Tracking Database v3.0, BYU [data set], available at: <https://www.scp.byu.edu/data/iceberg/> (last access: 13 July 2020), 2019.
- Collares, L. L., Mata, M. M., Kerr, R., Arigony-Neto, J., and Barbat, M. M.: Iceberg drift and ocean circulation in the northwestern Weddell Sea, Antarctica, *Deep-Sea Res. Pt. II*, 149, 10–24, <https://doi.org/10.1016/j.dsr2.2018.02.014>, 2018.
- Copernicus Climate Change Service: ERA5 hourly data on single levels from 1979 to present, Climate Data Store [data set], <https://doi.org/10.24381/cds.adbb2d47>, 2018.
- Dammann, D. O., Eriksson, L. E. B., Nghiem, S. V., Pettit, E. C., Kurtz, N. T., Sonntag, J. G., Busche, T. E., Meyer, F. J., and Mahoney, A. R.: Iceberg topography and volume classification using TanDEM-X interferometry, *The Cryosphere*, 13, 1861–1875, <https://doi.org/10.5194/tc-13-1861-2019>, 2019.
- Depoorter, M. A., Bamber, J. L., Griggs, J. A., Lenaerts, J. T. M., Ligtnerberg, S. R. M., Van Den Broeke, M. R., and Moholdt, G.: Calving fluxes and basal melt rates of Antarctic ice shelves, *Nature*, 502, 89–92, <https://doi.org/10.1038/nature12567>, 2013.
- Dryak, M. C. and Enderlin, E. M.: Analysis of Antarctic Peninsula glacier frontal ablation rates with respect to iceberg melt-inferred variability in ocean conditions, *J. Glaciol.*, 66, 457–470, <https://doi.org/10.1017/jog.2020.21>, 2020.
- Duprat, L. P. A. M., Bigg, G. R., and Wilton, D. J.: Enhanced Southern Ocean marine productivity due to fertilization by giant icebergs, *Nat. Geosci.*, 9, 219–221, <https://doi.org/10.1038/ngeo2633>, 2016.
- Eik, K. and Gudmestad, O. T.: Iceberg management and impact on design of offshore structures, *Cold Reg. Sci. Technol.*, 63, 15–28, <https://doi.org/10.1016/j.coldregions.2010.04.008>, 2010.
- Enderlin, E. M. and Hamilton, G. S.: Estimates of iceberg submarine melting from high-resolution digital elevation models: Application to Sermilik Fjord, East Greenland, *J. Glaciol.*, 60, 1111–1116, <https://doi.org/10.3189/2014JG14J085>, 2014.
- England, M. R., Wagner, T. J. W., and Eisenman, I.: Modeling the breakup of tabular icebergs, *Sci. Adv.*, 6, 1–9, <https://doi.org/10.1126/sciadv.abd1273>, 2020.
- European Space Agency (ESA): CryoSat-2 Ice Baseline C Level 1b data, ESA [data set], available at: <https://science-pds.cryosat.esa.int> (last access: 22 May 2020), 2019.
- European Space Agency (ESA): Sentinel-1 Level 1 Ground Range Detected data, Copernicus Open Access Hub [data set], available at: <https://scihub.copernicus.eu/dhus/>, last access: 30 July 2020.
- Fedotov, V. I., Cherepanov, N. V., and Tyshko, K. P.: Some Features of the Growth, Structure and Metamorphism of East Antarctic Landfast Sea Ice, in: *Antarctic Sea Ice: Physical Processes, Interactions and Variability*, edited by: Jeffries, M. O., American Geophysical Union, Washington DC, 74, 343–354, <https://doi.org/10.1029/ar074p0343>, 1998.
- Fichefet, T. and Morales Maqueda, M. A.: Modelling the influence of snow accumulation and snow-ice formation on the seasonal cycle of the Antarctic sea-ice cover, *Clim. Dynam.*, 15, 251–268, <https://doi.org/10.1007/s003820050280>, 1999.
- Gladstone, R. M., Bigg, G. R., and Nicholls, K. W.: Iceberg trajectory modeling and meltwater injection in the Southern Ocean, *J. Geophys. Res.-Oceans*, 106, 19903–19915, <https://doi.org/10.1029/2000jc000347>, 2001.
- Greene, C. A., Gwyther, D. E., and Blankenship, D. D.: Antarctic Mapping Tools for MATLAB, *Comput. Geosci.*, 104, 151–157, <https://doi.org/10.1016/j.cageo.2016.08.003>, 2017.
- Grosfeld, K., Schroder, M., Fahrbach, E., Gerdes, R., and Mackensen, A.: How iceberg calving and grounding change the circulation and hydrography in the Filchner Ice Shelf–Ocean System, *J. Geophys. Res.*, 106, 9039–9055, 2001.
- Gutt, J.: On the direct impact of ice on marine benthic communities, a review, *Polar Biol.*, 24, 553–564, <https://doi.org/10.1007/s003000100262>, 2001.

- Hamley, T. C. and Budd, W. F.: Antarctic Iceberg Distribution and Dissolution, *J. Glaciol.*, 32, 242–251, <https://doi.org/10.1017/s0022143000015574>, 1986.
- Han, H., Lee, S., Kim, J. I., Kim, S. H., and Kim, H. C.: Changes in a giant iceberg created from the collapse of the Larsen C Ice Shelf, Antarctic Peninsula, derived from Sentinel-1 and CryoSat-2 data, *Remote Sens.*, 11, 1–14, <https://doi.org/10.3390/rs11040404>, 2019.
- Helly, J. J., Kaufmann, R. S., Stephenson, G. R., and Vernet, M.: Cooling, dilution and mixing of ocean water by free-drifting icebergs in the Weddell Sea, *Deep-Sea Res. Pt. II*, 58, 1346–1363, <https://doi.org/10.1016/j.dsr2.2010.11.010>, 2011.
- Huppert, H. E. and Josberger, E. G.: The Melting of Ice in Cold Stratified water, *J. Phys. Oceanogr.*, 10, 953–960, [https://doi.org/10.1175/1520-0485\(1980\)010<0953:TMOIC>2.0.CO;2](https://doi.org/10.1175/1520-0485(1980)010<0953:TMOIC>2.0.CO;2), 1980.
- International Organization for Standardization: ISO 4355 Bases for design on structures – Determination of snow loads on roofs, 1998.
- Jacka, T. H. and Giles, A. B.: Antarctic iceberg distribution and dissolution from ship-based observations, *J. Glaciol.*, 53, 341–356, <https://doi.org/10.3189/002214307783258521>, 2007.
- Jansen, D., Schodlok, M., and Rack, W.: Basal melting of A-38B: A physical model constrained by satellite observations, *Remote Sens. Environ.*, 111, 195–203, <https://doi.org/10.1016/j.rse.2007.03.022>, 2007.
- Jenkins, A.: The impact of melting ice on ocean waters, *J. Phys. Oceanogr.*, 29, 2370–2381, [https://doi.org/10.1175/1520-0485\(1999\)029<2370:TIOPIO>2.0.CO;2](https://doi.org/10.1175/1520-0485(1999)029<2370:TIOPIO>2.0.CO;2), 1999.
- Joiris, C. R.: Seabird hotspots on icebergs in the Amundsen Sea, Antarctica, *Polar Biol.*, 41, 111–114, <https://doi.org/10.1007/s00300-017-2174-4>, 2018.
- Jongma, J. I., Driesschaert, E., Fichet, T., Goosse, H., and Renssen, H.: The effect of dynamic-thermodynamic icebergs on the Southern Ocean climate in a three-dimensional model, *Ocean Model.*, 26, 104–113, <https://doi.org/10.1016/j.ocemod.2008.09.007>, 2009.
- Kooyman, G. L., Ainley, D. G., Ballard, G., and Ponganis, P. J.: Effects of giant icebergs on two emperor penguin colonies in the Ross Sea, Antarctica, *Antarct. Sci.*, 19, 31–38, <https://doi.org/10.1017/S0954102007000065>, 2007.
- Kurtz, N. T. and Markus, T.: Satellite observations of Antarctic sea ice thickness and volume, *J. Geophys. Res.-Oceans*, 117, 1–9, <https://doi.org/10.1029/2012JC008141>, 2012.
- Kwok, R. and Cunningham, G. F.: ICESat over Arctic sea ice: Estimation of snow depth and ice thickness, *J. Geophys. Res.-Oceans*, 113, 1–17, <https://doi.org/10.1029/2008JC004753>, 2008.
- Laufkötter, C., Stern, A. A., John, J. G., Stock, C. A., and Dunne, J. P.: Glacial Iron Sources Stimulate the Southern Ocean Carbon Cycle, *Geophys. Res. Lett.*, 45, 13377–13385, <https://doi.org/10.1029/2018GL079797>, 2018.
- Leonard, K. C. and Maksym, T.: The importance of wind-blown snow redistribution to snow accumulation on Bellingshausen Sea ice, *Ann. Glaciol.*, 52, 271–278, <https://doi.org/10.3189/172756411795931651>, 2011.
- Li, T., Shokr, M., Liu, Y., Cheng, X., Li, T., Wang, F., and Hui, F.: Monitoring the tabular icebergs C28A and C28B calved from the Mertz Ice Tongue using radar remote sensing data, *Remote Sens. Environ.*, 216, 615–625, <https://doi.org/10.1016/j.rse.2018.07.028>, 2018.
- Ligtenberg, S. R. M., Helsen, M. M., and van den Broeke, M. R.: An improved semi-empirical model for the densification of Antarctic firm, *The Cryosphere*, 5, 809–819, <https://doi.org/10.5194/tc-5-809-2011>, 2011.
- Little, C. M., Gnanadesikan, A., and Hallberg, R.: Large-scale oceanographic constraints on the distribution of melting and freezing under ice shelves, *J. Phys. Oceanogr.*, 38, 2242–2255, <https://doi.org/10.1175/2008JPO3928.1>, 2008.
- MacAyeal, D. R., Okal, M. H., Thom, J. E., Brunt, K. M., Kim, Y. J., and Bliss, A. K.: Tabular iceberg collisions within the coastal regime, *J. Glaciol.*, 54, 371–386, <https://doi.org/10.3189/002214308784886180>, 2008.
- Martin, T. and Adcroft, A.: Parameterizing the fresh-water flux from land ice to ocean with interactive icebergs in a coupled climate model, *Ocean Model.*, 34, 111–124, <https://doi.org/10.1016/j.ocemod.2010.05.001>, 2010.
- Mazur, A. K., Wählin, A. K., and Kalén, O.: The life cycle of small-to medium-sized icebergs in the Amundsen sea embayment, *Polar Res.*, 38, 1–17, <https://doi.org/10.33265/polar.v38.3313>, 2019.
- McIntyre, N. F. and Cudlip, W.: Observation of a giant antarctic tabular iceberg by satellite radar altimetry, *Polar Rec.*, 23, 458–462, <https://doi.org/10.1017/S0032247400007610>, 1987.
- Merino, N., Le Sommer, J., Durand, G., Jourdain, N. C., Madec, G., Mathiot, P., and Tournaire, J.: Antarctic icebergs melt over the Southern Ocean: Climatology and impact on sea ice, *Ocean Model.*, 104, 99–110, <https://doi.org/10.1016/j.ocemod.2016.05.001>, 2016.
- Moon, T., Sutherland, D. A., Carroll, D., Felikson, D., Kehrl, L., and Straneo, F.: Subsurface iceberg melt key to Greenland fjord freshwater budget, *Nat. Geosci.*, 11, 49–54, <https://doi.org/10.1038/s41561-017-0018-z>, 2018.
- Morgan, V. I. and Budd, W. F.: The Distribution, Movement and Melt Rates of Antarctic Icebergs, Iceberg Utilization, Proceedings of the First International Conference and Workshops on Iceberg Utilization for Fresh Water Production, Weather Modification and Other Applications, Iowa State University, Ames, Iowa, USA, 2–6 October 1977, 220–228, 1978.
- Mouginot, J., Rignot, E., and Scheuchl, B.: Continent-Wide, Interferometric SAR Phase, Mapping of Antarctic Ice Velocity, *Geophys. Res. Lett.*, 46, 9710–9718, <https://doi.org/10.1029/2019GL083826>, 2019.
- NASA: MODIS Level 1B Calibrated Radiances at 500 meter resolution, LAADS DAAC [data set], <https://doi.org/10.5067/MODIS/MOD02HKM.061>, last access: 28 June 2020.
- Neshyba, S. and Josberger, E. G.: On the estimation of Antarctic iceberg melt rate, *J. Phys. Oceanogr.*, 10, 1681–1685, [https://doi.org/10.1175/1520-0485\(1980\)010<1681:OTEAOI>2.0.CO;2](https://doi.org/10.1175/1520-0485(1980)010<1681:OTEAOI>2.0.CO;2), 1980.
- Nøst, O. A. and Østerhus, S.: Impact of Grounded Icebergs on the Hydrographic Conditions Near the Filchner Ice Shelf, chapter in: *Ocean, Ice, and Atmosphere: Interactions at the Antarctic Continental Margin*, edited by: Jacobs, S. S., and Weiss, R. F., American Geophysical Union, Washington DC, 1998.

- Orheim, O.: Evolution of under Water Sides of Ice Shelves and Icebergs, *Ann. Glaciol.*, 9, 176–182, <https://doi.org/10.3189/S0260305500000574>, 1987.
- Otosaka, I. N., Shepherd, A., Casal, T. G. D., Coccia, A., Davidson, M., Di Bella, A., Fettweis, X., Forsberg, R., Helm, V., Hogg, A. E., Hvidegaard, S. M., Lemos, A., Macedo, K., Kuipers Munneke, P., Parrinello, T., Simonsen, S. B., Skourup, H., and Sørensen, L. S.: Surface Melting Drives Fluctuations in Airborne Radar Penetration in West Central Greenland, *Geophys. Res. Lett.*, 47, <https://doi.org/10.1029/2020GL088293>, 2020.
- Power, D., Youden, J., Lane, K., Randell, C., and Flett, D.: Iceberg detection capabilities of radarsat synthetic aperture radar, *Can. J. Remote Sens.*, 27, 476–486, <https://doi.org/10.1080/07038992.2001.10854888>, 2001.
- Rackow, T., Wesche, C., Timmermann, R., Hellmer, H. H., Juricke, S., and Jung, T.: A simulation of small to giant Antarctic iceberg evolution: Differential impact on climatology estimates, *J. Geophys. Res.-Oceans*, 3170–3190, <https://doi.org/10.1002/2016JC012513>, 2013.
- Raiswell, R., Hawkings, J. R., Benning, L. G., Baker, A. R., Death, R., Albani, S., Mahowald, N., Krom, M. D., Poulton, S. W., Wadhams, J., and Tranter, M.: Potentially bioavailable iron delivery by iceberg-hosted sediments and atmospheric dust to the polar oceans, *Biogeosciences*, 13, 3887–3900, <https://doi.org/10.5194/bg-13-3887-2016>, 2016.
- Remy, J. P., Becquevort, S., Haskell, T. G., and Tison, J. L.: Impact of the B-15 iceberg “stranding event” on the physical and biological properties of sea ice in McMurdo Sound, Ross Sea, Antarctica, *Antarct. Sci.*, 20, 593–604, <https://doi.org/10.1017/S0954102008001284>, 2008.
- Rignot, E., Jacobs, S., Mouginot, J., and Scheuchl, B.: Ice-shelf melting around antarctica, *Science*, 341, 266–270, <https://doi.org/10.1126/science.1235798>, 2013.
- Robinson, N. J. and Williams, M. J. M.: Iceberg-induced changes to polynya operation and regional oceanography in the southern Ross Sea, Antarctica, from in situ observations, *Antarct. Sci.*, 24, 514–526, <https://doi.org/10.1017/S0954102012000296>, 2012.
- Russell-Head, D. S.: The Melting of Free-Drifting Icebergs, *Ann. Glaciol.*, 1, 119–122, <https://doi.org/10.3189/s0260305500017092>, 1980.
- Scambos, T., Ross, R., Bauer, R., Yermolin, Y., Skvarca, P., Long, D., Bohlander, J., and Haran, T.: Calving and ice-shelf break-up processes investigated by proxy: Antarctic tabular iceberg evolution during northward drift, *J. Glaciol.*, 54, 579–591, <https://doi.org/10.3189/002214308786570836>, 2008.
- Schloesser, F., Friedrich, T., Timmermann, A., DeConto, R. M., and Pollard, D.: Antarctic iceberg impacts on future Southern Hemisphere climate, *Nat. Clim. Change*, 9, 672–677, <https://doi.org/10.1038/s41558-019-0546-1>, 2019.
- Shepherd, A., Gilbert, L., Muir, A. S., Konrad, H., McMillan, M., Slater, T., Briggs, K. H., Sundal, A. V., Hogg, A. E., and Engdahl, M. E.: Trends in Antarctic Ice Sheet Elevation and Mass, *Geophys. Res. Lett.*, 46, 8174–8183, <https://doi.org/10.1029/2019GL082182>, 2019.
- Silva, T. A. M., Bigg, G. R., and Nicholls, K. W.: Contribution of giant icebergs to the Southern Ocean freshwater flux, *J. Geophys. Res.*, 111, 1–8, <https://doi.org/10.1029/2004JC002843>, 2006.
- Smith, K. L., Robison, B. H., Helly, J. J., Kaufmann, R. S., Ruhl, H. A., Shaw, T. J., Twining, B. S., and Vernet, M.: Free-drifting icebergs: Hot spots of chemical and biological enrichment in the Weddell Sea, *Science*, 317, 478–482, <https://doi.org/10.1126/science.1142834>, 2007.
- Stuart, K. M. and Long, D. G.: Tracking large tabular icebergs using the SeaWinds Ku-band microwave scatterometer, *Deep-Sea Res. Pt. II*, 58, 1285–1300, <https://doi.org/10.1016/j.dsr2.2010.11.004>, 2011.
- Sulak, D. J., Sutherland, D. A., Enderlin, E. M., Stearns, L. A., and Hamilton, G. S.: Iceberg properties and distributions in three Greenlandic fjords using satellite imagery, *Ann. Glaciol.*, 58, 92–106, <https://doi.org/10.1017/aog.2017.5>, 2017.
- Tilling, R. L., Ridout, A., and Shepherd, A.: Estimating Arctic sea ice thickness and volume using CryoSat-2 radar altimeter data, *Adv. Space Res.*, 62, 1203–1225, <https://doi.org/10.1016/j.asr.2017.10.051>, 2018.
- Tournadre, J., Girard-Arduin, F., and Legeré, B.: Antarctic icebergs distributions, 2002–2010, *J. Geophys. Res.-Oceans*, 117, 2002–2010, <https://doi.org/10.1029/2011JC007441>, 2012.
- Tournadre, J., Bouhier, N., Girard-Arduin, F., and Remy, F.: Large icebergs characteristics from altimeter waveforms analysis, *J. Geophys. Res.-Oceans*, 120, 2121–2128, <https://doi.org/10.1002/2014JC010502>, 2015.
- Tournadre, J., Bouhier, N., Girard-Arduin, F., and Rémy, F.: Antarctic icebergs distributions 1992–2014, *J. Geophys. Res.-Oceans*, 121, 327–349, <https://doi.org/10.1002/2015JC011178>, 2016.
- Wagner, T. J. W., Wadhams, P., Bates, R., Elosegui, P., Stern, A., Vella, D., Abrahamsen, E. P., Crawford, A., and Nicholls, K. W.: The “footloose” mechanism: Iceberg decay from hydrostatic stresses, *Geophys. Res. Lett.*, 41, 5522–5529, <https://doi.org/10.1002/2014GL060832>, 2014.
- Wise, M. G., Dowdeswell, J. A., Jakobsson, M., and Larter, R. D.: Evidence of marine ice-cliff instability in Pine Island Bay from iceberg-keel plough marks, *Nature*, 550, 506–510, <https://doi.org/10.1038/nature24458>, 2017.
- Wu, S.-Y. and Hou, S.: Impact of icebergs on net primary productivity in the Southern Ocean, *The Cryosphere*, 11, 707–722, <https://doi.org/10.5194/tc-11-707-2017>, 2017.
- Zwally, H. J., Giovinetto, M. B., Li, J., Cornejo, H. G., Beckley, M. A., Brenner, A. C., Saba, J. L., and Yi, D.: Mass changes of the Greenland and Antarctic ice sheets and shelves and contributions to sea-level rise: 1992–2002, *J. Glaciol.*, 51, 509–527, <https://doi.org/10.3189/172756505781829007>, 2005.



# **APPENDIX B**

## **OBSERVING THE DISINTEGRATION OF THE A68A ICEBERG FROM SPACE**



# Observing the disintegration of the A68A iceberg from space

A. Braakmann-Folgmann<sup>a,\*</sup>, A. Shepherd<sup>a</sup>, L. Gerrish<sup>b</sup>, J. Izzard<sup>a</sup>, A. Ridout<sup>c</sup>

<sup>a</sup> Centre for Polar Observation and Modelling (CPOM), University of Leeds, Leeds LS2 9JT, UK

<sup>b</sup> British Antarctic Survey, Cambridge CB3 0ET, UK

<sup>c</sup> Centre for Polar Observation and Modelling (CPOM), University College London, London, UK

## ARTICLE INFO

Editor: Menghua Wang

### Keywords:

Tabular icebergs  
Basal melting  
Satellite altimetry  
ICESat-2  
CryoSat-2  
Freshwater flux  
Mass loss  
South Georgia  
A68

## ABSTRACT

Icebergs impact the physical and biological properties of the ocean where they drift, depending on the degree of melting. We use satellite imagery and altimetry to quantify the area, thickness, and volume change of the massive A68A iceberg from its calving off the Larsen-C Ice Shelf in July 2017 until January 2021, when it disintegrated. A68A thinned from  $235 \pm 9$  to  $168 \pm 10$  m, on average, and lost  $802 \pm 34$  Gt of ice in 3.5 years,  $254 \pm 17$  Gt of which was through basal melting (a lower bound for the immediate fresh water input into the ocean). Basal melting peaked at  $7.2 \pm 2.3$  m/month in the Northern Scotia Sea and an estimated  $152 \pm 61$  Gt of freshwater was released off South Georgia, potentially altering the local ocean properties, plankton occurrence and conditions for predators.

## 1. Introduction

Icebergs impact and interact with the Antarctic environment through a range of processes. This begins with their calving, which may influence the stability of their parent ice shelf (Rott et al., 1996) and flow of glaciers upstream (Rignot et al., 2004). As they drift, icebergs release cold fresh melt water, altering the local ocean properties (Helly et al., 2011; Jenkins, 1999) and facilitating sea ice growth (Bintanja et al., 2015; Merino et al., 2016). They also carry debris with terrigenous nutrients, which supply the majority of iron input to the Southern Ocean (Wu and Hou, 2017), fostering biological production (Biddle et al., 2015; Duprat et al., 2016; Smith et al., 2007). When icebergs ground, they impact marine benthic communities (Barnes, 2017; Gutt, 2001) and leave plough marks on the sea floor (Wise et al., 2017). Furthermore, large icebergs can act as a barrier disrupting the local ocean circulation (Grosfeld et al., 2001) or blocking access of penguin colonies to their feeding grounds (Kooyman et al., 2007). The response of icebergs to the warmer climates they drift through can also inform predictions on how the Antarctic ice shelves will react to climate change (Scambos et al., 2008; Shepherd et al., 2019).

A68A was the sixth largest iceberg ever recorded in satellite observations (Budge and Long, 2018), and had a significant potential to

impact its environment. Indeed when it calved from the Larsen-C Ice Shelf in July 2017, concerns were raised that its loss might trigger a collapse of the entire ice shelf (Hogg and Gudmundsson, 2017; Jansen et al., 2015). After residing close to its calving position for over a year, A68A started to move northwards through the Weddell Sea (Fig. 1). It reached the Scotia Sea in early 2020 and approached South Georgia at the end of 2020, where it started to disintegrate. Although this is a common trajectory for icebergs (Fig. 1 and Tournadre et al., 2016), the sheer size of A68A elevates its potential to impact ecosystems around South Georgia through release of fresh water and nutrients, through blockage and through collision with the benthic habitat (Grimm, 2021; Vernet et al., 2012). Here, we combine satellite imagery and satellite altimetry to chart changes in the A68A iceberg's area, freeboard, thickness, volume and mass over its lifetime to assess its disintegration and melt rate in different environments.

## 2. Data and methods

We track the iceberg's area and area change in satellite imagery. In total, 23 Sentinel-1, 18 Moderate Resolution Imaging Spectroradiometer (MODIS) and 14 Sentinel-3 scenes are used to manually delineate the iceberg's outlines using GIS software. While the Sentinel-1 Synthetic

\* Corresponding author.

E-mail address: [eeabr@leeds.ac.uk](mailto:eeabr@leeds.ac.uk) (A. Braakmann-Folgmann).

Aperture Radar (SAR) imagery offers all-weather capability and higher spatial resolution, MODIS and Sentinel-3 optical imagery have the advantage of a higher temporal resolution, but cannot be used during the polar night and on cloudy days. In optical imagery the spatial resolution is slightly lower and it is harder to distinguish sea ice from icebergs or clouds, which is the main error source. Therefore, we rely on Sentinel-1 data, if available close to the altimetry overpasses and use MODIS or Sentinel-3 data on the other occasions. To estimate the accuracy of our delineations we buffer the polygon outlines by two pixels and calculate the resulting difference in area. This gives a mean relative difference of 3.2%.

Changes in the iceberg's freeboard and thickness are derived from CryoSat-2 and ICESat-2 satellite altimetry. To generate a complete map of the initial iceberg freeboard and thickness, we collect all CryoSat-2 tracks over the part of the Larsen-C Ice Shelf that formed the A68A iceberg between 12 July 2016 and 11 July 2017 (Fig. 2), correcting for the mean ice motion of 696 m/year (Mouginot et al., 2019). To track changes in the iceberg freeboard while it is drifting, we collocate 15 overpasses from ICESat-2 and 9 overpasses from CryoSat-2 with the initial freeboard map, post them on a common 2-km grid, and difference them. For this collocation to the initial iceberg reference system, we digitize the iceberg outline in a near-coincident image using 7 Sentinel-1 and 17 MODIS scenes. We then transform this outline to maximize the overlapping area with respect to the outline of the previous overpass. At least for icebergs like A68A that are non-symmetric and when the general shape is preserved, this step-wise transformation yields the optimal rotation and translation parameters defining where the new overpass

samples the iceberg and which part of the initial freeboard map this corresponds to (Fig. 3). Grid cells of the initial map that are not covered by any track are filled using linear interpolation.

The CryoSat-2 data are processed from Level 1B baseline D using the Centre for Polar Observation and Modelling sea ice processing system (Tilling et al., 2018). For consistency, a common threshold retracker is applied to measurements acquired in both SAR and SAR interferometric mode and over all surface types. Iceberg freeboard is calculated by subtracting the adjacent mean sea surface height from the iceberg surface height. For ICESat-2 we use Level 2A, ATL03 photon data as a primary product, because iceberg heights are filtered out in the higher level products. For each track, we analyze the three strong beams separately and discard the weak beams. Low confidence flagged photons (2 and below) are filtered out and 150 photons each are averaged along-track, to reduce noise. We then extract the mean sea surface height, ocean tides and inverted barometer effect from Level 3A version 3 ATL07 data, interpolated to the ATL03 locations. These are subtracted from the photon heights, yielding sea surface heights that agree with the ATL07 sea surface heights, and to derive iceberg freeboard. Finally, we discard freeboard measurements from both altimeters below 20 and above 100 m and measurements outside the iceberg polygon derived from the near-coincident satellite imagery. To make the higher resolution ICESat-2 data comparable to the initial heights derived from CryoSat-2, we also filter out crevasses searching for local minima with a prominence of 3 or more and reject the outer 2 km at the edges.

Uncertainty estimates are a combination of the freeboard standard deviations and the impact of the collocation uncertainty. The collocation

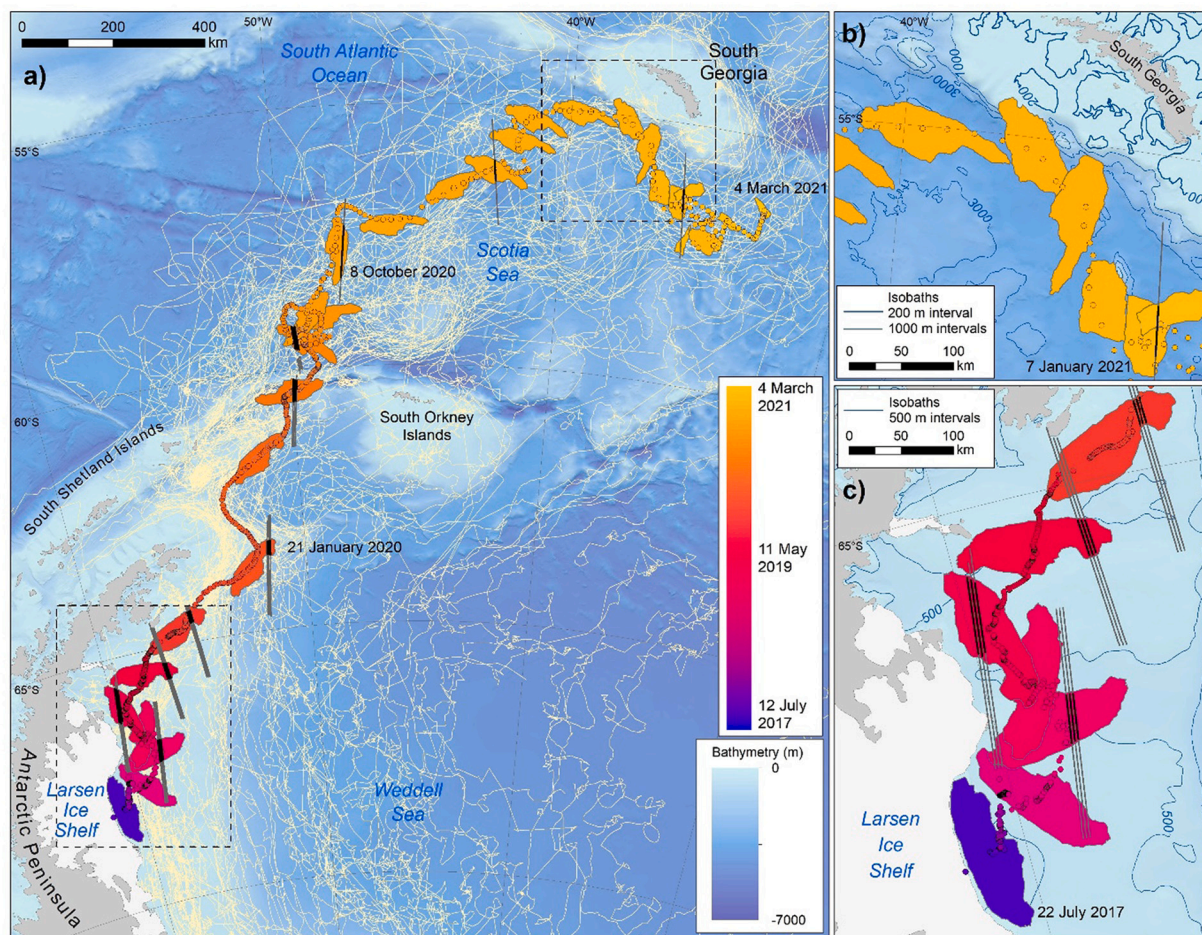


Fig. 1. Trajectory of A68A (circles colored by date) and historic icebergs (yellow lines, Budge and Long, 2018) overlain on a bathymetric map (GEBCO Compilation Group, 2019; Hogg et al., 2016). Selected outlines (date colour coded), altimetry overpasses (grey lines with black marking the parts that sample the iceberg) and key dates are also shown. Panels b and c are zoom regions of interest.

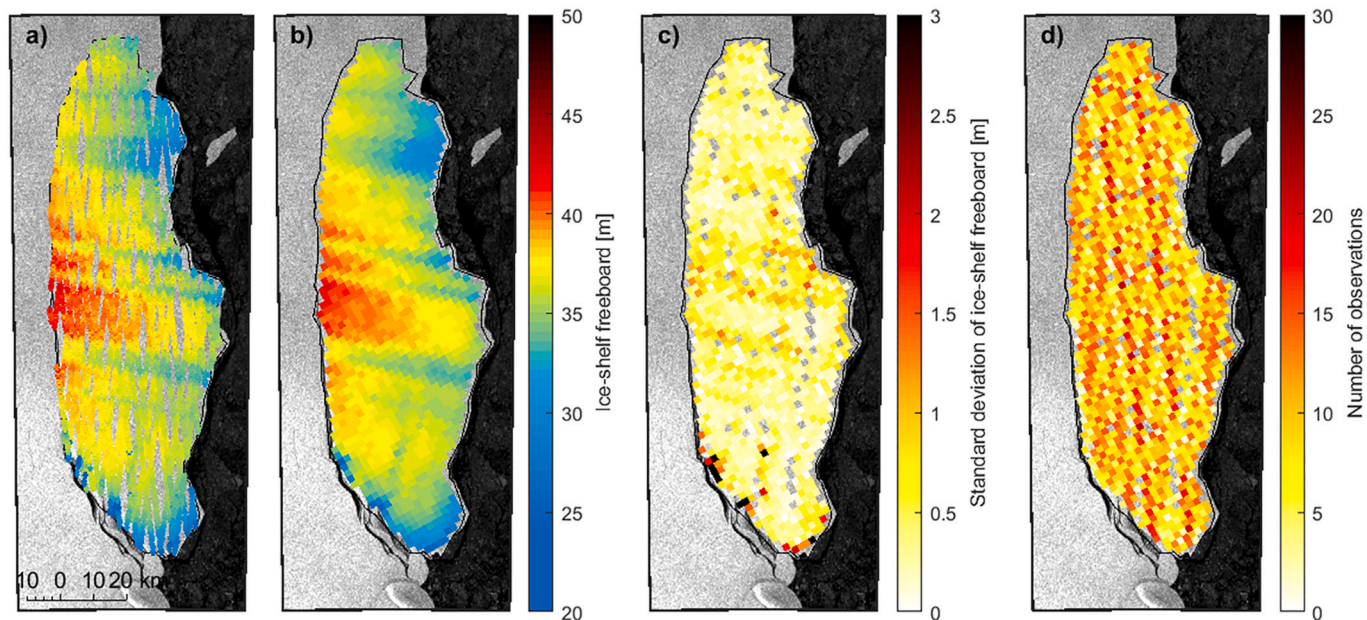


Fig. 2. Calculation of initial iceberg freeboard map: (a) CryoSat tracks over the Larsen-C Ice Shelf over 1 year (12 July 2016–11 July 2017) before the iceberg calved, cut to the area that later formed the iceberg. (b) The same measurements gridded at 2 km and empty grid cells filled with linear interpolation. (c) Standard deviation within each grid cell. (d) Number of observations averaged per grid cell. The background shows a Sentinel-1 image on 10 July 2017.

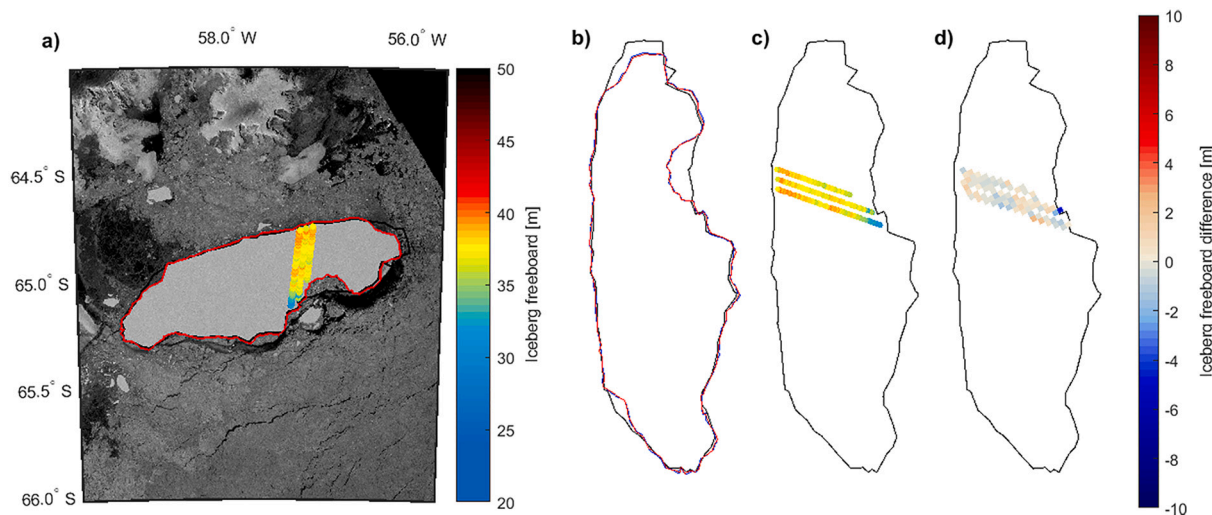


Fig. 3. Collocation of a sample ICESat-2 track and the corresponding Sentinel-1 image on 18 September 2019: For each altimetry overpass a near-coincident image is used to derive the iceberg’s outline at the time of the new overpass (red, panel a). The new outline is transformed to maximize the overlapping area with the previous outline (blue, panel b). This is done iteratively, so we know the transformation of the previous polygon with respect to the initial polygon (black) and can transform the new overpass to the initial situation (panel c). We then grid the new track on the same grid as the initial freeboard measurements and difference it with these initial heights (panel d).

uncertainty is mainly caused by the time separation between the altimetry overpass and the corresponding image. We perform a Monte Carlo simulation using 1000 samples that are normally distributed around the estimated translation and rotation assuming a maximum (3 sigma) daily rotation of 15 degrees and a maximum translation based on the drift speed of the iceberg scaled by the time separation. The drift speed is calculated as the path distance (Greene et al., 2017) from the locations given in the Antarctic Iceberg Tracking database (Budge and Long, 2018). We then calculate the freeboard difference for each of the 1000 slightly differently collocated samples and take their standard deviation as an estimate of the impact of erroneous collocation. This collocation uncertainty is combined with the standard deviations of the initial freeboard and of the new overpass using uncertainty propagation.

The freeboard standard deviations are calculated within each grid cell. When the whole track is averaged to derive the mean freeboard change at one point in time, the uncertainties of the involved grid cells are propagated. Rather than assume that our freeboard measurement errors are not correlated in space or time, we employ a more conservative approach and propagate the uncertainties using a full covariance matrix to account for their correlation (Storto et al., 2019). In the absence of independent freeboard measurements for verification, we assume that altimeter-derived freeboards recorded along the same track are 60% correlated and that the initial freeboards, which are derived from measurements acquired along several independent tracks, are 30% correlated. The mean standard deviation of the calculated freeboard change is 0.45 m, with collocation contributing 22%, the initial

freeboard contributing 29% and the new track contributing 49%.

Iceberg thickness  $H$  is derived from iceberg freeboard  $h_{fb}$  assuming hydrostatic equilibrium (Eq. 1). We treat ICESat-2 and CryoSat-2 measurements in the same way, presuming neither penetrates the snow layer. Because the iceberg survives for several years and travels a long distance passing through varying environmental conditions, we model the evolution of the snow layer and iceberg density based on ERA5 Reanalysis data (Copernicus Climate Change Service, 2018) of air temperature, wind speed and snow accumulation (Fig. 4, Braakmann-Folgmann et al., 2021). The iceberg's column-average density  $\rho_i$  reduces from 868 to 848  $\text{kg m}^{-3}$  during its drift (Ligtenberg et al., 2011), because the densest, pure glacial ice is melted from the bottom. We estimate the uncertainty in the column average and basal ice densities to be 10  $\text{kg m}^{-3}$  (Dryak and Enderlin, 2020) and 2  $\text{kg m}^{-3}$ , respectively. The density of the surface snow layer  $\rho_s$  reaches 465  $\text{kg m}^{-3}$  after 3.5 years (International Organization for Standardization, 1998) and snow depth  $h_s$  increases by 3.3 m. We estimate the snow density and depth uncertainties to be 50  $\text{kg m}^{-3}$  (Kurtz and Markus, 2012) and 20% (Kwok and Cunningham, 2008), respectively. As sea water density  $\rho_w$  we use 1024  $\text{kg m}^{-3}$  (Fichefet and Morales Maqueda, 1999) with an uncertainty of 2  $\text{kg m}^{-3}$ . Altogether, the mean uncertainty in thickness change is 5.3 m, with ice density uncertainty being the largest factor. To obtain a continuous representation of iceberg thickness in space and time, we fit a third order polynomial function of latitude, longitude and time to our observations of thickness change and combine this with the initial thickness map (supplementary animation, Braakmann-Folgmann et al., 2022).

$$H = \frac{\rho_w}{\rho_w - \rho_i} h_{fb} - \frac{(\rho_w - \rho_s)}{\rho_w - \rho_i} h_s \quad (1)$$

Iceberg volume is determined by multiplying iceberg thickness and area, interpolated to the times of the altimetry overpasses. Changes in the volume of the mother iceberg are then calculated by differencing

each volume estimate to the initial value. We differentiate between volume loss through fragmentation (area loss) and volume loss through basal melting (thickness change) by keeping either thickness or area constant. To convert volume change to mass change, we multiply the loss due to fragmentation by the column-average ice density at each point in time, and we multiply the basal thickness change by the density of pure glacial ice. Summing both components gives the total iceberg mass change. Uncertainties are propagated, and we find that the uncertainties in area and thickness change contribute 45% and 55%, respectively, to the uncertainty of volume change.

### 3. Results

The initial area of the A68A iceberg was  $5719 \pm 77 \text{ km}^2$ . Since A68A and A68B separated just after calving (Budge and Long, 2018, Fig. 5a), our initial polygon shows the outline of the A68A iceberg and all our results relate to A68A. During its lifetime, the iceberg's area gradually reduced both through larger break-ups and continuous processes (Figs. 1 and 6a). A larger break-up took place between 2018 and 2019 and another large piece, A68C, was lost in April 2020. In December 2020, the A68A iceberg gave birth to several children icebergs, named A68D-A68F (Budge and Long, 2018), rapidly reducing the area of the remaining largest part. Apart from these sudden losses, iceberg area also reduced gradually through side melting and smaller edge-wastings. Overall, the iceberg lost  $3206 \pm 78 \text{ km}^2$  up to 7 January 2021, when our last thickness measurement is, and  $5052 \pm 106 \text{ km}^2$  by 4 March 2021 - a  $56 \pm 8\%$  and  $88 \pm 4\%$  reduction in area of the mother iceberg, respectively. We find distinct patterns of area change according to the iceberg's geographical location (Fig. 6a), with a mean loss rate of  $200 \pm 82 \text{ km}^2$  per year in the Weddell Sea and a more than ten times higher loss rate of  $2807 \pm 199 \text{ km}^2$  per year in the Scotia Sea until 7 January 2021, when the iceberg is drifting in open ocean.

The maps of initial iceberg freeboard and thickness (Figs. 2 and 5a)

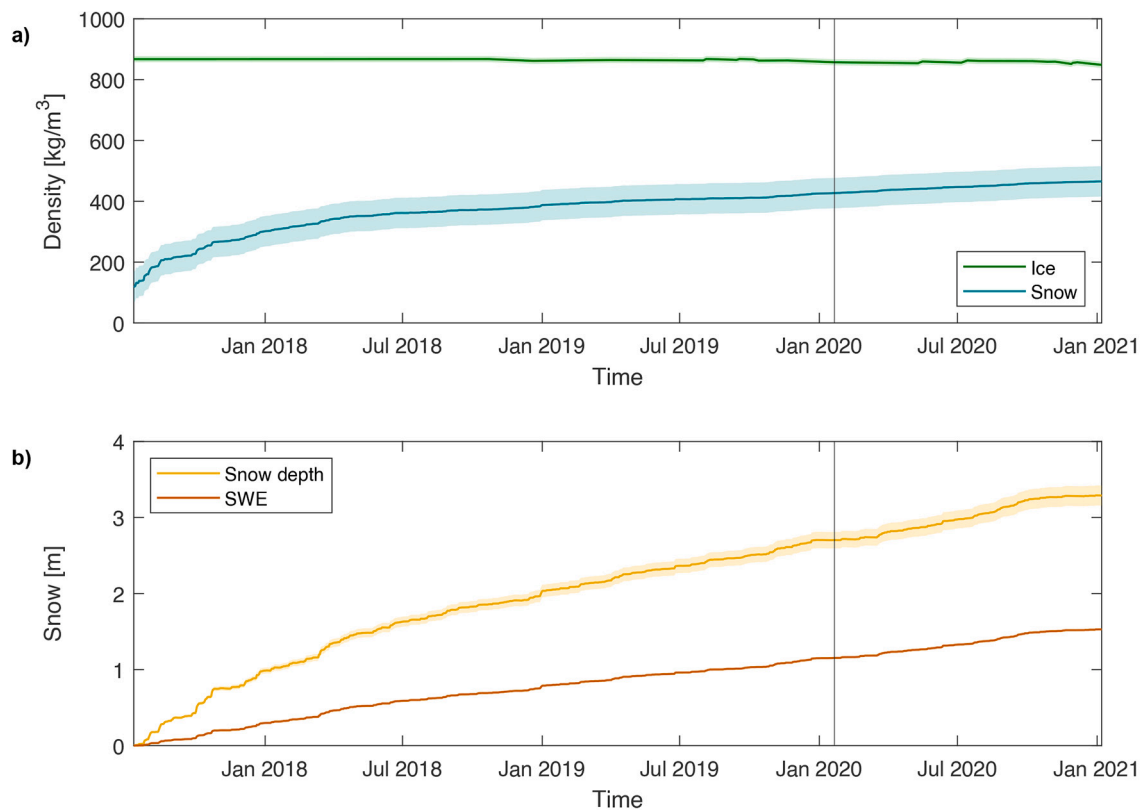
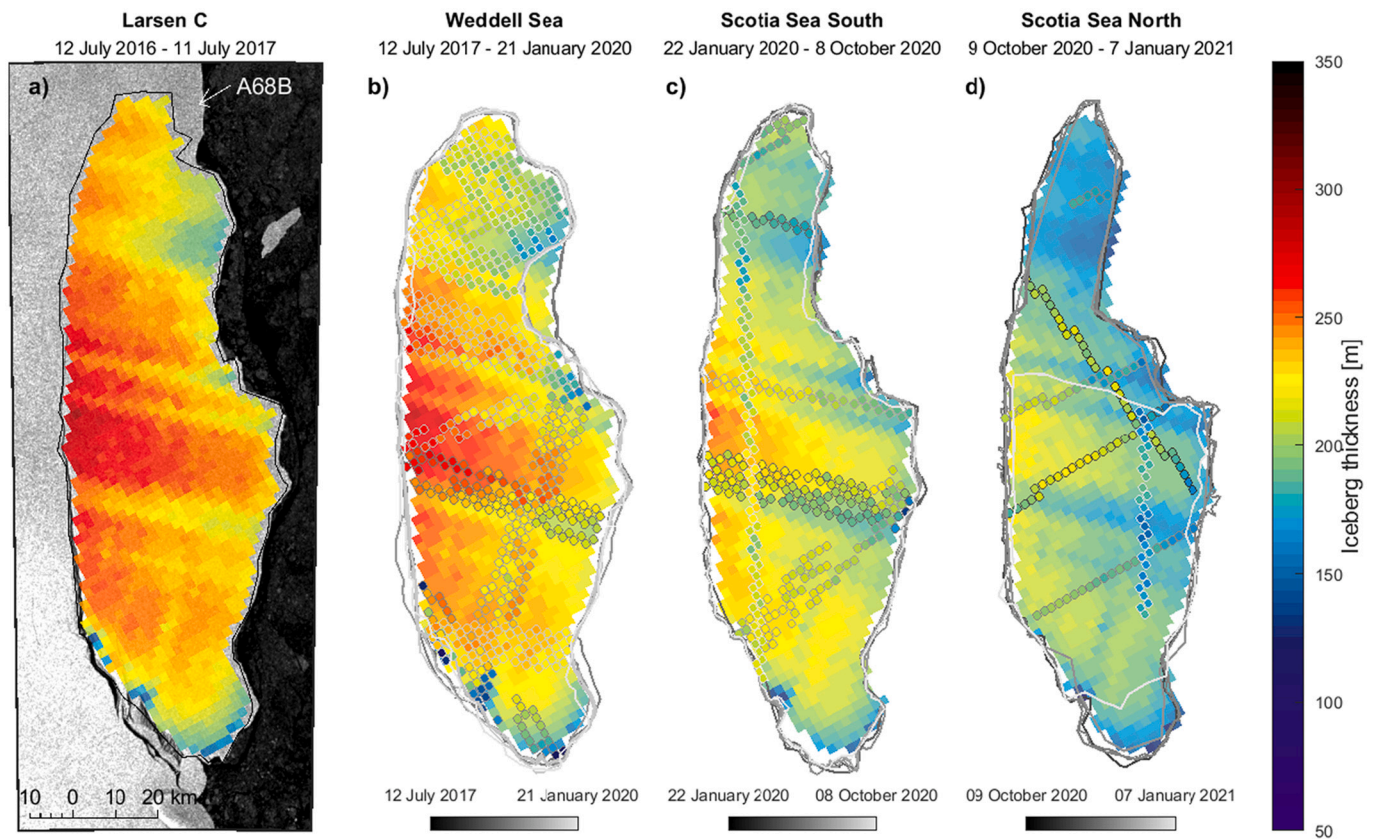


Fig. 4. Evolution of iceberg properties based on ERA-5 Reanalysis data (Copernicus Climate Change Service, 2018): (a) Iceberg density and snow density; (b) snow depth and snow water equivalent (SWE).



**Fig. 5.** Maps of the A68A iceberg thickness when it was still part of the Larsen-C Ice Shelf (a) and at later dates as it drifted through the Weddell and Scotia Seas (b-d). The initial thickness is superimposed on a Sentinel-1 image acquired on 10 July 2017, and the region from which A68B was formed is also indicated. On later dates, the iceberg thickness is computed at colocated altimetry overpasses (outlined gridcells, shaded according to date relative to the interval start) and modelled at the mid-point of each interval elsewhere.

reveal the iceberg's topography. The mean gridded initial freeboard is  $36.0 \pm 0.2$  m and the mean estimated initial iceberg thickness is  $235 \pm 9$  m. The iceberg was thicker on the side facing the Antarctic Peninsula and thinnest on the Southern tip, where the crack which separated the iceberg from the ice shelf started (Jansen et al., 2015), and in the North. Moreover, the iceberg is covered by longitudinal surface structures in the former ice shelf flow direction of a few meters depth, which extend across the iceberg's full width and are a few kilometers wide, widening towards the sea. These are not visible in optical or radar imagery, but revealed by the thickness. One of these features coincides with a suture zone (Jansen et al., 2013). Owing to the undulating topography, gridded freeboard heights range from 22.1 to 42.6 m, and this motivates our collocation of subsequent altimetry tracks to improve confidence in estimates of freeboard and thickness change.

The iceberg freeboard stays almost constant while in the Weddell Sea with a mean freeboard loss of  $0.2 \pm 0.1$  m/year (Fig. 6b), but starts to rapidly decrease once it enters the Scotia Sea, where the mean rate of freeboard lowering is  $5.7 \pm 0.4$  m/year. Marking the location of each track, we observe that the initially southern part of the iceberg is the most resilient to melting. This explains the positive outliers in the time series, which all stem from the southern part. For thickness change (Figs. 5, 6c and supplementary animation) we record a total reduction of  $67 \pm 5$  m, leaving the iceberg with a mean thickness of  $168 \pm 10$  m close to South Georgia. The mean melt rates are  $7.8 \pm 2.1$  m/year in the Weddell Sea and  $49.5 \pm 6.5$  m/year in the Scotia Sea ( $3.0 \pm 0.8$  m/month in the Southern and  $7.2 \pm 2.3$  m/month in the Northern Scotia Sea). We find good agreement (average RMSE 10 m, maximum RMSE 22 m) between our observed iceberg thickness and the model fit (Fig. 5). Another finding from our study is that CryoSat-2 and ICESat-2 freeboard and thickness measurements over the iceberg are comparable and can be

merged into a consistent time series (see Fig. 6b, c - especially the tracks on 5 and 16 May 2020, which are close in time).

The A68A iceberg's initial volume was  $1346 \pm 53$  km<sup>3</sup>. After 3.5 years, the volume of the mother iceberg had reduced by  $924 \pm 27$  km<sup>3</sup> (Fig. 6d), which is  $69 \pm 3\%$  of its initial value. Converted to mass loss this corresponds to  $802 \pm 34$  Gt lost from the mother iceberg. Fragmentation makes up for  $68 \pm 5\%$  of the total mass loss and basal melting accounts for the remaining  $32 \pm 3\%$ . While both processes contribute roughly equally in the Weddell Sea and increase as the iceberg drifts northwards, fragmentation becomes the dominant wastage factor as the iceberg falls apart and forms numerous children icebergs in the Northern Scotia Sea (Fig. 6d, Table 1). The total loss through basal melting ( $277 \pm 19$  km<sup>3</sup> or  $254 \pm 17$  Gt) can be considered as a lower estimate of the immediate freshwater flux along the iceberg's trajectory. However, smaller edge wastings will add to this and also larger children icebergs will eventually melt, but not necessarily at the location where they are lost.

#### 4. Discussion

Our findings compare well with previous studies of the Larsen-C Ice Shelf and of icebergs that followed similar trajectories. For example, our initial iceberg density of  $868$  kg m<sup>-3</sup> is consistent with the estimated  $\sim 15$  m firn air content derived from airborne observations (Holland et al., 2011) and our estimates and spatial distribution of initial iceberg thickness and freeboard agree very well with iceberg drafts derived from the same airborne campaign (Holland et al., 2009) and from in situ measurements collected along the suture zone (Jansen et al., 2013). Lopez-Lopez et al. (2021) estimated the area of A68A between 22 July 2017 and 26 January 2019 using a largely automated approach, and

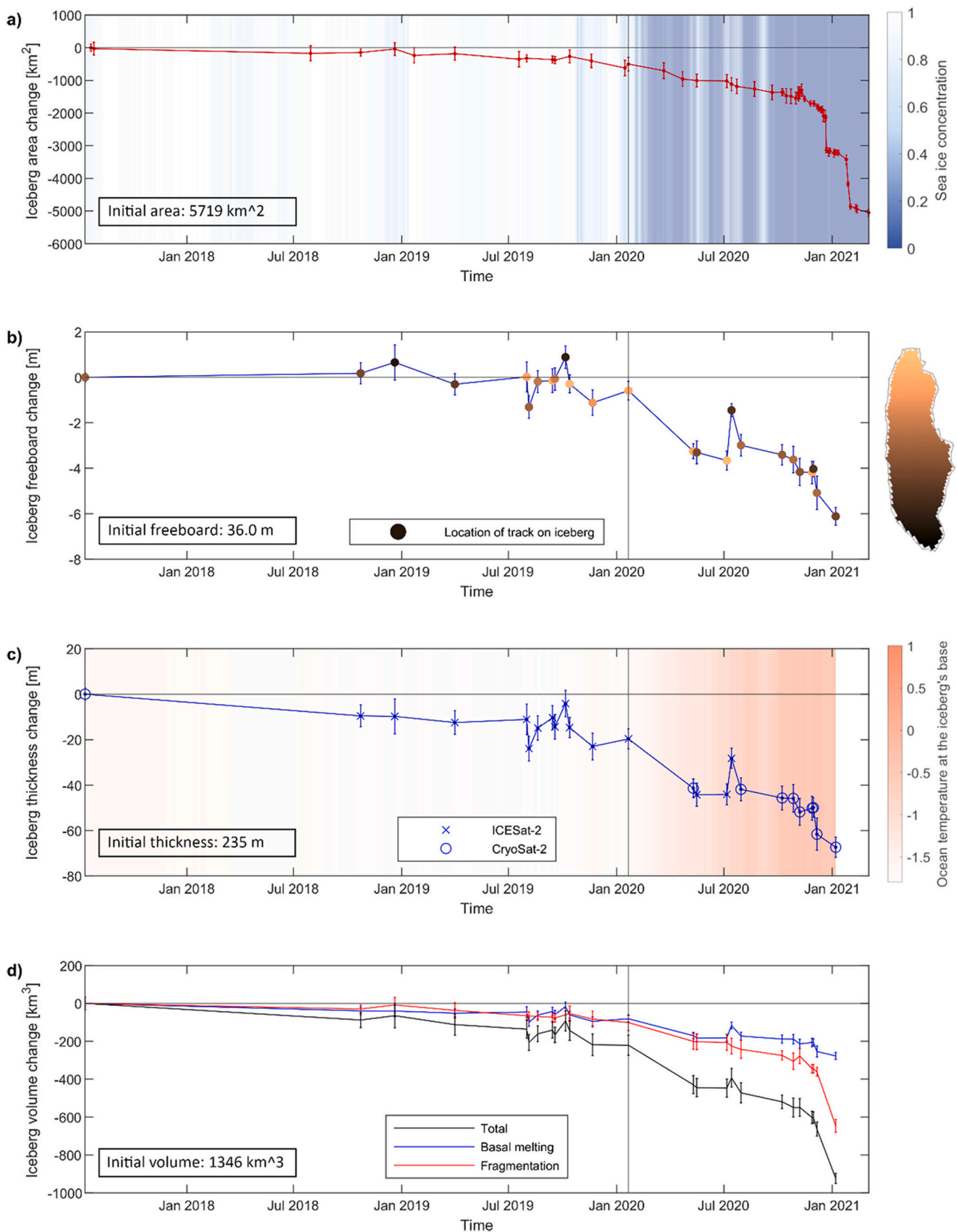


**Fig. 6.** Time series of changes in the A68A iceberg area (a), freeboard (b), thickness (c) and volume (d). The vertical line marks 21 January 2020, when the iceberg moved from the Weddell to the Scotia Sea (see Fig. 1). In panel (a) the background shading indicates sea ice concentration around the iceberg (OSI SAF, 2021) and in panel (c) the background shading indicates ocean temperature at the iceberg's base (Boyer et al., 2018).

**Table 1**

Annual change in the A68A iceberg area, thickness and volume in different regions along its trajectory.

Annual loss rate	Weddell Sea	Scotia Sea	Scotia Sea South	Scotia Sea North
Area [km <sup>2</sup> /year]	-200 ± 82	-2807 ± 199	-1205 ± 286	-7400 ± 298
Thickness [m/year]	-7.8 ± 2.1	-49.5 ± 6.5	-36.4 ± 9.5	-86.9 ± 27.4
Volume [km <sup>3</sup> /year]	-87.3 ± 21.0	-729.4 ± 50.4	-418.3 ± 75.7	-1621.7 ± 116.0
..through fragmentation	-44.7 ± 18.5	-538.3 ± 47.0	-244.1 ± 59.2	-1323.0 ± 90.9
..through melting	-42.6 ± 11.3	-191.2 ± 25.9	-174.2 ± 46.0	-298.7 ± 94.5

found a decrease of ~210 km<sup>2</sup>, which is close to our estimate of 236 km<sup>2</sup> over a similar period (22 July 2017 to 22 January 2019). Scambos et al. (2008) identified three types of breakup for the A22A iceberg, which took a similar path: rift calvings, edge wastings and rapid disintegration. The breakups of A68B and A68C were probably rift calvings along pre-existing fractures; the breakup of numerous children icebergs in the last few months of our survey were rapid disintegration likely caused by surface melting, and edge-wasting and side-melting are likely the reason for the remaining area reductions (Fig. 6a).

Previous studies have also reported similar rates of iceberg freeboard and thickness change. Scambos et al. (2008) recorded no change in freeboard (0 ± 1.3 m) for the A22A iceberg over 17 months until it reached the tip of the Antarctic Peninsula and a reduction by 11.7 ± 2.3 m/year during its passage to South Georgia; we find similar rates for A68A of 0.2 ± 0.1 m/year and 5.7 ± 0.4 m/year in the same locations. This comparison also shows that our colocation improves the melt rate accuracy with respect to using tracks that only sample similar parts of the iceberg. Han et al. (2019) estimated the rate of thickness change of A68A to be 12.89 ± 3.34 m/year between February and November 2018 at sparse crossing points of CryoSat-2 ground tracks. Although we do not have measurements for the same period, interpolation of our collocated estimates suggests a value of 7.0 ± 0.8 m which is in reasonable agreement. In the Weddell Sea, Jansen et al. (2007) report melt rates in the range 0 to 12 m per year for the A38B iceberg, in good agreement with our estimate of 7.8 ± 2.1 m/year for A68A. Iceberg melting increases significantly in the Scotia Sea, and our estimate of 49.5 ± 6.5 m/year for A68A is almost identical to the value of ~48 m/year found by Jansen et al. (2007) for A38B. Bouhier et al. (2018) recorded melt rates for the B17A iceberg of 68.4 m/year in Scotia Sea South and 180 m/year in the Scotia Sea North. These values are approximately double the melt rates we have calculated for A68A in the same location (Table 1). A possible explanation could be that B17A started out with significantly higher freeboard of around 50 m, which means that its draft was exposed to ocean currents at a greater depth, where the water temperature is higher (Boyer et al., 2018). Concerning the contributions of melting and breakage, Tournadre et al. (2015) found that melting contributes only 18% over the whole life cycle of all large Antarctic icebergs – which is a slightly lower estimate than the 32% which we find for A68A during our study period. However, previous studies (Bouhier et al., 2018; Scambos et al., 2008) found that fragmentation becomes the dominant factor towards the end, which is also apparent from our data (Fig. 6d, Table 1), and calculating volume loss until e.g. March 2021 (when our area change time series ends) would have likely increased the share of fragmentation.

The very distinct melt rates in the Weddell and Scotia Sea can be explained by the different environmental conditions: First of all, icebergs experience significantly higher water and air temperatures in the Scotia Sea compared to the Weddell Sea (Scambos et al., 2008; see also Fig. 6c). Secondly, icebergs drifting freely in the Scotia Sea (Schodlok et al., 2006) are no longer sheltered by sea ice (Fig. 6a), exposing them

to wave erosion at the sides, forming a subsurface ‘foot’, which leads to calving owing to buoyancy stress (the so-called ‘footloose mechanism’; Wagner et al., 2014). Apart from wave erosion at the waterline, ocean swell also induces strain on the iceberg, which can lead to crevasse and rift propagation (Li et al., 2018). Our observation that the initially southern part of the iceberg seems more stable (Fig. 6b) could be explained by the fact that this part is thinner (Figs. 2a and 5a) and therefore comes into contact with ocean water of a different temperature or current speed, as these are the two main drivers of iceberg melting (Bigg et al., 1997). In principle the iceberg could also have tilted to adjust its balance after break-offs from the northern part. Interestingly, we observe a notable thickness change in the Weddell Sea, although hardly any freeboard change was observed. This is because freeboard loss associated with basal melting and freeboard gain due to snow accumulation even out and hence a slow basal melting process can only be observed, when a snow layer is included in the calculations (Braakmann-Folgmann et al., 2021).

To constrain the intrusion of fresh water and nutrients, it is essential to determine where and by how much icebergs are melting (Silva et al., 2006). While volume loss due to basal melting serves as a lower bound estimate of freshwater and nutrient input, some of the area loss due to sidewall melting and edge-wastings also contribute, but are difficult to quantify in satellite observations. Children icebergs and larger edge-wastings, which form in larger calving events, travel further and take more time to melt (Tournadre et al., 2016). How quickly these melt depends on their size and the surrounding ocean conditions (Rackow et al., 2017; Stern et al., 2016); along the A68A trajectory, for example, melt rates vary from 10 to 100 m/year (Table 1) and ocean temperature at the iceberg’s base increases from -1.8 °C to just over +1 °C (Fig. 6c). Children icebergs of sufficient length will also fragment further (England et al., 2020). And unlike large tabular icebergs, smaller icebergs with lengths similar to their thickness frequently roll over (Hamley and Budd, 1986). To track the entire freshwater and nutrient input, the trajectories and melting of all fragmented pieces would have to be considered. Furthermore, the amount of bioavailable iron and nutrients delivered by icebergs also depends on the amount of sediments contained in the iceberg (Raiswell et al., 2016).

Despite these unknowns, our observations allow for an initial assessment of A68A’s impact on the ecosystem around South Georgia through scouring, melting and blockage. The closest recorded distance to the island was 62 km on 15 December 2020 with a mean draft of 141 ± 11 m. Seafloor bathymetry reveals a couple of shallower features within a distance of 52–65 km to the southern coastline (Fig. 1), where the iceberg could have grounded and where other icebergs may do so in future. Although A68A did not ground, it likely hit one of these features while turning (Fig. 1b). The shallowest bathymetry beneath the iceberg locations captured in satellite imagery is 150 m (Hogg et al., 2016). Although any scouring on the sea bed destroys the local benthic fauna (Barnes, 2017; Gutt, 2001), A68A’s turn will have affected only a small area. As it fragmented into smaller pieces, the risk of blockage to foraging grounds (Kooyman et al., 2007) for the millions of penguins and seals, raising their offspring on South Georgia (Clarke et al., 2012; Joiris et al., 2015), was largely averted. For future icebergs, this scenario is most likely at the western tip of the island, where icebergs of similar draft can approach up to a few kilometers. However, birds, seals and whales that regularly feed in the highly productive waters surrounding South Georgia (Atkinson et al., 2001; Joiris et al., 2015) could also be influenced by the large amount of melt water and nutrients released by icebergs as they drift near to the island, altering the ocean properties and plankton occurrence (Arrigo et al., 2002; Smith et al., 2013; Vernet et al., 2012). Overall, A68A spent at least 96 days (28 November 2020 to 4 March 2021, when our observations end) within 300 km off the coastline. Assuming its children icebergs melted at the same rate of 0.43 ± 0.17 m per day, we estimate that 152 ± 61 Gt of fresh water mixed with nutrients was released during this time. More research should be conducted to study the impact of this alteration on the marine life

around South Georgia. As this is a common iceberg trajectory, our results could also help to predict the disintegration of other large tabular icebergs and to include their impact in ocean models (England et al., 2020; Martin and Adcroft, 2010; Rackow et al., 2017).

## 5. Conclusions

We have characterized the evolution of the A68A iceberg from its calving off the Larsen-C Ice Shelf in July 2017 to its disintegration close to South Georgia in early-2021. Although the iceberg was tabular, it had significant undulations in topography across its surface. Thus, accurate collocation of the iceberg's orientation is required to derive reliable estimates of its freeboard and thickness change over time from satellite altimetry. We estimate that the average iceberg thickness reduced from  $235 \pm 9$  m at calving to  $168 \pm 10$  m near South Georgia. Combined with observations of its area change determined from satellite imagery, we estimate an initial volume of  $1346 \pm 53$  km<sup>3</sup> and  $802 \pm 34$  Gt of ice loss from the main iceberg in 3.5 years. Around one third ( $254 \pm 17$  Gt) of the mass loss was through basal melting, which provides a lower bound estimate of the direct freshwater input along the iceberg's trajectory. Losses due to side melting and break-offs of smaller pieces will add to the immediate freshwater flux, and larger children icebergs will also contribute as they melt. Near South Georgia we estimate a fresh water input of  $152 \pm 61$  Gt over  $\sim 3$  months, potentially impacting the island's rich ecosystem. We confirm that the distinct environmental conditions in the Weddell and Scotia Sea lead to rapidly increasing rates of melting and fragmentation once icebergs travel north of the Antarctic Peninsula. Our detailed maps of the A68A iceberg thickness change (Braakmann-Folgmann et al., 2022) will be useful for investigations of the impact of this calving event on the stability of the Larsen-C Ice Shelf, and for more detailed studies on the effects of meltwater and nutrients released in the vicinity of South Georgia. As this is a common iceberg trajectory, our results could also help to model the disintegration of other large tabular icebergs that take a similar path and to include their impact in ocean models.

Supplementary data to this article can be found online at <https://doi.org/10.1016/j.rse.2021.112855>.

## Data availability

All data used in this study are freely available: The iceberg trajectories are available from <https://www.scp.byu.edu/data/iceberg/>, CryoSat-2 data from <https://science-pds.cryosat.esa.int/>, ICESat-2 data from <https://openaltimetry.org/data/icesat2/> and <https://nsidc.org/data/atl03>, Sentinel-1 data from <https://scihub.copernicus.eu/dhus/> or <https://www.polarview.aq/antarctic>, Sentinel-3 data from <https://app.sentinel-hub.com/eo-browser>, MODIS data from <https://wvs.eartdata.nasa.gov/>, the ERA-5 data from <https://cds.climate.copernicus.eu/cdsapp#!/dataset/reanalysis-era5-single-levels>, sea ice concentration data from [ftp://osisaf.met.no/archive/ice/conc\\_amsr](ftp://osisaf.met.no/archive/ice/conc_amsr) and ocean temperature from <https://www.ncei.noaa.gov/data/oceans/woa/WOA18/DATA/temperature/>. The daily maps of iceberg thickness are available from Mendeley Data (Braakmann-Folgmann et al., 2022).

## Declaration of Competing Interest

The authors declare no conflict of interest.

## Acknowledgments

This work was supported by Barry Slavin and by NERC through National Capability funding, undertaken by a partnership between the Centre for Polar Observation Modelling and the British Antarctic Survey. We thank the three anonymous reviewers for their time and their positive and constructive comments that helped to improve this paper.

## References

- Arrigo, K.R., Van Dijken, G.L., Ainley, D.G., Fahnestock, M.A., Markus, T., 2002. Ecological impact of a large Antarctic iceberg. *Geophys. Res. Lett.* 29 <https://doi.org/10.1029/2001GL014160>, 8-1-8-4.
- Atkinson, A., Whitehouse, M.J., Priddle, J., Cripps, G.C., Ward, P., Brandon, M.A., 2001. South Georgia, Antarctica: a productive, cold water, pelagic ecosystem. *Mar. Ecol. Prog. Ser.* 216, 279-308. <https://doi.org/10.3354/meps216279>.
- Barnes, D.K.A., 2017. Iceberg killing fields limit huge potential for benthic blue carbon in Antarctic shallows. *Glob. Chang. Biol.* 23, 2649-2659. <https://doi.org/10.1111/gcb.13523>.
- Biddle, L.C., Kaiser, J., Heywood, K.J., Thompson, A.F., Jenkins, A., 2015. Ocean glider observations of iceberg-enhanced biological production in the northwestern Weddell Sea. *Geophys. Res. Lett.* 42, 459-465. <https://doi.org/10.1002/2014GL02850>.
- Bigg, G.R., Wadley, M.R., Stevens, D.P., Johnson, J.A., 1997. Modelling the dynamics and thermodynamics of icebergs. *Cold Reg. Sci. Technol.* 26, 113-135. [https://doi.org/10.1016/S0165-232X\(97\)00012-8](https://doi.org/10.1016/S0165-232X(97)00012-8).
- Bintanja, R., Van Oldenborgh, G.J., Katsman, C.A., 2015. The effect of increased fresh water from Antarctic ice shelves on future trends in Antarctic sea ice. *Ann. Glaciol.* 56, 120-126. <https://doi.org/10.3189/2015AoG69A001>.
- Bouhier, N., Tournadre, J., Rémy, F., Gourves-Cousin, R., 2018. Melting and fragmentation laws from the evolution of two large Southern Ocean icebergs estimated from satellite data. *Cryosphere* 12, 2267-2285. <https://doi.org/10.5194/tc-12-2267-2018>.
- Boyer, T.P., Garcia, Locarnini, Hernan E., Zweng, Ricardo A., Mishonov, Melissa M., Reagan, Alexey V., Weathers, James R., Baranova, Katharine A., Olga, K., Seidov, D., Smolyar, I.V., 2018. *World Ocean Atlas 2018*.
- Braakmann-Folgmann, A., Shepherd, A., Ridout, A., 2021. Changes in the area, thickness, and volume of the Thwaites 'B30' iceberg observed by satellite altimetry and imagery. *Cryosphere Discuss.* 1-27.
- Braakmann-Folgmann, A., Shepherd, A., Gerrish, L., Izzard, J., Ridout, A., 2022. A68A Iceberg Thickness Maps (Jul 2017-Jan 2021). <https://doi.org/10.17632/26dg4fwkbb.1>.
- Budge, J.S., Long, D.G., 2018. A comprehensive database for Antarctic iceberg tracking using scatterometer data. *IEEE J. Sel. Top. Appl. Earth Obs. Remote Sens.* 11, 434-442. <https://doi.org/10.1109/JSTARS.2017.2784186>.
- Clarke, A., Croxall, J.P., Poncet, S., Martin, A.R., Burton, R., 2012. Important bird areas: South Georgia. *Br. Bird* 105, 118-144.
- Copernicus Climate Change Service, 2018. ERA5 Hourly Data on Single Levels from 1979 to Present. <https://doi.org/10.24381/cds.adbb2d47>.
- Dryak, M.C., Enderlin, E.M., 2020. Analysis of Antarctic Peninsula glacier frontal ablation rates with respect to iceberg melt-inferred variability in ocean conditions. *J. Glaciol.* 66, 457-470. <https://doi.org/10.1017/jog.2020.21>.
- Duprat, L.P.A.M., Bigg, G.R., Wilton, D.J., 2016. Enhanced Southern Ocean marine productivity due to fertilization by giant icebergs. *Nat. Geosci.* 9, 219-221. <https://doi.org/10.1038/ngeo2633>.
- England, M.R., Wagner, T.J.W., Eisenman, I., 2020. Modeling the breakup of tabular icebergs. *Sci. Adv.* 6, 1-9. <https://doi.org/10.1126/sciadv.abb1273>.
- Fichefet, T., Morales Maqueda, M.A., 1999. Modelling the influence of snow accumulation and snow-ice formation on the seasonal cycle of the Antarctic sea-ice cover. *Clim. Dyn.* 15, 251-268. <https://doi.org/10.1007/s003820050280>.
- GEBCO Compilation Group, 2019. GEBCO 2019 Grid. <https://doi.org/10.5285/836f016a-33be-6ddc-e053-6c86abc0788e>.
- Greene, C.A., Gwyther, D.E., Blankenship, D.D., 2017. Antarctic mapping tools for MATLAB. *Comput. Geosci.* 104, 151-157. <https://doi.org/10.1016/j.cageo.2016.08.003>.
- Grimm, I., 2021. Assessing Effects of Iceberg A-68a on the Weddell Sea and South Georgia Ecosystems.
- Grosfeld, K., Schröder, M., Fahrbach, E., Gerdes, R., Mackensen, A., 2001. How iceberg calving and grounding change the circulation and hydrography in the Filchner Ice Shelf-Ocean System. *J. Geophys. Res.* 106, 9039-9055.
- Gutt, J., 2001. On the direct impact of ice on marine benthic communities, a review. *Polar Biol.* 24, 553-564. <https://doi.org/10.1007/s003000100262>.
- Hamley, T.C., Budd, W.F., 1986. Antarctic iceberg distribution and dissolution. *J. Glaciol.* 32, 242-251. <https://doi.org/10.1017/s0022143000015574>.
- Han, H., Lee, S., Kim, J.I., Kim, S.H., Kim, H.C., 2019. Changes in a giant iceberg created from the collapse of the Larsen C ice shelf, Antarctic Peninsula, derived from Sentinel-1 and CryoSat-2 data. *Remote Sens.* 11, 1-14. <https://doi.org/10.3390/rs11040404>.
- Helly, J.J., Kaufmann, R.S., Stephenson, G.R., Vernet, M., 2011. Cooling, dilution and mixing of ocean water by free-drifting icebergs in the Weddell Sea. *Deep. Res. Part II Top. Stud. Oceanogr.* 58, 1346-1363. <https://doi.org/10.1016/j.dsr2.2010.11.010>.
- Hogg, A.E., Gudmundsson, G.H., 2017. Commentary: impacts of the Larsen-C ice shelf calving event. *Nat. Clim. Chang.* 7, 540-542. <https://doi.org/10.1038/nclimate3359>.
- Hogg, O., Huvenne, V.A., Griffiths, H.J., Dorschel, B., Linse, K., 2016. A Bathymetric Compilation of South Georgia, 1985-2015. <https://doi.org/10.5285/ce8bf6be-4b5f-454c-9165-73ab4c3bf23>.
- Holland, P.R., Corr, H.F.J., Vaughan, D.G., Jenkins, A., Skvarca, P., 2009. Marine ice in Larsen ice shelf. *Geophys. Res. Lett.* 36, 1-6. <https://doi.org/10.1029/2009GL038162>.
- Holland, P.R., Corr, H.F.J., Pritchard, H.D., Vaughan, D.G., Arthern, R.J., Jenkins, A., Tedesco, M., 2011. The air content of Larsen ice shelf. *Geophys. Res. Lett.* 38, 1-6. <https://doi.org/10.1029/2011GL047245>.
- International Organization for Standardization, 1998. ISO 4355 Bases for Design on Structures - Determination of Snow Loads on Roofs.

- Jansen, D., Schodlok, M., Rack, W., 2007. Basal melting of A-38B: a physical model constrained by satellite observations. *Remote Sens. Environ.* 111, 195–203. <https://doi.org/10.1016/j.rse.2007.03.022>.
- Jansen, D., Luckman, A., Kulesa, B., Holland, P.R., King, E.C., 2013. Marine ice formation in a suture zone on the Larsen C ice shelf and its influence on ice shelf dynamics. *J. Geophys. Res. Earth Surf.* 118, 1628–1640. <https://doi.org/10.1002/jgrf.20120>.
- Jansen, D., Luckman, A., Cook, A., Bevan, S., Kulesa, B., Hubbard, B., Holland, P.R., 2015. Brief communication: newly developing rift in Larsen C ice shelf presents significant risk to stability. *Cryosphere* 9, 1223–1227. <https://doi.org/10.5194/tc-9-1223-2015>.
- Jenkins, A., 1999. The impact of melting ice on ocean waters. *J. Phys. Oceanogr.* 29, 2370–2381. [https://doi.org/10.1175/1520-0485\(1999\)029<2370:TIOmio>2.0.CO;2](https://doi.org/10.1175/1520-0485(1999)029<2370:TIOmio>2.0.CO;2).
- Joiris, C.R., Humphries, G.R.W., D'Hert, D., Robert, H., Beudels-Jamar, R.C., 2015. Major hotspots detected along the Scotia Ridge in autumn for southern right whales *Eubalaena australis*, Antarctic fur seals *Arctocephalus gazella* and Antarctic prions *Pachyptila desolata*. *Adv. Polar Sci.* 26, 282–291. <https://doi.org/10.13679/j.advps.2015.4.00282>.
- Kooyman, G.L., Ainley, D.G., Ballard, G., Ponganis, P.J., 2007. Effects of giant icebergs on two emperor penguin colonies in the Ross Sea, Antarctica. *Antarct. Sci.* 19, 31–38. <https://doi.org/10.1017/S0954102007000065>.
- Kurtz, N.T., Markus, T., 2012. Satellite observations of Antarctic sea ice thickness and volume. *J. Geophys. Res. Ocean* 117, 1–9. <https://doi.org/10.1029/2012JC008141>.
- Kwok, R., Cunningham, G.F., 2008. ICESat over Arctic sea ice: estimation of snow depth and ice thickness. *J. Geophys. Res. Ocean* 113, 1–17. <https://doi.org/10.1029/2008JC004753>.
- Li, Tian, Shokr, M., Liu, Y., Cheng, X., Li, Teng, Wang, F., Hui, F., 2018. Monitoring the tabular icebergs C28A and C28B calved from the Mertz Ice Tongue using radar remote sensing data. *Remote Sens. Environ.* 216, 615–625. <https://doi.org/10.1016/j.rse.2018.07.028>.
- Ligtenberg, S.R.M., Helsen, M.M., Van Den Broeke, M.R., 2011. An improved semi-empirical model for the densification of Antarctic firn. *Cryosphere* 5, 809–819. <https://doi.org/10.5194/tc-5-809-2011>.
- Lopez-Lopez, L., Parmiggiani, F., Moctezuma-Flores, M., Guerrieri, L., 2021. On the detection and long-term path visualisation of a-68 iceberg. *Remote Sens.* 13, 1–13. <https://doi.org/10.3390/rs13030460>.
- Martin, T., Adcroft, A., 2010. Parameterizing the fresh-water flux from land ice to ocean with interactive icebergs in a coupled climate model. *Ocean Model* 34, 111–124. <https://doi.org/10.1016/j.ocemod.2010.05.001>.
- Merino, N., Le Sommer, J., Durand, G., Jourdain, N.C., Madec, G., Mathiot, P., Tournadre, J., 2016. Antarctic icebergs melt over the Southern Ocean : climatology and impact on sea ice. *Ocean Model* 104, 99–110. <https://doi.org/10.1016/j.ocemod.2016.05.001>.
- Mouginot, J., Rignot, E., Scheuchl, B., 2019. Continent-Wide, Interferometric SAR Phase, Mapping of Antarctic Ice Velocity. *Geophys. Res. Lett.* 46, 9710–9718. <https://doi.org/10.1029/2019GL083826>.
- OSI SAF, 2021. AMSR-2 Sea Ice Concentration Product of the EUMETSAT Ocean and Sea Ice Satellite Application Facility.
- Rackow, T., Wesche, C., Timmermann, R., Hellmer, H.H., Juricke, S., Jung, T., 2017. A simulation of small to giant Antarctic iceberg evolution: differential impact on climatology estimates. *J. Geophys. Res. Ocean* 117, 3170–3190. <https://doi.org/10.1002/2016JC012513>.Received.
- Raiswell, R., Hawkings, J.R., Benning, L.G., Baker, A.R., Death, R., Albani, S., Mahowald, N., Krom, M.D., Poulton, S.W., Wadham, J., Tranter, M., 2016. Potentially bioavailable iron delivery by iceberg-hosted sediments and atmospheric dust to the polar oceans. *Biogeosciences* 13, 3887–3900. <https://doi.org/10.5194/bg-13-3887-2016>.
- Rignot, E., Casassa, G., Gogineni, P., Krabill, W., Rivera, A., Thomas, R., 2004. Accelerated ice discharge from the Antarctic Peninsula following the collapse of Larsen B ice shelf. *Geophys. Res. Lett.* 31, 2–5. <https://doi.org/10.1029/2004GL020697>.
- Rott, H., Skvarca, P., Nagler, T., 1996. Rapid collapse of northern Larsen ice shelf, Antarctica. *Science* 80 (271), 788–792. <https://doi.org/10.1126/science.271.5250.788>.
- Scambos, T., Ross, R., Bauer, R., Yermolin, Y., Skvarca, P., Long, D., Bohlander, J., Haran, T., 2008. Calving and ice-shelf break-up processes investigated by proxy: Antarctic tabular iceberg evolution during northward drift. *J. Glaciol.* 54, 579–591. <https://doi.org/10.3189/002214308786570836>.
- Schodlok, M.P., Hellmer, H.H., Rohardt, G., Fahrbach, E., 2006. Weddell Sea iceberg drift: five years of observations. *J. Geophys. Res. Ocean* 111, 1–14. <https://doi.org/10.1029/2004JC002661>.
- Shepherd, A., Gilbert, L., Muir, A.S., Konrad, H., McMillan, M., Slater, T., Briggs, K.H., Sundal, A.V., Hogg, A.E., Engdahl, M.E., 2019. Trends in Antarctic ice sheet elevation and mass. *Geophys. Res. Lett.* 46, 8174–8183. <https://doi.org/10.1029/2019GL082182>.
- Silva, T.A.M., Bigg, G.R., Nicholls, K.W., 2006. Contribution of giant icebergs to the Southern Ocean freshwater flux. *J. Geophys. Res.* 111, 1–8. <https://doi.org/10.1029/2004JC002843>.
- Smith, K.L., Robison, B.H., Helly, J.J., Kaufmann, R.S., Ruhl, H.A., Shaw, T.J., Twining, B.S., Vernet, M., 2007. Free-drifting icebergs: hot spots of chemical and biological enrichment in the Weddell Sea. *Science* 80 (317), 478–482. <https://doi.org/10.1126/science.1142834>.
- Smith, K.L., Sherman, A.D., Shaw, T.J., Sprintall, J., 2013. Icebergs as unique lagrangian ecosystems in polar seas. *Annu. Rev. Mar. Sci.* 5, 269–287. <https://doi.org/10.1146/annurev-marine-121211-172317>.
- Stern, A.A., Adcroft, A., Sergienko, O., 2016. The effects of Antarctic iceberg calving-size distribution in a global climate model. *J. Geophys. Res. Ocean* 1–14. <https://doi.org/10.1002/2016JC011835>.Received.
- Storto, A., Oddo, P., Cozzani, E., Coelho, E.F., 2019. Introducing along-track error correlations for altimetry data in a regional ocean prediction system. *J. Atmos. Ocean. Technol.* 36, 1657–1674. <https://doi.org/10.1175/JTECH-D-18-0213.1>.
- Tilling, R.L., Ridout, A., Shepherd, A., 2018. Estimating Arctic sea ice thickness and volume using CryoSat-2 radar altimeter data. *Adv. Sp. Res.* 62, 1203–1225. <https://doi.org/10.1016/j.asr.2017.10.051>.
- Tournadre, J., Bouhier, N., Girard-Arduin, F., Remy, F., 2015. Large icebergs characteristics from altimeter waveforms analysis. *J. Geophys. Res. Ocean* 120, 2121–2128. <https://doi.org/10.1002/2014JC010502>.
- Tournadre, J., Bouhier, N., Girard-Arduin, F., Rémy, F., 2016. Antarctic icebergs distributions 1992–2014. *J. Geophys. Res. Ocean* 121, 327–349. <https://doi.org/10.1002/2015JC011178>.
- Vernet, M., Smith, K.L., Cefarelli, A.O., Helly, J.J., Kaufmann, R.S., Lin, H., Long, D.G., Murray, A.E., Robison, B.H., Ruhl, H.A., Shaw, T.J., Sherman, A.D., Sprintall, J., Stephenson, G.R., Stuart, K.M., Twining, B.S., 2012. Islands of ice: influence of free-drifting Antarctic icebergs on pelagic marine ecosystems. *Oceanography* 25, 38–39. <https://doi.org/10.5670/oceanog.2012.72>.
- Wagner, T.J.W., Wadhams, P., Bates, R., Elosegui, P., Stern, A., Vella, D., Abrahamson, E. P., Crawford, A., Nicholls, K.W., 2014. The “footloose” mechanism: iceberg decay from hydrostatic stresses. *Geophys. Res. Lett.* 41, 5522–5529. <https://doi.org/10.1002/2014GL060832>.
- Wise, M.G., Dowdeswell, J.A., Jakobsson, M., Larter, R.D., 2017. Evidence of marine ice-cliff instability in Pine Island Bay from iceberg-keel plough marks. *Nature* 550, 506–510. <https://doi.org/10.1038/nature24458>.
- Wu, S.Y., Hou, S., 2017. Impact of icebergs on net primary productivity in the Southern Ocean. *Cryosphere* 11, 707–722. <https://doi.org/10.5194/tc-11-707-2017>.

# APPENDIX C

## MAPPING THE EXTENT OF GIANT ANTARCTIC ICEBERGS WITH DEEP LEARNING



# Mapping the extent of giant Antarctic icebergs with Deep Learning

Anne Braakmann-Folgmann<sup>1</sup>, Andrew Shepherd<sup>1,2</sup>, David Hogg<sup>3</sup>, Ella Redmond<sup>1</sup>

<sup>1</sup> Centre for Polar Observation and Modelling (CPOM), University of Leeds, Leeds, LS2 9JT, UK

<sup>2</sup> Geography and Environment Department, Northumbria University, Newcastle upon Tyne, NE1 8ST, UK

5 <sup>3</sup> School of Computer Science, University of Leeds, Leeds, LS2 9JT, UK

*Correspondence to:* Anne Braakmann-Folgmann (anne.bf@gmx.de)

**Abstract.** Icebergs release cold, fresh meltwater and terrigenous nutrients as they drift and melt, influencing the local ocean properties and encouraging sea ice formation and biological production. To locate and quantify the fresh water flux from Antarctic icebergs, changes in their area and thickness have to be monitored along their trajectories. While the locations of large icebergs are tracked operationally by manual inspection, delineation of their extent is not. Here, we propose a U-net approach to automatically map the extent of giant icebergs in Sentinel-1 imagery. This greatly improves the efficiency compared to manual delineations, reducing the time for each outline from several minutes to less than 0.01 sec. We evaluate the performance of our U-net and two state-of-the-art segmentation algorithms on 191 images. For icebergs, larger than covered by the training data, we find that U-net tends to miss parts. Otherwise, U-net is more robust to scenes with complex backgrounds, ignoring sea ice, smaller patches of nearby coast or other icebergs and outperforms the other two techniques achieving an  $F_1$  score of 0.84 and an absolute median deviation in iceberg area of 4.1 %.

## 1 Introduction

Icebergs influence the environment along their trajectory through the release of cold fresh water mixed with terrigenous nutrients (Duprat et al., 2016; Helly et al., 2011; Jenkins, 1999; Merino et al., 2016; Smith et al., 2007; Vernet et al., 2012). The more they melt, the higher the impact. However, this melting is not linear, but depends on the surrounding ocean temperature, current speed and many other variables that are hard to model or observe (Bigg et al., 1997; Bouhier et al., 2018; England et al., 2020; Jansen et al., 2007; Silva et al., 2006). Calculating fresh water input from satellite observations is possible and can partially be automated, but requires manual delineations of the iceberg outlines to calculate changes in iceberg area and to collocate altimetry tracks with a map of initial iceberg thickness to estimate basal melting (Braakmann-Folgmann et al., 2021, 2022). Here, we present an automated approach using a U-net (Ronneberger et al., 2015) to segment giant Antarctic icebergs in Sentinel-1 images and hence to derive their outline and area.

A number of methods have been proposed to automatically detect and segment icebergs in satellite radar imagery. Early work by Willis et al. (1996) was based on a simple thresholding technique and limited to certain iceberg sizes of a few hundred meters and certain wind conditions. Later, the Constant False Alarm Rate (CFAR) thresholding technique has been applied to detect icebergs in the Arctic (Frost et al., 2016; Gill, 2001; Power et al., 2001). Wesche and Dierking (2012) also used a



threshold based on a K-distribution fitted to observed backscatter coefficients of icebergs, sea ice and open ocean followed by morphological operations. Mazur et al. (2017) developed an algorithm for iceberg detection in the Weddell Sea based on thresholds for brightness, shape, size, etc. at five scale levels applied to ENVISAT ASAR data. Apart from thresholding, edge-detection techniques have been applied: Williams et al. (1999) used a standard edge-detection technique followed by pixel bonding (Sephton et al., 1994) applied to ERS-1 images during austral winter to detect and segment icebergs in East Antarctica. 35 Silva and Bigg (2005) extended this to ENVISAT images and improved the algorithm by using a slightly more sophisticated edge detection technique followed by a watershed segmentation and a classification step that takes area and shape into consideration, but also requires manual interventions. Collares et al. (2018) use the k-means algorithm (Macqueen, 1967) to segment icebergs, which are then manually tracked. Koo et al. (2021) employ a built-in segmentation technique similar to k-means using Google Earth Engine to segment Sentinel-1 images and then apply an incidence angle-dependent brightness 40 threshold to find icebergs. Calculating the similarity of the distance to centroid histograms of all detected icebergs, they then track one specific giant iceberg (B43). The most elaborate algorithm has been proposed by Barbat et al. (2019) using a graph-based segmentation and Ensemble Forest Committee classification algorithm with a range of hand-crafted features.

Despite the quantity and variety of previous approaches, a range of limitations has so far hindered the operational application 45 of an automated iceberg segmentation algorithm. Overall, previous studies have focused on smaller icebergs and perform worse for larger ones or are not even applicable there (Mazur et al., 2017; Wesche and Dierking, 2012; Willis et al., 1996). Our work extends previous studies with the goal to delineate specific giant icebergs. Giant icebergs make up a very small part of the total iceberg population, but hold the majority of the total ice volume (Tournadre et al., 2016), which makes them the most relevant for freshwater fluxes. Apart from iceberg size, there are many remaining challenges, resulting from the variable 50 appearance of icebergs as well as the surrounding ocean or sea ice in SAR imagery (Ulaby and Long., 2014). Some of the existing techniques are therefore limited to austral winter images and still require manual intervention (Silva and Bigg, 2005; Williams et al., 1999). Dark icebergs remain a problem for all existing methods using SAR images. Many studies also report degrading accuracies in high wind conditions (Frost et al., 2016; Mazur et al., 2017; Willis et al., 1996). Deformed sea ice or sea ice in general is also mentioned to lead to false detections (Koo et al., 2021; Mazur et al., 2017; Silva and Bigg, 2005; 55 Wesche and Dierking, 2012; Willis et al., 1996). And finally clusters of several bergs and berg fragments too close to each other have been found to pose a problem (Barbat et al., 2019b; Frost et al., 2016; Koo et al., 2021; Williams et al., 1999). Our work aims to delineate icebergs in a variety of environmental conditions as accurately as possible using a deep learning technique.

Deep neural networks can encode the most meaningful features themselves and are able to learn more complex non-linear 60 relationships. They therefore outperform classic machine learning techniques in most tasks (LeCun et al., 2015; Schmidhuber, 2015). U-net is a neural network that was originally developed for biomedical image segmentation (Ronneberger et al., 2015). It has since been applied to many other domains including satellite images and polar science (Andersson et al., 2021; Baumhoer et al., 2019; Dirscherl et al., 2021; Mohajerani et al., 2019, 2021; Poliyapram et al., 2019; Singh et al., 2020; Stokholm et al., 2022; Surawy-Stepney et al., 2023; Zhang et al., 2019). U-net works well with few training examples, trains quickly and still



65 achieves very good results (Ronneberger et al., 2015). A comparison between three network architectures (Deeplab, DenseNet  
and U-net) for river ice segmentation found that U-net provided the best balance between quantitative performance and good  
generalization (Singh et al., 2020). Baumhoer et al. (2019) used a U-net architecture to automatically delineate ice shelf fronts  
in Sentinel-1 images with good success (108 m average deviation). As the calving front to ocean boundary looks very similar  
to an iceberg to ocean boundary and both goals have to deal with comparable problems like near-by sea ice and varying  
70 appearance of the ice, ocean and sea ice surfaces, we decided to also employ a U-net.

## 2 Data and methods

This section describes the Sentinel-1 input data, generation of the manually derived outlines for training, validation and testing,  
the implementation of two standard segmentation methods and our U-net architecture. The goal is to derive the outlines of  
Antarctic icebergs, which are large enough to receive a name and to be tracked operationally. Therefore, we aim to generate a  
75 binary segmentation map, where the biggest iceberg present is selected and everything else – including smaller icebergs,  
iceberg fragments and adjacent land ice – is considered as background. This approach differs from most previous work, where  
the goal has been to find all icebergs and is targeted to monitor changes in area of these large bergs, but also to track how the  
icebergs rotate and to use their outline to automatically collocate altimetry overpasses (Braakmann-Folgmann et al., 2022).

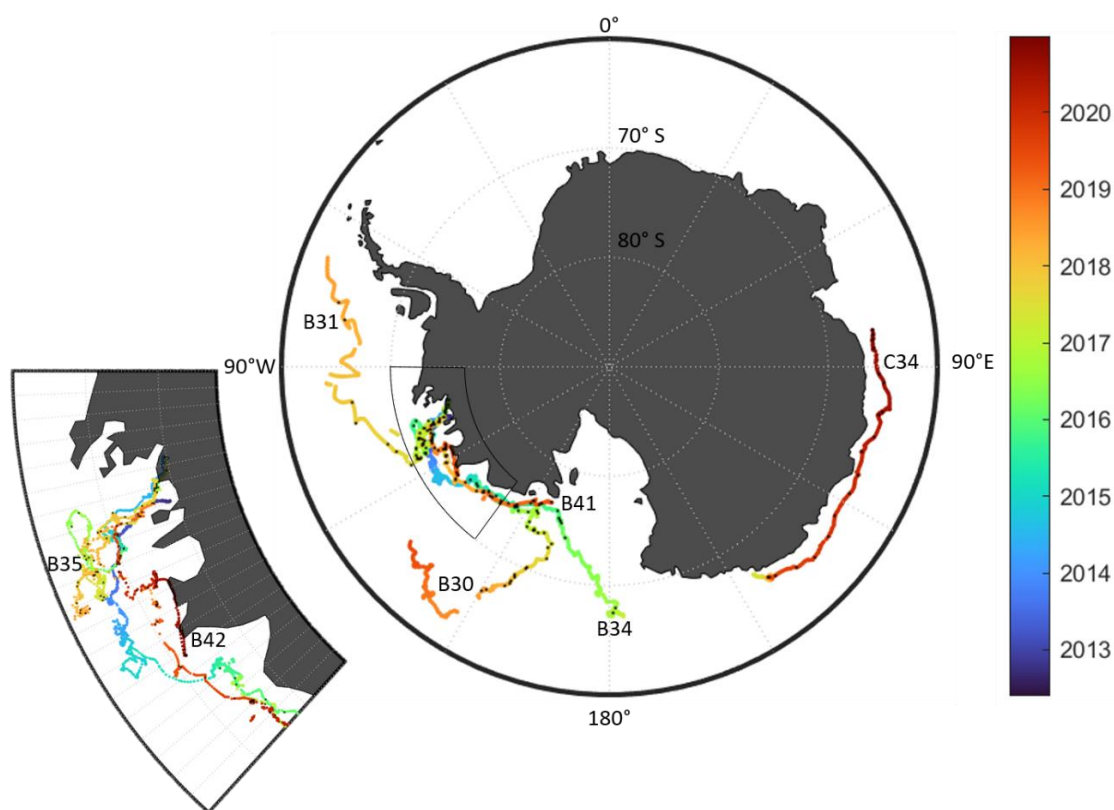
### 2.1. Sentinel-1 input imagery

80 The Sentinel-1 satellites measure the backscatter of the surface beneath them using Synthetic Aperture Radar (SAR). In  
contrast to optical imagery, SAR provides data throughout the polar night and independent of cloud cover (Ulaby and Long.,  
2014), which is frequent over the Southern Ocean. The Sentinel satellites are an operational satellite system with free data  
availability (Torres et al., 2012). Sentinel-1a (2014-present) and Sentinel-1b (2016-2022) had a combined repeat cycle of 6  
days (Torres et al., 2012), but the polar regions are sampled more frequently. We use the Level 1 Ground Range Detected  
85 (GRD) data. Depending on the geographic location around Antarctica, data is collected in either interferometric wide (IW) or  
extra wide (EW) swath mode. IW is a 250 km wide swath with 5 x 20 m native spatial resolution and EW is a 400 km wide  
swath with 20 x 40 m native resolution. We use both modes depending on availability. While HH (horizontal transmit and  
horizontal receive) polarised data is available across the Southern Ocean, HV (horizontal transmit and vertical receive) data is  
only available in some parts. As icebergs drift across these acquisition masks and HH has been found to give the best results  
90 for iceberg detection (Sandven et al., 2007), we use the HH polarised data only.

We pre-process and crop the Sentinel-1 images before applying the segmentation techniques. First, we apply the precise orbit  
file, remove thermal noise and apply a radiometric calibration. We also multilook the data with a factor of six to reduce speckle  
and image size, yielding a spatial resolution of 240 m. Then we apply a terrain correction using the GETASSE30 (Global Earth  
Topography And Sea Surface Elevation at 30 arc second resolution) digital elevation model and project the output on a polar  
95 stereographic map with true latitude of 71°S. These pre-processing steps are conducted in the Sentinel Application Platform



(SNAP). All icebergs that are longer than 18.5 km (10 nautical miles) or that encompass an area of at least 68.6 km<sup>2</sup> (20 square nautical miles) are named and tracked operationally every week by the National Ice Center (NIC). Also slightly smaller icebergs (longer than 6 km) are tracked by the Brigham Young University (Budge and Long, 2018), who release daily positions every few years. Therefore, we have a good estimate of where each of these giant icebergs should be and cannot only download 100 targeted Sentinel-1 images containing these icebergs, but also crop the images around the estimated central position to a size of 256 x 256 pixels. Hence, every input image contains a giant target iceberg. Some images contain several icebergs and in this case, we are only interested in the largest one. To ensure that the largest bergs fit within the image, we rescale images of icebergs with a major axis longer than 37 km (20 nautical miles). As the NIC also provides estimates of the semi major axes lengths, we apply the rescaling based on this. The rescaled images have a pixel resolution of 480 m instead. For all input 105 images, we scale the backscatter between the 1<sup>st</sup> and 99<sup>th</sup> percentile to enhance the contrast. In this step, we also replace pixels outside the satellite scene coverage with ones, and create a mask to discard the same pixels from the predictions.



110 **Figure 1: Spatial and temporal coverage of our dataset: The trajectories (by Budge and Long, 2018) of the seven selected icebergs are colour-coded according to time and black squares indicate the locations of the images used in this study.**

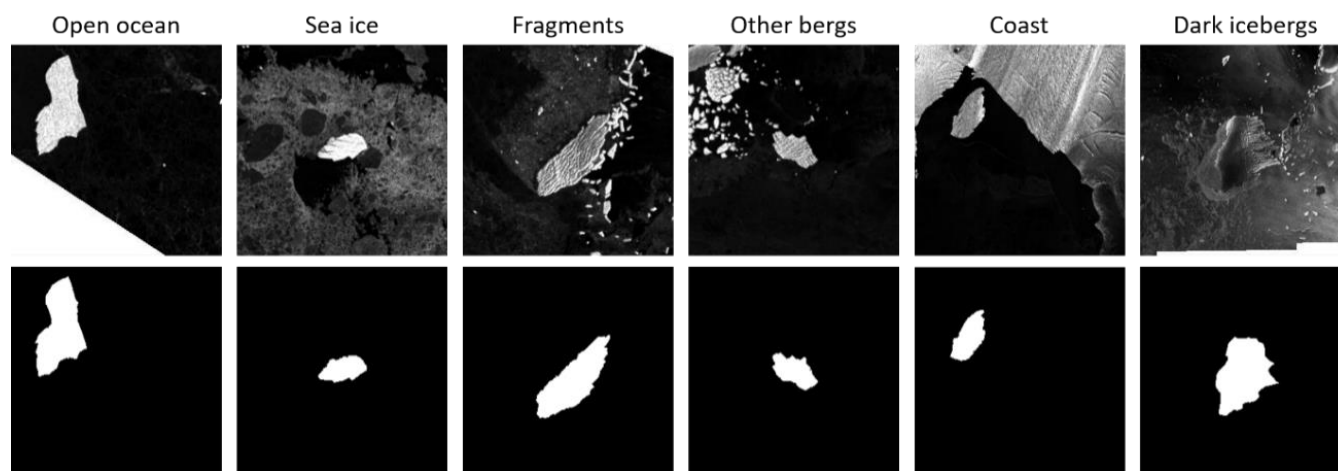
The overall dataset consists of 191 images, showing seven giant icebergs: B30, B31, B34, B35, B41, B42 and C34. These are between 54 and 1052 km<sup>2</sup> in size. B30 is the only iceberg that is initially longer than 37 km, so we rescale the first 27 images,



115 until its length drops below 37 km. A further two images of this iceberg are then used at normal resolution (Figure 4 first column shows rescaled images of B30 and the last one at normal resolution). Spatially, we cover different parts of the Southern Ocean including the Pacific and Indian Ocean side with a focus on the Amundsen Sea (see Figure 1). Temporally, our images span the years 2014-2020 and are scattered across all seasons. For each iceberg, the individual images are roughly one month apart. Far higher temporal sampling would be possible in terms of satellite image availability, but we aim to cover a wide range of environmental conditions, seasons and iceberg shapes and sizes. As these are highly correlated in subsequent images, we decided to use only one image per month.

## 120 2.2. Grouping of input images according to environmental conditions

The appearance of icebergs versus the surrounding ocean or sea ice depends on their roughness, the dielectric properties (e.g. moisture of the ice) and the angle of satellite overpass (Figure 2). While calm ocean appears as a dark surface in SAR images, wind roughened sea appears brighter depending on the relative wind direction versus the satellite viewing angle (Young et al., 1998). Thin sea ice has a similar backscatter to calm sea (Young et al., 1998), but rougher first-year ice already exhibits higher backscatter and multi-year ice can reach backscatter values overlapping with the range of typical iceberg backscatter (Drinkwater, 1998). Icebergs with dry, compact snow are usually bright targets in SAR images (Mazur et al., 2017; Wesche and Dierking, 2012; Young et al., 1998). However, surface thawing can reduce the iceberg backscatter significantly (Young and Hyland, 1997), meaning that those icebergs have the same or lower backscatter than the surrounding ocean and sea ice, and appear as dark objects (Wesche and Dierking, 2012; see our Figure 2, last column). Furthermore, giant tabular icebergs can exhibit a gradient (Barbat et al., 2019a) due to variations in backscatter with the viewing angle (Wesche and Dierking, 2012) or appear heterogeneous due to crevasses, (see Figure 2, third and last column), which also complicates segmentation and differentiation from the surrounding ocean and sea ice.



135 **Figure 2: Examples of input images (top row) and segmentation maps based on manually derived delineations (bottom row) in different environmental conditions. From left to right these are B31 in open ocean, B41 surrounded by sea ice, B42 with nearby fragments, C34 and another similar sized iceberg, B41 close to the coast and B30 appearing dark.**



We visually group all input images into different categories to assess the performance in different potentially challenging conditions. These groups are *open ocean*, *sea ice*, *fragments*, *other bergs*, *coast* and *dark icebergs* (Figure 2 shows one example each). We class an image as *dark iceberg*, if the iceberg appears as dark or does not stand out from the background, because both have a similar intensity of grey, making it hard to pick out the berg (Wesche and Dierking, 2012). Images that contain *coast* (i.e. nearby ice shelves or glaciers on the Antarctic continent) are grouped into this category. Due to very similar physical conditions, ice-shelves and icebergs are hard to differentiate. In some cases, several giant icebergs drift very close to each other and both are (partially) visible in our cropped images. If another berg of similar size is present, the algorithms might pick the wrong berg and therefore we introduce one group of *other bergs*. There is also one case where a bigger iceberg is partially visible, but we are aiming to segment the largest berg that is fully visible (e.g. Figure 5h). Fragments occur frequently in the vicinity of icebergs, as icebergs regularly calve smaller bits and pieces around their edges. We assign images to this category if the fragments pose a challenge because they are so close to the iceberg, that they are easily grouped together (Koo et al., 2021). The last challenge is *sea ice*. Young and flat sea ice usually appears homogenous and dark and does not pose a problem. However, older, ridged sea ice and other cases where the background appears grey rather than black with significant structure (Mazur et al., 2017) are grouped into this category. If the sea ice is not visually apparent (i.e. young and flat) and the background appears as dark and relatively homogenous or only contains fragments that are further away from the iceberg and hence there is no obvious challenge apparent to us, we class these images as *open ocean*. If several challenges are present (e.g. if *coast* and *sea ice* are visible), we assign the image to the most relevant group.

### 2.3. Manual delineation of iceberg perimeters

Although the goal is to develop an automated segmentation technique, we require manual delineations of iceberg extent for training and evaluation. We manually click the iceberg perimeter in GIS software to yield a polygon. The accuracy of such manual delineations is estimated to be 2-4 % of the iceberg area (Bouhier et al., 2018; Braakmann-Folgmann et al., 2021, 2022). We then create a binary map of the same size as the input image, where pixels within the manually derived polygon are defined as iceberg and everything else as background to allow a rapid evaluation of performance. Some examples of input images and their corresponding segmentation maps based on the manual outlines are shown in Figure 2. We regard the manually derived outlines as the most accurate and use these binary maps to train our neural network and to evaluate all automated segmentation techniques. When the area deviation of our automated segmentation techniques drops below 2-4 %, their prediction might be more accurate than the manual delineation. In any case, automated approaches are advantageous over manual delineations – especially when rolled out for numerous icebergs or in operational applications, as each outline takes several minutes to click manually.

### 2.4. Iceberg segmentation with k-means and Otsu

We implement two standard segmentation techniques as a baseline: Otsu thresholding and k-means. In both cases, we mask out the areas that had no satellite scene coverage by setting them to zero (black). For the first segmentation technique, we



smooth the input image with a 5x5 Gaussian kernel. Then we apply the Otsu threshold (Otsu, 1979) yielding a binary image.  
170 The Otsu threshold is determined automatically based on the image's greyscale histogram so that the within-class variance is  
minimised. To find an iceberg, we apply connected component analysis to the binary image and select the largest component.  
We also experimented with other thresholding techniques including adaptive mean and adaptive Gaussian thresholding, but  
found that the Otsu threshold gave the best results. Although different thresholding techniques have been proposed for iceberg  
detection (Frost et al., 2016; Mazur et al., 2017; Power et al., 2001; Wesche and Dierking, 2012; Willis et al., 1996), to our  
175 knowledge none of them have used the Otsu method. The second technique is k-means (Macqueen, 1967) with  $k=2$ . We use  
random centre initialisation and run the algorithm for 20 iterations or until an accuracy of 0.5 is reached. We repeat this 100  
times with different initialisations and take the result with the best compactness. Afterwards, we also perform a connected  
component analysis and select the largest component. K-means and a variation of it have also been applied to track selected  
icebergs by Collares et al. (2018) and Koo et al. (2021) respectively. Both our standard segmentation techniques are  
180 implemented using the OpenCV library (Bradski, 2000) for Python.

## 2.5. Iceberg segmentation with U-net

We suggest a U-net architecture to segment Sentinel-1 input images into the largest iceberg and background, which is based  
on the original U-net (Ronneberger et al., 2015) with some modifications. The input images are 256 x 256 one-channel  
backscatter images (as described in Section 2.1. and shown in Figure 2). The U-net is composed of an encoder that produces  
185 a compressed representation of the input image followed by a decoder that constructs a segmentation map from the compressed  
encoding with the same spatial resolution as the input (Figure 3). The encoder uses a number of convolutional and pooling  
layers to generate feature maps at increasing levels of abstraction and spatial scale. The decoder uses further convolutional  
layers and upsampling to construct the required segmentation map. Cross-links convey feature maps from different spatial  
scales in the encoder to the respective decoder stage, where they are combined with contextual feature maps from the decoder  
190 layer below. This allows U-net to produce accurate segmentations whilst also considering contextual features. We use padding  
in the convolutions and pooling operations, so that the feature maps remain the same size as the input at each level (spatial  
scale) and reduce by 50% in height and width between encoder levels. We also use depth-wise separable convolutions (Chollet,  
2017), which are more efficient. Furthermore, we added dropout of 0.3 in between the two convolutions per level to avoid  
over-fitting (Srivastava et al., 2014) and residual connections to aid the learning process and increase the accuracy (He et al.,  
195 2016). The outputs are one-channel 256 x 256 arrays, representing the probability that each pixel belongs to the iceberg class.  
During training these output maps are compared with the segmentation maps from our manually derived outlines to alter the  
network parameters accordingly. When evaluating the validation and test data output, we convert the probability map to a  
binary output, where 1 corresponds to the iceberg class and 0 to background (everything else), by thresholding it at 0.5. As we  
are only interested in the largest iceberg and would like to discard other smaller icebergs and iceberg fragments around, we  
200 also apply a connected component analysis and select the largest component (Figure 3).

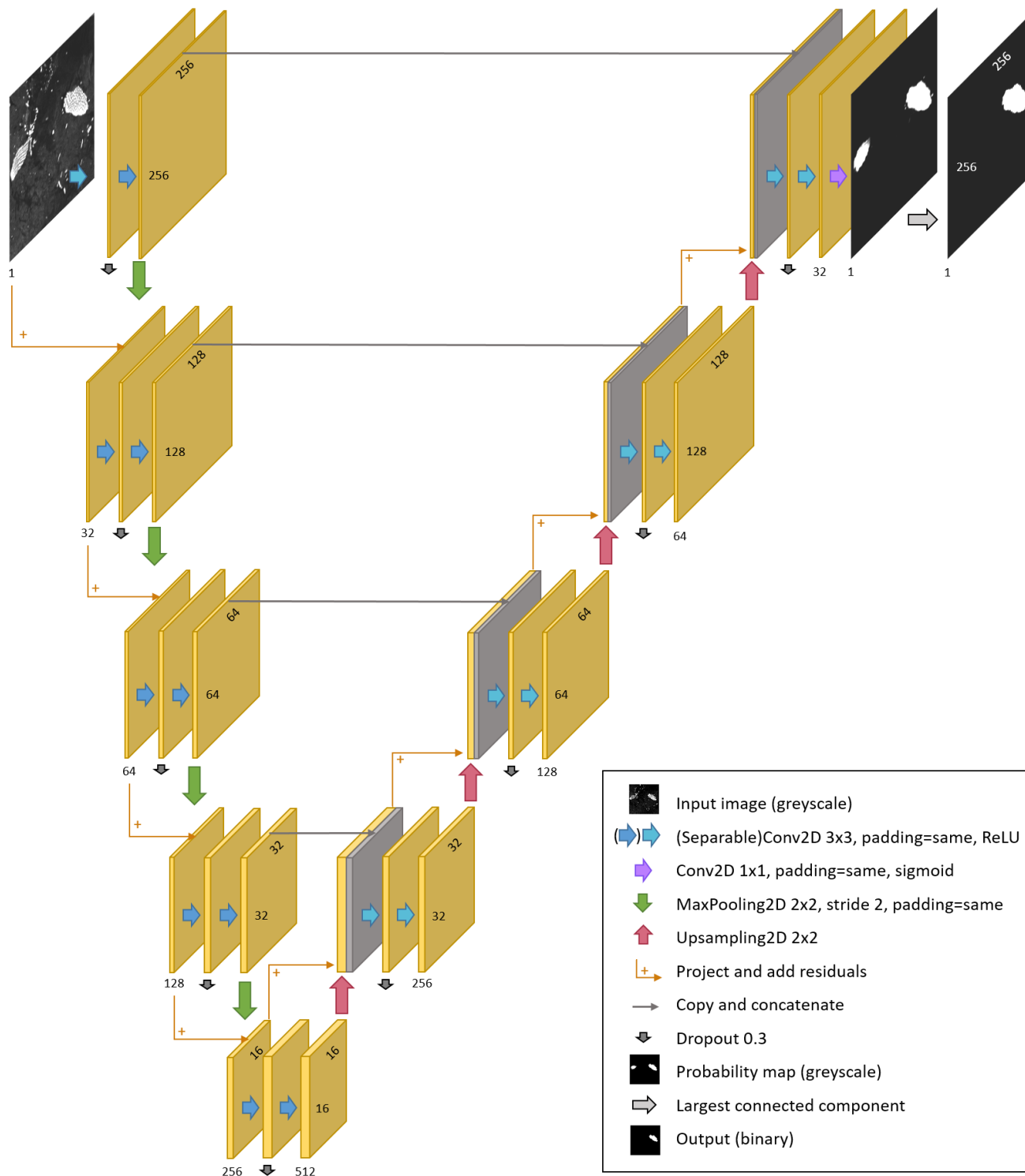


**Figure 3: Modified U-net architecture as used in this paper**



We train and evaluate the network using cross-validation. This means that we train seven different neural networks and always retain the images of one iceberg for testing as an independent dataset. The exact number of test images varies, as we have  
205 between 15 and 46 images per iceberg (Table 2). Although the images are roughly one month apart and cover a wide range of seasons and surroundings overall (e.g. near the calving front, surrounded by sea ice and within open ocean), we find that consecutive images of the same iceberg are often similar – both concerning iceberg shape, size and appearance as well as the surrounding. Therefore, we do not mix training and test data. On the other hand, and for the same reason, we find that it stabilises the training process, if we draw training and validation data from the same set of icebergs. 24 images are taken as  
210 validation data, which is used to set the best performing hyperparameters (i.e. network architecture, number of layers, optimizer, learning rate, loss function and batch size). It also determines when we stop the learning process to avoid overfitting. Depending on which iceberg was picked for testing, this leaves between 121-152 images for training. We train the network end-to-end using a binary cross entropy loss function and a batch size of one. Higher batch sizes had little impact on the performance and run time. The Adam optimizer (Kingma and Ba, 2015) is employed with an initial learning rate of 0.001. The  
215 learning rate is halved when the validation loss has not decreased for eight consecutive epochs. Training is stopped when the validation loss has not improved for 20 epochs. In practice, this means that the networks are trained for 57-193 epochs. The implementation is done in Python using Keras (Chollet and Others, 2015). Training takes up to 20 minutes on a Tesla P100 GPU with 25 GB RAM (Google Colab Pro). The prediction for 24 images takes 0.2 seconds.

### 3 Results and discussion

220 In this section, we present and discuss the results from the three different approaches (U-net, Otsu and k-means). The best visualisation of the results can be found in the supplementary animations (Braakmann-Folgmann, 2023), showing iceberg outlines from all methods and for all 191 images. There is one animation per iceberg. Our analysis in the following is based mainly on statistics, but we also show some examples. After an overall analysis, we assess the performance for each iceberg and evaluate the impact of iceberg size and different challenging environments. Finally, we compare our results to previous  
225 studies.

#### 3.1. Performance of the three methods

We evaluate the performance of the three methods compared to the manual delineations using a range of metrics. True positives (TP) are all correctly classified iceberg pixels and true negatives (TN) are all correctly classified background pixels. False positives (FP) are pixels that were classified as iceberg, but belong to the background according to manual delineations and  
230 false negatives (FN) are iceberg pixels in the manually derived segmentation map, which the algorithm has missed and erroneously classified as background. These are the basis for most evaluation metrics including the overall accuracy, the  $F_1$  score (also known as dice coefficient), misses (also known as false negative rate) and false alarms (also known as false positive rate). The detection rate is equal to the iceberg class accuracy and can be derived from 1-misses; hence, we do not list it



separately. In the case of a large class imbalance, the  $F_1$  score is much more meaningful than the overall accuracy. The iceberg  
235 class makes up only 5 % of all pixels, so we focus on the  $F_1$  score, but list the overall accuracy for completeness. Except the  
 $F_1$  score, all measures are given in percent. In addition to these metrics commonly used to evaluate segmentation algorithms,  
we also examine the accuracy of the resulting area estimates  $a_i$ . We calculate the mean absolute error (MAE) in area, the mean  
error (area bias) and the median absolute deviation (MAD) in area. We focus on the MAD, as it is robust to a few complete  
failures. However, some previous studies have reported the MAE in area, but most have reported the area bias, so we also list  
240 these for completeness. Areas  $a_i$  and  $\alpha_i$  are calculated as the sum of all iceberg pixels in the prediction and manually derived  
segmentation map respectively multiplied by the pixel area. All area deviations are relative deviations and given in percent  
compared to the iceberg area in the manually derived segmentation map. We also calculate the standard deviation for each  
metric. Only the MAD is given with the 25 % and 75 % quantiles instead.

$$245 \quad F_1 = \frac{2 TP}{2TP+FN+FP} \quad (1)$$

$$\text{Overall accuracy} = \frac{TN+TP}{TN+TP+FN+FP} \quad (2)$$

$$\text{Misses} = \frac{FN}{FN+TP} \quad (3)$$

$$250 \quad \text{False alarms} = \frac{FP}{FP+TN} \quad (4)$$

$$\text{MAE} = \frac{1}{n} \sum_{i=1}^n \frac{|a_i - \alpha_i|}{\alpha_i} \quad (5)$$

$$\text{Area bias} = \frac{1}{n} \sum_{i=1}^n \frac{a_i - \alpha_i}{\alpha_i} \quad (6)$$

$$255 \quad \text{MAD} = \text{median} \left( \frac{|a_i - \alpha_i|}{\alpha_i} \right) \quad (7)$$

Comparing the performance of all three techniques, we find that U-net outperforms Otsu and k-means in most metrics. It  
achieves a significantly higher  $F_1$  score (0.84 compared to 0.62, Table 1) and generates many fewer false alarms (0.4 % instead  
of 4.7 and 5.2 %). On the other hand, both standard segmentation methods have fewer misses than U-net (9 % and 13 %  
260 compared to 21 %). On this metric Otsu scores best. In terms of iceberg area, the predictions by U-net are much closer to the  
manually derived outlines in terms of MAE and bias. Otsu and k-means clearly suffer from a few total failures with over 100 %  
deviation, which bias these metrics in their cases. The MAD, which is less sensitive to such outliers, is similar for the three  
methods, with Otsu scoring best (3.6 %), followed by U-net (4.1 %) and k-means (5.1 %). The 25 %-quantiles are very similar  
for all three methods (2.0, 2.1 and 2.2 % respectively). On the 75 %-quantiles, U-net achieves slightly better results (12.1 %  
265 area deviation, compared to 13.8 % and 14.9 % for k-means and Otsu). This means that 75 % of all U-net predictions deviate  
from the manually derived area by 12.1 % or less. Overall, U-net scores better in most categories, but tends to miss parts and  
misclassify iceberg as background.



270

**Table 1: Performance metrics with standard deviations of U-net, Otsu and k-means across all test data sets (191 images). The median absolute area deviation (MAD) is given with 25 % and 75 % quantiles instead of standard deviation. Arrows indicate whether high (up) or low (down) numbers are desirable. The best score per metric is highlighted in bold.**

	F <sub>1</sub> score ↑	Overall accuracy [%] ↑	Misses [%] ↓	False Alarms [%] ↓	MAE in area [%] ↓	Area bias [%] ↓	MAD in area [%] ↓
<b>U-net</b>	<b>0.84 ± 0.30</b>	<b>99 ± 2</b>	21 ± 32	<b>0.4 ± 0.3</b>	<b>15 ± 26</b>	<b>-5 ± 29</b>	4.1 [2.1 – 12.1]
<b>Otsu</b>	0.62 ± 0.34	95 ± 13	<b>9 ± 28</b>	5.2 ± 0.3	170 ± 490	170 ± 490	<b>3.6 [2.0 - 14.9]</b>
<b>k-means</b>	0.62 ± 0.33	95 ± 12	13 ± 28	4.7 ± 0.3	150 ± 460	150 ± 460	5.1 [2.2 – 13.8]

### 3.2. Impact of iceberg size

Next, we evaluate how U-net performs for each of the seven different giant icebergs (Table 2, shaded in grey and Figure 4), to assess the impact of the chosen test data set and different iceberg sizes. Here, we find that B34 gives the best results. The dataset for this iceberg is the smallest (15 images), meaning that there are more images left for training and the background is usually not too challenging. B41 gives the lowest F<sub>1</sub> score. This dataset is the largest one, containing 46 images, and hence leaves the least number of images for training. Furthermore, B41 stays very close to its calving position for a while, which means that the first 13 images contain a significant amount of coast – often directly next to the iceberg (see Figure 4 first three images or supplementary animation for all images). In these cases all techniques pick the coast rather than the iceberg (as discussed later). The highest MAD and miss rate occur for iceberg B31. Because the images of B30 – our largest berg – are resized, this means that B31 appears largest in the images. Therefore, we believe that the large size of the berg, which U-net has not seen in the training data, cause U-net to miss parts of the iceberg (Figure 4 and Figure 5b, f). This is supported by the fact, that U-net misses large parts of B31 in the beginning (first few images in Figure 4), then misses smaller parts and once the iceberg has decreased to a size similar to other icebergs, U-net works fine (last four images of B31 in Figure 4). In general, we find quite variable performance depending on which iceberg is retained as test data. This is because the same challenges (e.g. iceberg size, shape, surrounding) occur in subsequent images of the same iceberg, even when they are one month apart (best seen in the supplementary animations). It is also the reason why we decided to evaluate the methods using cross-validation, as this makes the analysis less sensitive to the choice of a single iceberg as test data.

Also for Otsu and k-means the performance varies a lot depending on which iceberg is chosen as test data. The F<sub>1</sub> scores for Otsu range from 0.20 – 0.91, being lowest for C34 and highest for B31. Similarly, k-means also reaches the lowest F<sub>1</sub> score of 0.23 for C34 and the highest for B31 of 0.93. Compared to that, U-net is more consistent reaching F<sub>1</sub> scores between 0.68 – 0.97, but still exhibits significant variability. The fact that Otsu and k-means score so well for B31, also indicates that this data set is not hard per se. We rather suspect that we are challenging U-net too much when the iceberg in the test data is bigger than any iceberg in the training data. Neural networks are known to struggle with a domain-shift, where the test data is from a shifted version of the training data distribution and even more with out-of-domain samples from outside the training data

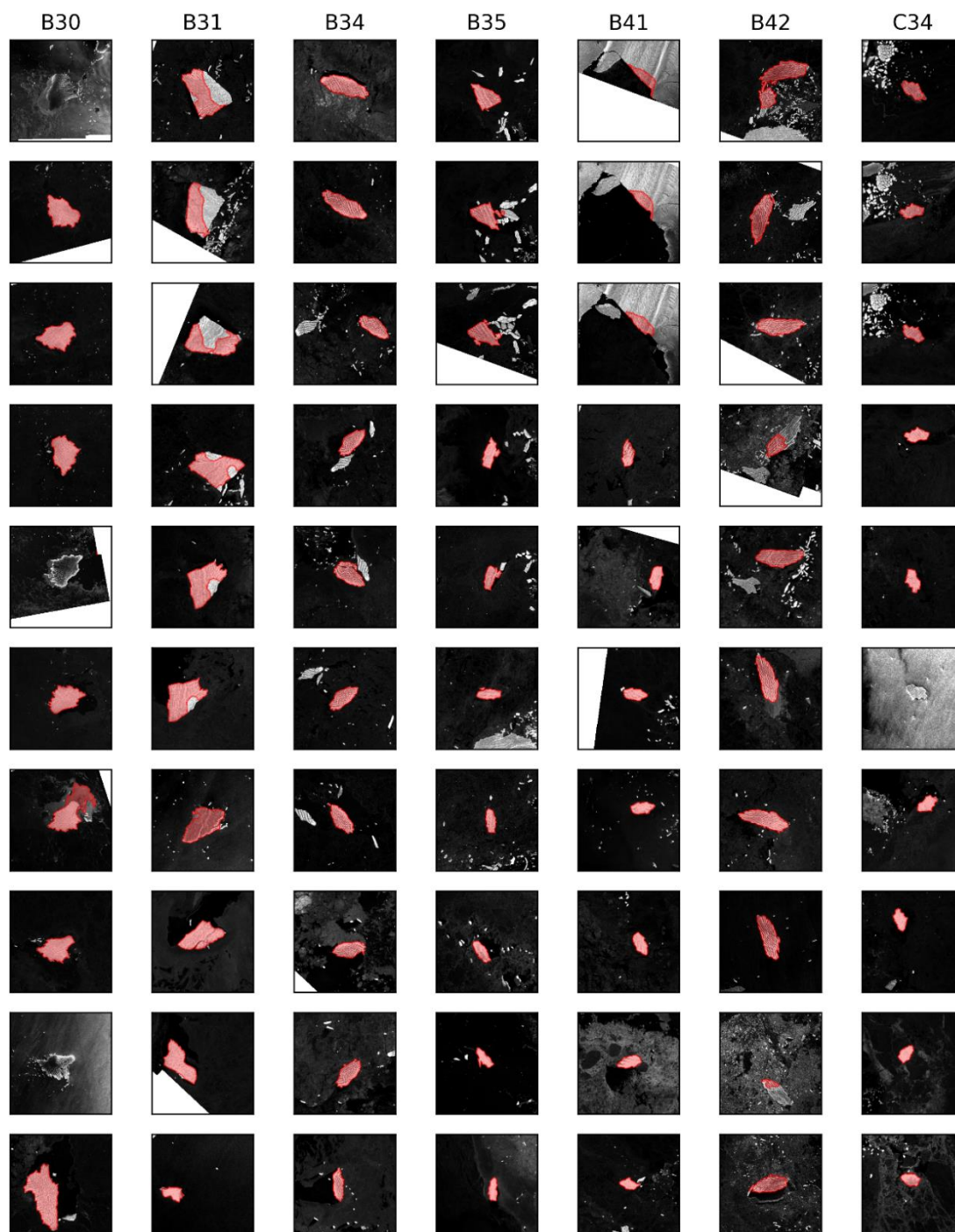
295



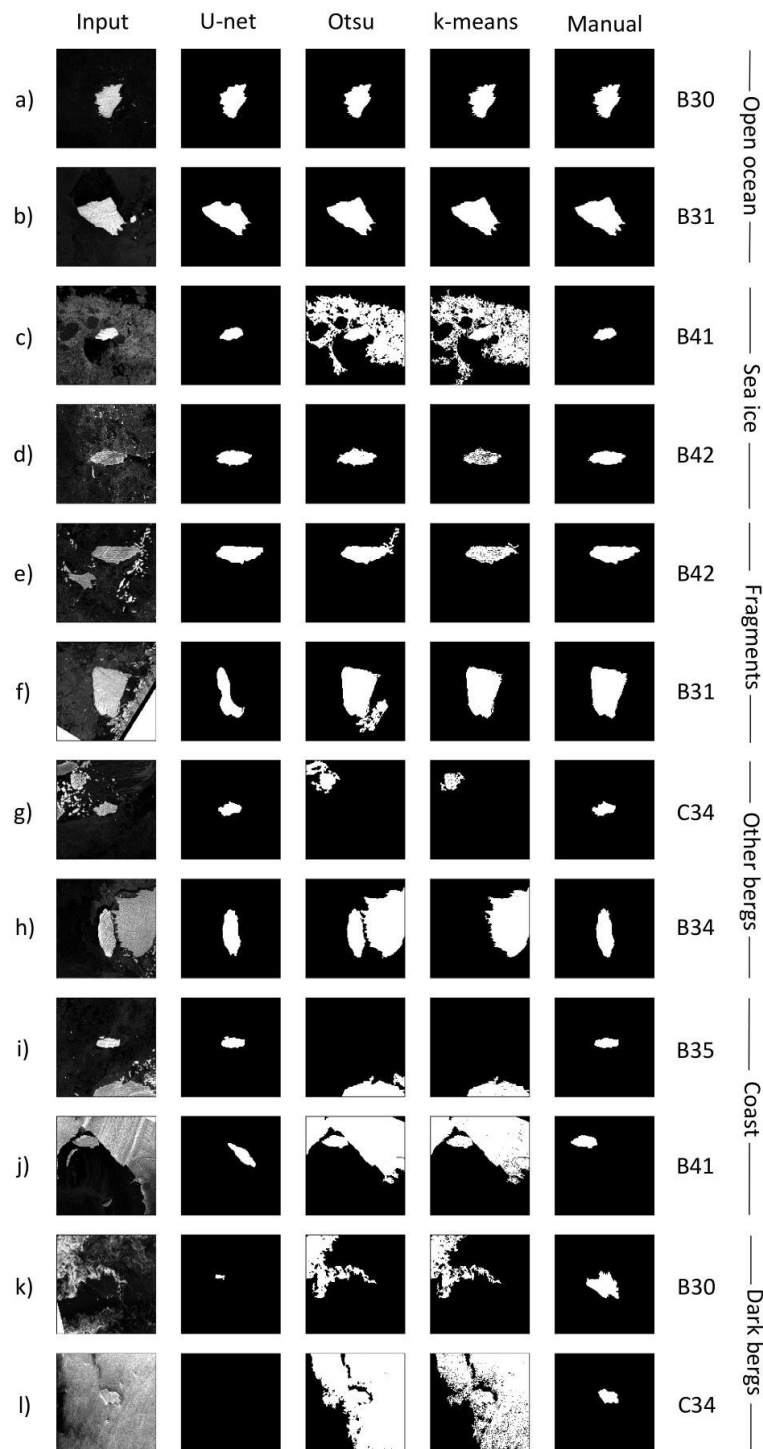
distribution (Gawlikowski et al., 2021). Both are caused by insufficient training data, not or barely covering these examples. Therefore, we recommend expanding the training data, before applying U-net operationally or to icebergs larger than covered by the current training data set. In contrast, iceberg B41, where U-net reaches the lowest F<sub>1</sub> score, poses an even greater problem to the other algorithms, meaning that this dataset is actually challenging. Finally, we observe that U-net achieves the lowest false alarm rate on each iceberg. Otsu generates most false alarms (highest rate for six out of seven icebergs), but also achieves the lowest miss rate for four out of seven icebergs. Except for B31, U-net consistently achieves the highest F<sub>1</sub> score. In terms of MAD in area, k-means and U-net score best on three out of the seven icebergs each.

**Table 2: Performance of the three methods for each test data set (iceberg). The number of images per iceberg and their minimum and maximum size is also given. Note that most images of B30 are rescaled, so it appears smaller in the images. Arrows indicate whether high (up) or low (down) numbers are desirable. The best score per iceberg and metric are highlighted in bold.**

		F <sub>1</sub> score ↑	Misses [%] ↓	False Alarms [%] ↓	MAD in area [%] ↓
<b>B30</b> 29 images 463-1052 km <sup>2</sup>	U-net	<b>0.90</b>	15	<b>0.3</b>	3.3
	Otsu	0.77	<b>9</b>	3.2	2.7
	k-means	0.79	12	2.4	<b>2.4</b>
<b>B31</b> 32 images 79-518 km <sup>2</sup>	U-net	0.79	34	<b>0.2</b>	13.6
	Otsu	0.91	<b>5</b>	1.6	3.0
	k-means	<b>0.93</b>	6	1.0	<b>1.9</b>
<b>B34</b> 15 images 97-241 km <sup>2</sup>	U-net	<b>0.97</b>	2	<b>0.2</b>	2.1
	Otsu	0.83	<b>1</b>	1.7	<b>1.2</b>
	k-means	0.80	8	1.6	8.3
<b>B35</b> 21 images 62-158 km <sup>2</sup>	U-net	<b>0.94</b>	<b>2</b>	<b>0.3</b>	6.9
	Otsu	0.66	9	2.3	7.4
	k-means	0.63	10	2.5	<b>4.0</b>
<b>B41</b> 46 images 54-116 km <sup>2</sup>	U-net	<b>0.68</b>	33	<b>0.7</b>	<b>3.5</b>
	Otsu	0.27	13	10.5	3.8
	k-means	0.29	<b>11</b>	10.1	5.6
<b>B42</b> 24 images 142-235 km <sup>2</sup>	U-net	<b>0.88</b>	13	<b>0.6</b>	<b>5.4</b>
	Otsu	0.84	<b>6</b>	1.7	8.9
	k-means	0.76	28	1.0	18.7
<b>C34</b> 24 images 61-101 km <sup>2</sup>	U-net	<b>0.81</b>	<b>20</b>	<b>0.4</b>	<b>3.7</b>
	Otsu	0.20	36	10.1	4.3
	k-means	0.23	32	9.1	5.2



310 **Figure 4: U-net derived iceberg outlines (red) plotted on top of the input images for 10 images per iceberg (columns). We always include the first and last image from each time series and sample the others equally in between. As the number of images per iceberg ranges from 15-46, this means that images of B34 are 1-2 months apart, while the images for B41 are 5 months apart in this figure. The full time series and results of all methods can be viewed in the supplementary animations (one per iceberg).**



315 **Figure 5: Examples of input images (first column) and segmentation maps generated by U-net (second column), Otsu (third column), k-means (fourth column), and from manual delineations (last column). We picked these images for illustration to cover each category of environmental conditions twice and to include all icebergs (labelled on the right).**



### 3.3. Impact of different environmental conditions

Grouping the images according to the surrounding environmental conditions (see Section 2.2.) allows us to judge how well each method can deal with the respective challenge (Figure 5, Table 3). Open ocean makes up most of the images (46 %) and all methods perform very well with  $F_1$  scores of 0.93-0.95 and MAD in area of 2.4-3.2 %. The Otsu threshold performs best, but the differences between the methods are very small. The two sample images (Figure 5a, b) also illustrate that the only problem in this category is rather that U-net generally tends to miss parts of B31 than open ocean in itself posing a problem. Sea ice occurs in 14 % of our images and overall U-net achieves the best  $F_1$  score (0.88 compared to 0.72 and 0.74), but the Otsu threshold gives a slightly better MAD in area (4.3 % rather than 4.8 % and 5.4 %). Visually, the U-net predictions seem to be the most robust, as sea ice is discarded reliably. In contrast, the two other methods sometimes connect patches of sea ice to the iceberg (Figure 5c), but also work fine in other cases (Figure 5d).

**Table 3: Performance of the three methods in different environmental conditions. The first column also indicates how often these conditions occur in our data set. Arrows indicate whether high (up) or low (down) numbers are desirable. The best values per category and metric are highlighted in bold.**

		$F_1$ score $\uparrow$	Misses [%] $\downarrow$	False Alarms [%] $\downarrow$	MAD in area [%] $\downarrow$
<b>Open ocean</b> (46 %)	U-net	0.93	11	<b>0.1</b>	2.8
	Otsu	<b>0.95</b>	<b>2</b>	0.4	<b>2.4</b>
	k-means	<b>0.95</b>	4	0.3	3.2
<b>Sea ice</b> (14 %)	U-net	<b>0.88</b>	14	<b>0.3</b>	4.8
	Otsu	0.72	<b>3</b>	2.4	<b>4.3</b>
	k-means	0.74	11	1.7	5.4
<b>Fragments</b> (24 %)	U-net	0.85	21	<b>0.4</b>	6.9
	Otsu	<b>0.94</b>	<b>2</b>	0.7	5.9
	k-means	<b>0.94</b>	7	<b>0.4</b>	<b>5.7</b>
<b>Other bergs</b> (3 %)	U-net	<b>0.96</b>	<b>6</b>	<b>0.0</b>	<b>5.9</b>
	Otsu	0.18	66	7.7	110
	k-means	0.10	86	5.7	11
<b>Coast</b> (8 %)	U-net	<b>0.34</b>	68	<b>1.8</b>	<b>18</b>
	Otsu	0.12	<b>38</b>	29.5	1200
	k-means	0.11	44	28.6	1200
<b>Dark bergs</b> (5 %)	U-net	<b>0.12</b>	92	<b>1.1</b>	<b>96</b>
	Otsu	<b>0.12</b>	<b>54</b>	34.3	450
	k-means	0.11	62	30.5	460



Iceberg fragments drifting in the direct proximity of the target iceberg were found in 24 % of our images. Overall, k-means scores best in this category with a MAD of 5.7 % compared to 5.9 % and 6.9 %. In terms of  $F_1$  score, Otsu and k-means both reach 0.94, whereas U-net only reaches 0.85. Visually, there are a few instances where Otsu connects more fragments to the  
335 iceberg than k-means and U-net (Figure 5e, f). This might be due to the Gaussian smoothing that we apply before the thresholding. We do not apply this step before k-means, and find that k-means tends to rather oversegment images, leaving small holes in the inside (Figure 5d, e). In the case of fragments, however, this turns out to be beneficial, as it allows k-means to reliably separate fragments from icebergs, even when they are very close by. The problem for U-net does not seem to be the actual fragments itself, as it rarely connects any fragments to the iceberg (Figure 5e, f). However, the images containing  
340 fragments are mostly from the large B31 and B42 icebergs, where U-net struggles due to their large extent. This can also be seen from the fact that U-net and k-means both generate only 0.4 % false alarms (fragments erroneously connected to the iceberg), but U-net has a much higher miss rate.

In 3 % of all images, another similar sized or bigger berg is (partially) visible. U-net scores best in all categories with a large margin, yielding an  $F_1$  score of 0.96 compared to 0.12 and 0.11 and MAD in area of 5.9 % compared to 11 % and 110 %. Also  
345 visually, it becomes clear that U-net reliably picks the target iceberg and discards any other ice, while Otsu and k-means often pick the wrong berg or connect both with each other (Figure 5g, h). Considering iceberg shape and size in a tracking scenario could help mitigate this phenomenon, though (Barbat et al., 2021; Collares et al., 2018; Koo et al., 2021).

Coast is present in 8 % of all images and U-net outperforms the other techniques, but also struggles in some cases. The  $F_1$  score is 0.34 for U-net and 0.12 and 0.11 for Otsu and k-means respectively. While U-net achieves a MAD of 18 %, the other  
350 methods yield over 1000 % each. Figure 5j illustrates what is happening in these cases: If too much coast is present, all algorithms pick the coast rather than the iceberg (and this is much larger than the iceberg, hence 1000 % deviation). However, U-net discards smaller parts of the coast around the image edges (Figure 5i). This is on the one hand because of the sliding convolution window and on the other hand, because U-net learns that the iceberg is usually in the centre (as we crop the images around the estimated position from operational iceberg tracking databases). Hence, U-net is able to correctly pick out the  
355 iceberg if not too much coast is present. For the same reason, it is easier for U-net to discard other bergs at the image edges. Interestingly, even when a lot of coast is present, U-net does not pick the full coast, but predicts either nothing or a small – almost iceberg shaped – part of the coast (Figure 5j). This could indicate that U-net even learns that only ice that is fully surrounded by water is an iceberg. A possible strategy to avoid misclassifications due to large amounts of coast would be the inclusion of a land mask (Barbat et al., 2019; Collares et al., 2018; Frost et al., 2016; Mazur et al., 2017; Silva and Bigg, 2005).  
360 However, ice shelves and glaciers advance and retreat regularly and especially the calving of icebergs themselves significantly alters the land mask. Thus, just after calving, the iceberg would be within the former land mask and could not be picked up. The last category of dark icebergs is the hardest and makes up 5 % of the overall data set. In these cases, all methods fail with  $F_1$  scores of 0.11-0.12 and the lowest MAD in area of 96 %. Again, it is interesting that U-net predicts either very small patches or nothing at all in these cases (Figure 5k, l), while the other two methods segment large areas of brighter looking ocean.



365 Potentially, U-net could learn to segment dark icebergs with a lot more training examples, but we only had ten such images in our overall data set. Finally, we would like to stress that the occurrence of these different environmental conditions will vary and our data set is not necessarily representative of all icebergs. We also find that the influence of iceberg size and environmental conditions cannot always be disentangled, as subsequent images of the same iceberg are often similar and the different environmental conditions are not spread equally across the different test data sets (individual icebergs).

### 370 **3.4. Comparison to previous studies**

Previous studies state different accuracy measures and due to the slightly different goal to detect all icebergs in a scene rather than finding one giant iceberg and accurately predicting its outline and area, they are not straightforward to compare. Two studies employ the k-means algorithm (Collares et al., 2018) or a variation of it (Koo et al., 2021), so we have indirectly compared U-net to them. None of them report any of our accuracy measures, though. Many of the previous approaches rely on some form of thresholding (Frost et al., 2016; Gill, 2001; Mazur et al., 2017; Power et al., 2001; Wesche and Dierking, 2012; Willis et al., 1996). We somehow covered these methods by comparing U-net to the Otsu threshold, but the exact approaches vary and none of them have applied the Otsu threshold. Two of the threshold-based methods report estimates for their area deviations. Wesche and Dierking (2012) state that iceberg area was overestimated by  $10 \pm 21$  % with their approach. In a following study, they find that for the correctly detected icebergs 13.3 % of the total area was missing (Wesche and Dierking, 2015), meaning a bias in the opposite direction. Mazur et al. (2017) find positive and negative area deviations of  $\pm 25$  % on average. For edge-detection based algorithms, Williams et al. (1999) find an overestimation of iceberg area by 20 % and Silva and Bigg (2005)'s approach yields an underestimation of iceberg area by 10-13 %. These are biases again and both approaches are limited to winter images. For U-net, we find a bias of  $-5.0 \pm 29.1$  %, which is lower than previous studies, but comes with a relatively high standard deviation due to some complete failures where the iceberg is not found at all. Previous studies only compare iceberg areas where icebergs were detected successfully. Barbat et al. (2019) report the lowest false positive (2.3 %) and false negative (3.3 %) rates, and the highest overall accuracy (97.5 %) of all previous studies. While their false negative rate is lower than our false negative rate (21 %), U-net achieves a lower false positive rate of 0.4 % and higher overall accuracy of 99 %. In a second study, Barbat et al. (2021) also analyse the area deviation of the detected icebergs and find average area deviations of  $10 \pm 4$  %, which is also the best score reported so far. They only consider correctly detected icebergs in this metric, though. We find a MAE of  $15 \pm 26$  % for U-net, which is slightly higher, but contains images where the iceberg was not found at all. These cases are not included in Barbat et al. (2021)'s estimates. Our MAD, which is less sensitive to such outliers, is 4.1 %, with 25 % and 75 % quantiles of 2.1 % and 12.1 %. These metrics compare favourably to all previous studies. We also demonstrate in our study, that the performance varies depending on the chosen test data set and therefore, all measures and comparisons can only give an indication of the real performance. Judging from the data we have and comparing our results on this to previous studies as good as possible, U-net proves to be a very promising approach. Qualitatively, previous studies have found degraded accuracies in challenging environmental conditions or excluded these from their datasets. Some studies report false detections due to sea ice (Koo et al., 2021; Mazur et al., 2017; Wesche and



Dierking, 2012) or only applied their algorithm to sea-ice free conditions (Willis et al., 1996). Moreover, several previous studies have also encountered problems with clusters of several bergs and berg fragments too close to each other (Barbat et al., 2019a; Frost et al., 2016; Koo et al., 2021; Williams et al., 1999). Also U-net shows slightly degraded performance in these situations (4.8 and 6.9 % MAD in area compared to 2.8 % in open ocean and  $F_1$  scores of 0.88 and 0.85 compared to 0.93), but still achieves satisfying results in most of these cases. The challenge of other big bergs does not occur in previous studies, since they were looking for all icebergs anyway. In terms of coast, many previous studies have employed a land mask (e.g. Barbat et al., 2019; Collares et al., 2018; Frost et al., 2016; Mazur et al., 2017; Silva and Bigg, 2005), but might miss newly calved bergs due to that. Finally, the problem of dark icebergs has been described in several papers (Mazur et al., 2017; Wesche and Dierking, 2012; Williams et al., 1999), but was rarely mentioned in the evaluation. This is likely because most previous studies use visual inspection to identify misses and false alarms (e.g. Barbat et al., 2019; Frost et al., 2016; Mazur et al., 2017; Wesche and Dierking, 2012; Williams et al., 1999). However, dark icebergs are hard to spot in SAR images even for humans, so they might be missed by the visual inspection, too, unless in our case we know that there must be an iceberg of a certain size and shape that we are looking for. Others limit their method to winter images, when dark icebergs do not occur (Silva and Bigg, 2005; Williams et al., 1999; Young et al., 1998).

#### 4 Conclusions

We have developed a novel algorithm to segment giant Antarctic icebergs in Sentinel-1 images automatically. It is the first study to apply a deep neural network for iceberg segmentation. Furthermore, it is also the first study specifically targeting giant icebergs. Comparing U-net to two state-of-the-art segmentation techniques (Otsu thresholding and k-means), we find that U-net outperforms them in most metrics. Across all 191 images, U-net achieves an  $F_1$  score of 0.84 and a median absolute area deviation of 4.1 %. Only the miss rate of Otsu and k-means is lower than for U-net, as we find that U-net overlooks parts of the iceberg appearing largest in the images, as in this case all training samples show smaller icebergs. We believe that this issue could be resolved with a larger training data set. U-net can reliably handle a variety of challenging environmental conditions including sea ice, nearby iceberg fragments, other bergs and small patches of nearby coast. It fails when too much coast is visible and when icebergs appear dark, though. In these cases, all existing algorithms fail, but such obvious errors could easily be picked out in a tracking scenario. Also compared to previous studies, we regard our results as promising. For an operational application, on the short-term further post-processing could be implemented to filter outliers, but on the long run, we would suggest to enlarge the training data set.

#### 425 Code availability

The code is available from the authors upon reasonable request.



### Data availability

Segmentation maps for all 191 images and from all three methods are shown in the supplementary animations (one animation per iceberg). DOI: [10.5281/zenodo.7875599](https://doi.org/10.5281/zenodo.7875599) (Braakmann-Folgmann, 2023). The Sentinel-1 images are freely available from  
430 <https://scihub.copernicus.eu/dhus/>.

### Author contributions

ABF, AS and DH designed the study. ER clicked most of the iceberg outlines, which are used as training data, during her internship, supervised by ABF. ABF also generated some of the outlines. ABF designed and implemented the U-net architecture, implemented the comparison methods, plotted the figures and wrote the manuscript. AS and DH supervised the  
435 work and suggested edits to the manuscript.

### Competing interests

The authors declare that they have no conflict of interest.

### Acknowledgement

This work was supported by Barry Slavin and by NERC through National Capability funding, undertaken by a partnership  
440 between the Centre for Polar Observation Modelling and the British Antarctic Survey. The Antarctic Mapping Toolbox (Greene et al., 2017) was used. We would also like to thank the European Space Agency's  $\phi$ -lab team for hosting Anne Braakmann-Folgmann during a three-month research visit and for several useful discussions and inspiration during this time and beyond. Thank you especially to Andreas Stokholm and Michael Marszalek.

### References

- 445 Andersson, T. R., Hosking, J. S., Pérez-Ortiz, M., Paige, B., Elliott, A., Russell, C., Law, S., Jones, D. C., Wilkinson, J., Phillips, T., Byrne, J., Tietsche, S., Sarojini, B. B., Blanchard-Wrigglesworth, E., Aksenov, Y., Downie, R. and Shuckburgh, E.: Seasonal Arctic sea ice forecasting with probabilistic deep learning, *Nat. Commun.*, 12(1), 1–12, <https://doi.org/10.1038/s41467-021-25257-4>, 2021.
- 450 Barbat, M. M., Wesche, C., Werhli, A. V. and Mata, M. M.: An adaptive machine learning approach to improve automatic iceberg detection from SAR images, *ISPRS J. Photogramm. Remote Sens.*, 156(August), 247–259, <https://doi.org/10.1016/j.isprsjprs.2019.08.015>, 2019a.



- Barbat, M. M., Rackow, T., Hellmer, H. H., Wesche, C. and Mata, M. M.: Three Years of Near-Coastal Antarctic Iceberg Distribution From a Machine Learning Approach Applied to SAR Imagery, *J. Geophys. Res. Ocean.*, 124(9), 6658–6672, <https://doi.org/10.1029/2019JC015205>, 2019b.
- 455 Barbat, M. M., Rackow, T., Wesche, C., Hellmer, H. H. and Mata, M. M.: Automated iceberg tracking with a machine learning approach applied to SAR imagery : A Weddell sea case study, *ISPRS J. Photogramm. Remote Sens.*, 172(December 2020), 189–206, <https://doi.org/10.1016/j.isprsjprs.2020.12.006>, 2021.
- Baumhoer, C. A., Dietz, A. J., Kneisel, C. and Kuenzer, C.: Automated extraction of antarctic glacier and ice shelf fronts from Sentinel-1 imagery using deep learning, *Remote Sens.*, 11(21), 1–22,  
460 <https://doi.org/10.3390/rs11212529>, 2019.
- Bigg, G. R., Wadley, M. R., Stevens, D. P. and Johnson, J. A.: Modelling the dynamics and thermodynamics of icebergs, *cold Reg. Sci. Technol.*, 26(2), 113–135, [https://doi.org/10.1016/S0165-232X\(97\)00012-8](https://doi.org/10.1016/S0165-232X(97)00012-8), 1997.
- Bouhier, N., Tournadre, J., Rémy, F. and Gourves-Cousin, R.: Melting and fragmentation laws from the evolution of two large Southern Ocean icebergs estimated from satellite data, *Cryosphere*, 12(7), 2267–2285,  
465 <https://doi.org/10.5194/tc-12-2267-2018>, 2018.
- Braakmann-Folgmann, A.: Segmentation maps of giant Antarctic icebergs, ,  
<https://doi.org/10.5281/zenodo.7875599>, 2023.
- Braakmann-Folgmann, A., Shepherd, A. and Ridout, A.: Tracking changes in the area, thickness, and volume of the Thwaites tabular iceberg “B30” using satellite altimetry and imagery, *Cryosphere*, 15(8), 3861–3876,  
470 <https://doi.org/10.5194/tc-15-3861-2021>, 2021.
- Braakmann-Folgmann, A., Shepherd, A., Gerrish, L., Izzard, J. and Ridout, A.: Observing the disintegration of the A68A iceberg from space, *Remote Sens. Environ.*, 270, 112855, <https://doi.org/10.1016/j.rse.2021.112855>, 2022.
- Bradski, G.: *The OpenCV Library*, Dr. Dobb’s J. Softw. Tools, 2000.
- 475 Budge, J. S. and Long, D. G.: A Comprehensive Database for Antarctic Iceberg Tracking Using Scatterometer Data, *IEEE J. Sel. Top. Appl. Earth Obs. Remote Sens.*, 11(2), 434–442, <https://doi.org/10.1109/JSTARS.2017.2784186>, 2018.
- Chollet, F.: Xception: Deep learning with depthwise separable convolutions, *Proc. - 30th IEEE Conf. Comput. Vis. Pattern Recognition, CVPR 2017*, 1800–1807, <https://doi.org/10.1109/CVPR.2017.195>, 2017.
- 480 Chollet, F. and Others, &: *Keras*, <https://github.com/fchollet/keras>, 2015.



- Collares, L. L., Mata, M. M., Kerr, R., Arigony-Neto, J. and Barbat, M. M.: Iceberg drift and ocean circulation in the northwestern Weddell Sea, Antarctica, *Deep. Res. Part II Top. Stud. Oceanogr.*, 149(March), 10–24, <https://doi.org/10.1016/j.dsr2.2018.02.014>, 2018.
- 485 Dirscherl, M., Dietz, A. J., Kneisel, C. and Kuenzer, C.: A novel method for automated supraglacial lake mapping in antarctica using sentinel-1 sar imagery and deep learning, *Remote Sens.*, 13(2), 1–27, <https://doi.org/10.3390/rs13020197>, 2021.
- Drinkwater, M. R.: Satellite Microwave Radar Observations of Antarctic Sea Ice, *Anal. SAR Data Polar Ocean.*, 145–187, [https://doi.org/10.1007/978-3-642-60282-5\\_8](https://doi.org/10.1007/978-3-642-60282-5_8), 1998.
- Duprat, L. P. A. M., Bigg, G. R. and Wilton, D. J.: Enhanced Southern Ocean marine productivity due to  
490 fertilization by giant icebergs, *Nat. Geosci.*, 9(3), 219–221, <https://doi.org/10.1038/ngeo2633>, 2016.
- England, M. R., Wagner, T. J. W. and Eisenman, I.: Modeling the breakup of tabular icebergs, *Sci. Adv.*, 6(51), 1–9, <https://doi.org/10.1126/sciadv.abd1273>, 2020.
- Frost, A., Ressel, R. and Lehner, S.: Automated iceberg detection using high resolution X - band SAR images, *Can. J. Remote Sens.*, 42(4), <https://doi.org/https://doi.org/10.1080/07038992.2016.1177451>, 2016.
- 495 Gawlikowski, J., Tassi, C. R. N., Ali, M., Lee, J., Humt, M., Feng, J., Kruspe, A., Triebel, R., Jung, P., Roscher, R., Shahzad, M., Yang, W., Bamler, R. and Zhu, X. X.: A Survey of Uncertainty in Deep Neural Networks, , 1–41 <http://arxiv.org/abs/2107.03342>, 2021.
- Gill, R. S.: Operational detection of sea ice edges and icebergs using SAR, *Can. J. Remote Sens.*, 27(5), 411–432, <https://doi.org/10.1080/07038992.2001.10854884>, 2001.
- 500 Greene, C. A., Gwyther, D. E. and Blankenship, D. D.: Antarctic Mapping Tools for MATLAB, *Comput. Geosci.*, 104, 151–157, <https://doi.org/10.1016/j.cageo.2016.08.003>, 2017.
- He, K., Zhang, X., Ren, S. and Sun, J.: Deep residual learning for image recognition, *Proc. IEEE Comput. Soc. Conf. Comput. Vis. Pattern Recognit.*, 2016-Decem, 770–778, <https://doi.org/10.1109/CVPR.2016.90>, 2016.
- Helly, J. J., Kaufmann, R. S., Stephenson, G. R. and Vernet, M.: Cooling, dilution and mixing of ocean water by  
505 free-drifting icebergs in the Weddell Sea, *Deep. Res. Part II Top. Stud. Oceanogr.*, 58(11–12), 1346–1363, <https://doi.org/10.1016/j.dsr2.2010.11.010>, 2011.
- Jansen, D., Schodlok, M. and Rack, W.: Basal melting of A-38B: A physical model constrained by satellite observations, *Remote Sens. Environ.*, 111(2), 195–203, <https://doi.org/10.1016/j.rse.2007.03.022>, 2007.
- Jenkins, A.: The impact of melting ice on ocean waters, *J. Phys. Oceanogr.*, 29(9), 2370–2381, [https://doi.org/10.1175/1520-0485\(1999\)029<2370:TIOMIO>2.0.CO;2](https://doi.org/10.1175/1520-0485(1999)029<2370:TIOMIO>2.0.CO;2), 1999.
- 510



- Kingma, D. P. and Ba, J. L.: Adam: A method for stochastic optimization, 3rd Int. Conf. Learn. Represent. ICLR 2015 - Conf. Track Proc., 1–15, 2015.
- Koo, Y., Xie, H., Ackley, S. F., Mestas-Nunez, A. M., Macdonald, G. J. and Hyun, C.-U.: Semi-automated tracking of iceberg B43 using Sentinel-1 SAR images via Google Earth Engine, *Cryosph.*, 15(May), 4727–4744, <https://doi.org/https://doi.org/10.5194/tc-15-4727-2021>, 2021.
- 515
- LeCun, Y., Bengio, Y. and Hinton, G.: Deep learning, *Nature*, 521(7553), 436–444, <https://doi.org/10.1038/nature14539>, 2015.
- Macqueen, J.: SOME METHODS FOR CLASSIFICATION AND ANALYSIS OF MULTIVARIATE OBSERVATIONS, in *Proceedings of the fifth Berkeley symposium on mathematical statistics and probability*, vol. 233, pp. 281–297, California: University of California Press., , 1967.
- 520
- Mazur, A. K., Wählin, A. K. and Krężel, A.: An object-based SAR image iceberg detection algorithm applied to the Amundsen Sea, *Remote Sens. Environ.*, 189, 67–83, <https://doi.org/10.1016/j.rse.2016.11.013>, 2017.
- Merino, N., Le Sommer, J., Durand, G., Jourdain, N. C., Madec, G., Mathiot, P. and Tournadre, J.: Antarctic icebergs melt over the Southern Ocean : Climatology and impact on sea ice, *Ocean Model.*, 104, 99–110, <https://doi.org/10.1016/j.ocemod.2016.05.001>, 2016.
- 525
- Mohajerani, Y., Wood, M., Velicogna, I. and Rignot, E.: Detection of glacier calving margins with convolutional neural networks: A case study, *Remote Sens.*, 11(1), 1–13, <https://doi.org/10.3390/rs11010074>, 2019.
- Mohajerani, Y., Jeong, S., Scheuchl, B., Velicogna, I., Rignot, E. and Milillo, P.: Automatic delineation of glacier grounding lines in differential interferometric synthetic-aperture radar data using deep learning, *Sci. Rep.*, 11(1), 1–10, <https://doi.org/10.1038/s41598-021-84309-3>, 2021.
- 530
- Otsu, N.: A Threshold Selection Method from Gray-Level Histograms, *IEEE Trans. Syst. Man. Cybern.*, C(1), 62–66, 1979.
- Poliyapram, V., Imamoglu, N. and Nakamura, R.: DEEP LEARNING MODEL FOR WATER / ICE / LAND CLASSIFICATION USING LARGE-SCALE MEDIUM RESOLUTION SATELLITE IMAGES, *IGARRS 2019 - 2019 IEEE Int. Geosci. Remote Sens. Symp.*, (d), 3884–3887, 2019.
- 535
- Power, D., Youden, J., Lane, K., Randell, C. and Flett, D.: Iceberg detection capabilities of radarsat synthetic aperture radar, *Can. J. Remote Sens.*, 27(5), 476–486, <https://doi.org/10.1080/07038992.2001.10854888>, 2001.
- Ronneberger, O., Fischer, P. and Brox, T.: U-net: Convolutional networks for biomedical image segmentation, *Lect. Notes Comput. Sci. (including Subser. Lect. Notes Artif. Intell. Lect. Notes Bioinformatics)*, 9351, 234–241, [https://doi.org/10.1007/978-3-319-24574-4\\_28](https://doi.org/10.1007/978-3-319-24574-4_28), 2015.
- 540

Sandven, S., Babiker, M. and Kloster, K.: Iceberg observations in the barents sea by radar and optical satellite images, in Proceedings of the Envisat Symposium, , 2007.

545 Schmidhuber, J.: Deep Learning in neural networks: An overview, *Neural Networks*, 61, 85–117, <https://doi.org/10.1016/j.neunet.2014.09.003>, 2015.

Sephton, A. J., Brown, L. M., Macklin, J. T., Partington, K. C., Veck, N. J. and Rees, W. G.: Segmentation of synthetic-aperture radar imagery of sea ice, *Int. J. Remote Sens.*, 15(4), 803–825, <https://doi.org/10.1080/01431169408954118>, 1994.

560 Silva, T. A. M. and Bigg, G. R.: Computer-based identification and tracking of Antarctic icebergs in SAR Computer-based identification and tracking of Antarctic icebergs in SAR images, , (May 2018), <https://doi.org/10.1016/j.rse.2004.10.002>, 2005.

Silva, T. A. M., Bigg, G. R. and Nicholls, K. W.: Contribution of giant icebergs to the Southern Ocean freshwater flux, *J. Geophys. Res.*, 111(July 2005), 1–8, <https://doi.org/10.1029/2004JC002843>, 2006.

555 Singh, A., Kalke, H., Loewen, M. and Ray, N.: River Ice Segmentation with Deep Learning, *IEEE Trans. Geosci. Remote Sens.*, 58(11), <https://doi.org/10.1109/TGRS.2020.2981082>, 2020.

Smith, K. L., Robison, B. H., Helly, J. J., Kaufmann, R. S., Ruhl, H. A., Shaw, T. J., Twining, B. S. and Vernet, M.: Free-drifting icebergs: Hot spots of chemical and biological enrichment in the Weddell Sea, *Science* (80-), 317(5837), 478–482, <https://doi.org/10.1126/science.1142834>, 2007.

560 Srivastava, N., Hinton, G., Krizhevsky, A., Sutskever, I. and Salakhutdinov, R.: Dropout: A simple way to prevent neural networks from overfitting, *J. Mach. Learn. Res.*, 15, 1929–1958, 2014.

Stokholm, A., Wulf, T., Kucik, A., Saldo, R., Buus-Hinkler, J. and Hvidegaard, S. M.: AI4SeaIce: Toward Solving Ambiguous SAR Textures in Convolutional Neural Networks for Automatic Sea Ice Concentration Charting, *IEEE Trans. Geosci. Remote Sens.*, 60, <https://doi.org/10.1109/TGRS.2022.3149323>, 2022.

565 Surawy-Stepney, T., Hogg, A. E., Cornford, S. L. and Davison, B. J.: Episodic dynamic change linked to damage on the thwaites glacier ice tongue, *Nat. Geosci.*, 16(1), 37–43, <https://doi.org/10.1038/s41561-022-01097-9>, 2023.

Torres, R., Snoeij, P., Geudtner, D., Bibby, D., Davidson, M., Attema, E., Potin, P., Rommen, B., Floury, N., Brown, M., Navas, I., Deghaye, P., Duesmann, B., Rosich, B., Miranda, N., Bruno, C., Abbate, M. L., Croci, R., Pietropaolo, A., Huchler, M. and Rostan, F.: GMES Sentinel-1 mission, *Remote Sens. Environ.*, 120, 9–  
570 24, <https://doi.org/10.1016/j.rse.2011.05.028>, 2012.

Tournadre, J., Bouhier, N., Girard-Ardhuin, F. and Rémy, F.: Antarctic icebergs distributions 1992–2014, *J. Geophys. Res. Ocean.*, 121(1), 327–349, <https://doi.org/10.1002/2015JC011178>, 2016.



- Ulaby, F. T. and Long, D. G.: Microwave radar and radiometric remote sensing, The University of Michigan Press., 2014.
- 575 Vernet, M., Smith, K. L., Cefarelli, A. O., Helly, J. J., Kaufmann, R. S., Lin, H., Long, D. G., Murray, A. E., Robison, B. H., Ruhl, H. A., Shaw, T. J., Sherman, A. D., Sprintall, J., Stephenson, G. R., Stuart, K. M. and Twining, B. S.: Islands of ice: Influence of free-drifting Antarctic icebergs on pelagic marine ecosystems, *Oceanography*, 25(3), 38–39, <https://doi.org/10.5670/oceanog.2012.72>, 2012.
- Wesche, C. and Dierking, W.: Iceberg signatures and detection in SAR images in two test regions of the Weddell  
580 Sea, Antarctica, *J. Glaciol.*, 58(208), 325–339, <https://doi.org/10.3189/2012J0G11J020>, 2012.
- Wesche, C. and Dierking, W.: Near-coastal circum-Antarctic iceberg size distributions determined from Synthetic Aperture Radar images, *Remote Sens. Environ.*, 156, 561–569, <https://doi.org/10.1016/j.rse.2014.10.025>, 2015.
- Williams, R. N., Rees, W. G. and Young, N. W.: A technique for the identification and analysis of icebergs in  
585 synthetic aperture radar images of Antarctica, *Int. J. Remote Sens.*, 20(15–16), 3183–3199, <https://doi.org/10.1080/014311699211697>, 1999.
- Willis, C. J., Macklin, J. T., Partington, K. C., Teleki, K. A., Rees, W. G. and Williams, G.: Iceberg detection using ers-1 synthetic aperture radar, *Int. J. Remote Sens.*, 17(9), 1777–1795, <https://doi.org/10.1080/01431169608948739>, 1996.
- 590 Young, N. W. and Hyland, G.: Applications of time series of microwave backscatter over the Antarctic region, in *Proceedings of the third ERS Scientific Symposium, 17-21 March 1997, Florence, Italy*, pp. 1007–1014, Frascati, Italy: European Space Agency, SP-414, , 1997.
- Young, N. W., Turner, D., Hyland, G. and Williams, R. N.: Near-coastal iceberg distributions in East Antarctica, 50-145°E, *Ann. Glaciol.*, 27, 68–74, <https://doi.org/10.3189/1998aog27-1-68-74>, 1998.
- 595 Zhang, E., Liu, L. and Huang, L.: Automatically delineating the calving front of Jakobshavn Isbræ from multitemporal TerraSAR-X images: A deep learning approach, *Cryosphere*, 13(6), 1729–1741, <https://doi.org/10.5194/tc-13-1729-2019>, 2019.